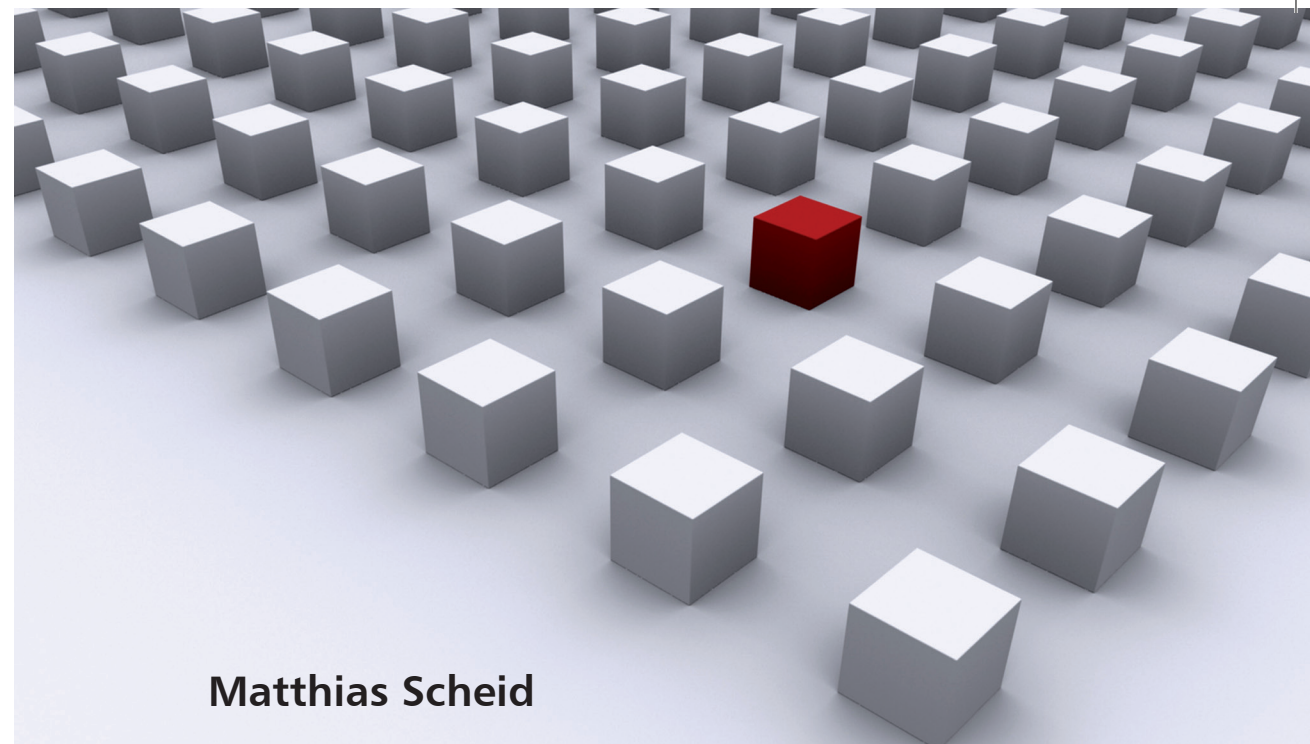


In recent years the research field of semiconductor spintronics has attracted considerable attention. This interest was fueled by the prospect of spin-based devices, which could possess enhanced functionalities compared to conventional charge-based microelectronics. However, in order to realize the building blocks for semiconductor spintronics devices a number of fundamental obstacles have to be overcome.

To this end, this thesis discusses several spin-related phenomena in two-dimensional electron gases, which can either be exploited as sources for spin currents/accumulations or which can be used for the efficient control of those spins. To be specific, it deals with coherent electron transport through wire geometries in the presence of spin-orbit interaction and/or magnetic fields. For the numerical calculations a powerful quantum transport code was used. The topics investigated in this thesis include spin ratchets, the phenomenon of current-induced spin accumulation and finally quantum interference spin phenomena in disordered systems.

Dissertationsreihe Physik - Band 12



Matthias Scheid

**Tailoring semiconductor
spintronics devices:
Tools for the creation and
control of spins in two-
dimensional electron gases**

Universitätsverlag Regensburg

Universitätsverlag Regensburg

ISBN 978-3-86845-047-7
gefördert von:

Alumni der physikalischen Fakultät
der Universität Regensburg e.V.



Universität Regensburg

Matthias Scheid

12
Dissertationsreihe
Physik



Matthias Scheid



Tailoring semiconductor
spintronics devices:
Tools for the creation and
control of spins in two-
dimensional electron gases

Tailoring semiconductor spintronics devices: Tools for the creation and control of spins in two-dimensional electron gases

Dissertation zur Erlangung des Doktorgrades der Naturwissenschaften (Dr. rer. nat.)
der naturwissenschaftlichen Fakultät II - Physik der Universität Regensburg
vorgelegt von

Matthias Scheid

aus Regensburg

September 2009

Die Arbeit wurde von Prof. Dr. Klaus Richter angeleitet.
Das Promotionsgesuch wurde am 24.09.2009 eingereicht.
Das Kolloquium fand am 03.02.2010 statt.

Prüfungsausschuss: Vorsitzender: Prof. Dr. Christian Back
1. Gutachter: Prof. Dr. Klaus Richter
2. Gutachter: Prof. Dr. Milena Grifoni
weiterer Prüfer: Prof. Dr. Ingo Morgenstern



Dissertationsreihe der Fakultät für Physik der Universität Regensburg, Band 12

Herausgegeben vom Präsidium des Alumnivereins der Physikalischen Fakultät:
Klaus Richter, Andreas Schäfer, Werner Wegscheider, Dieter Weiss

Matthias Scheid

**Tailoring semiconductor
spintronics devices:**

**Tools for the creation and
control of spins in two-
dimensional electron gases**

Universitätsverlag Regensburg

Bibliografische Informationen der Deutschen Bibliothek.
Die Deutsche Bibliothek verzeichnet diese Publikation
in der Deutschen Nationalbibliografie. Detaillierte bibliografische Daten
sind im Internet über <http://dnb.ddb.de> abrufbar.

1. Auflage 2010

© 2010 Universitätsverlag, Regensburg

Leibnitzstraße 13, 93055 Regensburg

Konzeption: Thomas Geiger

Umschlagentwurf: Franz Stadler, Designcooperative Nittenau eG

Layout: Matthias Scheid

Druck: Docupoint, Magdeburg

ISBN: 978-3-86845-047-7

Alle Rechte vorbehalten. Ohne ausdrückliche Genehmigung des Verlags ist es
nicht gestattet, dieses Buch oder Teile daraus auf fototechnischem oder
elektronischem Weg zu vervielfältigen.

Weitere Informationen zum Verlagsprogramm erhalten Sie unter:
www.univerlag-regensburg.de

Tailoring semiconductor spintronics devices: Tools for the creation and control of spins in two-dimensional electron gases

Dissertation zur Erlangung des Doktorgrades der Naturwissenschaften (Dr. rer. nat.)
der naturwissenschaftlichen Fakultät II - Physik der Universität Regensburg
vorgelegt von

Matthias Scheid
aus Regensburg
September 2009

Die Arbeit wurde von Prof. Dr. Klaus Richter angeleitet.
Das Promotionsgesuch wurde am 24.09.2009 eingereicht.
Das Kolloquium fand am 03.02.2010 statt.

Prüfungsausschuss: Vorsitzender: Prof. Dr. Christian Back
1. Gutachter: Prof. Dr. Klaus Richter
2. Gutachter: Prof. Dr. Milena Grifoni
weiterer Prüfer: Prof. Dr. Ingo Morgenstern



Dissertationsreihe der Fakultät für Physik der Universität Regensburg, Band 12

Herausgegeben vom Präsidium des Alumnivereins der Physikalischen Fakultät:
Klaus Richter, Andreas Schäfer, Werner Wegscheider, Dieter Weiss

Promotionsgesuch eingereicht am: 24.09.2009

Die Arbeit wurde angeleitet von: Prof. Dr. Klaus Richter

Prüfungsausschuss: Vorsitzender: Prof. Dr. Christian Back
1. Gutachter: Prof. Dr. Klaus Richter
2. Gutachter: Prof. Dr. Milena Grifoni
weiterer Prüfer: Prof. Dr. Ingo Morgenstern

1	Introduction	1
2	Spin dependent transport in nanostructures	7
2.1	Two-dimensional electron gases	9
2.1.1	Magnetic fields	10
2.1.2	Spin-orbit interaction	11
2.2	Landauer-Büttiker formalism	18
2.2.1	Scattering approach	18
2.2.2	Charge and spin currents	21
2.3	Green's function formalism for electron transport in nanostructures . .	26
2.3.1	Basic definitions	26
2.3.2	Numerical calculation scheme	30
3	Mesoscopic spin ratchets	37
3.1	Introduction	37
3.1.1	Ratchets: An overview	37
3.1.2	Spin ratchets: General idea	39
3.1.3	Coherent spin ratchets based on wire structures realized in 2DEGs	40
3.1.4	Self-consistent calculation of the voltage drop in wire geometries	43
3.1.5	Complementary methods for the creation of pure spin currents .	44

3.2	Resonant tunneling-based spin ratchets	45
3.2.1	Mechanism	45
3.2.2	Double-dot geometry realized in a 2DEG	46
3.2.3	Numerical results	49
3.3	Spin ratchets based on spin-orbit interaction	53
3.3.1	DC-transport in linear response	54
3.3.2	Creation of pure spin currents	56
4	Current-induced spin accumulation in wire geometries	67
4.1	Spin accumulation in semiconductors	68
4.2	Current-induced spin accumulation in quantum wires	70
4.2.1	Rashba spin-orbit interaction	71
4.2.2	Rashba and Dresselhaus spin-orbit interaction	74
4.2.3	Suppression of the current-induced spin accumulation in finite-sized systems	75
4.3	Extraction of current-induced spins	81
4.4	Electrical detection of current-induced spin accumulation	85
4.4.1	Detection principle	85
4.4.2	Detection by a lead with strong Zeeman splitting	88
4.4.3	Detection by a spin selective point contact	91
5	Coherent spin transport in disordered wires and the detection of the ratio α/β	95
5.1	System of choice	95
5.2	Quantum effects in the conductance of disordered wires	96
5.2.1	Weak localization and weak antilocalization	97
5.2.2	Universal conductance fluctuations	100
5.3	Suppression of spin relaxation in quantum wires	102
5.3.1	Narrow quantum wires	102
5.3.2	Rashba and Dresselhaus spin-orbit interaction of equal strength	109
5.4	All-electrical detection of the ratio α/β	112
5.4.1	Outline of the detection mechanism	112

5.4.2	Applicability of the detection mechanism	113
5.4.3	Influence of the cubic Dresselhaus term	116
6	Summary and perspectives	121
	References	125

CHAPTER 1

Introduction

The spin degree of freedom is a property of every particle. It is of quantum mechanical origin and has no classical correspondence. However, since it describes an angular momentum, in a simplified picture it is often identified with the self-rotation of the particle [1]. The spin angular momentum of a particle is given by $S = \hbar\sqrt{s(s+1)}$ and the projection to the z -axis by $S_z = \frac{\hbar}{2}m_s$, where the spin quantum number s is a multiple of $\frac{1}{2}$ and $m_s = -s, \dots, +s$.

Depending on the value of s , particles can be divided into two classes with different quantum statistical properties [2]. Particles with half integer spin quantum number $s = \frac{1}{2}, \frac{3}{2}, \frac{5}{2}, \dots$ are called fermions and obey Fermi-Dirac statistics. The wavefunction of a system of identical fermions has to be antisymmetric upon the exchange of two particles. A consequence of this requirement is the Pauli exclusion principle, which forbids two fermions to be in the same quantum state [3]. For instance, the electronic configuration of an atom is governed by this principle, yielding the structure of the periodic table of chemical elements. On the other hand, for particles with integer s we speak of bosons, which obey Bose-Einstein statistics. In contrast to fermions, two bosons are allowed to occupy the same quantum state. This leads to the intriguing effect of Bose-Einstein condensation [4], where at very low temperatures identical bosons accumulate in the single particle state of lowest energy.

The concept of spin has a long standing history [5]. The presence of spin was first noticed in the measurement of light absorption/emission spectra of atoms [6]. The principal, azimuthal and magnetic quantum numbers (n, l and m), accounting for the orbital motion of electrons in the Coulomb field of the core, were not enough to explain the spectra of atoms in a magnetic field. The spin quantum number s had also to be taken into account. Although the shortcoming of the atomic model with only three quantum numbers was well known, it took some time — mainly due to the lack of a

classical interpretation — until the presence of a spin angular momentum was accepted. Other early evidence for the existence of the spin degree of freedom had been provided by the famous experiment of Stern and Gerlach [7]. They sent a collimated beam of silver atoms through an inhomogeneous magnetic field, which exerted a force on the magnetic moment of the atoms. Due to an unpaired valence electron, the spin angular momentum of the silver atom has two possible orientations (generally referred to as spin-up and spin-down)¹. Therefore, the silver atoms experienced different forces depending on their spin state, yielding two separated beams, one of atoms with an unpaired spin-up electron and one of atoms with an unpaired spin-down electron.

Theoretically the quantum mechanical concept of spin was first introduced by W. Pauli, who extended the Schrödinger equation by a two-valued degree of freedom of non-classical origin [8]. A few years later P. Dirac derived his famous equation, which combined special relativity and quantum mechanics for elementary spin- $\frac{1}{2}$ particles. There, it was not necessary to artificially introduce the spin of the particle, but it emerged naturally from the derivation [9].

In this thesis we consider electronic transport in semiconductors, where the electrons have velocities much smaller than the speed of light. Therefore, we use the Pauli equation, which can be derived from the Dirac equation in the non-relativistic limit. Representing spin- $\frac{1}{2}$ particles, the electronic wavefunctions in the Pauli equation are given by two-component spinors.

Since those early years, many interesting spin-related effects have been identified [5], some of them even having a big technological impact.

For instance, in 1988 two groups discovered an effect called giant magnetoresistance [10, 11], which earned the scientists A. Fert and P. Grünberg the shared Nobel prize in physics in 2007. In structures composed of alternating layers of ferromagnetic and non-magnetic metals the resistivity strongly depends on the relative magnetization of the ferromagnetic layers, with high resistivity for anti-parallel and low resistivity for parallel orientation. Soon after its discovery, this robust effect found its way into commercial products, such as read heads for hard drives, magnetoresistive random access memory and magnetic field sensors [12].

Another example of the technological importance of the spin of particles is the magnetic resonance imaging technique. In modern medicine it is used for the visualization of the interior of the human body. It makes use of the precession of the nuclear spins of for example hydrogen atoms (as present in H₂O molecules) around externally applied magnetic fields [13]. In 2003 the Nobel prize in medicine was awarded to P. Lauterbur and P. Mansfield for their pioneering work on magnetic resonance imaging.

¹The orbital angular momentum of silver atoms is zero

Semiconductor spintronics

For present day information processing technologies, semiconductor-based microelectronics is an indispensable ingredient. Over the last decades, the increased miniaturization of commercial semiconductor devices has also caused computational power to rise steadily. Following an empirical law introduced by G. Moore [14] the number of transistors per square area on a computer chip doubles approximately every 1.5 years. Although their size constantly decreased, their basic operation principle remained unchanged, relying on charge transport in the classical, diffusive transport regime. Already at sizes above the atomic scale, the transistors will be impeded by increased heating or quantum mechanical processes (e.g. tunneling), which might limit their functionality [15]. Since state of the art transistors possess a channel length of only 45nm, soon the straightforward miniaturization will come to an end and devices with different functionalities have to be developed to further increase computational power.

In recent years, therefore the electron spin has moved into the focus of semiconductor research. The hope is to integrate the electron spin as an additional degree of freedom into existing devices, which are solely based on the electron charge. This field of research is commonly called semiconductor spintronics, with the term spintronics being an abbreviation for spin-based electronics or spin transport electronics [12, 16]. Encoding information in the spin of electrons allows for new functionalities compared to conventional charge-based microelectronics devices. Furthermore, they carry the prospect of lower power consumption, higher integration densities and non-volatility of memory [12, 17], to name but a few. In recent years, many promising spintronics device proposals have been put forward, most prominently including spin-based transistors [18, 19].

Current research mainly focuses on the goal of fabricating devices on a commercial scale in the near future, where the spin degree of freedom plays an important role. In order to be a profitable venture for a company, devices such as spin-based transistors or memory storage devices need to be able to outperform not only current conventional electronics devices, but to take the performance to a significantly higher level to warrant investment in new production facilities. Besides that, semiconductor spintronics also has to compete with the devices brought up in other promising fields of nano-scale physics such as molecular [20] or carbon-based electronics [21].

In order to be able to realize competitive semiconductor spintronics devices, there are certain prerequisites that need to be fulfilled [12]. Typically, they are (i) the creation of spin currents/accumulations, (ii) precise control over the spin state, (iii) long spin lifetimes and (iv) the detection of spin polarization. Those basic requirements can be illustrated using the famous paradigmatic device proposal of semiconductor spintronics, the Datta-Das spin transistor [18]. Its working principle is analogous to that of an electro-optic modulator, where the spin of the electron takes the role of the beam of polarized light. Spin polarized electrons are injected into a two-dimensional electron gas (2DEG) from a ferromagnetic contact. Those electrons then move ballistically in

the 2DEG in response to a bias voltage between the source and drain contacts, with the spin undergoing rotations due to spin-orbit interaction (SOI), which is present in the 2DEG. Since the strength of the SOI can be changed via gate voltages [22] it is also possible to efficiently control the orientation of the electron spin. For the detection another ferromagnetic contact is used. Depending on the spin polarization of the electron and the magnetization of the contact, the electrons can either enter the contact or are reflected. Therefore, as in conventional transistors, the on/off-state corresponds to the presence/absence of an electrical current.

In recent years a lot of progress has been made in the creation, control and detection of spins [16, 23, 24], culminating in the first experimental realization of gate-controlled spin precession in a spin transistor [25]. In the following we will briefly review those advances.

For the creation of spin polarization in semiconductors there exist several promising approaches. Due to the conductivity mismatch between metals and semiconductors, spin injection from ferromagnetic metals via Ohmic contacts is not very efficient [26]. Therefore, recent research has focused on the injection of spins from ferromagnets via tunnel- or Schottky-barriers [27, 28]. Alternatively, the problem of the conductivity mismatch can be avoided by using magnetic semiconductors as injectors [29, 30].

Spin polarization in semiconductors can also be created via optical orientation of the electrons. Exploiting the selection rules for transitions between different bands of the semiconductor, the irradiation with circularly polarized light can be used for the generation of a non-equilibrium spin accumulation [31].

However, even without the use of magnetic materials or optical methods it is possible to induce spin accumulations or spin polarized currents in semiconductors only by electrical means. In materials with SOI an electrical current causes an orientation of spins, which can be used for this purpose. The effects are called current-induced spin accumulation [32, 33] and spin Hall effect [34, 35], respectively. Furthermore, Zeeman spin splitting due to a strong external magnetic field has also been employed for the injection of spins, namely via spin selective narrow point contacts realized in 2DEGs [36]. The detection of the spins in semiconductors is closely related to their creation. Most of the methods just outlined can also be used in this regard. For instance, spins can be detected by ferromagnetic contacts [37], via the magneto-optic Kerr effect [38, 39] or by spin selective point contacts [36].

For the controlled manipulation of the spin state of the electron the most promising approach is the use of SOI, where the spin of the electron is coupled to its orbital motion. The Rashba SOI due to asymmetric quantum well confinement potentials is especially interesting, because its strength can be controlled electrically via gate voltages [22].

In spintronics applications, the information encoded in the electron spin should ideally be preserved during the operation of the device. However, in realistic semiconductors, spins relax due to scattering processes in the presence of SOI and/or due to the coupling to nuclear spins [24, 40]. In order to increase the spin lifetime there exist a variety of approaches, e.g. the growth of quantum wells along certain crystallographic

directions [41], the tuning of the strength of competing SOI mechanisms [42, 43] or quantum confinement [44]. The long spin coherence times achieved in quantum dots also make the electron spin an interesting candidate for the use as a quantum bit (qubit) in quantum information processing [45].

Purpose of this work

Despite the progress made in the creation, control and detection of spins in semiconductors over the last decade and the apparent simplicity of the Datta-Das spin transistor, only recently the functionality of such a spin transistor has been demonstrated experimentally [25]. However, in view of the basic requirements listed above, there are still many obstacles that have to be overcome [16, 23] on the road to commercial semiconductor spintronics devices.

Besides the aim of facilitating spintronics devices for commercial use, there is also the fundamental interest in the basics of spin related physics in semiconductors. Exciting theoretical predictions, as e.g. the spin Hall effect [34, 35] or the quantum spin Hall effect [46], have been experimentally verified in recent years [47, 48].

The topics presented in this thesis are fueled by both of those general motivations. There is the desire to qualitatively understand and quantitatively predict spin-related effects in semiconductors. On the other hand those effects form the basis of a variety of device proposals, which constitute a first step on the road to the realization of commercial semiconductor spintronics devices.

Therefore, in this thesis we concern ourselves with several spin-related phenomena in 2DEGs, which can either be exploited as sources for spin currents and spin accumulations or which can be used for the efficient control of those spins.

Contents of the thesis

The thesis is organized in the following way:

In chapter 2 we outline the general framework of coherent electron transport in 2DEGs. Specifically, in section 2.2 we consider spin-dependent transport through quantum wire geometries within the Landauer-Büttiker approach. For the efficient calculation of the transport properties of those devices, in section 2.3 we give a brief introduction to the Green's function formalism for electronic transport in semiconductors. We outline the numerical computation scheme, which is based on a discretized, tight-binding Hamiltonian. The equations given there allow us to evaluate the charge and spin currents, as well as the electron and spin densities in the wire geometries treated in this thesis.

In chapter 3 we consider the possibility of creating pure spin currents in the absence of net charge transport. To this end we use setups based on wire geometries in response to an ac-bias voltage, thereby generalizing the concept of particle/charge ratchets [49] to the realm of spin. After a brief introduction into the physics of ratchets and the

coherent spin ratchet mechanism, we perform numerical calculations showing the functionality of two specific spin ratchet setups. Namely, in section 3.2 we consider a double-dot geometry with position dependent magnetic field due to ferromagnetic stripes on top of the heterostructure and in section 3.3 we investigate a quantum wire with an array of electrostatic barriers in the presence of Rashba SOI.

In chapter 4 we explore the phenomenon of current-induced spin accumulation (CISA) in 2DEGs [50], where a non-equilibrium spin accumulation is created in response to an electrical current flowing in a system with SOI. The polarization of the spins depends on the relative size of the different SOI contributions and the direction of the electrical current with respect to the crystal lattice. This makes it possible to control the spin polarization by electrical means only. In section 4.2 we investigate the CISA in a quantum wire, where we especially focus on finite size effects and the interplay between Rashba and Dresselhaus SOI.

Typically, the CISA is large in systems with strong SOI, which are unfortunately also impeded by strong spin relaxation. However, in section 4.3 we will show that via a narrow side contact the CISA can be extracted into regions with long spin lifetimes, where it could be used for spintronics applications.

The chapter is closed with the outline of a possible all-electrical detection method for the CISA using a multiterminal geometry with a spin selective lead.

Finally, in chapter 5 we focus on the efficient control of spins in disordered quantum wires. We aim at identifying suitable systems, where spin relaxation is reduced, making them attractive for the realization of devices requiring coherent spin transport. Therefore, in section 5.3 we investigate the influence of confinement and the interplay between Rashba SOI, Dresselhaus SOI and an in-plane magnetic field on the quantum correction to the conductance and the universal conductance fluctuations.

For many device proposals the knowledge of the relative strength of the Rashba and Dresselhaus SOI contributions is of great importance for the control of the electron spin. Therefore, in section 5.4 we propose an efficient, all-electrical detection mechanism for the ratio between the strengths of Rashba and Dresselhaus SOI, using the results obtained earlier in that chapter.

Lastly in chapter 6 we review the most important results obtained in this thesis and discuss future directions and perspectives of semiconductor spintronics research.

CHAPTER 2

Spin dependent transport in nanostructures

The solid state of matter [51] usually consists of atoms arranged in an ordered way forming a periodic crystal lattice. The energy dispersion relation of such a solid consists of a set of energy bands. This fact can be understood when treating the most loosely bound (valence) electrons of the elementary atoms, from which this crystal is built, as free electrons. They are delocalized across the crystal and feel the periodic crystal-lattice potential. Due to Bloch's theorem valid for periodic potentials the band structure in the energy dispersion develops. The exact shape of those bands is determined by the composition of the crystal. Depending on the filling of these bands in the groundstate of the solid, we distinguish between metals, semiconductors and insulators. When the highest occupied band, the valence band, is only partially filled, we speak of metals, which are excellent electrical conductors. On the other hand, the valence band of semiconductors and insulators is completely filled in the groundstate and no electrical current can flow. Those two types of solids can be distinguished by the size of the energy band-gap E_g between the fully filled valence band and the empty conduction band. For semiconductors this band gap is smaller than 2 eV and thermal excitation can induce a non-negligible conductivity. A typical band profile of a III-V semiconductor with a direct band-gap, as e.g. GaAs, is sketched in Fig. 2.1. The valence band has p -type character and thus consists of three kinds of bands: A heavy hole (HHB), a light hole (LHB) and a spin-orbit split-off band (SOB). On the contrary, the conduction band (CB) is of s -type and contains only one kind of band. Each of those four bands shown in Fig. 2.1 is twofold degenerate due to the spin degree of freedom of the electrons. This degeneracy can be lifted, e.g., by a magnetic field or spin-orbit interaction, which we will address later in this chapter.

Since all physical properties of interest in this thesis are determined by electrons close to the Fermi energy, we can apply the Fermi liquid theory [51] to the electrons in the

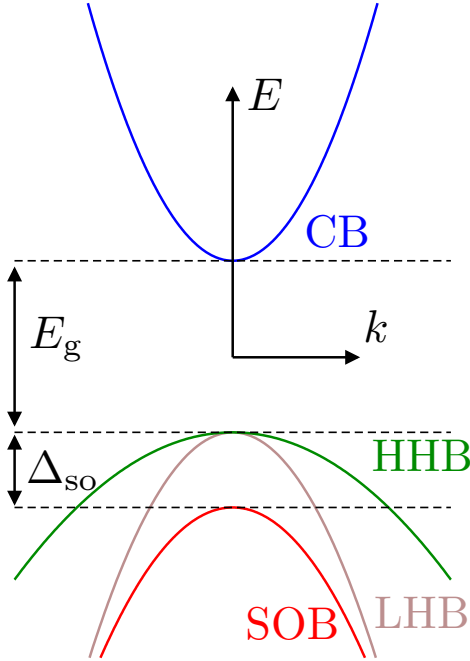


Figure 2.1: Sketch of the energy dispersion of a typical direct band-gap semiconductor such as GaAs. It includes the energetically lowest lying conduction band (CB) and the three highest valence bands, the heavy hole (HHB), the light hole (LHB) and the spin-orbit split-off band (SOB).

conduction band of the semiconductor. It states that electron–electron interactions can be neglected at low temperatures and the physics is well described in a single particle picture. For the electrons in the conduction band this yields the following effective mass Hamiltonian for a bulk semiconductor [52]:

$$H_0 = \frac{p_x^2 + p_y^2 + p_z^2}{2m^*} + E_c. \quad (2.1)$$

This Hamiltonian describes the case of free electrons, although with an effective mass m^* which is usually much smaller than the free electron mass m_0 . The effect of the electrostatic potential of the underlying crystal lattice is not directly included in Eq. (2.1) but encoded in the effective mass. In this model, the eigenfunctions are plane waves

$$\phi(\vec{r}) \propto e^{i\vec{k}\cdot\vec{r}}, \quad (2.2)$$

which do not show variations on the scale of the elementary crystal atoms. Therefore, $\phi(\vec{r})$ represents a coarse-grained version of the actual electronic wavefunction. Since this effective mass approximation has proven to be successful in describing the physics of conduction band electrons in semiconductors [52], we also adopt it for our purposes. The isotropy of the effective mass and the parabolic energy dispersion that are inherent in Eq. (2.1), are fair approximations for electrons close to the conduction band minimum E_c (i.e. for low electron densities) in many semiconductors, as e.g. GaAs. Theoretically, the value of m^* can be extracted from band structure calculations [53], such as the $\vec{k}\cdot\vec{p}$ Kane model. Experimentally, m^* can be determined, e.g., by cyclotron resonance measurements [51].

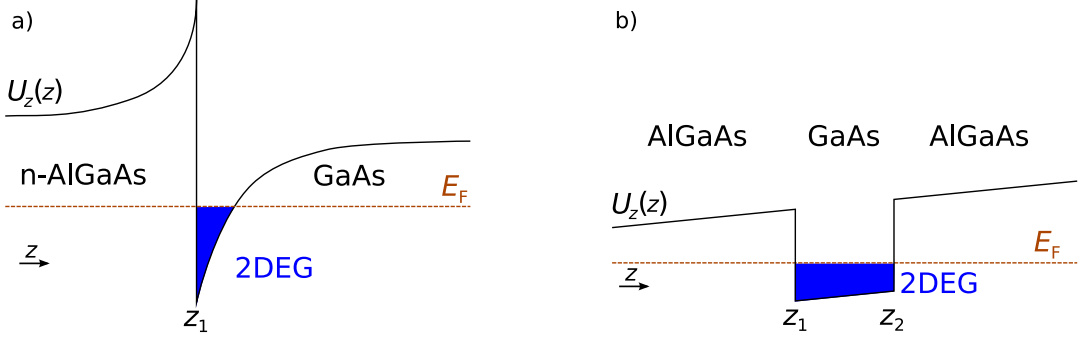


Figure 2.2: Electrostatic potential seen by the conduction band electrons in two kinds of semiconductor heterostructures, where a 2DEG is formed in a quantum well. a) Triangular quantum well established at the interface between n -AlGaAs and GaAs. b) Square quantum well in a AlGaAs/GaAs/AlGaAs layer structure.

2.1 Two-dimensional electron gases

In the past decades we have witnessed an enormous progress in the epitaxial growth of semiconductor heterostructures. Nowadays it is possible to create layered structures of different semiconductor materials with very high purity and nearly perfect interfaces. Those growth techniques allow to fabricate semiconductor heterostructures, where conduction electrons are confined in one dimension and can only move in the plane perpendicular to the confinement direction [54]. In Fig. 2.2 we sketch the electrostatic potential $U_z(z)$ (along the growth direction \hat{z}) experienced by conduction band electrons in two typical situations, where a two-dimensional electron gas (2DEG) emerges. In these cases, $U_z(z)$ is composed of the spatially dependent conduction band-edge profile $E_c(z)$ and optionally an electrostatic potential due to space charges (e.g. due to doping) and/or an externally applied bias voltage. Figure 2.2a shows a triangular quantum well, which forms, e.g., at the interface between n -doped AlGaAs and undoped GaAs and Fig. 2.2b shows a square quantum well, where a thin layer of the semiconducting material supporting the 2DEG, here GaAs, is sandwiched between layers of a different semiconducting material, here AlGaAs. In both quantum well structures, the Fermi energy lies above the minimum of the quantum well and therefore a 2DEG emerges. In view of Eq. (2.1), the Hamiltonian of such a heterostructure is given by [55]

$$H_{\text{HS}} = \frac{p_x^2 + p_y^2}{2m^*(z)} + p_z \frac{1}{2m^*(z)} p_z + U_z(z), \quad (2.3)$$

where we included the potential $U_z(z)$ and a position dependent effective mass $m^*(z)$ due to the different materials involved. For simplicity we assume very deep quantum wells, where in Fig. 2.2 the boundaries at $z = z_1$ for the triangular quantum well and at $z = z_1, z_2$ for the square quantum well can be approximated as infinitely high. Then we can neglect the position dependence of the effective mass and the resulting

Hamiltonian of the quantum well

$$H_{\text{QW}} = \frac{p_x^2 + p_y^2 + p_z^2}{2m^*} + U_z(z) \quad (2.4)$$

is separable in the three spatial coordinates. The eigenfunctions $\phi(x, y, z)$ of H_{QW} thus read

$$\phi(x, y, z) = e^{ik_x x} e^{ik_y y} \xi_m(z), \quad (2.5)$$

where the quantum numbers k_x and k_y are continuous due to the free motion in the (x, y) -plane and the quantum number m is discrete due to the confinement in z -direction. In the corresponding energy dispersion relation

$$E(k_x, k_y, m) = \frac{\hbar^2(k_x^2 + k_y^2)}{2m^*} + \epsilon_m \quad (2.6)$$

the sub-band energy values ϵ_m are dependent on the specific form of the potential $U_z(z)$. Here we consider the case, when only the lowest sub-band ($m = 1$) is populated, which is justified for low electron densities, when the Fermi energy is below the band edge of the second lowest sub-band ($m = 2$): $E_F < \epsilon_2$. For convenience we set $\epsilon_1 = 0$ and rewrite the effective Hamiltonian for the 2DEG as

$$H_{\text{2DEG}} = \frac{p_x^2 + p_y^2}{2m^*}. \quad (2.7)$$

For low temperatures (below a few Kelvin), when phase-breaking processes such as electron-phonon or electron-electron scattering are strongly reduced, electron transport is phase coherent over distances of up to a few microns, i.e. longer than the typical sizes of the systems investigated. Therefore, the Hamiltonian Eq. (2.7) is well suited for our purposes and marks the starting point of our further studies. To be more specific, we do not consider electron transport in a bulk 2DEGs but in geometries created on a 2DEG by further confinement. This confinement is generally incorporated in the Hamiltonian (2.7) by the addition of an electrostatic potential $U_{\text{conf}}(x, y)$, effectively restricting the motion of the electrons to an area of finite extension. To experimentally create confined structures on a 2DEG, e.g. lithographic methods, etching techniques or gate electrodes can be employed. For a detailed overview of the methods commonly used we refer to Refs. [54, 56] and references therein. Theoretically, we will treat transport through such geometries within the Landauer-Büttiker approach that will be the topic of section 2.2.

2.1.1 Magnetic fields

The influence of a magnetic field on the electrons in the 2DEG is twofold. As already mentioned earlier, the conduction band is doubly degenerate due to the spin degree of

freedom of the electron. Therefore, in general the Schrödinger equation, $H\Phi(x, y) = E\Phi(x, y)$, is a system of two coupled differential equations, where H , as given e.g. in Eq. (2.7), is not a scalar operator but rather a 2×2 matrix and the corresponding wave function $\Phi(x, y)$ is not a scalar function but given by a spinor

$$\Phi(x, y) = \begin{pmatrix} \Phi_1(x, y) \\ \Phi_2(x, y) \end{pmatrix}. \quad (2.8)$$

The spin degeneracy of the 2DEG can be lifted by the coupling of the spin magnetic moment $\vec{\mu}_s$ to a magnetic field \vec{B} and results in the energy splitting $\Delta E = -\vec{\mu}_s \cdot \vec{B}$, which is commonly referred to as the Zeeman effect. Quantum mechanically this effect is accounted for by the addition of the term [57]

$$H_Z = \frac{\mu_B g^*}{2} \vec{\sigma} \cdot \vec{B} \quad (2.9)$$

to the Hamiltonian of the 2DEG, where $\mu_B = e\hbar/(2m_0)$ is the Bohr magneton and $\vec{\sigma}$ is the vector of Pauli matrices. Furthermore, the electronic g -factor $g_0 \approx 2$ for free electrons is replaced by an effective g -factor g^* , which is a material parameter that can be obtained from bandstructure calculations [58] and can differ strongly from g_0 . In principle, the confinement of a quantum well results in an anisotropic g -factor in the 2DEG, with g_{\parallel}^* for magnetic fields in the plane of the 2DEG and g_{\perp}^* for B_z perpendicular to it [57]. However, we assume $g_{\parallel}^* = g_{\perp}^* = g^*$, since for the systems investigated in this thesis the Zeeman splitting due to B_z plays only a minor role.

Apart from the Zeeman coupling the magnetic field also has a direct influence on the orbital motion of the electrons. Classically the motion of a charged particle in a magnetic field leads to a force perpendicular to both the direction of motion and the magnetic field, the so-called Lorentz force. Quantum-mechanically this influence on the orbital motion of the electrons is incorporated via the so-called minimal substitution of the operator p_i by the generalized momentum $\pi_i = (p_i + eA_i)$ [7]. Since in this work we consider electrons strictly confined to the (x, y) -plane, the only magnetic field component that influences their orbital motion is B_z . This approximation is well justified, when the cyclotron radius due to an in-plane magnetic field is much larger than the width of the quantum well.

2.1.2 Spin-orbit interaction

Apart from the Zeeman effect, where the spin couples to an external magnetic field, the spin degeneracy in a semiconductor can also be lifted by a different mechanism. Namely, the magnetic field causing the energy splitting $\Delta E = -\vec{\mu}_s \cdot \vec{B}$ can also be a field inherent to the physical system. As the name spin-orbit interaction (SOI) suggests, the magnetic field we refer to is related to the orbital motion of the electrons. An electron moving in an electric field in the laboratory frame, experiences also a

magnetic field after a Lorentz transformation into its rest frame. This magnetic field couples to the electron's spin leading to an energy splitting due to SOI which is proportional to the electric field $\vec{E} \propto \vec{\nabla}U$ and described by a Hamiltonian of the general form [24]:

$$H_{\text{so}} \propto \vec{p} \cdot (\vec{\sigma} \times \vec{\nabla}U). \quad (2.10)$$

Probably the most prominent representation is the SOI in atomic physics, which was also the instance first discovered. There, the spin of an electron orbiting the nucleus couples to the magnetic field in the rest frame of the electron due to the Coulomb potential of the nucleus in the laboratory frame [1].

In the III-V semiconductor quantum wells, which are typically considered in this work, there are two important contributions to the SOI [57]. The Dresselhaus SOI appears due to the electric fields inherent in the periodic crystal structure in materials with bulk inversion asymmetry (BIA) of the lattice. The Rashba SOI on the other hand is present in semiconductor heterostructures with structural inversion asymmetry (SIA), where the confinement potential of the quantum well is asymmetric.

Rashba spin-orbit interaction

The 2DEGs under consideration in this thesis are usually realized in quantum wells built in layered structures from different semiconductor materials. A typical example for the electrostatic potential profile of such a quantum well is shown in Fig. 2.2. Its form $U_z(z) = E_c(z) + U_{\text{sc}}(z) + U_{\text{ext}}(z)$ is determined by the conduction band profile $E_c(z)$, the potential $U_{\text{sc}}(z)$ due to space charges, as e.g. introduced by doping, and an externally applied electrostatic potential $U_{\text{ext}}(z)$ [24]. Hence, a finite electric field $E_z = -(1/e)\partial U_z(z)/\partial z$ along the growth direction can be present, which in turn causes SOI. However, performing thorough calculations, it was found that the Rashba SOI experienced by the conduction band electrons is not, as naively expected, due to the electric field in the conduction band, but due to the corresponding one in the valence band [59]. Furthermore, not only the form of the electric field inside the quantum well is important for the strength of the SOI, but there are also contributions from interfaces [60], as e.g. at z_1 and z_2 of the quantum wells shown in Fig. 2.2.

This kind of SOI, which is based on the SIA of the semiconductor heterostructure, is known as the Rashba SOI, since it was first introduced by E. Rashba in 1959 [61]. More than two decades later, Y. Bychkov and E. Rashba were able to attribute the unusual pattern in the Shubnikov-de Haas (SdH) oscillations of 2DEGs [62] and two-dimensional hole gases (2DHGs) [63] realized at the interface of GaAs-Al_xGa_{1-x}As heterostructures to this kind of SOI¹ [64]. The Hamiltonian describing the Rashba SOI is given by:

$$H_{\text{R}} = \frac{\alpha}{\hbar}(\sigma_x p_y - \sigma_y p_x). \quad (2.11)$$

¹Therefore, the Rashba SOI is sometimes also called Bychkov-Rashba SOI.

Here, the parameter α denotes the strength of the Rashba SOI. For a uniform electric field $E_z = -(1/e)\partial[U_{\text{sc}}(z) + U_{\text{ext}}(z)]/\partial z$ due to the space charges and/or the external potential, and upon neglecting contributions from the interfaces (as justified, e.g., in deep quantum wells), this strength was found to have the value [65, 66]

$$\alpha = \frac{e\hbar^2}{2m^*} \frac{\Delta_{\text{so}}(2E_g + \Delta_{\text{so}})}{E_g(E_g + \Delta_{\text{so}})(3E_g + 2\Delta_{\text{so}})} E_z. \quad (2.12)$$

This quantity was calculated within the $\vec{k} \cdot \vec{p}$ Kane model taking into account the conduction band and the three valence bands², as sketched in Fig. 2.1. Here, the energy difference Δ_{so} denotes the spin-orbit splitting of the valence bands and E_g the direct bandgap between valence and conduction band. In view of Eq. (2.12) it is clear that α is most pronounced when E_g is relatively small, i.e. in so-called narrow gap semiconductors. Experimentally the value of α can be determined, e.g., from the beating pattern in the SdH oscillations [67]. In narrow gap semiconductors the highest values found were of the order of $\alpha = 10^{-11} \text{eV m}$ [24].

Since α depends on the electric field in the quantum well, it is not a fixed material parameter and there are several ways to change its value. During the growth process one can tailor quantum wells with the desired strength of the Rashba SOI by selectively adapting the doping in the heterostructure [68]. Furthermore, α can be controlled by an externally applied gate voltage via $U_{\text{ext}}(z)$ [22]. The latter method is especially promising, since it allows to change the strength of the Rashba SOI electrically even after the growth process is already completed. This could help for the realization of several semiconductor spintronics device proposals relying on an electrical control of the SOI, as e.g. spin field effect transistors [18, 19].

In contrast to a quantum well with SIA as sketched in Fig. 2.2, in a quantum well which possesses inversion symmetry with respect to the growth direction, the Rashba SOI is absent. Only when higher sub-bands of the quantum well are populated, a finite value for α can be recovered due to a contribution from the interfaces [69] even in symmetric quantum wells.

Dresselhaus spin-orbit interaction

The second important SOI contribution in 2DEGs realized in III-V zinc-blende semiconductors is due to the structure of the crystal lattice itself. The unit cell of a zinc-blende crystal consists of two atoms, where for the case of a III-V semiconductor the first (second) atom is from the third (fifth) main group, for example a Gallium (Arsenide) atom. Since the lattice is built from two sorts of atoms, the semiconductor possesses BIA and naturally electric dipoles exist between the neighboring Gallium and Arsenide atoms. In view of Eq. (2.10), the Dresselhaus SOI can be understood as a consequence of those spatially dependent electric fields [40]. The BIA of the crystal

²Due to the spin degree of freedom the model involves eight bands in total.

lattice is essential for the presence of a finite Dresselhaus SOI. For instance, in bulk silicon or diamond the Dresselhaus SOI is absent, since the unit cell of the diamond crystal lattice, which is equivalent to a zinc-blende lattice, consists of two equal atoms. The energy dispersion for semiconductors with this kind of SOI was calculated for the first time by G. Dresselhaus in 1955 [70]. For a coordinate system (x, y, z) chosen along the main crystallographic axes ($[100], [010], [001]$), the Hamiltonian describing the Dresselhaus SOI for electrons in the conduction band of a bulk semiconductor, is given by

$$H_D^{\text{bulk}} = \frac{\gamma}{\hbar^3} \vec{\sigma} \cdot \begin{pmatrix} p_x(p_z^2 - p_y^2) \\ p_y(p_x^2 - p_z^2) \\ p_z(p_y^2 - p_x^2) \end{pmatrix}, \quad (2.13)$$

where γ denotes the strength of the SOI. It is a material specific parameter and in contrast to the Rashba SOI strength it cannot be changed easily by electrical means. The exact value of γ is a controversial issue. Both experimentally and theoretically obtained values for γ differ strongly depending on the systems and methods used. Even in GaAs, the most studied III-V semiconductor material, no consensus has been reached yet, with estimates in the range of $8.5 \cdot 10^{-30} \text{ eVm}^3 < \gamma < 34.5 \cdot 10^{-30} \text{ eVm}^3$ [71].

Since electrons confined to a quantum well essentially only move in a plane, the corresponding Dresselhaus SOI Hamiltonian for a 2DEG can be obtained by averaging the momentum in the growth direction over the first subband of the quantum well. For a quantum well grown in $[001]$ -direction we receive two contributions, namely [72, 73]

$$H_{D1} = \frac{\beta}{\hbar} [\sigma_x(p_x \cos 2\phi - p_y \sin 2\phi) - \sigma_y(p_x \sin 2\phi + p_y \cos 2\phi)], \quad (2.14)$$

which is linear in momentum, from now on referred to as linear Dresselhaus contribution, and

$$H_{D3} = \frac{\gamma}{\hbar^3} \left[\sigma_x \left(-\frac{1}{2} p_x^2 p_y \sin 2\phi - p_x p_y^2 \cos 2\phi + \frac{1}{2} p_y^3 \sin 2\phi \right) + \sigma_y \left(\frac{1}{2} p_x^3 \sin 2\phi + p_x^2 p_y \cos 2\phi - \frac{1}{2} p_x p_y^2 \sin 2\phi \right) \right], \quad (2.15)$$

which is cubic in momentum and therefore called cubic Dresselhaus SOI. For convenience and the later use in chapters 4 and 5, in Eqs. (2.14) and (2.15) we introduced a new coordinate system which is rotated around the $[001]$ -direction by the angle ϕ with respect to the old one. In contrast to the Rashba SOI, the Dresselhaus SOI depends on the growth direction of the quantum well and the structures realized on the corresponding 2DEG. The strength of the linear Dresselhaus SOI is given by $\beta = \gamma \langle k_z^2 \rangle$, where $\langle k_z^2 \rangle$ can be estimated as $\langle k_z^2 \rangle = (\pi/D)^2$ for an infinitely deep quantum well of width D . In view of those results it is obvious that the linear term is the dominating contribution in quantum wells of small thickness D . For this reason we will mostly neglect H_{D3} in the rest of this thesis, nevertheless discussing possible alterations of

the results stemming from the presence of the cubic Dresselhaus term. In contrast to the parameter γ , the strength of the linear Dresselhaus contribution β (together with the Rashba contribution) can be extracted experimentally rather precisely from time-resolved Faraday rotation measurements [74].

Electronic properties of a 2DEG with spin-orbit interaction

Having introduced both Rashba and Dresselhaus SOI, we now briefly outline how their presence affects the physics of the 2DEG. We consider the case, where the cubic Dresselhaus term is negligible, as e.g. in very thin quantum wells. The 2DEG Hamiltonian with SOI linear in momentum then reads ($\phi = 0$, i.e. $\hat{x} \parallel [100]$):

$$H = \frac{p_x^2 + p_y^2}{2m^*} + \frac{\alpha}{\hbar}(\sigma_x p_y - \sigma_y p_x) + \frac{\beta}{\hbar}(\sigma_x p_x - \sigma_y p_y). \quad (2.16)$$

The corresponding energy dispersion relation is given by [19]

$$E_{\pm}(k_x, k_y) = \frac{\hbar^2(k_x^2 + k_y^2)}{2m^*} \pm \sqrt{(\alpha k_x + \beta k_y)^2 + (\alpha k_y + \beta k_x)^2}. \quad (2.17)$$

When only one kind of SOI is present, i.e. either $\alpha = 0$ or $\beta = 0$, it is isotropic and only depends on the absolute value of \vec{k} . On the other hand when both SOI contributions are finite, the energy dispersion becomes anisotropic, which has also important implications on the transport of electrons, as we will see later in this thesis. As an example in Fig. 2.3a we show the energy dispersion for one specific choice of α/β .

Due to its particular form, the SOI contributions in Eq. (2.16) are often written as momentum dependent magnetic fields, since they can be recast as a Zeeman coupling term

$$H_R + H_{D1} = \frac{\mu_B g^*}{2} \vec{\sigma} \cdot \vec{B}_{\text{so}}(p_x, p_y) \quad (2.18)$$

with the momentum dependent magnetic field due to SOI:

$$\vec{B}_{\text{so}}(p_x, p_y) = \frac{2}{\mu_B g^* \hbar} \begin{pmatrix} \alpha p_y + \beta(p_x \cos 2\phi - p_y \sin 2\phi) \\ -\alpha p_x - \beta(p_x \sin 2\phi + p_y \cos 2\phi) \\ 0 \end{pmatrix}. \quad (2.19)$$

This way of writing the SOI is especially convenient when we deal with systems, where both SOI and a Zeeman splitting due to a magnetic field are present as in chapter 5 of this thesis. In Figs. 2.3b-d we illustrate the dependence of \vec{B}_{so} on the in-plane momentum (k_x, k_y) for three special cases. When only Rashba SOI is present \vec{B}_{so} always points perpendicular to the direction of the momentum, see Fig. 2.3b. In a 2DEG with only linear Dresselhaus SOI the direction of \vec{B}_{so} is dependent on the electron

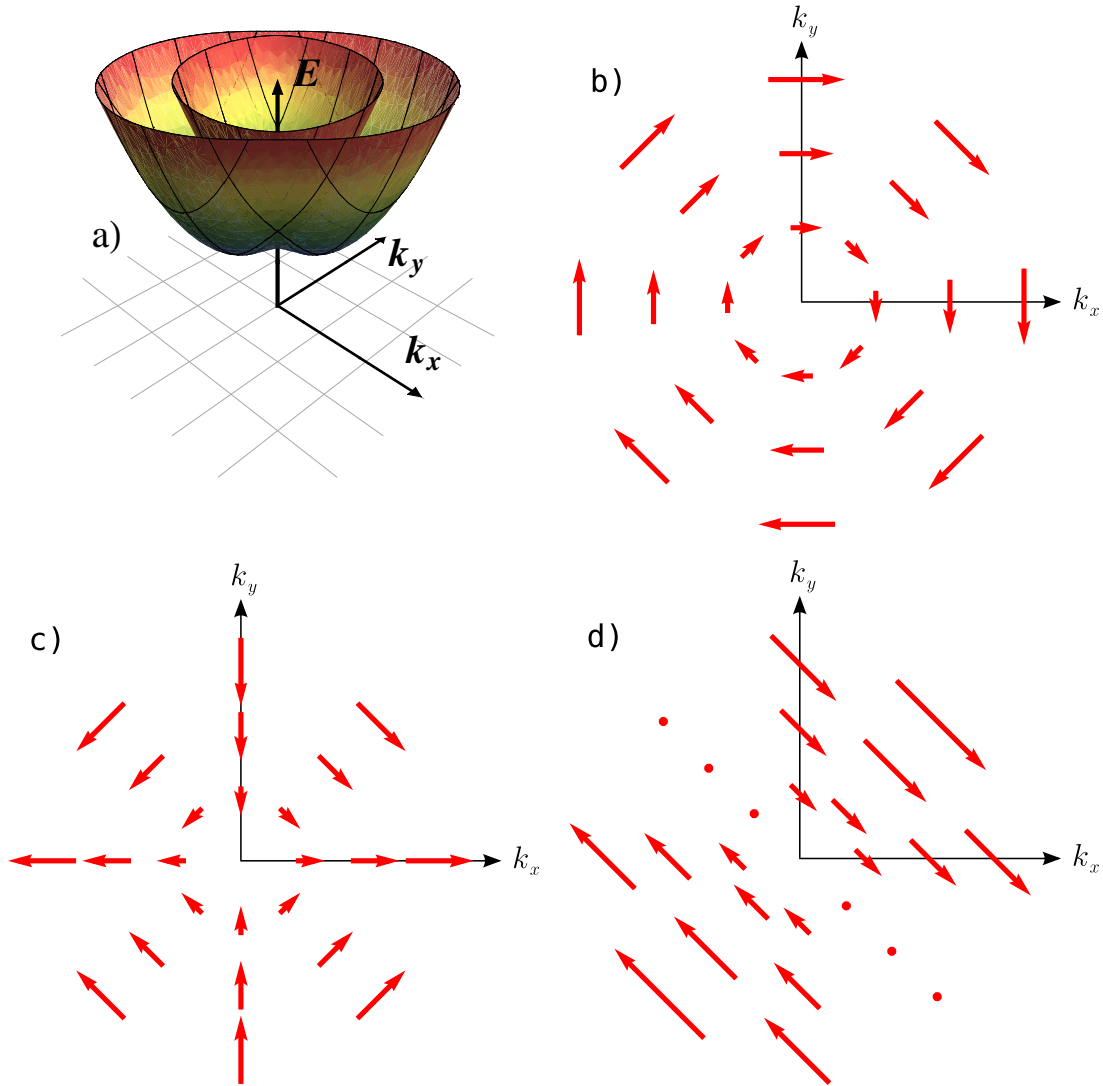


Figure 2.3: a) Representative example for the energy dispersion of a 2DEG with finite Rashba and linear Dresselhaus SOI $\alpha = 1.5\beta$, Eq. (2.17); b)-d) Effective magnetic field \vec{B}_{so} , Eq. (2.19), due to Rashba and Dresselhaus SOI for certain wavevectors $\vec{k} = (k_x, k_y)$; b) only Rashba SOI, i.e. $\beta = 0$; c) only Dresselhaus SOI, i.e. $\alpha = 0$; d) equal strength of Rashba and Dresselhaus SOI, i.e. $\alpha = \beta$

momentum with respect to the underlying crystal lattice, see Fig. 2.3c. And finally, when both contributions are equal, i.e. $\alpha = \pm\beta$, the effective magnetic field \vec{B}_{so} is oriented along the $[1\bar{1}0]$ - or $[110]$ -direction, respectively, regardless of the momentum, which only determines the strength of \vec{B}_{so} . In this special case the spin is a good quantum number and therefore it holds the promise of very long spin lifetimes and consequently it has attracted increasing attention lately. In this thesis, specifically in chapters 4 and 5, we also put a special emphasis on this case.

Spin relaxation in 2DEGs

So far we only considered solids with perfect crystal structure. However, in realistic semiconductors impurities and lattice defects are present, giving rise to electron scattering. At finite temperatures also electron-phonon scattering becomes important. In the presence of SOI those scattering mechanisms can also give rise to spin relaxation. For conduction band electrons in semiconductors there exist several important spin relaxation mechanisms [16, 40], which we will briefly review now:

The scattering of electrons at impurities or phonons gives rise to a randomization of the electron momentum. In-between the scattering events the electrons move ballistically and precess around the effective magnetic field due to SOI, see Eq. (2.19). Due to the momentum randomization consequently also this effective magnetic field is randomized, giving rise to a randomization of the spin state, which is called D'yakonov-Perel' spin relaxation (DPSR) [75].

Opposed to this kind of spin relaxation, in the Elliott-Yafet mechanism [76, 77] the spins are randomized at the scattering events (due to impurities or phonons) themselves and not during the motion in-between them. Due to SOI the spinor of the electron wavefunction usually is no eigenstate but a mixture between spin-up and spin-down. Hence, at each scattering event there exists a small possibility to flip the spin. Therefore, the importance of this type of spin relaxation increases with increasing number of scattering events. This is contrary to DPSR which can even be suppressed, when the distance between two consecutive scattering events become too short and does not allow for a sufficient precession of the spin in the effective SOI field.

Those two mechanisms are typically the dominating sources for spin relaxation in n -type semiconductors [16]. The wire geometries considered in this thesis are realized in 2DEGs formed in III-V semiconductor quantum wells. There, in general DPSR is stronger than the Elliott-Yafet mechanism, which can, however, become important when DPSR is suppressed [78].

In addition to D'yakonov-Perel' and Elliott-Yafet spin relaxation other mechanisms exist, which are usually not important in the typical systems considered here. The Bir-Aronov-Pikus spin relaxation mechanism [79] is caused by the exchange coupling of electrons and holes and is important especially in p -doped semiconductors. There, the conduction band electrons and valence band holes interchange their spin angular momentum. Since strong spin relaxation of the Elliot-Yafet type is present for those holes, the relaxation occurs in the valence band and as a consequence the spin information is lost.

Finally, there also exists spin relaxation due to hyperfine coupling of the electron spin to the spins of the nuclei of the semiconductor material, in case the respective nuclei possess a spin angular momentum. This mechanism becomes especially important when the electrons are confined to a certain area and feel the spins of only a limited number of nuclei, as e.g. in small-sized quantum dots.

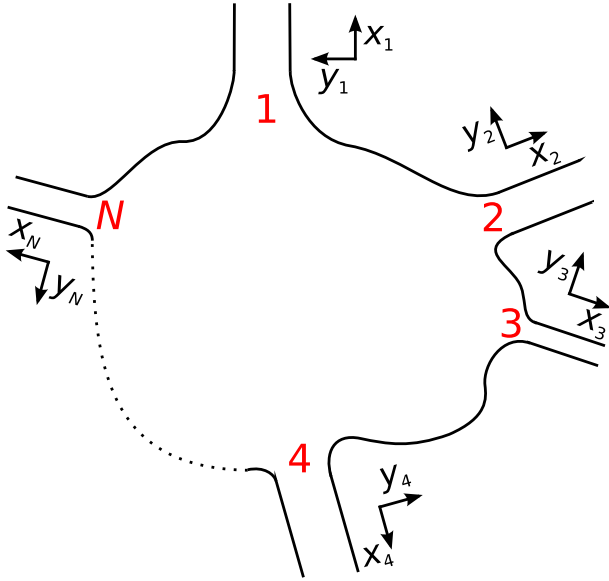


Figure 2.4: Sketch of a typical geometry to which the Landauer-Büttiker theory can be applied: A finite-sized scattering region with $i = 1, \dots, N$ attached semi-infinite leads (labeled by red numbers). For the subsequent calculations a local coordinate system (x_i, y_i) was introduced for every lead. Here, the coordinate x_i is parallel to the lead direction and points away from the scattering region.

2.2 Landauer-Büttiker formalism

The geometries investigated in this thesis are nanostructures of finite extension, which are created on a 2DEG by confinement potentials. They can be of arbitrary shape and are connected to a certain number of ohmic contacts via leads. An example for a typical geometry under consideration is sketched in Fig. 2.4.

Voltage differences between those contacts induce compensating electron currents, which we calculate within the Landauer-Büttiker formalism [80, 81]. There, the conductances of the system are related to the transmission probabilities of the electrons between the leads attached to the central region. The contacts are modeled by electronic reservoirs in thermal equilibrium, which have a well defined chemical potential and maintain a Fermi-Dirac distribution.

2.2.1 Scattering approach

A convenient tool for the use in the Landauer-Büttiker theory is the so-called scattering approach [52, 82]. In this formalism, one calculates the transmission probabilities between asymptotic scattering states of the leads that are attached to the nanostructure. The central element of this approach is the scattering matrix $\mathbf{S}(E)$, which contains the scattering properties of the nanostructure at a given energy E .

We consider a geometry as shown in Fig. 2.4. The central region, which models the system under consideration, will be called the scattering region from now on. It possesses

a finite extension and is connected to N semi-infinite leads³. Within the scattering approach we can treat scattering regions with arbitrary electrostatic potentials (including disorder), SOI and magnetic fields. The leads are assumed to be uniform⁴ in the x -direction⁵, i.e. along the lead, but can be subject to arbitrary potentials and fields, which depend on the transversal y -direction. Far away from the scattering region we describe the asymptotic scattering states in those leads by the eigenstates of the corresponding quantum wire of infinite extension. The Hamiltonian of a given lead i in the most general form reads:

$$H_{L_i} = \frac{\pi_x^2 + \pi_y^2}{2m^*} + U_{\text{conf}}(y) + H_{\text{spin}} \quad (2.20)$$

including the spin-dependent potentials Eqs. (2.9), (2.11), (2.14) and (2.15):

$$H_{\text{spin}} = H_Z + H_R + H_{D1} + H_{D3} \quad (2.21)$$

The eigenstates of H_{L_i} can be written as:

$$\Phi_n^{i\pm}(x, y) = \frac{1}{\sqrt{|v_n|}} e^{ik_x x} \chi_n^i(y), \quad (2.22)$$

where $v_n = \hbar^{-1}(\partial E(n, k_x)/\partial k_x)$ is the group velocity of eigenstate n , which is obtained from the energy dispersion $E(n, k_x)$ of mode n . In Eq. (2.22) we differentiate between outgoing states Φ_n^{i+} where $v_n > 0$, leaving the scattering region into lead i and incoming states Φ_n^{i-} with $v_n < 0$, entering the scattering region from lead i . The spinors $\chi_n^i(y)$ are the normalized, transverse eigenfunctions of H_{L_i} . They are the solutions of the equation

$$H_{L_i}^{(p_x \rightarrow \hbar k_x)} \chi_n^i(y) = E \chi_n^i(y), \quad (2.23)$$

where the momentum operators p_x in H_{L_i} , Eq. (2.20), have been replaced by $\hbar k_x$. For any given energy E there exists only a finite number of solutions $\chi_n^i(y)$ of Eq. (2.23): $n = 1, \dots, M_i(E)$. The $M_i(E)$ propagating modes of the wire will be called the channels of lead i .

Far away from the scattering region any given scattering state $\Psi^i(x, y)$ inside lead i can be constructed as a linear combination of the states $\Phi_n^{i\pm}(x, y)$ given in Eq. (2.22):

$$\Psi^i(x, y) = \sum_{n \in i} (a_n^i \Phi_n^{i-}(x, y) + b_n^i \Phi_n^{i+}(x, y)). \quad (2.24)$$

³Although, it does not directly reflect the experimental reality, in the scattering approach we assume semi-infinite leads with an electronic reservoir attached at infinity for the sake of computational simplicity.

⁴In principle, it is also possible to consider potentials that are periodic in x -direction. The numerical tools developed in Ref. [83] can also be used in that case.

⁵When there is no danger of confusing the coordinates of different leads, we drop the subscript i from (x_i, y_i) .

Here, the coefficients a_n^i refer to incoming states from reservoir i , while b_n^i refer to outgoing states into the reservoir i . In the scattering approach those quantities are related in the following way

$$b_n^i = \sum_{i'} \sum_{n' \in i'} S_{n,n'}^{i,i'} a_{n'}^{i'}, \quad (2.25)$$

where the scattering matrix \mathbf{S} is of the form

$$\mathbf{S} = \begin{pmatrix} \mathbf{r}^{1,1} & \mathbf{t}^{1,2} & \dots & \mathbf{t}^{1,N} \\ \mathbf{t}^{2,1} & \mathbf{r}^{2,2} & \dots & \mathbf{t}^{2,N} \\ \vdots & \vdots & \ddots & \vdots \\ \mathbf{t}^{N,1} & \mathbf{t}^{N,2} & \dots & \mathbf{r}^{N,N} \end{pmatrix}. \quad (2.26)$$

The subblocks $\mathbf{r}^{i,i}$ and $\mathbf{t}^{i,i'}$ are composed of $M_i \times M_i$ and $M_i \times M_{i'}$ entries, respectively, and read

$$\mathbf{r}^{i,i} = \begin{pmatrix} r_{1,1}^{i,i} & r_{1,2}^{i,i} & \dots & r_{1,M_i}^{i,i} \\ r_{2,1}^{i,i} & r_{2,2}^{i,i} & \dots & r_{2,M_i}^{i,i} \\ \vdots & \vdots & \ddots & \vdots \\ r_{M_i,1}^{i,i} & r_{M_i,2}^{i,i} & \dots & r_{M_i,M_i}^{i,i} \end{pmatrix}, \quad (2.27)$$

$$\mathbf{t}^{i,i'} = \begin{pmatrix} t_{1,1}^{i,i'} & t_{1,2}^{i,i'} & \dots & t_{1,M_{i'}}^{i,i'} \\ t_{2,1}^{i,i'} & t_{2,2}^{i,i'} & \dots & t_{2,M_{i'}}^{i,i'} \\ \vdots & \vdots & \ddots & \vdots \\ t_{M_i,1}^{i,i'} & t_{M_i,2}^{i,i'} & \dots & t_{M_i,M_{i'}}^{i,i'} \end{pmatrix}. \quad (2.28)$$

The elements of the scattering matrix denote the amplitudes for transition between the asymptotic scattering states of the N leads. As common in literature, we distinguish between reflection $r_{n,m}^{i,i}$ and transmission amplitudes $t_{n,m}^{i,j}$ whether the incoming and outgoing leads are equal or not:

$$S_{n,n'}^{i,i'} = \begin{cases} r_{n,n'}^{i,i} & \text{for } i = i' \\ t_{n,n'}^{i,i'} & \text{for } i \neq i' \end{cases}. \quad (2.29)$$

For example, the coefficient $r_{n,n'}^{i,i}$ describes the amplitude for an incoming wave from channel n' in lead i to be backscattered into channel n of the same lead. On the other hand $t_{n,n'}^{i,i'}$ accounts for the amplitude of a wave in the incoming channel n' from lead i' to be transmitted into channel n of lead i . Although we omitted the parameter E in the preceding equations for the sake of brevity, it is important to note that the scattering matrix \mathbf{S} and all the coefficients a_n^i , b_n^i are dependent on energy.

The particular choice for the normalization of the states in Eq. (2.22) yields a conserved probability current inside the leads. As a direct consequence the scattering matrix is

unitary [52, 82], i.e. $\mathbf{S}\mathbf{S}^\dagger = \mathbf{S}^\dagger\mathbf{S} = \mathbf{1}$. Written in terms of scattering matrix elements the equation

$$\sum_{n' \in i} |r_{n,n'}^{i,i}|^2 + \sum_{i' \neq i} \sum_{n'' \in i'} |t_{n,n''}^{i,i'}|^2 = 1, \quad (2.30)$$

accounts for the conservation of incoming probabilities into the mode $n \in i$, while

$$\sum_{n' \in i} |r_{n',n}^{i,i}|^2 + \sum_{i' \neq i} \sum_{n'' \in i'} |t_{n'',n}^{i',i}|^2 = 1, \quad (2.31)$$

accounts for the conservation of outgoing probabilities from the mode $n \in i$. Summation of Eqs. (2.30) and (2.31) over all channels $n \in i$ yields the relations

$$R^{i,i} + \sum_{i' \neq i} T^{i,i'} = M_i, \quad (2.32)$$

$$R^{i,i} + \sum_{i' \neq i} T^{i',i} = M_i, \quad (2.33)$$

with the total number of occupied subbands in lead i being M_i . Furthermore, here we introduced the transmission and reflection probabilities

$$T^{i,i'} = \sum_{n' \in i'} \sum_{n \in i} |t_{n,n'}^{i,i'}|^2, \quad R^{i,i} = \sum_{n' \in i} \sum_{n \in i} |r_{n,n'}^{i,i}|^2. \quad (2.34)$$

2.2.2 Charge and spin currents

To analyze the transport properties of a particular system, (among others) we will evaluate charge and spin currents in the leads of this device. Their derivation will be the topic of this section.

In this thesis we consider two kinds of leads based on quantum wires with hard wall confinement, i.e.

$$U_{\text{conf}}(y) = U_{\text{HW}}(y) = \begin{cases} 0 & \text{for } 0 < y < W \\ \infty & \text{otherwise} \end{cases}. \quad (2.35)$$

In the wire geometries investigated in chapter 3, the spin degeneracy in the scattering region is lifted by Zeeman coupling or SOI. However, it is connected to leads described by

$$H_{\text{L}} = \frac{p_x^2 + p_y^2}{2m^*} + U_{\text{HW}}(y), \quad (2.36)$$

i.e. without any additional potentials or fields [Eq. (2.20) with $H_{\text{spin}} = 0$ and $\pi_i = p_i$]. The eigenfunctions of the infinite quantum wire described by Eq. (2.36) are given by

$$\Phi_{(n,\sigma)}^{\pm}(x,y) = \frac{1}{\sqrt{|v_n|}} e^{ik_x x} \chi_n(y) \Sigma(\sigma), \quad (2.37)$$

where the transverse eigenfunctions

$$\chi_n(y) = \sqrt{\frac{2}{W}} \sin\left(\frac{n\pi y}{W}\right) \quad (2.38)$$

and the spinorial part

$$\Sigma(+)=\begin{pmatrix} \cos\frac{\theta}{2}e^{-i\phi/2} \\ \sin\frac{\theta}{2}e^{i\phi/2} \end{pmatrix}, \quad \Sigma(-)=\begin{pmatrix} -\sin\frac{\theta}{2}e^{-i\phi/2} \\ \cos\frac{\theta}{2}e^{i\phi/2} \end{pmatrix} \quad (2.39)$$

are decoupled. Here, the angles (θ, ϕ) describe the position of the spin quantization axis \hat{u} on the Bloch sphere:

$$\hat{u} = \begin{pmatrix} \sin\theta\cos\phi \\ \sin\theta\sin\phi \\ \cos\theta \end{pmatrix}. \quad (2.40)$$

Since there is no spin dependent potential inside the leads, the propagating modes are spin degenerate and thus we label them by the quantum number of the transversal mode $n = 1, \dots, M_i/2$ and the spin index $\sigma = \pm$. The energy dispersion has the form $E(k_x, n) = \hbar^2 k_x^2 / (2m^*) + \varepsilon_n$ where $\varepsilon_n = \hbar^2 \pi^2 n^2 / (2m^* W^2)$ denotes the discrete energy levels of the transversal modes.

Before moving on to the rigorous calculation of the currents within the non-equilibrium Green's function approach in the next section, we now present a heuristic derivation of the expressions for charge and spin currents inside the leads described by Eq. (2.36), following the treatment of Ref. [82]. In order to better understand the physics behind those expressions we choose to illustrate the derivation within the Landauer-Büttiker theory, which provides an intuitive physical picture.

As already mentioned, each lead i is connected to a big electronic reservoir with chemical potential μ_i and the corresponding Fermi-Dirac electron distribution

$$f_{\text{FD}}(E; \mu_i, \mathcal{T}) = \frac{1}{1 + e^{(E - \mu_i)/(k_B \mathcal{T})}}. \quad (2.41)$$

For the derivation we assume a uniform temperature \mathcal{T} in the entire system and thus from now on we omit this parameter from the notation. For the calculations carried out later in this thesis we explicitly set $\mathcal{T} = 0$.

Each lead is populated with electrons according to the Fermi-Dirac distribution of the corresponding reservoir. Since we consider phase coherent transport inside the

leads and the scattering region, those electrons keep this distribution until they are thermalized in one of the N reservoirs. Furthermore, we assume that due to the large size of the reservoir every electron exiting the outgoing lead can find an unoccupied state inside the reservoir and no electrons are reflected back into the lead.

The squared amplitude $[a_{(n,\sigma)}^i(E)]^2$ corresponds to the probability of the incoming channel $(n, \sigma) \in i$ to be populated. Therefore, we ascribe the distribution function of the respective lead to the squared amplitude of the incoming channels

$$[a_{(n,\sigma)}^i(E)]^2 = f_{\text{FD}}(E; \mu_i). \quad (2.42)$$

Then the total scattering wavefunction in lead i at energy E reads

$$\Psi^i(x, y; E) = \sum_{i'} \sum_{(n', \sigma') \in i'} \sqrt{f_{\text{FD}}(E; \mu_{i'})} \Psi_{(n', \sigma') \in i'}^i(x, y; E). \quad (2.43)$$

Here, we introduced the scattering wavefunction $\Psi_{(n', \sigma') \in i'}^i(x, y; E)$ valid for the case, when only the incoming channel (n', σ') from lead i' is populated, i.e. $a_{(n,\sigma)}^i = \delta_{i,i'} \delta_{n,n'} \delta_{\sigma,\sigma'}$:

$$\Psi_{(n', \sigma') \in i'}^i(x, y) = \begin{cases} \Phi_{(n', \sigma')}^{i-}(x, y) + \sum_{(n, \sigma) \in i} r_{n, \sigma; n', \sigma'}^{i, i} \Phi_{(n, \sigma)}^{i+}(x, y) & \text{for } i = i' \\ \sum_{(n, \sigma) \in i} t_{n, \sigma; n', \sigma'}^{i, i'} \Phi_{(n, \sigma)}^{i+}(x, y) & \text{for } i \neq i' \end{cases}, \quad (2.44)$$

where we used the lead eigenfunctions as defined in Eq. (2.37) and omitted the energy dependence of the wavefunctions from the notation.

Charge current

In order to evaluate the charge current in a lead we now consider the probability current due to a specific wavefunction. For the scattering wavefunction $\Psi^i(x, y; E)$ in lead i (with width W_i), see Eq. (2.43), this current is given by

$$I_i^{\text{P}}(E) = \int_0^{W_i} dy [\Psi^i(x, y; E)]^\dagger \hat{J}_x \Psi^i(x, y; E), \quad (2.45)$$

where the current operator reads

$$\hat{J}_x = \frac{\hbar}{2mi} \left(\overrightarrow{\frac{\partial}{\partial x}} - \overleftarrow{\frac{\partial}{\partial x}} \right). \quad (2.46)$$

The expression for the charge current can then be obtained straightforwardly by integrating the probability current $I_i^{\text{P}}(E)$ over energy and by multiplying it with the

charge of the electron:

$$\begin{aligned}
I_i &= \frac{e}{h} \int_0^\infty dE \left[f_{\text{FD}}(E; \mu_i) (M_i(E) - R^{i,i}(E)) \right. \\
&\quad \left. - \sum_{i' \neq i} f_{\text{FD}}(E; \mu_{i'}) T^{i,i'}(E) \right] \\
&\stackrel{(2.32)}{=} \frac{e}{h} \int_0^\infty dE \sum_{i' \neq i} [f_{\text{FD}}(E; \mu_i) - f_{\text{FD}}(E; \mu_{i'})] T^{i,i'}(E). \tag{2.47}
\end{aligned}$$

In the limit of zero temperature $[f_{\text{FD}}(E; \mu_i) \stackrel{k_B T=0}{=} \theta(\mu_i - E)]$ and linear response $[\mu_i \approx \mu_{i'} \approx E_F; (\mu_i - \mu_{i'}) \rightarrow 0]$ the currents are determined by the transmission probabilities at the Fermi energy $T^{i,i'}(E_F)$:

$$I_i = \frac{e}{h} \sum_{i' \neq i} (\mu_i - \mu_{i'}) T^{i,i'}(E_F). \tag{2.48}$$

This relation is known as the famous Landauer-Büttiker formula. Usually it is written in terms of voltages $V_i = \mu_i/(-e)$ and conductances $G^{i,i'} = G_0 T^{i,i'}$

$$I_i = \sum_{i' \neq i} (V_{i'} - V_i) G^{i,i'}, \tag{2.49}$$

where $G_0 = e^2/h$ is the conductance quantum.

Spin current

The spin current in a lead without magnetic fields or SOI can be evaluated along the same lines as for the charge current. To this end, we employ the commonly used spin current operator [84], which for our system reads

$$\vec{J}_x^S = \frac{\hbar}{2} \vec{\sigma} \hat{J}_x, \tag{2.50}$$

with \hat{J}_x as defined in Eq. (2.46). Since \vec{J}_x^S commutes with the Hamiltonian of Eq. (2.36), the spin current is a conserved quantity in the leads and therefore well defined. For the wave-function $\Psi^i(x, y; E)$ the spin probability current with respect to the arbitrary spin quantization axis \hat{u} then reads

$$I_i^{\text{P,S}}(E) = \int_0^{W_i} dy [\Psi^i(x, y; E)]^\dagger \left(\vec{J}_x^S \cdot \hat{u} \right) \Psi^i(x, y; E). \tag{2.51}$$

In the following the spin indices $\sigma = \pm$ refer to the spin eigenstates in $\pm \hat{u}$ -direction. As for the charge current, integration of this probability current over energy yields the

total spin current inside lead i [85, 86]:

$$I_i^S = -\frac{1}{4\pi} \int_0^\infty dE \left[-f_{\text{FD}}(E; \mu_i) R_S^{i,i}(E) - \sum_{i' \neq i} f_{\text{FD}}(E; \mu_{i'}) T_S^{i,i'}(E) \right]. \quad (2.52)$$

Here we introduced the spin-reflection and spin-transmission probabilities

$$R_S^{i,i}(E) = R_{+,+}^{i,i}(E) + R_{+,-}^{i,i}(E) - R_{-,+}^{i,i}(E) - R_{-,-}^{i,i}(E), \quad (2.53)$$

$$T_S^{i,i'}(E) = T_{+,+}^{i,i'}(E) + T_{+,-}^{i,i'}(E) - T_{-,+}^{i,i'}(E) - T_{-,-}^{i,i'}(E), \quad (2.54)$$

with

$$R_{\sigma,\sigma'}^{i,i}(E) = \sum_{\substack{n \in i \\ n' \in i}} |r_{n\sigma,n'\sigma'}^{i,i}(E)|^2, \quad T_{\sigma,\sigma'}^{i,i'}(E) = \sum_{\substack{n \in i \\ n' \in i'}} |t_{n\sigma,n'\sigma'}^{i,i'}(E)|^2 \quad (2.55)$$

being the lead- and spin-resolved reflection and transmission probabilities.

The expression for the spin current can be simplified even further by making use of the unitarity of the scattering matrix. Summing Eq. (2.30) over all channels n with spin state σ in lead i we receive a relation between the spin-transmission and spin-reflection probabilities:

$$R_{\sigma,+}^{i,i}(E) + R_{\sigma,-}^{i,i}(E) + \sum_{i' \neq i} \left(T_{\sigma,+}^{i,i'}(E) + T_{\sigma,-}^{i,i'}(E) \right) = \frac{1}{2} M_i(E). \quad (2.56)$$

Subtracting this equation with $\sigma = -$ from the one with $\sigma = +$ yields

$$R_S^{i,i}(E) + \sum_{i' \neq i} T_S^{i,i'}(E) = 0. \quad (2.57)$$

With this relation at hand, the spin current in lead i , Eq. (2.52), reads

$$I_i^S = \frac{1}{4\pi} \int_0^\infty dE \sum_{i' \neq i} \left(f_{\text{FD}}(E; \mu_{i'}) - f_{\text{FD}}(E; \mu_i) \right) T_S^{i,i'}(E). \quad (2.58)$$

For the case of zero temperature and linear response the spin current can be recast in the simple form

$$I_i^S = \frac{1}{4\pi} \sum_{i' \neq i} \left(\mu_{i'} - \mu_i \right) T_S^{i,i'}(E_F). \quad (2.59)$$

Equation (2.58) was derived for normal leads, i.e. without SOI or magnetic fields, as they will be used in chapter 3. On the other hand, in chapters 4 and 5 we consider leads with potentials that couple to the spin of the electron. Then the spin is subjected

to change, which for SOI implies nonzero spin currents even in an equilibrium situation [87, 88]. Therefore, the possibility of defining a meaningful spin current operator in that region is still a matter of controversy [89], including the unsolved problem of the experimental accessibility of such a quantity. However, in chapters 4 and 5 we are not interested in spin currents and thus we do not face a problem in using this more general kinds of leads. All of the quantities to be evaluated in those chapters, as e.g. charge currents and electron/spin densities, will be introduced in the subsequent section within the framework of the non-equilibrium Green's function approach. There we will also see that the expression for the charge current, Eq. (2.47), is valid in general and not limited to the leads described by Eq. (2.36). Furthermore, we obtain results equivalent to the ones presented in chapters 4 and 5, even if we use the spin degenerate leads, Eq. (2.36). The effects investigated in those chapters are not substantially influenced by the choice of the leads, since the essential physics happens inside the scattering region for the cases considered.

2.3 Green's function formalism for electron transport in nanostructures

In the previous section we treated transport in 2DEGs based on the scattering approach within the Landauer-Büttiker formalism. It provides a very intuitive physical picture and is perfectly suited for the systems under investigation in this thesis. Nevertheless, for reasons of numerical implementation it is advantageous to furthermore introduce the non-equilibrium Green's function (NEGF) formalism [90, 91], which is a very powerful tool for the investigation of systems at finite bias and with interactions. However, we will restrict the presentation of the theory to the case of non-interacting systems, which are described by a single particle Hamiltonian, see e.g. Eq. (2.1), where the NEGF formalism is equivalent to the Landauer-Büttiker formalism. The goal of this section is to summarize the most important results of the NEGF theory that are relevant for our purposes. The numerical implementation of those results then enables us to efficiently calculate the transport properties of interest. However, for a detailed, self-contained introduction to the field we refer to textbooks [56, 92].

2.3.1 Basic definitions

The starting point for our considerations is the Hamiltonian of the system

$$\mathcal{H} = H_0 + \mathcal{V}, \quad (2.60)$$

which is composed of two parts, namely a single particle Hamiltonian H_0 as given e.g. in Eq. (2.7) and a term \mathcal{V} accounting for interactions or perturbations.

For the introduction of the basic concepts of the NEGF formalism, we will use the

language of second quantization and therefore introduce fermionic creation c_i^\dagger and annihilation operators c_i , which obey the following anticommutation relations

$$\{c_i^\dagger, c_j^\dagger\} = \{c_i, c_j\} = 0, \quad \{c_i^\dagger, c_j\} = \delta_{ij}. \quad (2.61)$$

The creation (annihilation) operator c_i^\dagger (c_i) generates (removes) an electron with the single-particle wavefunction φ_i . The fermionic field operators are then defined by

$$\phi^\dagger(\vec{r}) = \sum_i \varphi_i^*(\vec{r}) c_i^\dagger, \quad (2.62)$$

$$\phi(\vec{r}) = \sum_i \varphi_i(\vec{r}) c_i, \quad (2.63)$$

with the complete set of single-particle wavefunctions $\{\varphi_i\}$. The Green's functions used in the NEGF formalism in the context of electronic transport by definition refer to correlation functions (denoted by $\langle \cdot \rangle$) of those field operators ϕ and ϕ^\dagger .

The relevant Green's functions to be used in this chapter are defined as

$$\mathcal{G}^r(\vec{r}, t; \vec{r}', t') = -\frac{i}{\hbar} \theta(t - t') \langle \{\phi_{\text{H}}(\vec{r}, t), \phi_{\text{H}}^\dagger(\vec{r}', t')\} \rangle, \quad (2.64)$$

$$\mathcal{G}^a(\vec{r}, t; \vec{r}', t') = \frac{i}{\hbar} \theta(t' - t) \langle \{\phi_{\text{H}}(\vec{r}, t), \phi_{\text{H}}^\dagger(\vec{r}', t')\} \rangle, \quad (2.65)$$

$$\mathcal{G}^<(\vec{r}, t; \vec{r}', t') = \frac{i}{\hbar} \langle \phi_{\text{H}}^\dagger(\vec{r}', t') \phi_{\text{H}}(\vec{r}, t) \rangle \quad (2.66)$$

and are called the retarded \mathcal{G}^r , advanced \mathcal{G}^a and lesser $\mathcal{G}^<$ Green's functions, respectively. Here, the explicitly time-dependent field operators [93]

$$\phi_{\text{H}}(\vec{r}, t) = U^\dagger(t, t_0) \phi(\vec{r}) U(t, t_0) \quad (2.67)$$

in the Heisenberg picture are used, with the time evolution operator defined as

$$U(t, t_0) = \hat{\text{T}} e^{\frac{i}{\hbar} \int_{t_0}^t dt' \mathcal{H}(t')}, \quad (2.68)$$

where $\hat{\text{T}}$ denotes the standard time-ordering operator.

For the non-interacting system⁶, i.e. $\mathcal{H} = H_0$, one can show that the retarded Green's function is a solution of the following differential equation:

$$\left(i\hbar \frac{\partial}{\partial t} - H_0 \right) \mathcal{G}_0^r(\vec{r}, t; \vec{r}', t') = \delta(t - t') \delta(\vec{r} - \vec{r}'). \quad (2.69)$$

Since we assume that the system under investigation is in a steady state, we can perform a Fourier transformation and write down the corresponding equation for the retarded Green's functions in the energy domain⁷

$$[E - H_0 + i\eta] \mathcal{G}_0^r(\vec{r}, \vec{r}'; E) = \delta(\vec{r} - \vec{r}'). \quad (2.70)$$

⁶The Green's functions of the non-interacting system are denoted by the subscript "0".

⁷ $\eta > 0$ is a infinitesimal, real number.

An explicit solution for $\mathcal{G}_0^r(\vec{r}, \vec{r}'; E)$ can be given in terms of eigenfunctions $\{\varphi_i\}$ of the Hamiltonian H_0 [52]

$$\mathcal{G}_0^r(\vec{r}, \vec{r}'; E) = \sum_i \frac{\varphi_i(\vec{r})\varphi_i^*(\vec{r}')}{E - \epsilon_i + i\eta}, \quad \text{with } H_0\varphi_i(\vec{r}) = \epsilon_i\varphi_i(\vec{r}). \quad (2.71)$$

On the other hand, the lesser Green's function in the energy domain is given by the fluctuation-dissipation theorem [92]

$$\mathcal{G}_0^<(\vec{r}, \vec{r}'; E) = i f_{\text{FD}}(E, \mu) A(\vec{r}, \vec{r}'; E), \quad (2.72)$$

which is valid under equilibrium conditions with uniform chemical potential μ and temperature \mathcal{T} . Here, $f_{\text{FD}}(E, \mu)$ again denotes the Fermi-Dirac distribution function, while the spectral density $A(\vec{r}, \vec{r}'; E)$ is given by

$$\begin{aligned} A(\vec{r}, \vec{r}'; E) &= i \left(\mathcal{G}_0^r(\vec{r}, \vec{r}'; E) - \mathcal{G}_0^a(\vec{r}, \vec{r}'; E) \right) \\ &= 2\pi \sum_i \varphi_i(\vec{r})\varphi_i^*(\vec{r}')\delta(E - \epsilon_i). \end{aligned} \quad (2.73)$$

Having outlined the relevant relations for a non-interacting system, we now also include a finite interaction potential \mathcal{V} in Eq. (2.60), assuming that \mathcal{V} vanishes in the far past (future) and has been (will be) switched on (off) adiabatically. This makes it possible to treat \mathcal{V} within a perturbative expansion to the Green's functions of the non-interacting system. At the time when we evaluate the quantities of interest, we assume that the total system is in a steady state, i.e. then also \mathcal{V} is time-independent. Therefore, it is convenient to consider Green's functions in the energy domain. A rather lengthy calculation, which we omit since it does not help the physical understanding, yields an implicit equation for the retarded Green's function of the interacting system [52, 83, 92]. It has the form of a Dyson equation and reads

$$\mathcal{G}^r(\vec{r}, \vec{r}'; E) = \mathcal{G}_0^r(\vec{r}, \vec{r}'; E) + \int d\vec{r}_1 d\vec{r}_2 \mathcal{G}_0^r(\vec{r}, \vec{r}_1; E) \mathcal{V}(\vec{r}_1, \vec{r}_2) \mathcal{G}^r(\vec{r}_2, \vec{r}'; E). \quad (2.74)$$

For the sake of brevity, from now on we will omit all spatial integrals and all parametric dependencies and rewrite Eq. (2.74) in the compact form

$$\mathcal{G}^r = \mathcal{G}_0^r + \mathcal{G}_0^r \mathcal{V} \mathcal{G}^r. \quad (2.75)$$

Making use of this relation one can derive equations for the relevant transport properties in a system composed of a scattering region and several attached leads, see Fig. 2.4, with each lead i possessing a fixed chemical potential μ_i . Now one commonly associates the unperturbed Hamiltonian H_0 with the isolated systems of scattering region, described by H_S , and leads, described by H_{L_i} for lead i ,

$$H_0 = H_S + \sum_i H_{L_i}, \quad (2.76)$$

while treating the coupling between the leads and the scattering region as a perturbation $\mathcal{V} = \sum_i (H_{L_i,S} + H_{S,L_i})$. A straightforward calculation employing Eq. (2.75) yields for the retarded Green's function of the scattering region [52]

$$\mathcal{G}_S^r = (E - H_S - \Sigma^r + i\eta)^{-1}, \quad (2.77)$$

where Σ^r is the retarded self-energy introduced by the leads. It is given by

$$\Sigma^r = \sum_i \Sigma_{L_i}^r = \sum_i H_{S,L_i} \mathcal{G}_{0,L_i}^r H_{L_i,S}, \quad (2.78)$$

with \mathcal{G}_{0,L_i} being the Green's function of the isolated lead i . Hence, in \mathcal{G}_S^r the coupling of the scattering region to the leads is solely given by the term Σ^r .

Being able to calculate the retarded Green's function of the scattering region, we can obtain the charge current inside any given lead i via the Meir-Wingreen formula [94]. It can be applied to a wide range of systems with various interactions. However, in steady state and for the single-particle picture used here, it reads

$$I_i = \frac{e}{h} \int dE \sum_{i'} \text{Tr} [\Gamma_{L_i} \mathcal{G}_S^r \Gamma_{L_{i'}} \mathcal{G}_S^a] (f_{\text{FD}}(E, \mu_i) - f_{\text{FD}}(E, \mu_{i'})), \quad (2.79)$$

where $\Gamma_{L_i} = i [\Sigma_{L_i}^r - (\Sigma_{L_i}^r)^\dagger]$. Comparing Eqs. (2.47) and (2.79), which both express the charge current in lead i , we notice their similar form. Indeed, the equality of those equations, i.e.

$$T^{i,i'} = \text{Tr} [\Gamma_{L_i} \mathcal{G}_S^r \Gamma_{L_{i'}} \mathcal{G}_S^a], \quad (2.80)$$

can be shown via the so-called Fisher-Lee relations [95–97]. There, the retarded Green's functions of the scattering region are projected onto the asymptotic states in the leads, yielding the respective transmission and reflection amplitudes, Eq. (2.29). For the case of ideal leads without SOI and magnetic fields those relations are given by [52]

$$\begin{aligned} \mathbf{S}_{n,n'}^{i,i'}(E) &= \delta_{i,i'} \delta_{n,n'} \mathbf{1} - i\hbar \sqrt{v_n(E)v_{n'}(E)} \times \\ &\times \int_0^{W_i} dy_i \int_0^{W_{i'}} dy_{i'} \chi_n^*(y_i) \mathcal{G}_S^r(x_i = 0, y_i; x_{i'} = 0, y_{i'}; E) \chi_{n'}(y_{i'}), \end{aligned} \quad (2.81)$$

with the velocity $v_n(E) = \hbar^{-1} (\partial E(k_x, n) / \partial k_x) = \sqrt{2(E - \varepsilon_n) / m^*}$ for the transversal mode n in the respective lead. The integrations run over the interface between scattering region and the respective leads i and i' , where W_i and $W_{i'}$ denote their widths. As before, \mathcal{G}_S^r is given in the 2×2 matrix representation accounting for the spin degree of freedom, and therefore also $\mathbf{S}_{n,n'}^{i,i'}$ is a 2×2 matrix in spin space. In Ref. [83] a similar relation was derived using a discrete, tight-binding Hamiltonian, which we will introduce in the next section. In that work, the equality (2.80) was confirmed for a more

general type of leads, namely the case of leads with arbitrary (periodic) potentials. Having found a way to calculate transport properties of the system via the retarded Green's functions, we now outline how to obtain the lesser Green's function of the scattering region $\mathcal{G}_S^<$. Its knowledge allows us to calculate electron and spin densities via

$$n(x, y) = -\frac{i}{2\pi} \int_{-\infty}^{\infty} dE \operatorname{Tr}[\mathcal{G}_S^<(\vec{r}, \vec{r}; E)] \quad (2.82)$$

$$s_i(x, y) = -\frac{i}{4\pi} \int_{-\infty}^{\infty} dE \operatorname{Tr}[\sigma_i \mathcal{G}_S^<(\vec{r}, \vec{r}; E)]. \quad (2.83)$$

For the evaluation of $\mathcal{G}_S^<$ we use the so-called Keldysh equation, which for the system considered here reads [91, 92]

$$\mathcal{G}_S^< = \mathcal{G}_S^r \Sigma^< (\mathcal{G}_S^r)^\dagger, \quad (2.84)$$

with the lesser self-energy $\Sigma^< = \sum_i H_{S,L_i} \mathcal{G}_{0,L_i}^< H_{L_i,S}$, where $\mathcal{G}_{0,L_i}^<$ is the lesser Green's function of the isolated lead i . Using Eqs. (2.72) and (2.73) it can be expressed in terms of the retarded self-energies $\Sigma_{L_i}^r$ of the individual leads i

$$\Sigma^< = - \sum_i f_{\text{FD}}(E, \mu_i) \left[\Sigma_{L_i}^r - (\Sigma_{L_i}^r)^\dagger \right]. \quad (2.85)$$

2.3.2 Numerical calculation scheme

Having introduced all the relevant equations for the evaluation of the transport properties of multiterminal coherent conductors, we now present the specific calculation scheme employed in this thesis. Especially in view of Eqs. (2.79), (2.82) and (2.83), which are the quantities of interest here, we have to evaluate the retarded, Eq. (2.77), and lesser Green's function, Eq. (2.84), of the scattering region. We will tackle this task numerically by discretizing the single-particle Hamiltonian of the system on a square lattice with a discrete set of basis states $\{|q\rangle\}$:

$$\tilde{H} = \sum_{q,r} |q\rangle \langle r| \tilde{H}(q, r). \quad (2.86)$$

The position q on the lattice is given by

$$q = q_x \hat{x} + q_y \hat{y}, \quad (2.87)$$

where the $q_{x(y)}$ are integer multiples of the lattice constant a and \hat{x} (\hat{y}) is the unit-vector in the x (y)-direction. A sketch of a typical discretized region is shown in Fig. 2.5. Due to its discrete nature, the Hamiltonian can be written in matrix form with entries

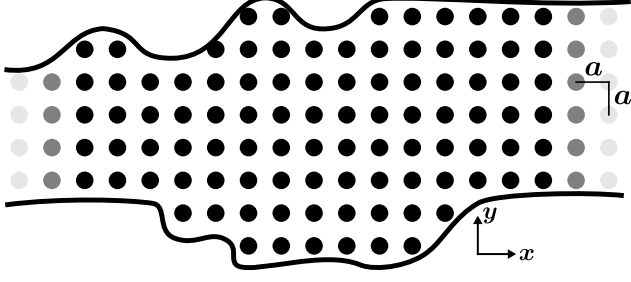


Figure 2.5: Sketch of a nanostructure discretized on a square lattice with lattice spacing a .

$\tilde{H}(q, r)$. Owing to the spin degree of freedom, $\tilde{H}(q, r)$ itself is a 2×2 matrix. Furthermore, we refer to the entries $\tilde{H}(q, q)$ as on-site matrix elements, while the entries $\tilde{H}(q, r \neq q)$ between different sites are called hopping matrix elements.

We now derive the discrete counterpart to the Hamiltonian of the 2DEG in the so-called tight-binding approximation [52, 56], where we take into account arbitrary electrostatic potentials, $U_{\text{es}}(x, y)$, magnetic fields, Eq. (2.9), and SOI, Eqs. (2.11), (2.14), (2.15):

$$H = \frac{\pi_x^2 + \pi_y^2}{2m^*} + H_{\text{R}} + H_{\text{D1}} + H_{\text{D3}} + H_{\text{Z}}(x, y) + U_{\text{es}}(x, y). \quad (2.88)$$

The terms of Eq. (2.88) not containing any momentum operators, such as the Zeeman coupling H_{Z} or any electrostatic potential U_{es} only yield on-site entries to \tilde{H} . As an example we consider the electrostatic potential $U_{\text{es}}(x, y)$ which is a continuous function of the spatial coordinates x and y . It enters the tight-binding Hamiltonian element $\tilde{H}(q, q)$ via its value $U_{\text{es}}(q_x, q_y)$ at site q . To describe the system appropriately, the lattice spacing should be chosen small enough to resolve the spatial variations of all terms of the Hamiltonian (2.88). On the other hand, partial derivatives of the form $\partial^{(n)}/(\partial x^{(m)} \partial y^{(n-m)})$ are present in the kinetic term and the SOI terms $H_{\text{R}}, H_{\text{D1}}, H_{\text{D3}}$. Upon application to a wavefunction Φ the relevant partial derivatives can be approximated using the method of finite differences [98]. Up to correction terms of order $\mathcal{O}(a^2)$ they read [99]:

$$\frac{\partial}{\partial x} \Phi(q_x, q_y) = \frac{\Phi(q_x + a, q_y) - \Phi(q_x - a, q_y)}{2a}, \quad (2.89a)$$

$$\frac{\partial}{\partial y} \Phi(q_x, q_y) = \frac{\Phi(q_x, q_y + a) - \Phi(q_x, q_y - a)}{2a}, \quad (2.89b)$$

$$\frac{\partial^2}{\partial x^2} \Phi(q_x, q_y) = \frac{\Phi(q_x + a, q_y) - 2\Phi(q_x, q_y) + \Phi(q_x - a, q_y)}{a^2}, \quad (2.89c)$$

$$\frac{\partial^2}{\partial y^2} \Phi(q_x, q_y) = \frac{\Phi(q_x, q_y + a) - 2\Phi(q_x, q_y) + \Phi(q_x, q_y - a)}{a^2}, \quad (2.89d)$$

$$\frac{\partial^3}{\partial x^2 \partial y} \Phi(q_x, q_y) = \frac{\Phi(q_x + a, q_y + a) - \Phi(q_x + a, q_y - a)}{2a^3} \quad (2.89e)$$

$$+ \frac{2\Phi(q_x, q_y - a) - 2\Phi(q_x, q_y + a)}{2a^3} \\ + \frac{\Phi(q_x - a, q_y + a) - \Phi(q_x - a, q_y - a)}{2a^3},$$

$$\frac{\partial^3}{\partial x \partial y^2} \Phi(q_x, q_y) = \frac{\Phi(q_x + a, q_y + a) + \Phi(q_x + a, q_y - a)}{2a^3} \quad (2.89f)$$

$$+ \frac{2\Phi(q_x - a, q_y) - 2\Phi(q_x + a, q_y)}{2a^3} \\ + \frac{-\Phi(q_x - a, q_y + a) - \Phi(q_x - a, q_y - a)}{2a^3},$$

$$\frac{\partial^3}{\partial x^3} \Phi(q_x, q_y) = \frac{\Phi(q_x + 2a, q_y) - 2\Phi(q_x + a, q_y)}{2a^3} \quad (2.89g)$$

$$+ \frac{2\Phi(q_x - a, q_y) - \Phi(q_x - 2a, q_y)}{2a^3},$$

$$\frac{\partial^3}{\partial y^3} \Phi(q_x, q_y) = \frac{\Phi(q_x, q_y + 2a) - 2\Phi(q_x, q_y + a)}{2a^3} \quad (2.89h)$$

$$+ \frac{2\Phi(q_x, q_y - a) - \Phi(q_x, q_y - 2a)}{2a^3}.$$

With those equations at hand the tight-binding Hamiltonian matrix $\tilde{H} = t_0 \bar{H}$, corresponding to Eq. (2.88), has the following entries:

$$\bar{H}(q, q) = 4 \cdot \mathbf{1} + \bar{U}_{\text{es}}(q) \cdot \mathbf{1} + \sum_{i=x,y,z} \bar{B}_i(q) \sigma_i, \quad (2.90a)$$

$$\bar{H}(q, q \pm a\hat{x}) = -1 \cdot \mathbf{1} \pm i\bar{\alpha}\sigma_y \pm i\bar{\beta}(\sigma_y \sin 2\phi - \sigma_x \cos 2\phi) \\ \pm 2i\bar{\gamma}\sigma_x \cos 2\phi, \quad (2.90b)$$

$$\bar{H}(q, q \pm a\hat{y}) = -1 \cdot \mathbf{1} \mp i\bar{\alpha}\sigma_x \pm i\bar{\beta}(\sigma_x \sin 2\phi + \sigma_y \cos 2\phi) \\ \mp 2i\bar{\gamma}\sigma_y \cos 2\phi, \quad (2.90c)$$

$$\bar{H}(q, q \pm a\hat{x} \pm a\hat{y}) = \mp 0.5i\bar{\gamma}(\sigma_x + \sigma_y) \sin 2\phi \\ \pm i\bar{\gamma}(\sigma_y - \sigma_x) \cos 2\phi, \quad (2.90d)$$

$$\bar{H}(q, q \mp a\hat{x} \pm a\hat{y}) = \pm 0.5i\bar{\gamma}(\sigma_y - \sigma_x) \sin 2\phi \\ \pm i\bar{\gamma}(\sigma_x + \sigma_y) \cos 2\phi, \quad (2.90e)$$

$$\bar{H}(q, q \pm 2a\hat{x}) = \pm 0.5i\bar{\gamma}\sigma_y \sin 2\phi, \quad (2.90f)$$

$$\bar{H}(q, q \pm 2a\hat{y}) = \pm 0.5i\bar{\gamma}\sigma_x \sin 2\phi, \quad (2.90g)$$

where we introduced the tight-binding energy parameter $t_0 = \hbar^2/(2m^*a^2)$ and dimensionless parameters (denoted by a bar) characterizing the energy $\bar{E} = E/t_0$, the SOI strengths $\bar{\alpha} = (m^*a/\hbar^2)\alpha$, $\bar{\beta} = (m^*a/\hbar^2)\beta$, $\bar{\gamma} = [m^*/(\hbar^2a)]\gamma$ and the Zeeman splitting

$\bar{B}_i = [g^* m^* \mu_B a^2 / (\hbar^2)] B_i$. The potential energy $\bar{U}_{\text{es}} = U_{\text{es}}/t_0$ is composed of all electrostatic potentials present in the system. For convenience, in the following chapters we will usually use those dimensionless quantities when presenting results from the tight-binding calculations.

The effect of the perpendicular magnetic field component B_z on the orbital motion of the electrons can be accounted for by multiplying the entry $\bar{H}(q, r)$ of the Hamiltonian matrix with the so-called Peierls phase [52, 83]

$$\Phi_{\text{P}}(q, r) = \exp \frac{ie}{\hbar} \int_q^r d\vec{l} \cdot \vec{A}(x, y) . \quad (2.91)$$

yielding

$$\tilde{H}(q, r) = t_0 \Phi_{\text{P}}(q, r) \bar{H}(q, r) . \quad (2.92)$$

The tight-binding Hamiltonian matrix as given in Eqs. (2.90a)-(2.90g) is valid for spatially uniform SOI strengths α , β and γ . However, in this thesis we consider two cases where the Rashba SOI strength α is position dependent, namely in sections 3.3 and 4.3. In the hopping matrix elements $\bar{H}(q, q \pm a\hat{x})$ and $\bar{H}(q, q \pm a\hat{y})$ we then have to take the averaged value of $\bar{\alpha}$ at both sites involved [83], i.e. $\bar{\alpha} = 0.5[\bar{\alpha}(q) + \bar{\alpha}(q \pm a\hat{x})]$ and $\bar{\alpha} = 0.5[\bar{\alpha}(q) + \bar{\alpha}(q \pm a\hat{y})]$, respectively.

Finally, the effect of disorder can be included via an additional electrostatic disorder potential U_{d} in the 2DEG Hamiltonian. In particular, in this work we adopt a disorder model developed by Anderson [100], where the total disorder potential consists of delta-type impurities at random positions. It is especially suited for the numerical implementation, where it has been successfully employed for the investigation of a variety of problems related to impurity scattering in 2DEGs [101, 102]. In the tight-binding Hamiltonian \tilde{H} it can be included via the potential energy term $\bar{U}_{\text{d}}(q)$, which for each site q is a randomly chosen value from the interval $[-\bar{U}_{\text{dis}}/2; \bar{U}_{\text{dis}}/2]$. The elastic mean free path l of the electrons can be estimated using Fermi's golden rule. In a 2DEG without SOI and for the specific model used here it is given by [103]:

$$l = 48a \sqrt{\bar{E}_{\text{F}}} / \bar{U}_{\text{dis}}^2 . \quad (2.93)$$

Although the value of l is modified in the presence of SOI, for realistic strengths of the SOI, Equation (2.93) nevertheless represents a good estimate of the actual value and we refer to it, when we use the term mean free path in the following chapters.

Since we neglected correction terms of the order $\mathcal{O}(a^2)$ in the course of the derivation of the tight-binding Hamiltonian, naturally the quality of the approximation close to the band minimum increases the smaller we choose the lattice spacing⁸ a . To visualize this, in Fig. 2.6 we compare the exact energy dispersion relation of an extended 2DEG

$$E(k_x, k_y) = \frac{\hbar^2(k_x^2 + k_y^2)}{2m^*} \quad (2.94)$$

⁸Special attention is needed, when $\bar{\gamma} \ll 1$ is not fulfilled anymore. Then the band structure away from the band minimum at $k_i a = 0$ is distorted due to the discretized cubic Dresselhaus term and can give rise to unphysical results in the numerical calculations.

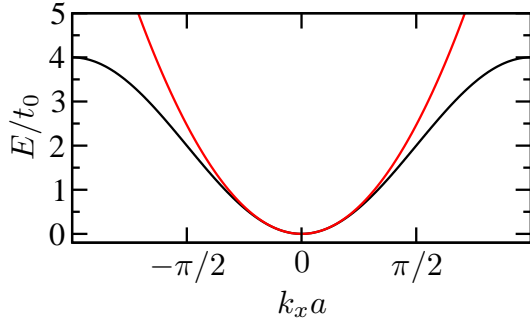


Figure 2.6: Energy dispersion relation $E(k_x, k_y = 0)$, Eq. (2.94), of a 2DEG described by $H_0 = (p_x^2 + p_y^2)/(2m^*)$ (red line) and the corresponding tight binding version $E_{\text{tb}}(k_x, k_y = 0)$ (black line), Eq. (2.95).

to the corresponding one of its discretized counterpart [52]

$$E_{\text{tb}}(k_x, k_y) = \frac{\hbar^2}{2m^*a^2} [4 - 2\cos(k_x a) - 2\cos(k_y a)]. \quad (2.95)$$

While they agree well for energies close to the band minimum, for higher energies $E \geq t_0$ they start to deviate. Therefore, in the numerical calculations of the following chapters we will choose the Fermi energy to be significantly below $E_F < t_0$.

Having introduced the general form of the tight-binding Hamiltonian \tilde{H} , we now determine the corresponding lattice Green's functions. Like \tilde{H} they are only defined for a set of discrete position vectors q and therefore can also be written in matrix-form. For a system discretized on N lattice sites, both \tilde{H} and $\tilde{\mathcal{G}}$ are square matrices of dimension $2N$, with the factor "2" arising from the spin degree of freedom of the electrons. As we will see in the course of this section, the essential calculations that are needed to evaluate the transport properties then reduce to multiplications and inversions of finite sized matrices.

For example, the retarded lattice Green's function of the scattering region can be obtained from Eq. (2.77), which for the discretized system reads

$$\tilde{\mathcal{G}}_S^r = (E\mathbf{1} - \tilde{H}_S - \tilde{\Sigma}^r + i\eta\mathbf{1})^{-1}. \quad (2.96)$$

Here, the expression in the brackets is a matrix whose inversion gives us the corresponding lattice Green's function $\tilde{\mathcal{G}}_S^r$. We already know the Hamiltonian matrix of the finite sized scattering region \tilde{H}_S and therefore we only have to evaluate the self-energy of the leads $\tilde{\Sigma}^r$. For semi-infinite leads this can be done analytically [52, 56] for some special cases, as e.g. for leads without SOI and magnetic fields, or numerically for more general cases [83]. Although the semi-infinite leads naturally possess an infinite number of lattice sites, still the retarded self-energy matrix

$$\tilde{\Sigma}^r = \sum_i \tilde{\Sigma}_{L_i}^r = \sum_i \tilde{H}_{S,L_i} \tilde{\mathcal{G}}_{0,L_i}^r \tilde{H}_{L_i,S} \quad (2.97)$$

is of finite size, since in the tight-binding approximation the coupling terms $\tilde{H}_{L_i,S}$ and \tilde{H}_{S,L_i} only have finite entries for lattice sites close to the interface between lead i and

the scattering region. With the knowledge of the retarded lattice Green's function of the scattering region, Eq. (2.96), and the retarded lattice self energy, Eq. (2.97), we can also straightforwardly determine the lesser lattice Green's function of the scattering region, via Eqs. (2.84) and (2.85).

In principle we could employ Eq. (2.96) to calculate the retarded Green's function of the scattering region and in turn also its transport properties. However, in practice the straightforward use of Eq. (2.96) strongly limits the sizes of the geometries, which can be investigated numerically in a feasible amount of time. Therefore, methods have been developed which allow us to reduce the computational effort. One prominent technique is the so-called recursive Green's function method (RGFM) [104], which we also use for the calculations carried out in this thesis. There one makes use of the fact, that it is not important to know the full expression for the Green's function to determine the transmission and reflection amplitudes of the system via the Fisher-Lee relations, Eq. (2.81), but it is sufficient to calculate the Green's function between the interfaces of the respective leads. The idea behind the RGFM is to calculate the Green's function of isolated parts of the system and then to join them via Eq. (2.75), where the hopping matrix between the isolated parts takes the role of the perturbation \mathcal{V} . For a quantum wire structure connected to two leads, which are opposite each other, it is especially effective and also easy to apply. There, one usually starts with the non-interacting lattice Green's function of a column of lattice sites next to one of the leads. Then one subsequently attaches the lattice sites in the scattering region, column after column via Eq. (2.75) until reaching the other side of the scattering region.

This procedure, which is summarized in detail e.g. in Refs. [56, 83], yields a set of coupled equations, which can be solved by recursion, hence the name of the method. Although, in total there are more calculation steps involved in the RGFM, the size of the matrices that have to be inverted and multiplied is much smaller than the one in Eq. (2.96). Since the total computation time is mainly determined by the time needed for matrix inversions, the big advantage of the RGFM compared to the straightforward application of Eq. (2.96) is the significantly reduced computation time.

For more complicated structures, as e.g. rings or multiterminal geometries, the recursive Green's function method can also be used. However, there the partitioning of the structure into vertical slices is not always the best choice. In order to achieve a high efficiency also for those cases, additional techniques were developed, which determine an optimal partitioning for the respective structure. This method is highly flexible and described in detail in Ref. [83, 105, 106].

For the numerical calculation of the relevant transport properties in this thesis we evaluate the lattice Green's functions with a program based on the quantum transport code developed by M. Wimmer [83] making use of the equations outlined in this section. It includes the optimizations described above and therefore represents a very powerful tool for the determination of charge/spin currents and densities in multiterminal mesoscopic systems of arbitrary shape.

CHAPTER 3

Mesoscopic spin ratchets

The generation of spin polarized currents is a very important element for the operation of many semiconductor spintronics applications, as e.g. the prototypical Datta-Das spin-transistor [18]. Here we consider the possibility of creating these currents in wire geometries realized in two-dimensional electron gases (2DEGs). To be specific, we focus on the generation of pure spin currents in the absence of net charge transport in ratchet setups, i.e. upon application of an unbiased ac-driving voltage between source and drain contacts.

In this chapter we first give an introduction to the concept of ratchets, with a special emphasis on directed spin transport. After outlining their basic working principle, we investigate in detail two specific realizations of a quantum wire-based coherent spin ratchet.

3.1 Introduction

3.1.1 Ratchets: An overview

Ratchets (together with pumps [107]) are devices, which can convert unbiased ac-perturbations into directed motion in one preferential direction. There are two specific requirements, which have to be fulfilled by the ratchet to be operable [49, 108]. On the one hand the system has to display a broken symmetry, which is mostly achieved via asymmetric (ratchet) potentials, as e.g. the saw-tooth potential depicted in Fig. 3.1, where the spatial inversion symmetry with respect to the direction of transport is broken. On the other hand, the ratchet has to be operated away from thermal equilibrium, in order to break detailed balance symmetry. As a consequence of the second law of

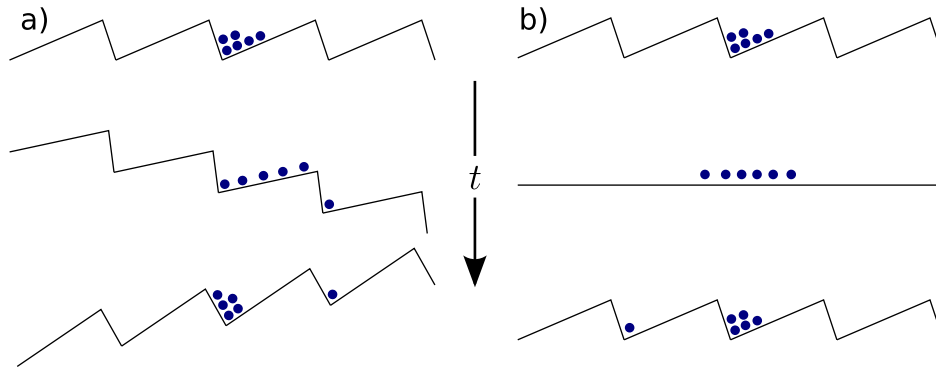


Figure 3.1: Illustration of the working principle of a) a rocking ratchet and b) a flashing ratchet. Three typical driving situations are shown with time elapsing from top to bottom.

thermodynamics it is not possible to transform unbiased, random fluctuations in thermal equilibrium into usable work.

Having identified the necessary conditions for the operation of a ratchet, in the following we will briefly recapitulate important aspects of ratchet physics. More details on the wide field of ratchets and directed transport in general can be found in the review articles of Refs. [49, 108].

One possible way of classifying ratchets is via the form of the (periodic) driving, which forces the system out of equilibrium. To illustrate some typical working principles, here we outline two prominent classes of ratchets [49]. Rocking ratchets are operated by an additional external driving force that periodically tilts the ratchet potential back and forth. An example is visualized in Fig. 3.1a, where the particles can cross the potential barriers (e.g. via thermal activation) more easily in the forward bias (middle image in Fig. 3.1a) than in the backward bias situation (lower image in Fig. 3.1a). This results in net particle transport in the forward direction. For flashing ratchets on the other hand no superimposed external force tilts the whole ratchet potential, but the shape of the individual potential barriers themselves is changed. For instance, the potential can be switched on and off periodically, as shown in Fig. 3.1b. The particles are concentrated in the respective minima, when the potential is on, while they move around randomly (e.g. due to Brownian motion) when the potential is turned off. Upon turning the potential back on, the particles again accumulate in the potential valleys corresponding to their new position. For the present example, the particles on average move to the left, since the neighboring valley left of each minimum is closer than the corresponding valley on the right.

Most studies of ratchet phenomena were carried out in the context of Brownian motors. They are systems governed by Brownian motion, where thermal noise plays a crucial role rendering the dynamics dissipative. Brownian motors are realized, e.g., as protein motors in the cells of organisms [109, 110]. In addition, there is a lot of research in the development of artificial Brownian motors realized in inorganic nano-scale sys-

tems [108]. Those devices can be of importance for future technological applications, e.g. for the transport of charges [111] or heat [112].

Ratchets (Brownian motors) were initially studied in the context of classical dynamics. However, for systems on the nanometer scale quantum effects come into play, which also have a significant effect on the ratchet dynamics [113]. In addition to crossing the potential barriers via thermal activation, the particles can also pass those barriers via tunneling processes. These are competing mechanisms possessing a different temperature dependence, with tunneling processes dominating at low temperatures. This leads to the possibility of a current reversal under a change of the temperature [113], a feature which is not present in ratchets governed by classical dynamics.

Although dissipation is an essential ingredient for the operation of Brownian motors, when dissipation is absent it is nevertheless possible to achieve directed ratchet-type transport in the quantum regime. In this thesis we will focus on this situation, where the particle transport is governed by coherent dynamics and which can be achieved at low temperatures in confined geometries in 2DEGs, as outlined in chapter 2. In those coherent ratchets, the driving is usually realized by the application of ac-bias voltages to metallic contacts patterned on the 2DEG. The coherent charge ratchet effect has been experimentally verified in several geometries, where the spatial inversion symmetry was broken due to the asymmetric shape of the geometry used [111, 114, 115]. In Ref. [111] a quantum wire with an array of asymmetric constrictions was investigated in response to a periodically changing bias voltage between source and drain contacts. The driving period was chosen small compared to the relevant time-scales of electron transport, hence the name adiabatic rocking ratchet. In this experiment, carried out at low temperatures, the authors observed a significant rectification of the charge current, i.e. a net transport of electrons. Furthermore they were able to confirm the inversion of the direction of the ratchet current upon temperature variation. As for the case of dissipative quantum ratchets [113] this feature is a clear indication that quantum effects play an important role in those experiments.

3.1.2 Spin ratchets: General idea

Complementary to the (quantum) particle/charge ratchet mechanism, in this thesis we will focus on a generalization of those concepts to the case of spin. With the experiments of Refs. [111, 115] serving as motivation, here we also consider coherent transport in quantum wire structures realized in 2DEGs in response to an adiabatic ac-driving. In this respect, a straightforward extension is given by considering separate potentials for particles with spin-up and spin-down polarizations. When the spatial inversion symmetry is broken oppositely for opposite spin orientations, spin-up and spin-down particles on average move in opposite directions. This represents the ideal vision of a spin ratchet, namely the notion of net spin transport in the absence of net particle transport. For electrons a spin dependent asymmetric potential can be achieved by a spatially varying magnetic field $\vec{B}(x)$ via the position dependent Zeeman splitting, as

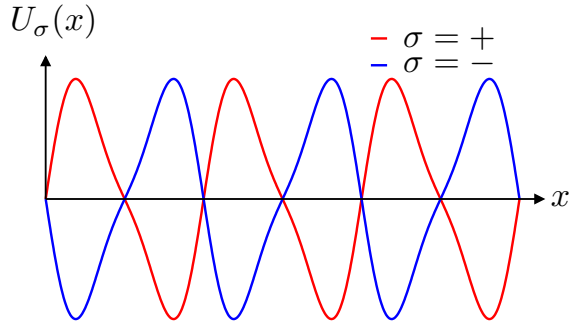


Figure 3.2: Effective potential landscape $U_\sigma(x)$ seen by spin-up (red curve) and spin-down electrons (blue curve) due to a spatially dependent Zeeman splitting. The spatial inversion symmetry is broken oppositely for spin-up and spin-down electrons.

visualized in Fig. 3.2.

However, the generalization of the ratchet concept to the realm of spin is less straightforward than Fig. 3.2 suggests. The spin state of an electron is not a fixed quantity as its charge, but it is subject to change in the presence of spin-orbit interaction (SOI) and magnetic fields. Therefore, we cannot restrict our considerations to a separate analysis of the ratchet effect for spin-up and spin-down electrons, respectively, but we have to take into account spin precession and spin-flip processes. Hence, net spin transport can be achieved not only via the preferential transport of particles with spin in a specific direction but also via manipulation of those particles' spin state. In this respect, our goal is to identify suitable systems, which give rise to net dc-spin currents while at the same time net charge transport is strongly reduced or even completely absent. Complementary to the coherent spin ratchets treated in this thesis and investigated already earlier by us [86, 116], directed ratchet-type spin transport has also been shown recently in one-dimensional systems with electron-electron interactions [117] and in quantum wires with dissipative dynamics [118–120], the latter extending the work of Ref. [113] to the case with spin. In Ref. [118] Smirnov, et al. considered a quantum wire with Rashba SOI and a periodic array of asymmetric potential barriers in response to an unbiased ac-rocking. They were able to show that in the presence of dissipation a spin current of reasonable size can be created, while on average no charges are transported in the ratchet setup. Their device is the dissipative analog to the coherent spin ratchet, which we will investigate in section 3.3.

3.1.3 Coherent spin ratchets based on wire structures realized in 2DEGs

Having outlined the general concepts of ratchet physics, here we now specify the coherent spin ratchet setup to be investigated in this thesis. Namely, we consider quantum wires, which are oriented in the x -direction and embedded in a 2DEG in the (x, y) -plane. Furthermore, we focus on two kinds of mechanisms for the manipulation of the spin state of the electrons to achieve the desired spin ratchet effect. In section 3.2 we employ spatially non-uniform magnetic fields $\vec{B}(x, y)$ in quantum dot structures and in section 3.3 we make use of the interplay of SOI and electrostatic potential barriers.

Details of the specific setups will be given later in the respective sections.

In order to be able to define an unambiguous expression for the spin current we consider normal leads, where spin dependent potentials are absent, see Eq. (2.36). Thus SOI or magnetic fields are only present in the scattering region of length L , i.e. for $-L/2 \leq x \leq L/2$.

To demonstrate the working principle of the spin ratchet, we evaluate the charge/spin currents in response to a finite, applied bias. To this end we use the expressions for the currents derived within the Landauer-Büttiker formalism in Sec. 2.2.2. For coherent transport in a quantum wire the charge current, Eq. (2.47), inside the right lead reads

$$I = \frac{e}{h} \int_0^\infty dE [f(E; \mu_R) - f(E; \mu_L)] T(E). \quad (3.1)$$

with the chemical potentials μ_L of the left and μ_R of the right lead, respectively.

Opposed to the total transmission probability, which in a two-terminal setup is equal between both leads $T(E) = T^{\text{RL}}(E) = T^{\text{LR}}(E)$ [52], the spin transmission probability (and naturally also the spin current) can differ from lead to lead: $T_S^{\text{RL}}(E) \neq T_S^{\text{LR}}(E)$. This is a direct consequence of the spin-dependent potentials in the scattering region. Hence, it is necessary to specify the lead where the spin current is evaluated. In the following we calculate the spin current inside the right lead, where we make use of Eq. (2.58) derived in Sec. 2.2.2:

$$I^S = \frac{1}{4\pi} \int_0^\infty dE [f(E; \mu_L) - f(E; \mu_R)] T_S(E). \quad (3.2)$$

Here we abbreviated the spin transmission into the right lead by $T_S(E) = T_S^{\text{RL}}(E)$.

The expressions for the charge, Eq. (3.1), and spin current, Eq. (3.2), are valid in a steady-state situation at a fixed bias voltage¹ $U_0 = (\mu_L - \mu_R)$. Since the envisioned spin ratchets are ac-driven systems, in principle we would have to explicitly account for a time dependent change in the bias voltage and the corresponding voltage drop across the device. However, in this thesis we consider an ac-driving that is adiabatic, i.e. the external bias $\mu_L - \mu_R$ is varied on a timescale much longer than the relevant timescale for the electron transport through the system. It is set by the typical time spent by an electron in the scattering region before escaping into one of the leads. The functionality of coherent charge ratchets in this regime has already been verified experimentally in Ref. [111].

Without loss of generality we employ an adiabatic unbiased square-wave driving with period t_0 . There, the chemical potential of the left/right reservoir

$$\mu_{L/R}(t) = \begin{cases} E_F \pm U_0/2 & \text{for } 0 \leq t < t_0/2 \\ E_F \mp U_0/2 & \text{for } t_0/2 \leq t < t_0 \end{cases} \quad (3.3)$$

¹Although V_0 is the actual bias voltage, we will also interchangeably refer to the difference between the chemical potentials of the leads $U_0 = -eV_0$ as a bias voltage.

is periodically $[\mu_{L/R}(t) = \mu_{L/R}(t + t_0)]$ switched between the two rocking conditions, which we label according to the bias voltage $\mu_L - \mu_R$ with $\pm U_0$ ($U_0 > 0$).

Within the assumption of adiabatic driving, we can consider the ratchet to be in a steady state in-between the switching events. Hence, we can use the above stated expressions for charge, Eq. (3.1), and spin current, Eq. (3.2), to evaluate the averaged currents in the spin ratchet. For the square-wave driving considered the currents are obtained by performing the average between the two rocking situations $+U_0$ and $-U_0$:

$$\begin{aligned} \langle I(E_F, U_0) \rangle &= \frac{1}{2} [I(E_F, +U_0) + I(E_F, -U_0)] \\ &= -\frac{e}{2h} \int_0^\infty dE \Delta f_{\text{FD}}(E; E_F, U_0) \Delta T(E; U_0), \end{aligned} \quad (3.4)$$

$$\begin{aligned} \langle I^{\text{S}}(E_F, U_0) \rangle &= \frac{1}{2} [I^{\text{S}}(E_F, +U_0) + I^{\text{S}}(E_F, -U_0)] \\ &= \frac{1}{8\pi} \int_0^\infty dE \Delta f_{\text{FD}}(E; E_F, U_0) \Delta T_{\text{S}}(E; U_0), \end{aligned} \quad (3.5)$$

where

$$\Delta f_{\text{FD}}(E; E_F, U_0) = f_{\text{FD}}(E; E_F + U_0/2) - f_{\text{FD}}(E; E_F - U_0/2), \quad (3.6)$$

$$\Delta T(E; U_0) = T(E; +U_0) - T(E; -U_0), \quad (3.7)$$

$$\Delta T_{\text{S}}(E; U_0) = T_{\text{S}}(E; +U_0) - T_{\text{S}}(E; -U_0). \quad (3.8)$$

A generalization of the charge and spin ratchet currents to a different kind of adiabatic driving is straightforward:

$$\langle I^{(\text{S})} \rangle = (1/t_0) \int_0^{t_0} dt I^{(\text{S})}(E_F, U(t)). \quad (3.9)$$

In linear response the infinitesimal voltage difference $U_0 \rightarrow 0$ does not explicitly enter the scattering matrix from which the transmission probabilities are calculated. As a direct consequence, the quantities $\Delta T(E; U_0 = 0) = \Delta T_{\text{S}}(E; U_0 = 0) = 0$ vanish and thus no charge, Eq. (3.4), or spin ratchet currents, Eq. (3.5), can be created. Therefore, we have to consider a finite driving bias voltage U_0 for the operation of the spin ratchet. As in the theoretical model employed for the description of the charge ratchet in Ref. [111], we add the term $\delta U_{\text{es}}(x, y)$ to the respective linear response Hamiltonian, which accounts for the voltage drop across the quantum wire. Specifically it describes the change of the electrostatic potential at finite bias from the equilibrium situation. For the bias voltage $U_0 = \mu_L - \mu_R$ it obeys the following boundary condition inside the left/right lead

$$\delta U_{\text{es}}(\vec{r} \in \text{L/R}) = \pm U_0/2, \quad (3.10)$$

while its form inside the scattering region is not known a priori. In this thesis we will determine δU_{es} in two different ways. First we employ heuristic models for the voltage drop in order to carry out proof-of-principle calculations showing the functionality of the proposed setups. Those models, which are based on sound physical arguments, are adjusted to the specific physical situation and will be discussed later, together with the respective setups. As a second step, we self-consistently solve the Schrödinger equation and the Poisson equation to obtain $\delta U_{\text{es}}(x, y)$ in the scattering region, which we will describe in detail now.

3.1.4 Self-consistent calculation of the voltage drop in wire geometries

The spin ratchets introduced in the previous section require their operation at finite bias voltages. Therefore, it is important to account for the voltage drop between the left and right lead in the best way possible. In this section we outline an efficient method to self-consistently determine this voltage drop in wire geometries on the Hartree level. To this end we adopt the approach introduced in Ref. [121].

The electrostatic potential U_{es} due to the charge density of the respective system

$$\rho_{\text{c}}(\vec{r}) = -e[n(\vec{r}) - n_{\text{d}}(\vec{r})] \quad (3.11)$$

can be calculated via the Poisson equation

$$\vec{\nabla}^2 U_{\text{es}}(\vec{r}) = \frac{e\rho_{\text{c}}(\vec{r})}{\varepsilon_r \varepsilon_0}, \quad (3.12)$$

where ε_0 is the vacuum permittivity and ε_r is the material specific relative static permittivity. The electron density $n(\vec{r})$ of the system can be calculated straightforwardly from the lesser Green's function, see Eq. (2.82), as we described in section 2.3. On the other hand $n_{\text{d}}(\vec{r})$, the density distribution of the donors in the semiconductor heterostructure, is not known to us. However, $n_{\text{d}}(\vec{r})$ does not change upon variation of system parameters, as e.g. the Fermi energy or the bias voltage. Therefore, it is convenient to absorb the electrostatic potential in equilibrium $U_{\text{es}}^0(\vec{r})$ in the confinement potential $U_{\text{conf}}(x, y)$ of the quantum wire, which we model by a hard-wall potential [122]. As a consequence we do not have to know the exact distribution of the donors $n_{\text{d}}(\vec{r})$, but it is enough to consider the rearrangement of electrons in the 2DEG, $\delta n = n - n_0$, upon application of a bias voltage. The change in the electrostatic potential $\delta U_{\text{es}} = U_{\text{es}} - U_{\text{es}}^0$ due to the charge rearrangement [123] is obtained by solving the corresponding Poisson equation

$$\vec{\nabla}^2 \delta U_{\text{es}}(\vec{r}) = -\frac{e^2}{\varepsilon_r \varepsilon_0} [n(\vec{r}) - n_0(\vec{r})]. \quad (3.13)$$

For the evaluation of $\delta U_{\text{es}}(\vec{r})$ it is useful to rewrite $\delta U_{\text{es}}(\vec{r}) = \delta U_{\text{lead}}(\vec{r}) + \delta U_{\text{sr}}(\vec{r})$ [123, 124], thereby separating the contributions from the leads, $\delta U_{\text{lead}}(\vec{r})$, and the rearrangement of the electrons in the scattering region, $\delta U_{\text{sr}}(\vec{r})$. Here, $\delta U_{\text{lead}}(\vec{r})$ solves the Laplace equation $\vec{\nabla}^2 \delta U_{\text{lead}}(\vec{r}) = 0$ with the boundary conditions $\delta U_{\text{lead}}(x = \pm L/2) = \mp U_0/2$ and is therefore given by a linear slope between both contacts [124]. On the other hand $\delta U_{\text{sr}}(\vec{r})$ solves the Poisson equation

$$\vec{\nabla}^2 \delta U_{\text{sr}}(\vec{r}) = -\frac{e^2}{\varepsilon_r \varepsilon_0} [n(\vec{r}) - n_0(\vec{r})]. \quad (3.14)$$

with boundary conditions $\delta U_{\text{sr}}(x = \pm L/2) = 0$. For the solution of Eq. (3.14) we assume that the electron density inside the leads is much higher than in the scattering region. Later on, in the numerical calculations this is realized by the introduction of an additional electrostatic offset potential in the scattering region. As a result the electrostatic potential profile close to the leads is flat, i.e. $n(\vec{r}) \approx n_0(\vec{r})$, which enables us to calculate δU_{sr} from the Poisson equation (3.14) with vanishing δU_{sr} for $|\vec{r}| \rightarrow \infty$, yielding

$$\delta U_{\text{sr}}(\vec{r}) = \frac{e^2}{4\pi\varepsilon_r\varepsilon_0} \int d^2r' \frac{n(\vec{r}') - n_0(\vec{r}')}{|\vec{r} - \vec{r}'|}. \quad (3.15)$$

Using those equations we can now self-consistently calculate the form of the electrostatic potential $\delta U_{\text{es}}(x, y)$ at finite bias voltages. We start with an initial guess for $\delta U_{\text{es}}(x, y)$ and calculate the electron density $n(x, y)$ for this case via Eq. (2.82). By solving Eq. (3.15) we obtain a new $\delta U_{\text{es}}(x, y)$, which in turn can be used to calculate the corresponding $n(x, y)$. This procedure is repeated until the difference between the electron densities of two successive iteration steps is smaller than an initially defined threshold value, i.e. convergence is reached.

In practice, we do not directly iterate between Eqs. (2.82) and (3.15), but we use the so-called Newton-Raphson method, which for the wire geometries discussed in this thesis is described in detail in Ref. [121]. The method has been successfully applied to similar non-equilibrium problems [125, 126] and significantly improves the convergence of the self-consistent calculations.

3.1.5 Complementary methods for the creation of pure spin currents

Since the generation of pure spin currents is a very intriguing prospect for spintronics applications, a variety of devices with this ability have been proposed and realized in recent years. Here we briefly summarize a few promising approaches, which are complementary to the spin ratchet mechanism treated in this chapter. We focus specifically on the generation of spin currents inside 2DEGs in response to bias/gate voltages and without using optical excitation or spin injection from ferromagnetic materials.

A prominent example for the generation of spin currents are adiabatic spin pumps. Adiabatic pumps can be operated at zero bias between source and drain contacts via the cyclic variation of at least two system parameters [127], e.g. gate voltages or magnetic fields. In contrast, ratchets require only a single driving parameter, but have to be operated at non-equilibrium conditions. By properly tuning the system parameters, pure spin currents — in the absence of net charge transport — can be produced by the spin pumps. There, one uses either SOI [128] or the coupling of the spins to external magnetic fields [129] to facilitate the directed spin transport. The first experimental realization of an adiabatic spin pump [130] is based on the latter proposal, where the spin polarized currents were detected via the transverse electron focussing technique [36]. The concepts for the creation of pure spin currents described so far rely on the periodic modulation of either bias voltages (rocking ratchets) or other system parameters (adiabatic pumps). In contrast to ratchets and pumps there exists also the possibility to create pure spin currents in response to dc-bias. This is achieved in a multiterminal geometry, where (at least) one of the leads is used as a voltage probe, i.e. it carries no net charge current. However, still electrons can enter and leave this lead and give rise to a net spin current there. For instance, spin accumulations created in a 2DEG can diffuse into a voltage probe lead, resulting in a spin polarized input current, while the compensating currents exiting the lead are unpolarized due to the non-magnetic nature of the contacts attached [131]. Furthermore, in the spin Hall effect transverse spin currents in a 2DEG with SOI are induced by a longitudinal charge current [35]. Although the spin Hall current vanishes in an extended, disordered 2DEG with SOI linear in momentum [132, 133], the spin Hall effect can give rise to pure spin currents in the leads of mesoscopic, multiterminal geometries [134].

3.2 Resonant tunneling-based spin ratchets

In this section we put forward a generic spin ratchet mechanism based on coherent, resonant transport of electrons through double well or double-dot geometries realized in semiconductor heterostructures. We first outline the general mechanism as it could be applied to a variety of systems. Then we focus on the specific configuration of a double quantum dot structure realized in a 2DEG, where we perform calculations showing the functionality of the proposed spin ratchet mechanism.

3.2.1 Mechanism

For the illustration of the general mechanism we consider the one-dimensional electrostatic potential profile shown in Fig. 3.3a. It serves as a simplified model for the realistic physical setups that we will investigate later in this section. The system is divided into four regions (R1-R4) via electrostatic barriers. Due to the confinement

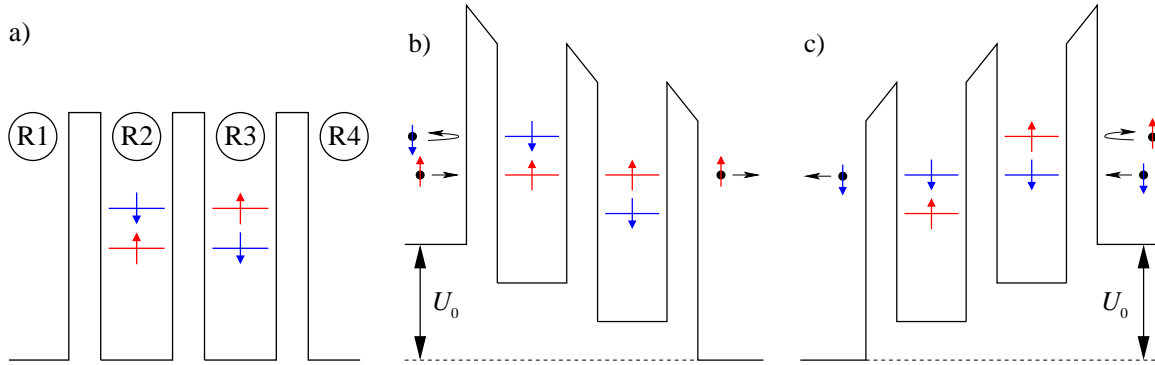


Figure 3.3: a) One-dimensional potential landscape illustrating the working principle of a resonant tunneling-based spin ratchet. It consists of four regions R1-R4 divided by three barriers. In the regions R2 and R3 the discrete energy levels of spin-up and spin-down electrons are split oppositely, e.g. via the Zeeman coupling of the electron spin to a magnetic field. Upon application of a bias, $\pm U_0$, the transmission probability is enhanced for spin-up or spin-down electrons, respectively (panels b,c).

introduced by those barriers, the energy levels in regions R2 and R3 are discrete below the barriers. They are furthermore identical in both regions due to the symmetry exhibited by the potential landscape. On the other hand in regions R1 and R4 a continuous energy spectrum is available for the electronic states.

In addition, we assume a finite Zeeman splitting in R2 and R3, which is opposite in both regions and results in the alignment of the energy levels of electrons with opposite spin polarization. In order to achieve spin selective transport, the energy levels of one spin orientation can be brought into resonance by the application of a finite bias voltage across the device, see Figs. 3.3b,c. Now the transmission of electrons with this spin state is strongly enhanced by resonant tunneling compared to the one of electrons possessing the opposite spin orientation, where the levels are not aligned. Considering both forward (Fig. 3.3b) and backward bias (Fig. 3.3c) we see that the spin polarization of the output current is opposite for opposite signs of bias voltage. Hence, the system constitutes an ideal prototype of a spin ratchet: A pure spin current is created in the absence of net charge transport upon unbiased ac-driving.

3.2.2 Double-dot geometry realized in a 2DEG

We now investigate a particular physical system that is able to create pure spin currents based the method just described. We consider a quantum wire in x -direction embedded in a 2DEG in the (x, y) -plane. In the central part of this wire, two quantum dots are formed, e.g. by side gates at positions x_1 , x_2 and x_3 , see Fig. 3.4a. Such double-dot geometries have been put forward to serve as spin filters [135, 136] or sources for pure spin currents [137]. However, the quantum dots in those proposals are operated in the Coulomb blockade regime, whereas here transport is fully coherent due to the strong

coupling to the leads.

For the following calculations we choose InAs as the host material of the 2DEG, which possesses the parameters $m^* = 0.024 m_0$, $g^* = 15$ and $\varepsilon_r = 15.15$. Furthermore, we fix the lattice spacing as $a = 10$ nm and choose the dimensions of the double-dot geometry as follows: While inside the leads and the dots the width of the quantum wire is $W = 200$ nm, at the point contacts x_1 , x_2 and x_3 it narrows down to $W_0 = 60$ nm. Furthermore, two neighboring point contacts are separated by $L_D = 450$ nm.

To realize the opposite spin splitting of the energy levels in those quantum dots, we consider two ferromagnetic stripes with opposite magnetization ($\vec{M} = \pm M\hat{y}$) on top of the semiconductor heterostructure. Due to the fringe fields of those ferromagnetic stripes, the electrons in the plane of the 2DEG experience a non-uniform magnetic field $\vec{B}(x, y)$, which is depicted in Fig. 3.4b for fixed transversal coordinate y . Since B_y is the

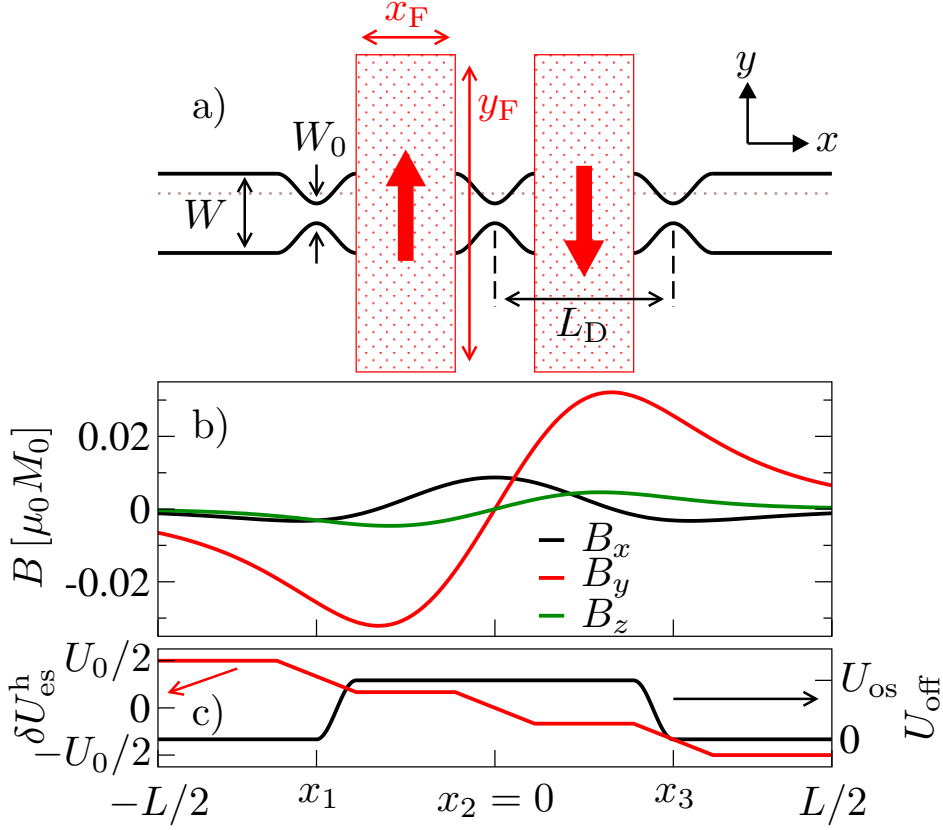


Figure 3.4: a) Setup of the resonant-tunneling spin ratchet: Two open quantum dots realized in a 2DEG with two ferromagnetic stripes possessing opposite magnetization patterned on top of the semiconductor heterostructure. b) Magnetic fringe fields of the ferromagnetic stripes at fixed y along the dotted line indicated in panel a). c) Heuristic voltage drop model δU_{es}^h (red line) and additional electrostatic offset potential U_{off} (black line).

dominating component in this setup, in the following we assign the spin quantization axis to the y -direction. Using a ferromagnetic material such as Dysprosium, which possesses a saturation magnetization $\mu_0 M \approx 3 \text{ T}$ [138], magnetic field strengths of up to 0.5 T can be achieved in near surface 2DEGs [139], where the distance between the ferromagnetic stripes and the 2DEG can be of the order of only a few tens of nanometers.

In summary, the realization of the resonant tunneling spin ratchet outlined in Fig. 3.4 is experimentally feasible with present day material processing techniques. It is described by the Hamiltonian

$$H = \frac{\pi_x(x, y)^2 + \pi_y(x, y)^2}{2m^*} + \frac{g^* \mu_B}{2} \vec{B}(x, y) \cdot \vec{\sigma} + U_{\text{conf}}(x, y) + \delta U_{\text{es}}(x, y), \quad (3.16)$$

with the hard-wall confinement $U_{\text{conf}}(x, y)$ of the double-dot geometry and the electrostatic potential $\delta U_{\text{es}}(x, y)$ accounting for the voltage drop in the system. The magnetic field $\vec{B}(x, y)$ due to a ferromagnetic stripe with uniform magnetization \vec{M} can be calculated using standard magnetostatics [140, 141]:

$$\vec{B}(\vec{r}) = -\frac{\mu_0}{4\pi} \vec{\nabla} \oint_S da' \frac{\hat{n} \cdot \vec{M}}{|\vec{r} - \vec{r}'|}. \quad (3.17)$$

In the Coulomb gauge the corresponding vector potential $\vec{A}(\vec{r})$, which enters Eq. (3.16) via the generalized momentum $\pi_i(x, y) = p_i + eA_i(x, y)$, is given by the expression

$$\vec{A}(\vec{r}) = \frac{\mu_0}{4\pi} \oint_S da' \frac{\vec{M} \times \hat{n}}{|\vec{r} - \vec{r}'|}. \quad (3.18)$$

In Eqs. (3.17) and (3.18) the integral runs over the whole surface S of the ferromagnetic stripe and \hat{n} is the unit vector perpendicular to the surface.

For the specific geometry investigated in this section we consider both ferromagnetic stripes to be positioned symmetrically on top of the two point contacts at a distance $z_{\text{2DEG}} = 50 \text{ nm}$ above the 2DEG. They possess identical size with dimensions $x_{\text{F}} = 250 \text{ nm}$, $y_{\text{F}} = 800 \text{ nm}$, $z_{\text{F}} = 250 \text{ nm}$ along the three coordinate axes. As an experimentally accessible value we choose $\mu_0 M = 2.5 \text{ T}$ for their magnetization [142]. Since the work presented here is part of a collaborative work, a setup similar to the one shown in Fig. 3.4a was already investigated in Ref. [121]. There it was mainly studied as a test case for the self-consistent determination of δU_{es} in mesoscopic systems, which we already briefly recapitulated in section 3.1.3. Although, at the end of this section we also perform calculations, using this technique for the self-consistent evaluation of δU_{es} , here we mostly consider the heuristic voltage drop model $\delta U_{\text{es}}^{\text{h}}$ shown in Fig. 3.4c. As we will see later this constitutes a good description of the system. Furthermore, in contrast to Ref. [121] where only the component B_y was assumed to be finite, here we include the full magnetic field profile of the setup. Since the other magnetic field components B_x and B_z can give rise to spin precession or

spin flips [85, 86], their inclusion might reduce the performance of the proposed spin ratchet setup and therefore it is important to take them into account.

We note that this setup is only one possible candidate making use of the resonant-tunneling mechanism for the creation of pure spin currents. As an alternative, the potential profile shown in Fig. 3.3 can also be realized in the conduction band profile of semiconductor heterostructures along the growth direction. In this respect, devices such as resonant tunneling diodes [143, 144] come to mind. There, the opposite Zeeman splitting in regions R2 and R3 can be implemented by the use of either oppositely magnetized ferromagnetic semiconductor materials or paramagnetic materials with g -factors of opposite sign in the presence of a uniform magnetic field.

3.2.3 Numerical results

In order to confirm the spin ratchet functionality of the double-dot geometry shown in Fig. 3.4, we numerically calculate its transport properties under non-equilibrium conditions. However, to get an idea of the positions of the energy levels inside the two quantum dots we first determine the total transmission of this device in linear response as a function of the Fermi energy in the absence of magnetic fields. For the energies considered in Fig. 3.5a, transport through the constrictions only happens via resonant tunneling and we witness the appearance of several pairs of sharp transmission peaks, which correspond to the positions of the discrete energy levels in both dots. They are present as doublets due to the inter-dot tunnel splitting.

Going beyond the linear response approximation we have to specify the form of the voltage drop $\delta U_{\text{es}}(x, y)$ in the scattering region. We initially consider the heuristic model for $\delta U_{\text{es}}^{\text{h}}$ shown in Fig. 3.4c, where the total voltage difference between the two leads drops equally at the three constrictions at x_1 , x_2 and x_3 . In view of Fig. 3.3, we now choose the Fermi energy to lie close to one of the energy levels of the quantum dots, namely at $E_{\text{F}} = 1.87$ meV. In Fig. 3.5b we present the corresponding spin-resolved I - U_0 characteristics, where we defined the current for electrons with spin state σ by

$$I_{\sigma} = \frac{e}{h} \int_0^{\infty} dE [f(E; \mu_{\text{L}}) - f(E; \mu_{\text{R}})] \sum_{\sigma'} T_{\sigma, \sigma'}^{\text{R,L}}(E). \quad (3.19)$$

As expected, we find that the transmission under forward bias is dominated by electrons with spin-up polarization and under backward bias by spin-down electrons. The energy levels of the two dots are aligned for one sort of spins at the bias $U_{\text{ext}} \approx \pm 0.16$ meV, giving rise to the pronounced maximum (minimum) in the curves shown in Fig. 3.5b. In view of Fig. 3.3 the condition of alignment is reached, when the voltage drop at the central barrier is equal to the Zeeman splitting of the energy levels in the quantum dots. As expected for this specific model, U_{ext} corresponds to approximately three times the Zeeman splitting.

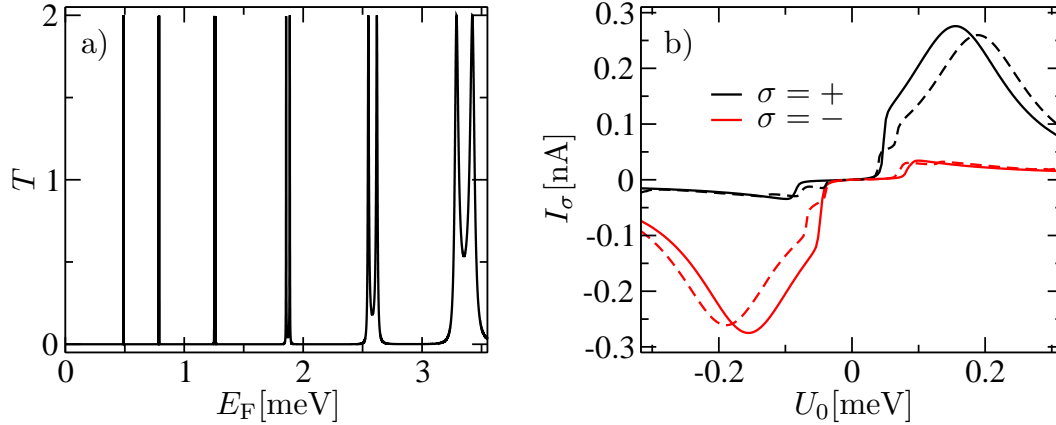


Figure 3.5: a) Total transmission $T(E, U_0 = 0)$ of the double-dot geometry at zero magnetic field and in linear response as a function of the Fermi energy. b) Spin resolved $I-U_0$ characteristics using the heuristic voltage drop model δU_{es}^h for $E_F = 1.87$ meV. Solid lines: symmetrically placed ferromagnetic stripes; dashed lines: ferromagnetic stripes shifted by 100 nm into $+y$ -direction from the symmetric setup. The spin-up (down) current is shown as black (red) line.

Upon application of an adiabatic ac-driving, this spin-asymmetric $I-U_0$ characteristics implies high spin ratchet currents, see Eq. (3.5), with small accompanying charge ratchet currents which average to approximately zero, see Eq. (3.4). Also for Fermi energies close to other energy levels of the quantum dots we obtain an analogous behavior, shown in Fig. 3.6a. Since the width of the transmission peaks increases with E_F (see Fig. 3.5a), also the magnitude of the currents increases with E_F as we observe in Fig. 3.6a. On the other hand, the increased width of the transmission peaks at higher energies also implies increased currents of spins, whose levels are not aligned. This results in a reduction of the spin polarization ratio of the current $P_I = (I_+ - I_-)/(I_+ + I_-)$. In Refs. [85, 86] we investigated the same setup of ferromagnetic stripes, patterned on top of a quantum wire without constrictions. There we found that at a position in-between the two ferromagnetic stripes, where B_y is zero, the finite magnetic field component B_x can induce spin-flips (see Fig. 3.4b around x_2). Those spin-flips are absent for the case of ferromagnetic stripes placed symmetrically (with respect to the y -direction) on the quantum wire. However, when they are deposited away from the wire along the y -direction, the probability of spin-flips strongly increases. Now the question arises, whether we can also observe a corresponding behavior in the quantum wire with constrictions that we investigate here. Therefore, in Fig. 3.5b we also show the spin resolved $I-U_0$ characteristics (dashed lines) for a setup, where the ferromagnetic stripes were shifted from the symmetric configuration by 100 nm in positive y -direction. Compared to the symmetric case (solid lines) there are no radical changes in the functional dependence of the currents, indicating that spin-flips are largely absent. This can be explained by the reduced quantum mechanical probability to find the

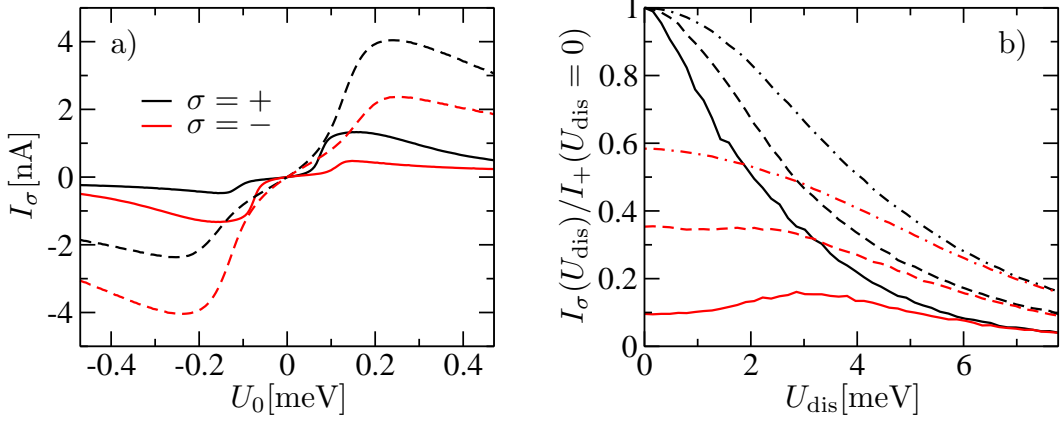


Figure 3.6: a) Spin resolved I - U characteristics of the double-dot ratchet with the heuristic voltage drop model $\delta U_{\text{es}}^{\text{h}}$ for $E_{\text{F}} = 2.58$ meV (solid lines) and $E_{\text{F}} = 3.35$ meV (dashed lines). b) Spin resolved currents I_{σ} as a function of the disorder strength \bar{U}_{dis} normalized to the spin-up current in the clean system $I_{+}(\bar{U}_{\text{dis}} = 0)$. Solid lines: $E_{\text{F}} = 1.87$ meV, $U_0 = 0.16$ meV; dashed lines: $E_{\text{F}} = 2.58$ meV, $U_0 = 0.16$ meV; dash-dotted lines: $E_{\text{F}} = 3.35$ meV, $U_0 = 0.24$ meV. In both panels the spin-up (down) current is shown as black (red) line.

electron at the position of the central constriction (at x_2) due to the presence of the constriction there. Therefore, also transitions between spin-up and spin-down subbands at x_2 are strongly reduced compared to the case of the straight wire in Refs. [85, 86]. As a consequence, we can state that the spin ratchet mechanism is stable against the displacement of the ferromagnetic stripes.

Finally, we also investigate the robustness of the spin ratchet mechanism when disorder is present in the 2DEG. In Fig. 3.6b we show the dependence of the spin-resolved currents as a function of the Anderson disorder strength $U_{\text{dis}} = \bar{U}_{\text{dis}}\hbar^2/(2m^*a^2)$, see section 2.3.2. As expected for a device relying on the resonant tunneling of particles, the spin ratchet mechanism is sensitive to disorder and is even completely destroyed for $U_{\text{dis}} \geq 6$ meV. However, compared to this threshold value for U_{dis} the Zeeman splitting $\Delta E_{\text{Z}} \approx 0.052$ meV of spin-up and spin-down levels inside the dot is rather small. This indicates that the proposed setup can work in a realistic experimental situation, e.g. in InAs based quantum wells which possess mean free paths of up to several microns [145].

Having confirmed the operability of this double-dot geometry as a spin ratchet using the heuristic voltage drop model shown in Fig. 3.4c, we now turn our attention to the self-consistent determination of the electrostatic potential δU_{es} at finite bias. To get better convergence for the calculation of δU_{es} we introduce an additional potential offset in the quantum dots U_{off} (shown in Fig. 3.4c), which possesses the maximum value $U_{\text{os}} = 3.17$ meV. Furthermore, we fix the Fermi energy at $E_{\text{F}} = 5.07$ meV, which due to the shift U_{os} , is close to the resonant energy level, which we also chose for the

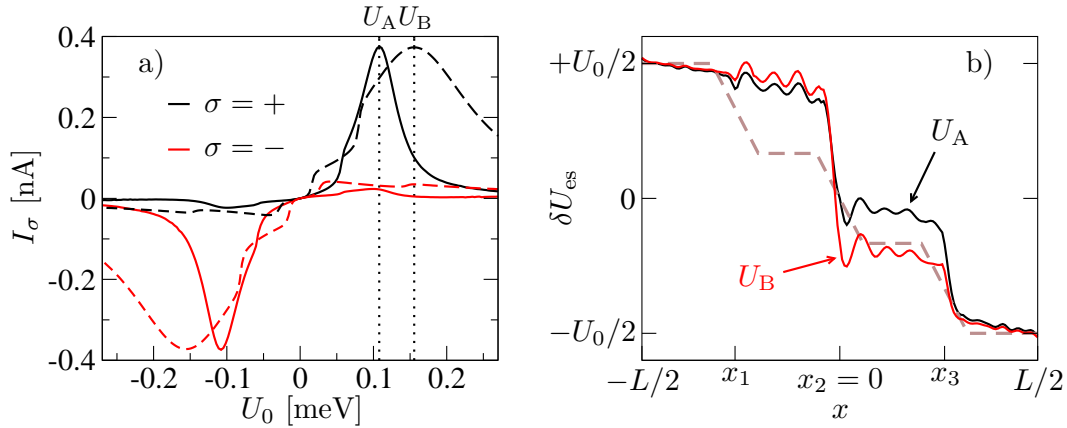


Figure 3.7: a) Spin resolved I - U_0 characteristics of the double-dot ratchet with the self-consistently calculated voltage drop δU_{es} (solid lines) and the heuristic model voltage drop $\delta U_{\text{es}}^{\text{h}}$ (dashed lines). The calculations were performed at $E_{\text{F}} = 5.07$ meV including the offset potential $U_{\text{os}} = 3.17$ meV in the quantum dots, see Fig. 3.4c. The spin-up (down) current is shown as black (red) line. b) The corresponding voltage drop δU_{es} for two values of bias voltages U_{A} and U_{B} as indicated in panel a). Here, δU_{es} was averaged over the transversal coordinate y for fixed x . For comparison also the heuristic voltage drop model $\delta U_{\text{es}}^{\text{h}}$ is shown as dashed line.

calculations in Fig. 3.5b.

In Fig. 3.7a we show the corresponding spin resolved I - U_0 curves for the self-consistently determined δU_{es} (solid lines). We observe a behavior analogous to Fig. 3.5b with electrons of opposite spin orientation dominating the transport for opposite bias voltages. In comparison to the heuristic voltage drop model $\delta U_{\text{es}}^{\text{h}}$ (results shown as dashed lines), the maximum (minimum) of the spin-resolved currents I_{σ} appears at a smaller bias $\pm U_{\text{A}}$. Furthermore, at high bias the magnitude of the currents is significantly smaller in the self-consistent calculation. Both observations can be explained by taking into account the particular form of δU_{es} around the central constriction (at x_2), which separates the two quantum dots. Compared to the heuristic model, where one third ($U_0/3$) of the total voltage drops at each constriction, in the selfconsistent calculations we find that δU_{es} changes by more than $U_0/3$ around x_2 , as shown in Fig. 3.7b. There we present the spatial profile of δU_{es} (averaged over the transversal coordinate y for fixed x) for two different bias voltages. In analogy to $\delta U_{\text{es}}^{\text{h}}$ we witness the emergence of a step structure in δU_{es} due to the constrictions in the quantum wire. In view of those findings, we can state that the heuristic voltage drop model $\delta U_{\text{es}}^{\text{h}}$ (shown as dashed line) constitutes a fair approximation of the actual situation and therefore the results obtained with $\delta U_{\text{es}}^{\text{h}}$, see Figs. 3.5 and 3.6, indeed are reliable.

3.3 Spin ratchets based on spin-orbit interaction

In this section we present a further ratchet setup, which can be used for the efficient creation of pure spin currents. To this end we consider a straight quantum wire (see Fig. 3.8a), i.e. $U_{\text{conf}}(x, y) = U_{\text{conf}}(y)$, with SOI of Rashba type in the scattering region. To avoid unwanted reflections at the abrupt interfaces between the spin-orbit free leads and the scattering region with finite SOI, we adiabatically turn on the Rashba SOI (see Fig. 3.8b). For the rest of this section we fix the spin quantization axis in the y -direction, which is the natural choice for a quantum wire with Rashba SOI, that is oriented in x -direction. Furthermore, we introduce an array of N_B identical potential barriers in the center of the wire (see Fig. 3.8c), which is described by the following electrostatic potential

$$U_{\text{barr}}(x) = \begin{cases} \frac{1}{2}U_B \left[1 - \cos\left(\frac{2\pi(x+N_B L_B/2)}{L_B}\right) \right] & \text{for } |x| < N_B L_B/2 \\ 0 & \text{else} \end{cases}. \quad (3.20)$$

The interplay between the SOI and the potential barriers will prove to be essential for the operability of the spin ratchet. Such potential barriers can, e.g., be realized by the application of a voltage to gates [146] placed on top of the semiconductor heterostructure, which harbors the 2DEG.

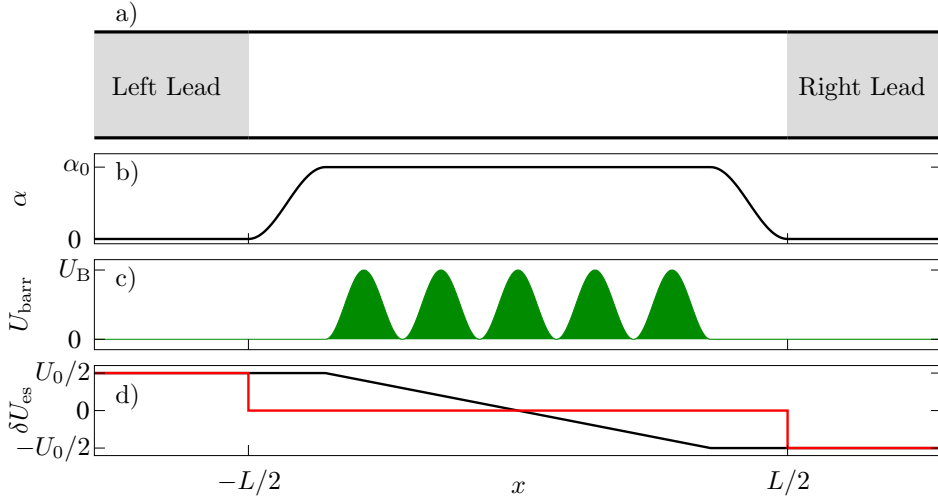


Figure 3.8: a) Spin ratchet setup, consisting of an ideal quantum wire along the x -direction; b) the strength of the Rashba SOI $\alpha(x)$; c) the electrostatic potential barriers $U_{\text{barr}}(x)$; d) the linear voltage drop model $\delta U_{\text{es}}^{\text{lin}}(x)$ (black line) and the symmetric voltage drop only at the interfaces between scattering region and leads $\delta U_{\text{es}}^{\text{int}}(x)$ (red line).

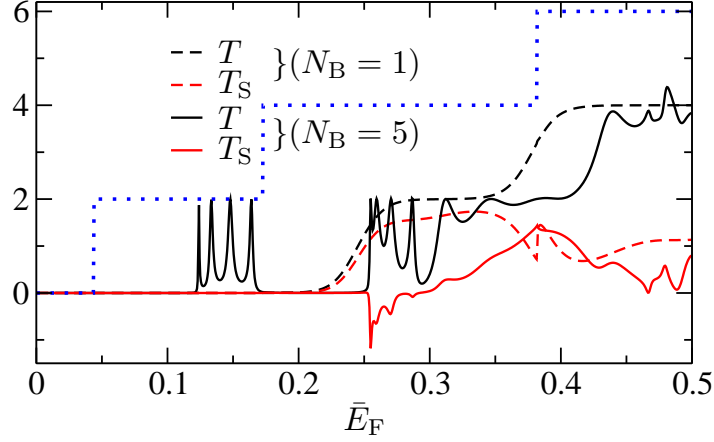


Figure 3.9: Charge (spin) transmission probability T (T_S) as a function of the Fermi energy for a single barrier (dashed lines) or $N_B = 5$ barriers (solid lines). Parameters: $L_B = 50a/N_B$, $\bar{\alpha}_0 = 0.1$, $W = 15a$, $\bar{U}_B = 0.22$. The dotted blue line shows the total transmission probability for the case without SOI and potential barriers, i.e. $\bar{\alpha}_0 = 0$ and $N_B = 0$.

In conclusion, the Hamiltonian of this system reads

$$H = \frac{p_x^2 + p_y^2}{2m^*} + U_{\text{conf}}(y) + U_{\text{barr}}(x) + \delta U_{\text{es}}(x, y) + H_R, \quad (3.21)$$

where we use the symmetrized version of the Rashba SOI Hamiltonian, Eq. (2.11), to account for the spatially varying SOI strength $\alpha(x)$:

$$H_R = \frac{\alpha(x)}{\hbar} \sigma_x p_y - \frac{1}{2\hbar} \sigma_y [\alpha(x) p_x + p_x \alpha(x)]. \quad (3.22)$$

Furthermore, in Eq. (3.21) we include the electrostatic potential $\delta U_{\text{es}}(x, y)$ due to the rearrangement of charges at finite bias. We will specify its particular form in section 3.3.2.

3.3.1 DC-transport in linear response

Before turning our attention to the operation of the spin ratchet under ac-rocking with finite bias, it is insightful to investigate the dc-transport properties of the ratchet setup in the linear response regime, i.e. $\delta U_{\text{es}}(x, y) = 0$, in analogy to Ref. [147].

First we consider the case of a single barrier, i.e. $N_B = 1$ in Eq. (3.20), which is similar to the geometry used in Ref. [148], where spin filtering was achieved via a single constriction in a quantum wire with Rashba SOI. In Fig. 3.9 we show the (spin) transmission probability of this setup. Compared to the step structure exhibited by a perfect quantum wire due to conductance quantization [149, 150] (shown as dotted blue

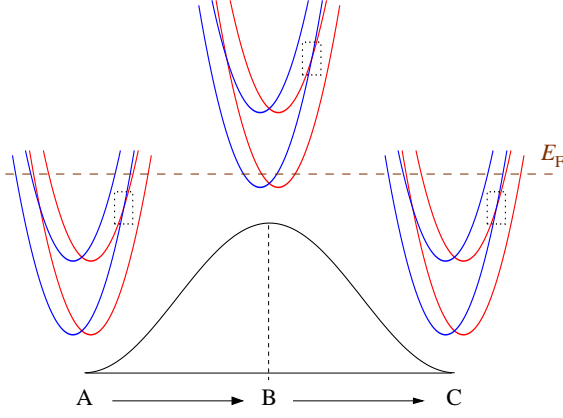


Figure 3.10: Sketch of the energy dispersion $E(k_x)$ for two transverse modes of the quantum wire in the presence of an electrostatic barrier shown at three different positions (A)-(C). The spin-splitting due to SOI is indicated by the shift of the parabolas in $\pm k_x$ -directions. The black square highlights an avoided crossing of transversal modes with different spin polarization, where the spin-flips can happen, see Eq. (3.23). The Fermi energy is shown as dashed line.

line), here the total transmission $T(E)$ is reduced. The onset of the plateaus is shifted by an energy which roughly corresponds to the height of the barrier \bar{U}_B and furthermore the steps are smeared due to tunneling through the barrier. In the whole range of Fermi energies considered we observe that the transmission is strongly spin polarized in $+y$ direction, i.e. $T_S \geq 0$, which is due to the presence of both the barrier and the SOI as we will argue now. To this end, in Fig. 3.10 we show the transversal sub-bands of the quantum wire relative to the Fermi energy E_F at three different positions A-C in the vicinity of a potential barrier. In Refs. [147, 148] it was conjectured that upon traversing the barrier (A \rightarrow B \rightarrow C), first higher transversal modes of the wire become depleted (see position B in Fig. 3.10), while after passing the barrier the SOI gives rise to a spin dependent repopulation of those higher modes, when the Fermi energy passes the anticrossing (indicated by a dashed square in Fig. 3.10) on the way from position B to C. For the simplest situation of two occupied transversal modes and a single barrier the spin transmission can be estimated as [147]

$$T_S = 2P_{\text{sf}}, \quad \text{where} \quad P_{\text{sf}} = 1 - e^{-\lambda} \quad (3.23)$$

is the transition probability between subbands with different spin polarization ($n = 1, \sigma$) \leftrightarrow ($n = 2, -\sigma$). This quantity was evaluated in Ref. [148] using Landau-Zener theory [151, 152], where $\lambda \geq 0$ describes the adiabaticity of the transition and depends on the form of the barrier, the confinement potential and the SOI. This parameter is increased for a longer constriction, or for a broader potential barrier as in the setup investigated here. Indeed, in Ref. [106] we have shown that T_S increases with the length of the constriction. The case of a higher number of transversal modes involved in the spin polarization mechanism was investigated in detail in Ref. [153]. Of course, spin filtering due to the mechanism just described is not limited to barriers and constrictions but is present whenever the quantum wire is not uniform along the longitudinal direction. Among others, also quantum wire structures with side pockets [154] or kinks are expected to provide a substantial spin polarization.

Although the single barrier already produces a significant amount of spin polarization, there nevertheless exist several reasons to investigate also the case of multiple barriers. As we will show later in this section, upon ac-rocking the multi-barrier setup allows for higher spin ratchet currents compared to the single barrier case. On the other hand, also in dc-transport it is advantageous to consider such a periodic array of barriers. Both the model based on Landau Zener transitions, see Eq. (3.23), and the numerical calculations shown in Fig. 3.9 confirm that for the single barrier case the spin polarization is fixed along a specific direction², here along $+y$, but independent of the Fermi energy. This is a drawback of this specific setup, since for spintronics applications it is desirable to be able to control not only the degree of spin polarization of the output current but also its polarization direction. However, extending the setup to a finite number of barriers adds new functionalities to the device, namely the possibility of resonant tunneling for energies below the barrier. This can be observed in Fig. 3.9, where we show the (spin) transmission probability for a wire with $N_B = 5$ barriers (solid lines). In the transmission probability $T(E)$ features due to resonant tunneling are superimposed onto the step structure observable for the single barrier case, see e.g. the onset of the minibands at energies around $\bar{E}_F \approx 0.15$ and 0.27 . Although $T(E)$ is finite for Fermi energies, where only one transversal subband in the leads is occupied ($\bar{E}_F \leq 0.173$), the spin transmission vanishes in this situation due to the invariance of the Rashba SOI under time-reversal symmetry [155]. However, if the wire supports several transversal modes, subbands with different spin state can be mixed and we observe a substantial spin polarization. As already mentioned the feature of resonant tunneling now also gives rise to a crossover from positive to negative spin polarization and vice versa upon variation of the system parameters, as e.g. the Fermi energy (see Fig. 3.9 around $\bar{E}_F \approx 0.3$) or the SOI strength (see Ref. [106]). This is a clear difference to the single barrier case where $T_S > 0$ for all Fermi energies considered.

3.3.2 Creation of pure spin currents

Having shown the usability of the proposed setup as a spin filter, in the following we will also confirm its ability to produce spin ratchet currents in the absence of net charge transport. We again consider the device shown in Fig. 3.8. Based on the Hamiltonian (3.21) we calculate the charge and spin ratchet currents, see Eqs. (3.4) and (3.5), respectively. We have already seen that it is necessary to work at finite bias. Therefore, we first specify the form of δU_{es} that we use for the following calculations. In the quantum wire considered here, the finite voltage difference between the two leads is most likely to drop at the N_B potential barriers. As a first step we assume a linear voltage drop in the region of the barriers, visualized in Fig. 3.8d. For a fixed

²The direction is given by the current direction and the sign of α_0 .

bias voltage U_0 it reads

$$\delta U_{\text{es}}^{\text{lin}}(x) = \begin{cases} U_0/2 & \text{for } x < -N_{\text{B}}L_{\text{B}}/2 \\ U_0x/(N_{\text{B}}L_{\text{B}}) & \text{for } |x| < N_{\text{B}}L_{\text{B}}/2 \\ -U_0/2 & \text{for } x > N_{\text{B}}L_{\text{B}}/2 \end{cases} . \quad (3.24)$$

For bias voltages small compared to the height U_{B} of the barriers, Eq. (3.24) is a crude but fair estimate of the distribution of the electrostatic potential in this device [156]. In order to gain a better understanding of the behavior of the ratchet upon ac-driving we perform a symmetry analysis of the spin-resolved transmission probabilities [86, 155]. Namely, the Hamiltonian Eq. (3.21) is invariant under the operation of

$$\hat{\mathcal{P}} = -i\hat{\mathcal{C}}\hat{R}_{\text{U}}\hat{R}_x\sigma_z \quad (3.25)$$

since the symmetry relations

$$\delta U_{\text{es}}^{\text{lin}}(x) = -\delta U_{\text{es}}^{\text{lin}}(-x), \quad U_{\text{barr}}(x) = U_{\text{barr}}(-x), \quad \alpha(x) = \alpha(-x) \quad (3.26)$$

are fulfilled. Here, \hat{R}_x inverts the x -coordinate, \hat{R}_{U} switches the sign of the bias voltage ($\pm U_0 \leftrightarrow \mp U_0$) and $\hat{\mathcal{C}}$ is the operator of complex conjugation.

As we have shown in Refs. [85, 86], this invariance yields a relation between the spin-resolved transmission probabilities of the two rocking situations

$$T_{\sigma,\sigma'}(E, \pm U_0) = T_{\sigma',\sigma}(E, \mp U_0) \quad (3.27)$$

that we use to simplify the expressions for the charge and spin ratchet currents. In this respect the vanishing quantity

$$\Delta T = \sum_{\sigma,\sigma'} T_{\sigma,\sigma'}(E, +U_0) - \sum_{\sigma,\sigma'} T_{\sigma',\sigma}(E, -U_0) \stackrel{(3.27)}{=} 0 \quad (3.28)$$

implies a vanishing charge ratchet current $\langle I \rangle$, Eq. (3.4), while the equality

$$\Delta T_{\text{S}} = 2 [T_{+,-}(E, +U_0) - T_{-,+}(E, +U_0)] \quad (3.29)$$

enables us to simplify the expression for the spin ratchet current, Eq. (3.5),

$$\langle I^{\text{S}}(U_0) \rangle = \frac{1}{4\pi} \int_0^\infty dE \Delta f(E; U_0) [T_{+,-}(E, +U_0) - T_{-,+}(E, +U_0)]. \quad (3.30)$$

Since $\langle I(U_0) \rangle = 0$ for arbitrary driving amplitude, all the information about the efficiency of the spin-ratchet is encoded in the ratchet spin transmission given in Eq. (3.29). Due to the symmetries of the system we only need to evaluate the spin-flip transmission probabilities $T_{+,-}$ and $T_{-,+}$ for one of the two rocking situations. In linear response, as expected, the ratchet spin current vanishes, i.e. $\langle I^{\text{S}}(U_0 = 0) \rangle = 0$, due to $T_{+,-}(E, U_0 = 0) = T_{-,+}(E, U_0 = 0)$ [147], see Eq. (3.27).

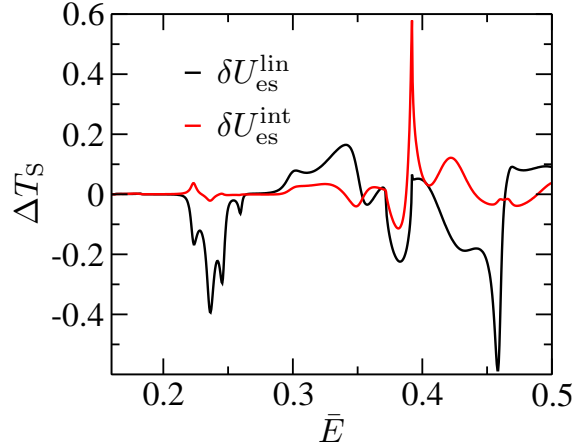


Figure 3.11: Ratchet spin transmission ΔT_S for the driving amplitude $\bar{U}_0 = 0.02$ as a function of the injection energy for two different voltage drop models, see Fig. 3.8d: linear voltage drop $\delta U_{\text{es}}^{\text{lin}}$ (black line) and a symmetric voltage drop $\delta U_{\text{es}}^{\text{int}}(x, y)$ at the interfaces between the scattering region and the leads (red line). Parameters: $N_B = 5$, $L_B = 10a$, $\bar{\alpha}_0 = 0.15$, $W = 15a$, $\bar{U}_B = 0.22$.

In Fig. 3.11 we show ΔT_S at finite driving bias as a function of the injection energy for the same system as already considered in Fig. 3.9. We employ the two voltage drop models shown in Fig. 3.8d, namely the linear voltage drop $\delta U_{\text{es}}^{\text{lin}}$, Eq. (3.24), and $\delta U_{\text{es}}^{\text{int}}$, where all the voltage drops symmetrically at the interfaces between the scattering region and the leads. For the linear voltage drop model (black line) a pronounced ΔT_S can be observed, which is mostly larger than the corresponding ΔT_S for $\delta U_{\text{es}}^{\text{int}}$ (red line), where the only pronounced peak is present at $\bar{E}_F \approx 0.39$. This peak is caused by the opening of a new mode in one of the leads.

To understand this dependence of ΔT_S on the particular voltage drop model, we employ the Landau-Zener model from Ref. [148], which describes transitions between transversal subbands with opposite spin polarization. In Ref. [157], the expression given in Eq. (3.23) was extended to include a finite voltage drop:

$$P_{\text{sf}} = 1 - \exp \left\{ \frac{\eta}{\partial(U_{\text{barr}} + \delta U_{\text{es}})/\partial x} \right\}, \quad (3.31)$$

where η is a factor that depends on the strength of the SOI and the confinement potential of the quantum wire. We see, that this spin-flip transition probability depends on the amplitude of the driving voltage via the gradient $\partial(U_{\text{barr}} + \delta U_{\text{es}})/\partial x$ yielding different transition probabilities for forward and backward bias. Since the transitions are induced when the degeneracy points (see e.g. square in Fig. 3.10) cross the Fermi energy, the value of $\partial(\delta U_{\text{es}})/\partial x$ in the vicinity of the barriers is important for the appearance of the spin ratchet effect. Therefore, this model predicts finite ΔT_S for the linear voltage drop $\delta U_{\text{es}}^{\text{lin}}$ due to $P_{\text{sf}}(+U_0) \neq P_{\text{sf}}(-U_0)$, and vanishing ΔT_S for $\delta U_{\text{es}}^{\text{int}}$ due to $P_{\text{sf}}(+U_0) = P_{\text{sf}}(-U_0)$. This is in good agreement with the results shown in Fig. 3.11

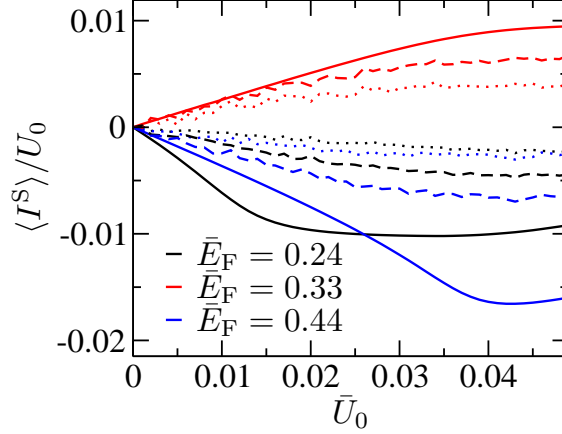


Figure 3.12: Spin ratchet conductance $\langle I^S \rangle / U_0$ as a function of the driving amplitude \bar{U}_0 for three different Fermi energies, $\bar{E}_F = 0.24$ (black lines), $\bar{E}_F = 0.33$ (red lines), $\bar{E}_F = 0.44$ (blue lines). Results are shown for a clean system (solid lines) and for systems with Anderson disorder of strength $\bar{U}_{\text{dis}} = 0.5$ (dashed lines) and $\bar{U}_{\text{dis}} = \sqrt{2}/4$ (dotted lines). Parameters: $N_B = 5$, $L_B = 10a$, $\bar{\alpha}_0 = 0.15$, $W = 15a$, $\bar{U}_B = 0.22$.

and we can state that the spin ratchet effect is provided by the deformation of the potential barriers due to $\delta U_{\text{es}}^{\text{lin}}$.

As we will see later, indeed the linear voltage drop model provides a good description of the actual electrostatic potential δU_{es} and therefore we will use it for the further calculations.

With those results in mind, we expect the spin ratchet mechanism to be enhanced for higher driving amplitudes U_0 , since then also the difference of $\partial(U_{\text{barr}} + \delta U_{\text{es}})/\partial x$ between the two rocking conditions will be enhanced. Indeed, in Fig. 3.12 we witness a linear increase of the spin ratchet conductance $\langle I^S \rangle / U_0$ with the driving amplitude \bar{U}_0 for the three representative Fermi energies shown.

A typical feature of quantum ratchets is the difficulty to predict the direction of transport in advance [49]. Also here, the sign and the magnitude of the spin ratchet current critically depends on the geometry and the parameters of the ratchet device. This is visualized in Fig. 3.13, where we show ΔT_S as a function of both the injection energy and the strength of the SOI. It changes sign as a function of the injection energy and/or the strength of the SOI, which is a typical signature of a ratchet mechanism [49]. Furthermore, in agreement with Ref. [155], we observe that the spin ratchet transmission ΔT_S is zero for energies where only one transversal mode is open in both leads. At energies³ $E \in [E_n - U_0/2; E_n + U_0/2]$ the rectification mechanism is different from the one due to the bias-dependent Landau-Zener transition probabilities given in Eq. (3.31). Namely, inside those energy corridors the number of occupied transversal modes in the

³ $E_n = \hbar^2 \pi^2 n^2 / (2m^* W^2)$ denotes the energy where the n -th transversal mode opens in a hard-wall quantum wire of width W .

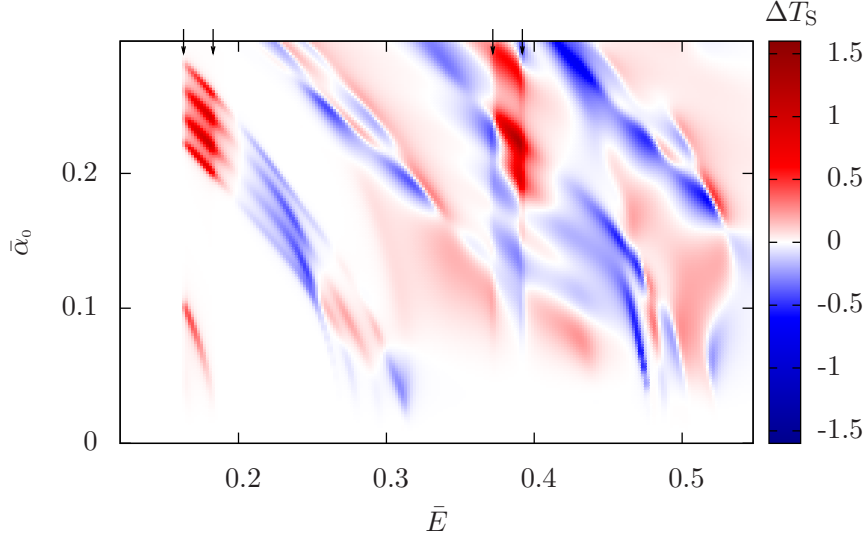


Figure 3.13: Ratchet spin transmission ΔT_S as a function of the injection energy and the Rashba SOI strength. Parameters: $N_B = 5$, $L_B = 10a$, $W = 15a$, $\bar{U}_B = 0.22$, $\bar{U}_0 = 0.02$.

left and right lead differs by one, which is also responsible for the discontinuities in ΔT_S at energies $E = E_n \pm U_0/2$, which we indicated by arrows. As for dc-transport, features related to resonant tunneling are apparent in Fig. 3.13. For instance, there is an array of peaks, which is shifted from $\bar{E} \approx 0.3$ for small SOI towards lower energies for increasing strength $\bar{\alpha}_0$. This dependence, which is quadratic in $\bar{\alpha}_0$ can be explained straightforwardly by taking into account the energy shift of the minimum in the energy dispersion relation due to Rashba SOI: $\Delta E = -m^* \alpha_0^2 / \hbar^2$.

Influence of disorder

Although we considered purely ballistic electron transport until now, experimentally it is not possible to fabricate 2DEGs, where the electrons are not impeded by impurity scattering. In this case scattering at electrostatic potentials due to dopants and/or crystal defects yields a momentum randomization and spin relaxation as described in section 2.1.2. Since spin relaxation presumably limits the performance of the spin ratchet, we now consider the more realistic case of a wire with disorder. In Fig. 3.12 in addition to the case of the ballistic (disorder free) quantum wire (solid lines) we also show the spin ratchet conductance for a disordered quantum wire (dashed and dotted lines). There we introduced disorder of Anderson type (see section 2.3.2) in the central region, where the barriers are present, i.e. for $|x| \leq N_B L_B / 2$. We clearly see that although the overall value of $\langle I^S \rangle / U_0$ is reduced compared to the ballistic case,

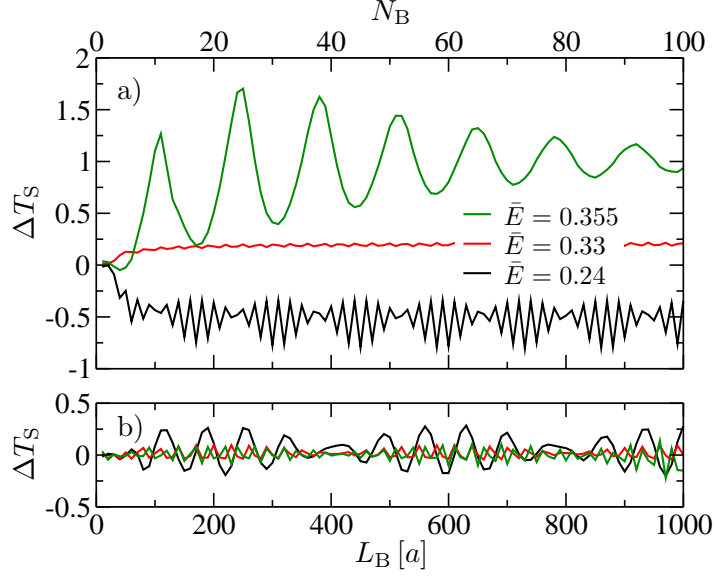


Figure 3.14: Ratchet spin transmission ΔT_S for three different values of \bar{E} as a function of a) the number N_B of potential barriers with $L_B = 10a$ and b) the length of the barrier L_B for $N_B = 1$. Parameters: $\bar{\alpha}_0 = 0.15$, $W = 15a$, $\bar{U}_B = 0.22$, $\bar{U}_0 = 0.02$.

the surviving spin ratchet conductance still has a reasonable magnitude.

To get an estimate of the corresponding mean free path in those calculations, we now exemplarily fix the lattice spacing at $a = 10$ nm and select InAs with $m^* = 0.024 m_0$ as the material of choice. Then for the results reported in Fig. 3.12 the width of the wire is $W = 150$ nm and the length of one barrier is $L_B = 100$ nm. Furthermore, the strength of the Rashba SOI has a value in reach of present day experiments [158], namely $\alpha_0 \approx 4.76 \cdot 10^{-11}$ eV m. The corresponding mean free path $l = 48a \sqrt{\bar{E}_F / \bar{U}_{\text{dis}}^2}$, Eq. (2.93), is then of the order of one micron (two microns) for $\bar{U}_{\text{dis}} = 0.5$ ($\bar{U}_{\text{dis}} = \sqrt{2}/4$) and all Fermi energies considered. In very clean InAs quantum wells even longer mean free paths have been observed [145]. This proves that it should be possible to observe output signals of reasonable magnitude also in a realistic experimental situation.

Multibarrier vs. single barrier case

Having confirmed the functionality of the spin-orbit ratchet mechanism for a system with $N_B = 5$, naturally the question arises, what role the number of barriers plays for its efficiency. Therefore, in Fig. 3.14a we show ΔT_S as a function of the number of barriers for three representative injection energies. We see that for all cases considered the spin ratchet transmission increases from a rather small value for $N_B = 1$ to a significant size for $N_B \geq 5$. We now argue that this increase is caused by the new functionalities for $N_B \geq 2$, as e.g. resonant tunneling, and that it is independent of

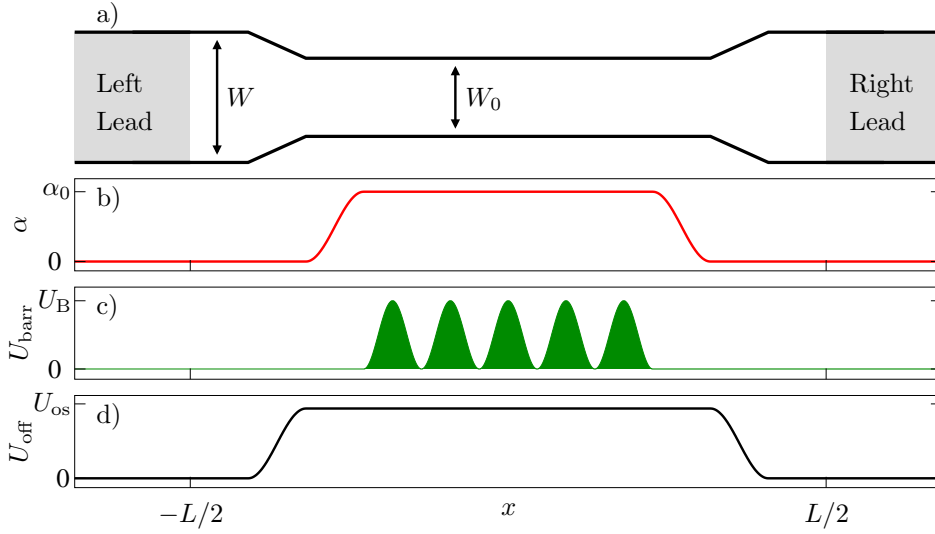


Figure 3.15: a) Spin ratchet setup used for the self-consistent calculations of $\delta U_{\text{es}}(x, y)$. It consists of a quantum wire of width W along the x -direction with a constriction of width W_0 in the central region; b) the strength of the Rashba SOI $\alpha(x)$; c) the electrostatic potential barriers $U_{\text{barr}}(x)$; d) an additional electrostatic potential offset $U_{\text{off}}(x)$.

the increasing length $N_B L_B$ of the central region. In Fig. 3.14b we show ΔT_S for a single barrier as a function of the barrier length L_B . For a better comparison, in both panels the total length of the device, $N_B L_B$, given on the x -axis is chosen to be equal. In contrast to Fig. 3.14a, in Fig. 3.14b the magnitude of ΔT_S does not change significantly with increasing $N_B L_B$ but it shows an oscillatory behavior around zero. Also in the curves shown in Fig. 3.14a periodic modulations of ΔT_S under the variation of N_B are present. When transport is governed by resonant tunneling (black curve), i.e. for $\bar{E}_F = 0.24$, we even observe a beating pattern due to oscillations with two different frequencies. All those oscillations are related to commensurability between the different lengthscales of the system, such as the spin precession length $L_{\text{so}} = \hbar^2/(m^* \alpha)$, the length of the individual barriers L_B or the total length of the central region with SOI.

Self-consistently determined voltage drop

So far we have presented proof-of-principle calculations using the linear voltage drop model $\delta U_{\text{es}}^{\text{lin}}$. Now we go one step further and perform self-consistent calculations on the redistribution of the electrons in the system upon application of a finite bias voltage. To this end we follow the approach presented in section 3.1.3 and employ a system,

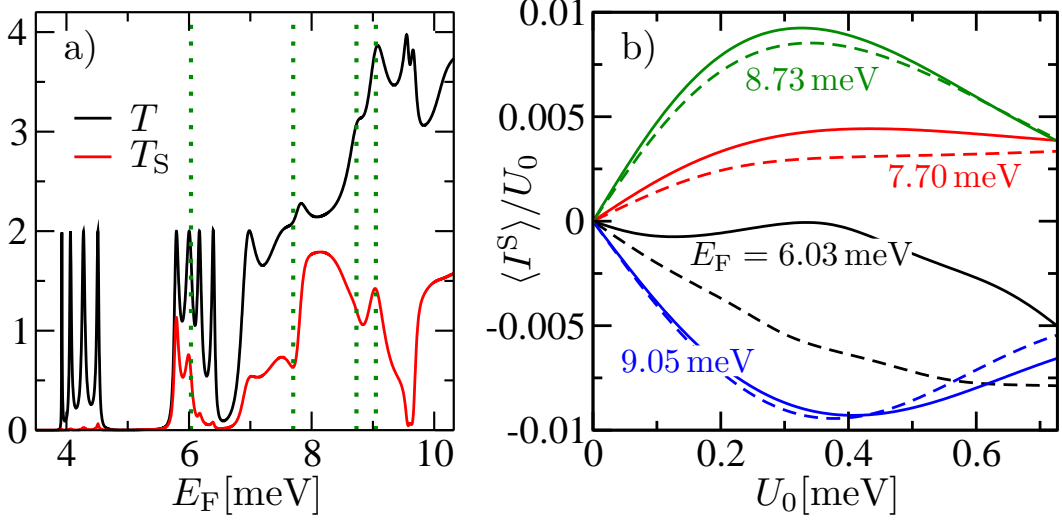


Figure 3.16: a) Charge (spin) transmission probability in linear response for the system outlined in Fig. 3.15. b) Ratchet spin conductance $\langle I^S \rangle / U_0$ as a function of the driving voltage U_0 for four different values of E_F , see vertical lines in panel a). The results of the linear voltage drop model $\delta U_{es}^{lin}(x, y)$ (dashed lines), Eq. (3.24), and the self-consistently determined $\delta U_{es}(x, y)$ (solid lines) are compared. Common parameters: $L_B = 100$ nm, $N_B = 5$, $\alpha_0 = 4.76 \cdot 10^{-11}$ eV m, $W = 250$ nm, $W_0 = 150$ nm, $U_B = 3.17$ meV, $U_{os} = 2.38$ meV.

which is slightly different from the one outlined in Fig. 3.8. Namely, as shown in Fig. 3.15a, we consider a quantum wire, which is wider in the leads than in the central region where SOI and the electrostatic barriers are present (see Figs. 3.15b,c). Furthermore, we introduce an additional electrostatic potential offset in the central region (see Fig. 3.15d). Both this offset and the widening of the wire towards the leads guarantee that the electron density inside the leads is larger than in the central region. Only then the self-consistent calculation yields converging results for $\delta U_{es}(x, y)$. For the 2DEG material we choose InAs with the parameters $m^* = 0.024 m_0$, $g^* = 15$ and $\epsilon_r = 15.15$. Furthermore, the lattice spacing is set to $a = 10$ nm.

To aid the understanding of the following results we first present the transmission of this device in linear response in Fig. 3.16a. There we observe that, as in Fig. 3.9, the output electrons are spin polarized in a wide range of Fermi energies. Furthermore, features due to resonant tunneling become apparent.

We now focus on the case of ac-driving at finite bias voltage, noting that the self-consistently obtained $\delta U_{es}(x, y)$ is also invariant with respect to the symmetry operation given in Eq. (3.25), i.e. the relation (3.27) is still valid. This is caused by the symmetries exhibited by the system and utilization of the same computational scheme for both forward and backward bias. Therefore, as for the linear voltage drop model, also in the self-consistent calculations the charge ratchet current $\langle I \rangle$ vanishes exactly. In Fig. 3.16b we present the spin ratchet conductance $\langle I^S \rangle / U_0$, see Eq. (3.3), as a

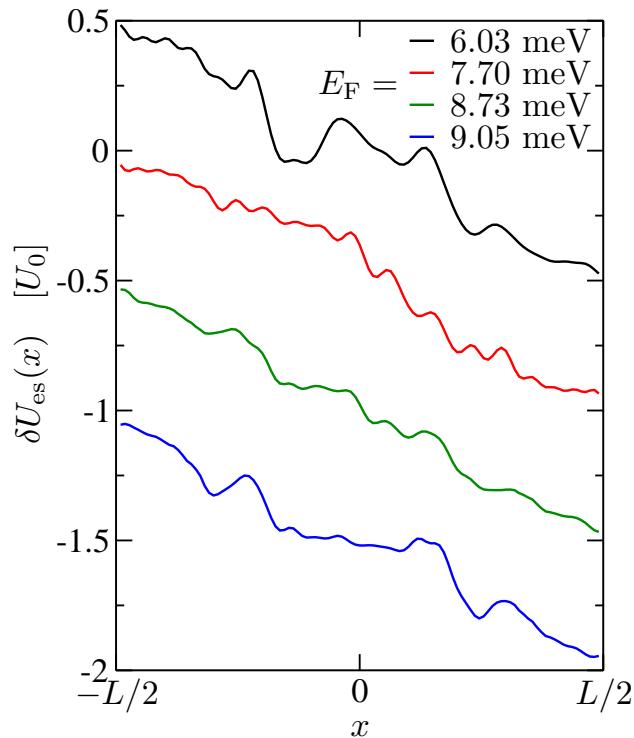


Figure 3.17: Form of the self-consistently determined voltage drop $\delta U_{\text{es}}(x, y)$ averaged over the transversal y -direction for four different values of E_{F} . For clarity, they are vertically offset by a value of $-0.5U_0$ each. Parameters: $L_{\text{B}} = 100$ nm, $N_{\text{B}} = 5$, $\alpha_0 = 4.76 \cdot 10^{-11}$ eV m, $W = 250$ nm, $W_0 = 150$ nm, $U_{\text{B}} = 3.17$ meV, $U_{\text{os}} = 2.38$ meV, $U_0 = 0.24$ meV.

function of the amplitude of the driving voltage U_0 . We compare the results of the linear voltage drop model $\delta U_{\text{es}}^{\text{lin}}(x, y)$ (dashed lines) with those obtained from the self-consistent calculation of $\delta U_{\text{es}}(x, y)$ (solid lines) for several representative Fermi energies indicated by vertical lines in Fig. 3.16a. Except for the case where transport is dominated by resonant tunneling, namely at $E_{\text{F}} = 6.03$ meV, the self-consistent calculations and the linear voltage drop model yield very similar results for $\langle I^{\text{S}} \rangle$.

In Fig. 3.17 we show the spatial distribution of the self-consistently calculated voltage drop δU_{es} along the wire. We see that the linear ramp is indeed a good approximation for the three higher Fermi energy values considered. This also explains the good qualitative agreement in Fig. 3.16b between the curves for the self-consistently determined δU_{es} and the linear voltage drop $\delta U_{\text{es}}^{\text{lin}}$, Eq. (3.24), respectively. For the case of $E_{\text{F}} = 6.03$ meV the resulting voltage drop shows the most pronounced non-monotonic behavior. This causes a misalignment of the energy levels in the potential valleys and therefore a reduction of the resonant miniband transport. As a consequence for this Fermi energy the spin ratchet current is overestimated in the linear voltage drop model.

In conclusion, we have shown that a quantum wire with SOI and a periodic electrostatic potential modulation can act as a source for dc-spin current upon ac-driving. Most remarkably it is possible to achieve directed spin transport in the presence of symmetrical potential barriers, since the necessary symmetry breaking is provided by the SOI. Although this spin ratchet can provide significant spin current signals, it has a drawback in comparison to the resonant-tunneling based spin ratchet investigated in

section 3.2. Namely, it is hard to predict at what energies and SOI strengths the device works optimally. Furthermore, the sign of the output spin current is not known a priori. However, this property also has an advantage compared to the resonant-tunneling based spin ratchet. Namely, it allows to change the polarization direction of the output current by simple electrical means, i.e. by changing the Fermi energy or the strength of the Rashba SOI via gate voltages, rendering the device very flexible.

CHAPTER 4

Current-induced spin accumulation in wire geometries

Proposals for semiconductor spintronics applications and devices usually rely on spin polarized currents, as investigated in chapter 3, or on a local non-equilibrium distribution of spins, in other words on an accumulation of spins. In this chapter we investigate the phenomenon of current-induced spin accumulation (CISA), where – as the name already suggests – an electrical current induces a finite spin accumulation in the material. To be specific, we focus on CISA in a two-dimensional electrons gas (2DEG) with spin-orbit interaction (SOI) and its possible usability for semiconductor spintronics applications. We consider CISA caused by spin relaxation due to the interplay of static impurities and either Rashba SOI or both Rashba and Dresselhaus SOI. After introducing the basic concepts and explaining the effect in the next section, we take a closer look at the magnitude of the CISA in quantum wire geometries, especially focussing on certain conditions when CISA is suppressed from the value expected in a bulk 2DEG. Next, we investigate the possibility of extracting those current-induced spins into a region without SOI, where due to the absence of spin relaxation they can be useful for semiconductor spintronics applications. Finally, in the last section of this chapter we present an all-electrical detection mechanism for the CISA as an alternative to the existing optical techniques.

4.1 Spin accumulation in semiconductors

In a semiconductor the equilibrium electron density n_0 is given by

$$n_0 = \int_{-\infty}^{\infty} dE D(E) f_{\text{FD}}(E), \quad (4.1)$$

where $D(E)$ is the density of states and $f_{\text{FD}}(E)$ is the Fermi-Dirac distribution function. In this thesis we focus on 2DEGs in the degenerate limit, i.e. $f_{\text{FD}}(E) = \theta(\mu - E)$, yielding a simple relation between the equilibrium density n_0 and the chemical potential μ of the 2DEG:

$$n_0 = D_{2\text{D}}(E)\mu \quad (4.2)$$

where $D_{2\text{D}}(E) = m^*/(\pi\hbar^2)$ denotes the two-dimensional density of states. Specifically, in a non-magnetic material the equilibrium densities for spin-up n_+ and spin-down electrons n_- are equal $n_+ = n_- = n_0/2$.

Under non-equilibrium conditions, e.g. when a current is induced by a voltage difference between metallic contacts, the definition of a chemical potential is problematic. However, for small applied voltages and in systems with diffusive dynamics as considered in this chapter, it is common practice to define a local quasichemical potential $\mu(\vec{r})$, which is determined from the local electron density $n(\vec{r})$ [24], for a 2DEG yielding

$$\mu(\vec{r}) = \frac{\pi\hbar^2}{m^*}n(\vec{r}). \quad (4.3)$$

However, in such a situation also the densities of spin-up and spin-down electrons need not be equal anymore $n_+(\vec{r}) \neq n_-(\vec{r})$, and the difference between the quasichemical potential of spin-up $\mu_+(\vec{r}) = (2\pi\hbar^2/m^*)n_+(\vec{r})$ and spin-down electrons $\mu_-(\vec{r}) = (2\pi\hbar^2/m^*)n_-(\vec{r})$ is called spin accumulation $\mu_s(\vec{r}) = \mu_+(\vec{r}) - \mu_-(\vec{r})$, which we visualize in Fig. 4.1. The spin accumulation is related to the spin density defined in Eq. (2.83) via¹

$$\vec{\mu}_s = \frac{4\pi\hbar^2}{m^*}\vec{s}. \quad (4.4)$$

A non-equilibrium spin accumulation in a non-magnetic semiconductor can be created in a variety of ways, for instance via a current flowing from a ferromagnet. While the efficiency of spin injection in metallic systems has been demonstrated experimentally by Johnson and Silsbee [159], the direct spin injection (across an Ohmic contact) from a ferromagnet into a semiconductor is hampered by their conductivity mismatch [26]. Therefore, it is advantageous to inject spins through a tunnel- or a Schottky-barrier, as

¹Due to this direct proportionality, in the rest of the chapter we interchangeably also call s_i spin accumulation.

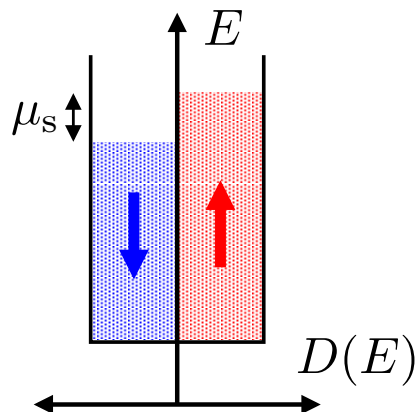


Figure 4.1: Spin accumulation μ_s in a 2DEG: The density of states $D_{\uparrow/\downarrow}(E) = \frac{m^*}{2\pi\hbar^2}$ is equal for spin-up and spin-down, however the states are not equally filled, resulting in different quasi-chemical potentials for the two spin orientations, hence a finite spin accumulation μ_s .

has been successfully demonstrated in recent years [27, 28]. An intriguing alternative to the injection from ferromagnetic metals is offered by the use of magnetic semiconductors, circumventing the problem of the conductivity mismatch. In this respect, spin injection into non-magnetic semiconductors has been reported, achieving very high spin polarization ratios [29, 30].

Another possibility to induce $\mu_s \neq 0$ in a semiconductor is optical orientation, where a non-equilibrium spin accumulation is created by the irradiation of circularly polarized light [31]. There, the angular momentum of the photons is absorbed by the charge carriers of the material yielding a spin accumulation due to the selection rules for transitions between different bands of the semiconductor.

Spin accumulation in a 2DEG can also be created intrinsically not relying on magnetic materials or optical excitation. For instance, a charge current in a semiconductor with SOI causes a non-equilibrium accumulation of spins. This effect — called current-induced spin accumulation (CISA) — is provided by the interplay of scattering and SOI [160]. Although, the CISA has a long-standing history [32, 33, 50] with the first prediction of CISA dating back 30 years, in III-V semiconductors it has been confirmed experimentally only recently, namely in quantum wells [161, 162] and strained bulk semiconductors [163].

As we will see in the remainder of this chapter, the CISA depends on the specific form of the SOI in the material and on the direction of the current. For example, a current in a 2DEG with Rashba SOI induces a spin accumulation that is polarized in-plane and perpendicular to the direction of the current, as visualized in Fig. 4.2. Specifically, when inverting the direction of the current, the polarization direction of the CISA is also reversed.

Finally, we also mention the related spin Hall effect, where — as in the phenomena of CISA — spins get oriented by an electrical current in a medium with SOI [89]. One distinguishes between an extrinsic [34] and intrinsic version [35], the former due to spin-dependent scattering of the electrons at impurities and the latter due to spin precession caused by the SOI in a clean system. In experiments the spin Hall effect

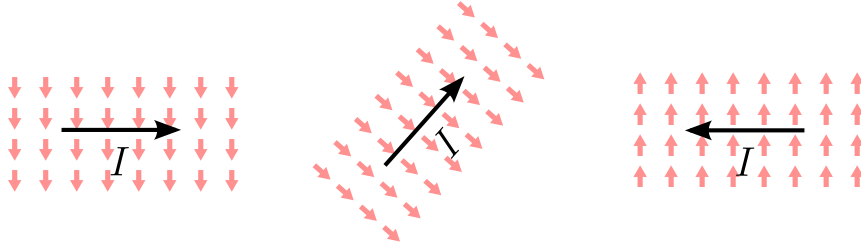


Figure 4.2: Current-induced spin accumulation (indicated by light red arrows) in a 2DEG with Rashba SOI (three examples shown). The polarization direction is perpendicular to the current direction (black arrow).

manifests itself in oppositely polarized non-equilibrium spin accumulations at opposite boundaries of the investigated sample [164], in contrast to the CISA, which is a phenomenon observable in the bulk of the material.

4.2 Current-induced spin accumulation in quantum wires

The phenomenon of CISA in 2DEGs has been the subject of several investigations, both experimentally [164] and theoretically [50, 165]. It is the aim of this section to explore the influence of confinement on the CISA. To be specific, we consider a uniform quantum wire oriented along the x -direction with Rashba, Eq. (2.11), and Dresselhaus SOI, Eq. (2.14):

$$H = \frac{p_x^2 + p_y^2}{2m^*} + H_R + H_{D1} + U_d(x, y) + U_{\text{conf}}(y). \quad (4.5)$$

The disorder potential $U_d(x, y)$, created by static impurities, is introduced in the scattering region of length L , while the two semi-infinite leads connected to the right and left are free of disorder. For the numerical calculations local Anderson disorder with a characteristic strength \bar{U}_{dis} was used, as described in section 2.3.2. Unless stated otherwise, in this section we set $\bar{U}_{\text{dis}} = 2$ and $\bar{E}_F = 0.5$ yielding an elastic mean free path of $l \approx 7.4a$, see Eq. (2.93). It is shorter than any length scale characterizing the system and thus ballistic processes can be ignored.

We furthermore apply a bias $U_0 = \mu_L - \mu_R$ between the left and the right contact and thus generate a current in x -direction. Here, U_0 is chosen small enough for the linear response approximation to be fulfilled. Due to the disorder in the scattering region the (disorder averaged) electron density $\langle n \rangle$ decreases from left to right as shown in Fig. 4.3. For fixed y this decrease can be well approximated by a linear slope in x -direction, a clear signature of diffusive transport in the quantum wire. Close to the hard wall boundaries an oscillatory behavior of $\langle n \rangle$ can be observed due to the finite

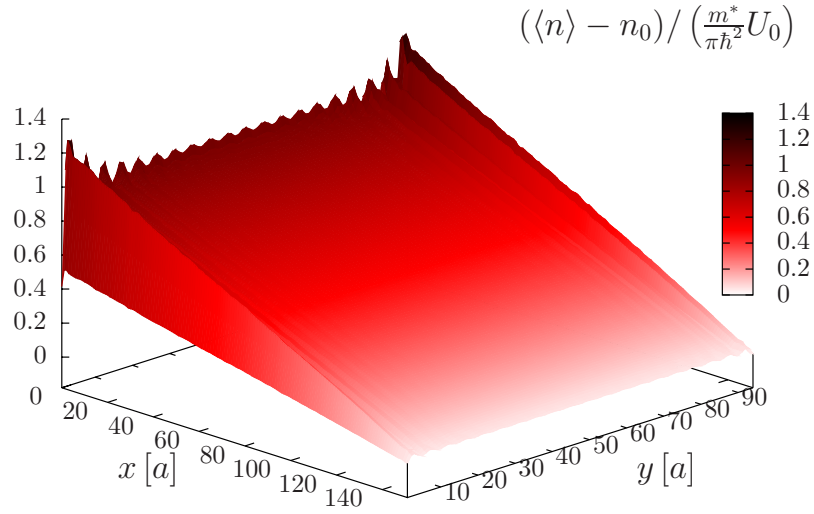


Figure 4.3: The non-equilibrium electron density $\langle n \rangle - n_0$ averaged over 50000 disorder configurations for a system with $L_{so} = 15a$, $W = 94a$ and $L = 150a$.

number of transversal modes. However, in the center of the wire the electron density is almost constant for fixed x : $d\langle n \rangle / dy \approx 0$.

4.2.1 Rashba spin-orbit interaction

As a first step we now consider the case of a quantum wire with Rashba SOI. In Refs. [50, 166] the components of \vec{s} for a 2DEG with Rashba SOI in response to an electric field were calculated within the Kubo formalism:

$$s_x^{2\text{DEG}} = \frac{em^*\tau}{2\pi\hbar^3}\alpha E_y, \quad (4.6a)$$

$$s_y^{2\text{DEG}} = -\frac{em^*\tau}{2\pi\hbar^3}\alpha E_x, \quad (4.6b)$$

$$s_z^{2\text{DEG}} = 0. \quad (4.6c)$$

For our purposes, considering the case of an electric field along the x -direction, $\vec{E} = E_x \hat{x}$, we rewrite those equations by using the connection between the gradient of the electron density dn/dx and the electric field E_x as it is valid for diffusive systems:

$$E_x = \frac{\pi\hbar^2}{m^*e} \frac{dn}{dx} \quad (4.7)$$

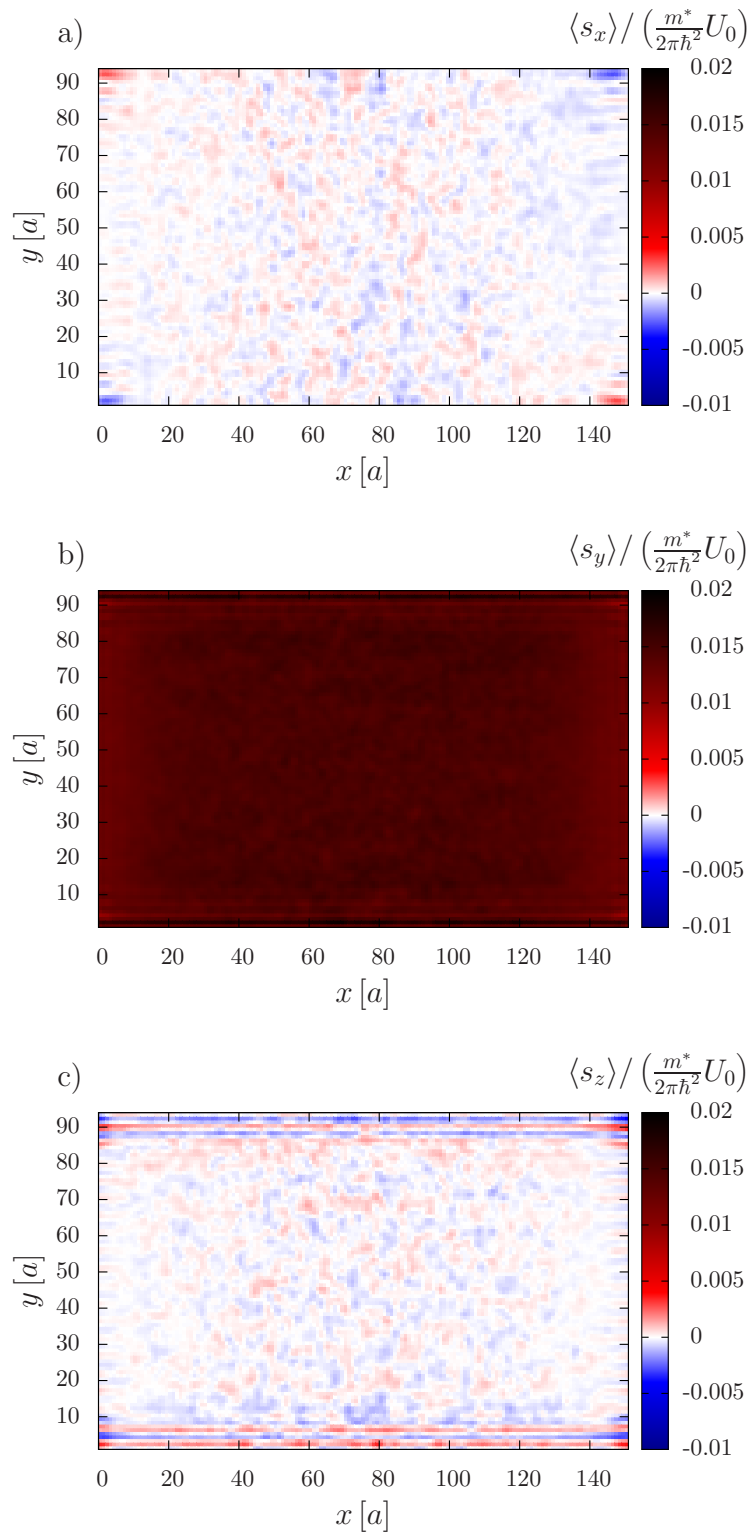


Figure 4.4: The spin accumulation components a) $\langle s_x \rangle$, b) $\langle s_y \rangle$ and c) $\langle s_z \rangle$, averaged over 50000 disorder configurations for a quantum wire with $L_{\text{so}} = 15a$, $W = 94a$ and $L = 150a$.

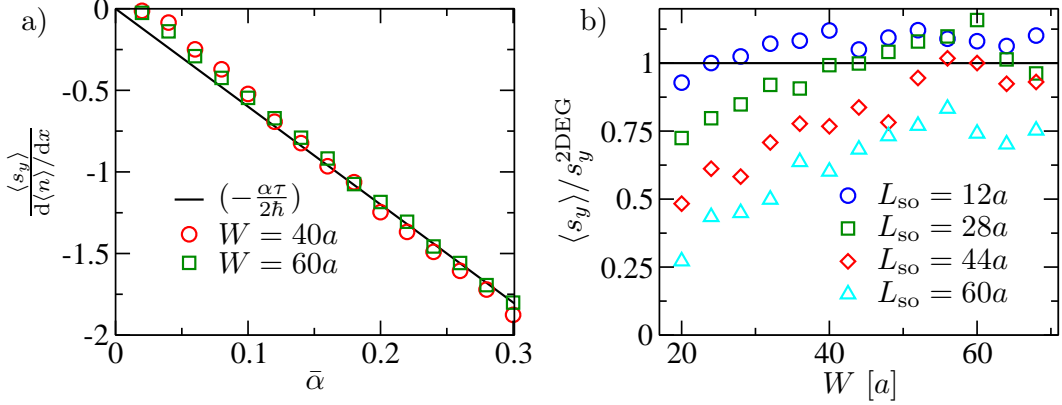


Figure 4.5: a) The numerically calculated ratio $\langle s_y \rangle / (d\langle n \rangle / dx)$ as a function of the Rashba SOI strength $\bar{\alpha}$ for two different widths W of a quantum wire with $L = 100a$. The solid line shows the corresponding value expected in a 2DEG, see Eq. (4.8). b) Ratio between the numerically determined CISA in a quantum wire $\langle s_y \rangle$ and the value expected in a 2DEG $s_y^{2\text{DEG}}$, see Eq. (4.8), as a function of the size of the disordered region $W \times L$ (with $L = 3W$) for several values of the spin precession length $L_{\text{so}} = \pi a / \bar{\alpha}$.

yielding the only finite component

$$s_y^{2\text{DEG}} = -\frac{\alpha\tau}{2\hbar} \frac{dn}{dx}. \quad (4.8)$$

To check this prediction, we numerically calculate the disorder averaged components $\langle s_i \rangle$ of the CISA. As expected, in Figs. 4.4a and 4.4c we observe that on average $\langle s_x \rangle$ and $\langle s_z \rangle$ vanish in the center of the wire, while they exhibit small but finite values close to the hard-wall boundaries and/or the interfaces with the leads. On the other hand, the component $\langle s_y \rangle$, shown in Fig. 4.4b, is finite throughout the wire and in a good approximation constant in the center of the disordered region. To check also the quantitative agreement with the prediction from Eq. (4.8) we now average both $d\langle n \rangle / dx$ and $\langle s_y \rangle$ inside a square region of size $20a \times 15a$ in the center of the wire and compute their ratio $\langle s_y \rangle / (d\langle n \rangle / dx)$. For large $\bar{\alpha}$ in Fig. 4.5a we observe a nice agreement of our simulations with the value expected in a 2DEG, see Eq. (4.8). For small values of $\bar{\alpha}$, the spin precession length² $L_{\text{so}} = \pi a / \bar{\alpha}$, becomes comparable to the width of the quantum wire and the length of the disordered region. In this regime the typical time an electron spends in the disordered region is not long enough for the spin to be randomized efficiently, which is a precondition for the appearance of CISA [160]. Then spin dynamics is essentially ballistic causing deviations from the diffusive theory. This size-dependence is visualized in Fig. 4.5b, where we plot the ratio $\langle s_y \rangle / s_y^{2\text{DEG}}$ against the size of the disordered region for four different Rashba SOI strengths. For

²The spin precession length corresponds to the distance of ballistic motion after which a spin is rotated by an angle 2π under the influence of the SOI.

$L_{\text{so}} = 12a$ the CISA in the wire takes values close to those expected in a bulk 2DEG, while for the other three data sets we clearly see a suppression of the CISA for small system sizes. In accordance with the supposition that the value of L_{so} relative to the size of the system is the decisive parameter for the absence of CISA in the quantum wire, we observe that for increasing L_{so} the suppression is more pronounced at a fixed system size. At the end of this section we will return to this issue and provide further analytical evidence that the finite size of the disordered region is indeed responsible for the suppression of the CISA.

4.2.2 Rashba and Dresselhaus spin-orbit interaction

We will now extend the considerations of the previous paragraphs by including also the linear Dresselhaus SOI, Eq. (2.14). While the spin accumulation created in a 2DEG with only Rashba SOI is always polarized perpendicular to the electric field, the interplay between Rashba and Dresselhaus SOI gives rise to a rich dynamics in the magnitude and polarization-direction of the CISA. Calculations for 2DEGs with both Rashba and Dresselhaus SOI were performed in Ref. [165] by using the Kubo-formalism and in Ref. [167] by solving the Boltzmann equation, predicting the following values for the components of the CISA:

$$s_x^{\text{2DEG}} = \frac{em^*\tau}{2\pi\hbar^3}(\beta E_x + \alpha E_y), \quad (4.9a)$$

$$s_y^{\text{2DEG}} = \frac{em^*\tau}{2\pi\hbar^3}(-\alpha E_x - \beta E_y), \quad (4.9b)$$

$$s_z^{\text{2DEG}} = 0, \quad (4.9c)$$

for a coordinate system (x, y, z) along the principal crystallographic axes ($[100]$, $[010]$, $[001]$).

We now consider a different coordinate system, where the quantum wire is oriented along the x -direction, which spans an angle ϕ with the $[100]$ crystal axis. Then $E_y = 0$ and the finite CISA contributions read:

$$s_x^{\text{2DEG}} = \frac{\tau}{2\hbar} \frac{dn}{dx} \beta \cos 2\phi, \quad (4.10a)$$

$$s_y^{\text{2DEG}} = -\frac{\tau}{2\hbar} \frac{dn}{dx} (\alpha + \beta \sin 2\phi). \quad (4.10b)$$

To test whether we can reproduce this behavior, we investigate the CISA for different wire orientations with respect to the crystal lattice. We find that $\langle s_z \rangle$ is essentially zero and thus in Fig. 4.6 we only show the components $\langle s_x \rangle$ and $\langle s_y \rangle$ at fixed SOI strengths α and β as a function of the angle ϕ . In view of Fig. 4.5b the size of the disordered region was chosen large enough for the CISA not to be suppressed from the value expected in a bulk 2DEG and consequently we observe a nice agreement of our numerical calculations with the results from Eqs. (4.10a) and (4.10b).

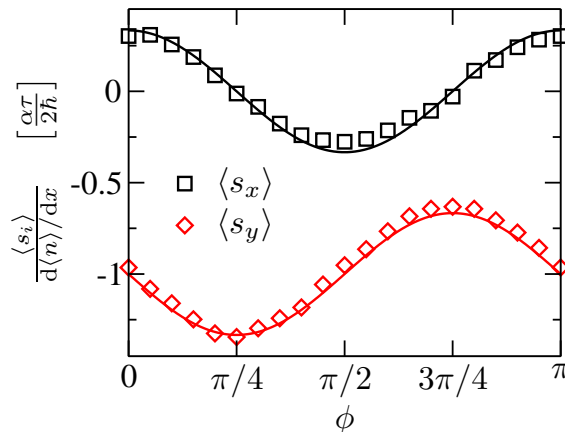


Figure 4.6: Components of the CISA $\langle s_x \rangle$, $\langle s_y \rangle$ divided by the gradient of the electron density $d\langle n \rangle/dx$ as a function of the angle ϕ between the wire direction \hat{x} and the [100] crystal axis. The symbols, which show the values from the numerical calculations, are compared to the predictions from Eqs. (4.10a) and (4.10b) presented as solid lines. Parameters for the numerical calculation: $\bar{\alpha} = 0.15$, $\bar{\beta} = 0.05$, $W = 120a$, $L = 200a$, $N_d = 10000$, $\bar{E}_F = 0.4$.

4.2.3 Suppression of the current-induced spin accumulation in finite-sized systems

We have seen earlier in this section that in quantum wires confinement causes a suppression of the CISA from the value expected in a bulk 2DEG. As we will show now, it is also important to take into account the interplay between Rashba and Dresselhaus SOI to fully understand the suppression of the CISA in finite-sized structures. In particular we demonstrate that the correspondence between the numerical calculations in quantum wires and the theoretical predictions for 2DEGs breaks down when α and β are (nearly) equal. In Fig. 4.7a we present the components $\langle s_x \rangle$ and $\langle s_y \rangle$ of the CISA for fixed Dresselhaus SOI strength β with respect to the strength of the Rashba SOI α for different sizes $L \times L$ of the disordered region. There we observe deviations of our numerical results from the predictions for a bulk 2DEG (plotted as dotted brown lines), see Eqs. (4.10a) and (4.10b), when the strengths of both SOI contributions are comparable: For $\alpha \approx \beta$ the spin accumulation is reduced and it completely vanishes at $\alpha = \beta$. The shape of the dip around $\alpha = \beta$ is dependent on the size of the system. We observe that the dip becomes sharper for increasing L , while for all system sizes $\langle \vec{s} \rangle = 0$ at $\alpha = \beta$.

We can gain further insight into the origin of the differences between our numerical results and the values predicted for bulk 2DEGs, Eqs. (4.10a) and (4.10b), by performing analytical calculations based on diffusion equations. To this end we use the coupled diffusion equations for charge and spin derived in Ref. [168] for a 2DEG with both Rashba and Dresselhaus SOI. They are valid in the regime where the \vec{s} varies slowly

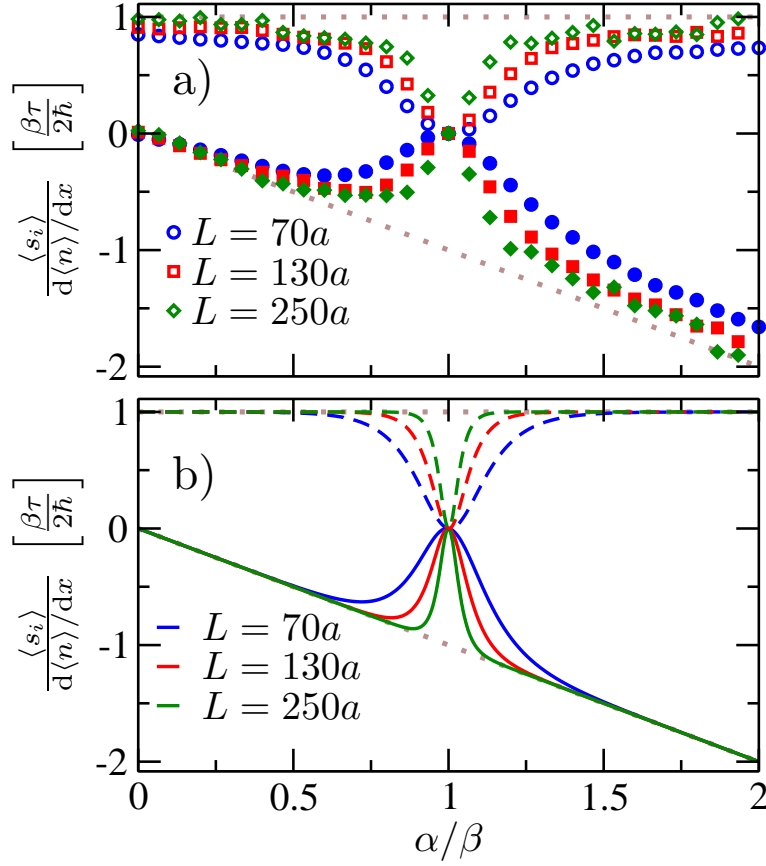


Figure 4.7: CISA components $\langle s_x \rangle$ (open symbols/dashed lines) and $\langle s_y \rangle$ (filled symbols/solid lines) as a function of the ratio α/β for different system sizes. The results for an extended 2DEG, Eqs. (4.9a) and (4.9b), are shown as dotted brown lines. a) Numerical tight-binding calculation with parameters $N_d = 5000$, $\phi = 0$, $\bar{\beta} = 0.15$ for a wire where the width and the length of the disordered region were chosen to be equal $L = W$. b) Results of the diffusion equation calculations, Eqs. (4.15a) and (4.15b).

on scales of the mean free path, i.e. $\alpha k_F \tau / \hbar \ll 1$ and $\beta k_F \tau / \hbar \ll 1$. For the choice of $\hat{x} \parallel [100]$, i.e. $\phi = 0$, they read in our notation

$$\begin{aligned}
 D\nabla^2 n & - K_{s-c} \left[\alpha \left(\frac{\partial s_y}{\partial x} - \frac{\partial s_x}{\partial y} \right) + \beta \left(\frac{\partial s_x}{\partial x} - \frac{\partial s_y}{\partial y} \right) \right] \\
 & = 0,
 \end{aligned} \tag{4.11a}$$

$$\begin{aligned}
 D\nabla^2 s_x & + K_p \left[\alpha \frac{\partial s_z}{\partial x} + \beta \frac{\partial s_z}{\partial y} \right] - K_{s-c} \left[-\alpha \frac{\partial n}{\partial y} + \beta \frac{\partial n}{\partial x} \right] \\
 & = \frac{4Dm^2}{\hbar^4} (\alpha^2 + \beta^2) s_x + 8\alpha\beta \frac{Dm^2}{\hbar^4} s_y,
 \end{aligned} \tag{4.11b}$$

$$\begin{aligned}
D\nabla^2 s_y &+ K_p \left[\beta \frac{\partial s_z}{\partial x} + \alpha \frac{\partial s_z}{\partial y} \right] - K_{s-c} \left[-\beta \frac{\partial n}{\partial y} + \alpha \frac{\partial n}{\partial x} \right] \\
&= \frac{4Dm^2}{\hbar^4} (\alpha^2 + \beta^2) s_y + 8\alpha\beta \frac{Dm^2}{\hbar^4} s_x,
\end{aligned} \tag{4.11c}$$

$$\begin{aligned}
D\nabla^2 s_z &- K_p \left[\alpha \left(\frac{\partial s_x}{\partial x} + \frac{\partial s_y}{\partial y} \right) + \beta \left(\frac{\partial s_y}{\partial x} + \frac{\partial s_x}{\partial y} \right) \right] \\
&= \frac{8Dm^2}{\hbar^4} (\alpha^2 + \beta^2) s_z.
\end{aligned} \tag{4.11d}$$

In these equations terms containing the prefactor $K_p = 4Dm/\hbar^2$ account for the precession of the spins due to SOI and terms with the prefactor $K_{s-c} = (2\tau Dm^2/\hbar^5) (\alpha^2 - \beta^2)$ describe the spin-charge coupling.

At the singular point $\alpha = \pm\beta$ the charge and spin diffusion equations (4.11a)-(4.11d) are decoupled, i.e. $K_{s-c} = 0$. The spin dynamics is then totally independent of the charge degree of freedom and consequently no spin accumulation due to an electrical current can exist. The importance of this condition was first recognized in Ref. [169], where it was argued that in a bulk 2DEG the CISA takes the values given in Eqs. (4.9a)-(4.9c), except for the singular points $\alpha = \pm\beta$, where it is absent. To understand this behavior we take a closer look at the spin relaxation in the 2DEG, which is an important ingredient for the establishment of the CISA [160]. For any $|\alpha| \neq |\beta|$ the spin relaxation length is finite and thus smaller than the infinitely extended 2DEG yielding finite CISA. However for $\alpha = \pm\beta$ the spin relaxation length becomes infinite and thus special attention is needed when taking the limits in the course of the calculations, causing the discrepancy between Ref. [169] and Refs. [165, 167].

Using the diffusion equations (4.11a)-(4.11d) we can also circumstantiate that the reduction of the CISA around $\alpha = \beta$ observed in Fig. 4.7a can be explained by the finite size of the disordered region as indicated by the narrowing of the dip with increasing system size. We begin by solving the diffusion equations (4.11a)-(4.11d) for a region which is infinitely extended in the y -direction but has a finite length L in x -direction, which is the direction of current flow. Due to the translational invariance in the y -direction, perpendicular to the current, there is no dependence of the densities n and \vec{s} on y . To simplify the calculations and motivated by our numerical results we furthermore assume a constant slope for the electron density along the x -direction, $n' = dn/dx$, the absence of spin accumulation polarized perpendicularly to the 2DEG, $s_z = 0$, and the absence of spin accumulation in the disorder free leads attached to the central region at $x = 0$ and $x = L$. Therefore, we choose as appropriate set of boundary conditions:

$$s_x(x = 0) = s_y(x = 0) = s_x(x = L) = s_y(x = L) = 0. \tag{4.12}$$

With these assumptions Eqs. (4.11b) and (4.11c) simplify to

$$\frac{\hbar^4}{4m^2} \nabla^2 s_x - \frac{\tau}{2\hbar} (\alpha^2 - \beta^2) \beta n' = [(\alpha^2 + \beta^2) s_x + 2\alpha\beta s_y], \quad (4.13a)$$

$$\frac{\hbar^4}{4m^2} \nabla^2 s_y - \frac{\tau}{2\hbar} (\alpha^2 - \beta^2) \alpha n' = [(\alpha^2 + \beta^2) s_y + 2\alpha\beta s_x], \quad (4.13b)$$

and can be solved straightforwardly, yielding the following analytical expressions for the position dependent spin accumulations $s_x(x)$ and $s_y(x)$:

$$s_x(x) = \frac{\tau}{2\hbar} n' \left[\begin{aligned} & \beta - \frac{(\alpha + \beta)(1 - e^{-(2m/\hbar^2)(\alpha-\beta)L})}{4 \sinh\left((2m/\hbar^2)(\alpha - \beta)L\right)} e^{(2m/\hbar^2)(\alpha-\beta)x} \\ & + \frac{(\alpha - \beta)(1 - e^{-(2m/\hbar^2)(\alpha+\beta)L})}{4 \sinh\left((2m/\hbar^2)(\alpha + \beta)L\right)} e^{(2m/\hbar^2)(\alpha+\beta)x} \\ & + \frac{(\alpha + \beta)(1 - e^{(2m/\hbar^2)(\alpha-\beta)L})}{4 \sinh\left((2m/\hbar^2)(\alpha - \beta)L\right)} e^{-(2m/\hbar^2)(\alpha-\beta)x} \\ & - \frac{(\alpha - \beta)(1 - e^{(2m/\hbar^2)(\alpha+\beta)L})}{4 \sinh\left((2m/\hbar^2)(\alpha + \beta)L\right)} e^{-(2m/\hbar^2)(\alpha+\beta)x} \end{aligned} \right], \quad (4.14a)$$

$$s_y(x) = \frac{\tau}{2\hbar} n' \left[\begin{aligned} & -\alpha + \frac{(\alpha + \beta)(1 - e^{-(2m/\hbar^2)(\alpha-\beta)L})}{4 \sinh\left((2m/\hbar^2)(\alpha - \beta)L\right)} e^{(2m/\hbar^2)(\alpha-\beta)x} \\ & + \frac{(\alpha - \beta)(1 - e^{-(2m/\hbar^2)(\alpha+\beta)L})}{4 \sinh\left((2m/\hbar^2)(\alpha + \beta)L\right)} e^{(2m/\hbar^2)(\alpha+\beta)x} \\ & - \frac{(\alpha + \beta)(1 - e^{(2m/\hbar^2)(\alpha-\beta)L})}{4 \sinh\left((2m/\hbar^2)(\alpha - \beta)L\right)} e^{-(2m/\hbar^2)(\alpha-\beta)x} \\ & - \frac{(\alpha - \beta)(1 - e^{(2m/\hbar^2)(\alpha+\beta)L})}{4 \sinh\left((2m/\hbar^2)(\alpha + \beta)L\right)} e^{-(2m/\hbar^2)(\alpha+\beta)x} \end{aligned} \right]. \quad (4.14b)$$

Since we are interested in the values of s_x and s_y away from the interfaces, in Fig. 4.7b we plot these components in the center of the disordered region at $x = L/2$. They read

$$s_x(L/2) = \frac{\tau}{2\hbar} n' \left[\beta - \frac{(\alpha + \beta)}{2 \cosh \left((m/\hbar^2)(\alpha - \beta)L \right)} + \frac{(\alpha - \beta)}{2 \cosh \left((m/\hbar^2)(\alpha + \beta)L \right)} \right], \quad (4.15a)$$

$$s_y(L/2) = \frac{\tau}{2\hbar} n' \left[-\alpha + \frac{(\alpha + \beta)}{2 \cosh \left((m/\hbar^2)(\alpha - \beta)L \right)} + \frac{(\alpha - \beta)}{2 \cosh \left((m/\hbar^2)(\alpha + \beta)L \right)} \right]. \quad (4.15b)$$

For lengths L exceeding the effective spin-orbit lengths $L_{\text{so}}^{\pm} = \hbar^2/(m^*|\alpha \pm \beta|)$ the correction terms with dependence on L can be neglected and we recover the values expected in a bulk 2DEG, namely $s_x^{\text{2DEG}} = \tau n' \beta / (2\hbar)$ and $s_y^{\text{2DEG}} = -\tau n' \alpha / (2\hbar)$. In the opposite regime ($L \ll L_{\text{so}}^+$ and/or $L \ll L_{\text{so}}^-$) the correction terms completely (partly) cancel the bulk value at (around) the points $\alpha = \pm\beta$. This supports our findings from the numerical tight binding calculations, namely that the width of the dip around $\alpha = \beta$ becomes narrower for increasing length L .

Comparing the results of Fig. 4.7a and Fig. 4.7b, we observe that in the diffusion equation calculations the suppression is less effective, i.e. the width of the dip is narrower in Fig. 4.7b than in Fig. 4.7a for systems of comparable size. There are several possible reasons for this discrepancy. On the one hand, the validity of Eqs. (4.11a)-(4.11d) is limited to the diffusive regime, while the numerics describe the full quantum mechanics of the problem. For reasons of computational feasibility, in the numerics we have to choose values for α and β , where the conditions $\alpha k_{\text{F}} \tau / \hbar \ll 1$ and/or $\beta k_{\text{F}} \tau / \hbar \ll 1$ are not strictly fulfilled, giving rise to deviations of the two approaches. Furthermore, in the numerics the CISA is not zero at the interfaces to the leads $x = 0$ and $x = L$, a condition we assessed in the diffusion equation calculations. Finally, in Eqs. (4.15a) and (4.15b) we evaluated the CISA in the center of the wire at $x = L/2$, thereby possibly overestimating its value compared to the numerics, where we averaged the CISA over a region of finite size in the center of the disordered region.

For the calculations shown in Fig. 4.7a we used disordered, quadratic regions of size $L \times L$, which might also explain the differences between Fig. 4.7a and Fig. 4.7b, where the width of the disordered region was assumed to be infinite. However, as we show in Fig. 4.8a the CISA is independent of the width of the wire, i.e. the suppression is solely due to the finite length of the disordered region, at least for $W \gtrsim L$. Of course, when

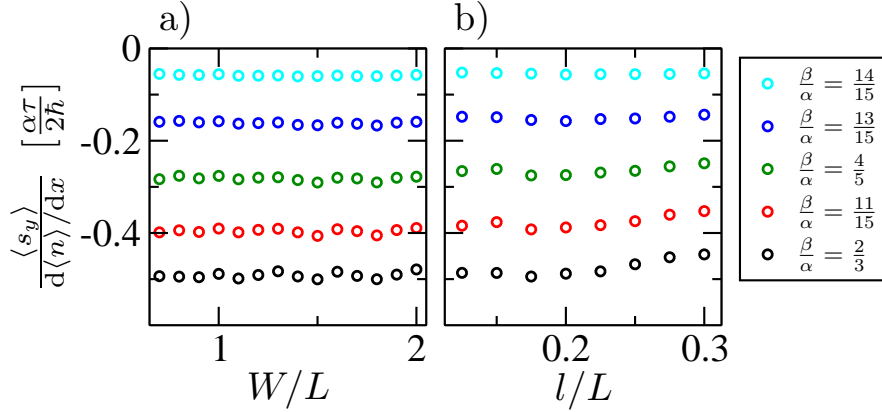


Figure 4.8: Spin accumulation $\langle s_y \rangle / (d\langle n \rangle / dx)$ as a function of a) the mean free path l (fixed width $W = 50a$) and b) the width of the wire (fixed disorder strength $\bar{U}_{\text{dis}} = 2$) for several different ratios β/α . Parameters: $\bar{\alpha} = 0.15$, $\bar{E}_F = 0.5$, $L = 40a$ and $N_d = 3000$.

this condition is not fulfilled, also the finite width can induce a reduction of the CISA via the suppression of the spin relaxation, which will be investigated more closely in section 5.3.1. We already observed this reduction in Fig. 4.5a, where at small $\bar{\alpha}$ the CISA was smaller for $W = 40a$ than for $W = 60a$ for wires with equal L .

Although the analytical calculations do not perfectly match the results from the numerical tight-binding simulations, there is nevertheless much qualitative agreement between both approaches. For instance, the form of the dip in the diffusion equation calculations does not depend on the degree of disorder in the system, i.e. the scattering time τ does not appear in the correction terms of Eqs. (4.15a) and (4.15b) but is only present in the overall prefactor. In Fig. 4.8b we confirm that this is also the case in the numerical simulations, where we observe that $\langle s_y \rangle / s_y^{2\text{DEG}}$ is in good approximation constant upon variation of the mean free path for several values of β/α .

Coming back to the case of only Rashba SOI, we can use the results from Eqs. (4.15a) and (4.15b) to explain the suppression of the CISA in Fig. 4.5b for spin precession lengths larger than the size of the disordered region. Setting $\beta = 0$ in Eqs. (4.15a) and (4.15b), we obtain the CISA in the center of a disordered region with infinite width but finite length L , subject to only Rashba SOI:

$$s_x(L/2) = 0 \quad (4.16a)$$

$$s_y(L/2) = \frac{\tau}{2\hbar} n' \left[-\alpha + \frac{\alpha}{\cosh\left((m^*/\hbar^2)\alpha L\right)} \right] \quad (4.16b)$$

As expected for the pure Rashba case [50], s_x is zero and $s_y = -\alpha\tau n' / (2\hbar)$ when L is much longer than the spin precession length $L \gg L_{\text{so}} = \hbar^2 / (m^*\alpha)$. For L comparable to L_{so} the second term in the sum of Eq. (4.16b) is no longer negligible and causes a

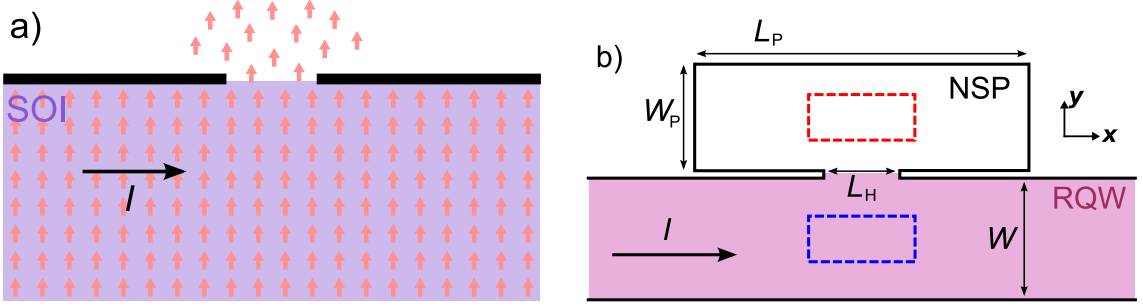


Figure 4.9: a) Setup for the extraction of current-induced spins from a region with SOI into a region with small or negligible spin relaxation. b) Geometry used for the numerical calculations to investigate the extraction of current-induced spins. In a quantum wire with Rashba SOI (RQW) the current-induced spins are created and they are extracted into a side pocket without SOI (NSP). The red/blue square indicates the region over which $\langle s_y \rangle$ is averaged yielding $\langle s_y^P \rangle$ and $\langle s_y^B \rangle$, respectively.

reduction (or even complete suppression for $L \ll L_{so}$) of s_y from the bulk 2DEG value $s_y^{2DEG} = -\alpha\tau n'/(2\hbar)$, which is in line with the numerical results from Fig. 4.5b.

In conclusion, we have provided arguments that an infinitely extended 2DEG shows the behavior given in Refs. [165, 167], except for the singular case of $\alpha = \pm\beta$ where CISA vanishes regardless of the system size. In a finite-sized sample, however, the CISA around $\alpha = \pm\beta$ is suppressed from the bulk value, when one of the effective spin-orbit lengths $L_{so}^{\pm} = \frac{\hbar^2}{m(\alpha \pm \beta)}$ exceeds the size of the system. Apart from the finite size, there are also other mechanisms, which render this suppression of the CISA around $\alpha = \pm\beta$ detectable in experiments. We refer to the application of an ac-bias voltage [169] and/or the inclusion of the cubic Dresselhaus term [170], which both cause a broadening of the dip of the spin accumulations around $\alpha = \pm\beta$.

4.3 Extraction of current-induced spins

Operating spintronics devices, as e.g. spin transistors [18], naturally requires spin polarized currents and/or a local non-equilibrium spin accumulation. Ideally, one would like to work with a spin accumulation that is as large as possible, but on the other hand it should not be impeded by spin relaxation. However, both the magnitude of the CISA and the spin relaxation increase with the strength of the SOI. Therefore, it is difficult to work with those current-induced spins created in a semiconductor with SOI, since their existence is dependent on a current flowing in the 2DEG and quickly the equilibrium value of $\mu_S = 0$ will establish after turning the current off.

In this section — as a possible way out of this dilemma — we investigate the possibility to extract spins from a region of the 2DEG with strong Rashba SOI, where they

are created by an electrical current, into a region with zero or negligibly small SOI. The extracted spins are not subject to spin relaxation anymore and possess a fixed polarization, which does not decay. Whereas the feasibility of such an extraction setup has first been discussed in Ref. [171] using diffusion equations, we will now present numerical tight-binding calculations on that matter analyzing the specific conditions under which this extraction setup can work in practice. The following results remain valid also when Dresselhaus SOI is present, as only the magnitude and direction of the spin polarization will change in correspondence to the results of the previous section. In Fig. 4.9a we show a promising candidate for the spin extraction setup. It consists of a 2DEG which is divided into two areas (e.g. via side gates) which are connected by an opening of finite extension. In order to control the strength of the Rashba SOI, two separate top gates above the upper and lower half plane of the 2DEG, respectively, can be used. Applying a voltage to those top gates changes the strength of the Rashba SOI and one can therefore tune α in the lower/upper half plane to be large/zero. In order to numerically study the spin accumulation that can be extracted to a region without SOI we focus on the setup shown in Fig. 4.9b, where a side pocket without SOI (NSP) of size $L_P \times W_P$ is connected to a quantum wire with constant finite Rashba SOI (RQW) of infinite length and a width W via a contact of size L_H . For the calculations we use the Hamiltonian Eq. (4.5) introduced earlier in this chapter, where $U_{\text{conf}}(x, y)$ accounts for the hard-wall confinement potential of the extraction geometry shown in Fig. 4.9b. Disorder of strength $\bar{U}_{\text{dis}} = 2$ is present inside the RQW in the central region of length $L \geq L_P$ and everywhere inside the NSP. Since we consider a spatially dependent Rashba SOI we have to use the anti-symmetrized version of the Rashba Hamiltonian, Eq. (2.11),

$$H_R = \frac{1}{2}\sigma_x\{\alpha(y), p_y\} - \alpha(y)\sigma_y p_x, \quad (4.17)$$

to ensure its Hermiticity.

We now investigate the conditions under which spins from the RQW can be efficiently extracted into the NSP. In Fig. 4.10, we show the impurity averaged spin accumulation $\langle s_y \rangle$ of three distinctive systems with fixed spin precession length $L_{\text{so}} = 12a$. For an infinite interface $L_H \rightarrow \infty$ between the RQW and the NSP, Fig. 4.10a, the spin accumulation extracted into the NSP is very small. This is in agreement with Ref. [172], where it was shown that no current-induced spins can be injected across an infinite interface into a region without SOI, when the scattering time τ is equal in both regions. Nevertheless, when the size of the contact is made smaller, Fig. 4.10b, we observe that the spin accumulation inside the NSP increases, reaching a value comparable to the CISA in the bulk of the RQW when the size of the opening is comparable to L_{so} , see Fig. 4.10c. For all three cases shown in Fig. 4.10 we limited the presentation of the CISA to the component $\langle s_y \rangle$. Being the only finite component in the RQW, we observe that also in the NSP the other two components are small compared to $\langle s_y \rangle$, which demonstrates that the spin state of the electron is not fundamentally changed upon crossing the contact.

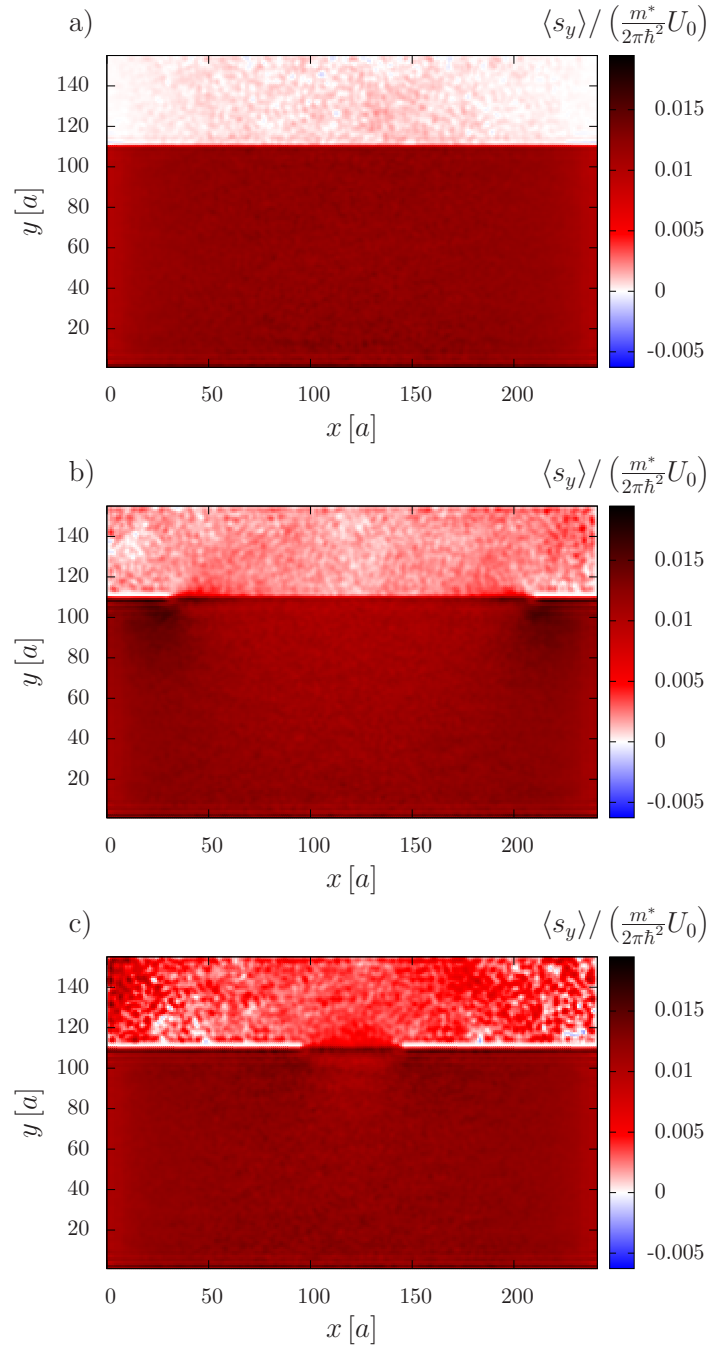


Figure 4.10: a) Spin accumulation $\langle s_y \rangle$ averaged over $N_d = 72000$ disorder configurations. Common parameters: $\bar{E}_F = 0.38$, $L = 240a$. a) A quantum wire of width $W = 156a$ with an abrupt drop of the SOI strength from $\bar{\alpha} = \pi/12$ ($L_{so} = 12a$) for $y < 112a$ to zero for $y \geq 112a$. b) Extraction setup shown in Fig. 4.9b with $W = 111a$, $L_H = 180a$, $L_P = 240a$, $W_P = 44a$ and $L_{so} = 12a$. c) Same as panel b) with $L_H = 50a$.

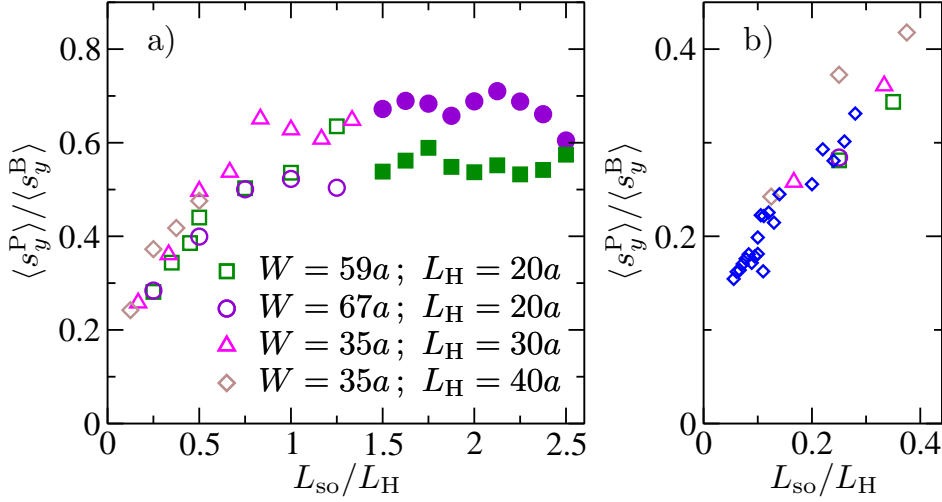


Figure 4.11: Ratio $\langle s_y^P \rangle / \langle s_y^B \rangle$ between the averaged spin accumulations in the NSP and the RQW as a function of the relative size of the spin precession length L_{so} and the size of the contact L_H . a) For four combinations of W and L_H the spin precession length L_{so} was varied. Parameters: $\bar{E}_F = 0.38$, $L = 100$, $L_P = 80a$, $W_P = 14a$. Open symbols: $N_d = 20000$, filled symbols: $N_d = 60000$. b) Close up view for small values of L_{so}/L_H . The blue diamonds were extracted from the geometry shown in Fig. 4.10b,c ($W = 111a$, $L_P = 240a$, $W_P = 44a$, $\bar{E}_F = 0.38$, $L = 240a$ and $N_d = 72000$) for several different combinations of L_{so} and L_H . We also replot the data points from panel a) that lie in the range of L_{so}/L_H shown.

In order to quantify the extraction efficiency, we evaluate the relative size of the spin accumulation in the NSP $\langle s_y^P \rangle$ and in the RQW $\langle s_y^B \rangle$, where $\langle s_y^{P(B)} \rangle$ refers to $\langle s_y \rangle$ averaged over the red (blue) rectangular region shown in Fig. 4.9b. In Fig. 4.11 we plot the ratio $\langle s_y^P \rangle / \langle s_y^B \rangle$ as a function of L_{so}/L_H for various values of wire width W and contact size L_H . We observe that starting from small L_{so}/L_H , the spin accumulation increases with L_{so} , approaching a value $\approx 0.5 - 0.7$, which is in between the estimates 0.5 and 1 from diffusion equation calculations using two different types of boundary conditions, respectively [173]. Hence, we can state that the extraction efficiency is especially good, when the size of the contact is chosen smaller than the spin precession length due to the SOI in the RQW.

The asymptotic behavior for small L_{so}/L_H shown in Fig. 4.11b suggests a finite value $\langle s_y^P \rangle / \langle s_y^B \rangle > 0$ for $(L_{so}/L_H) \rightarrow 0$, which would be in disagreement with the results from Ref. [172]. Unfortunately, we cannot approach this limit further, because we are limited to $L_{so}/L_H > 0.05$ by the size of the geometries, which can be treated numerically in a reasonable amount of time.

4.4 Electrical detection of current-induced spin accumulation

Having dealt with various issues on the creation and manipulation of current-induced spins in the previous sections, we now turn our attention to the detection of the CISA. So far the experimental verifications of the CISA involved the use of optical techniques [161–163]. In this section we follow an alternative path and present an all-electrical detection mechanism for the CISA in a disordered 2DEG with SOI.

4.4.1 Detection principle

In Ref. [174] the possibility of electrically detecting the CISA by a ferromagnetic contact in a multi-terminal setup was discussed. In that setting the CISA generates a voltage drop in the ferromagnet and/or a torque on its magnetization. Motivated by this work, here we consider a four terminal geometry, visualized in Fig. 4.12. In contrast to Ref. [174], we focus on an implementation without ferromagnetic contacts.

The application of a voltage difference $V_1 - V_2 > 0$ between leads L1 and L2 results in an electrical current in the Hall bar in $-x$ -direction. The disorder of strength $\bar{U}_{\text{dis}} = 2$ in the scattering region ensures that the transport in the device is diffusive, i.e. the mean free path is shorter than the relevant length scales of the device. As we have seen in the preceding sections, for the Rashba SOI considered here, in the Hall bar a spin polarization along the y -direction will arise induced by the current of electrons flowing from L2 to L1. The two lateral leads L3 and L4 serve as voltage probes and thus are biased to carry no current ($I_3 = I_4 = 0$). However, as we have shown in the previous section, the spin accumulation created in the Hall bar can diffuse out into the side contacts. The spin polarization ratio of this diffusion current depends on the strength of the SOI in the Hall bar and the opening size of the contact.

In Ref. [174] one of the voltage probe side contacts was chosen to be a ferromagnet. Using diffusion equations the authors were able to show that the CISA gives rise to a voltage drop in the ferromagnet. With those results in mind, here we consider lead L3 to be spin selective, i.e. only spins with a specific polarization are allowed to enter. Then we can relate the voltage V_3 to the CISA in the wire, as we will show in the following.

In linear response, the current in the Landauer-Büttiker formalism in lead i of a N -terminal structure is given by Eq. (2.49),

$$I_i = \frac{e^2}{h} \sum_{j=1}^N (V_j - V_i) T^{i,j}, \quad (4.18)$$

where $T^{i,j}$ is the transmission probability from lead j to lead i . Fixing $V_1 = -V_2 = V_0/2$ and demanding $I_3 = I_4 = 0$ we obtain coupled equations for the voltages V_3 and V_4

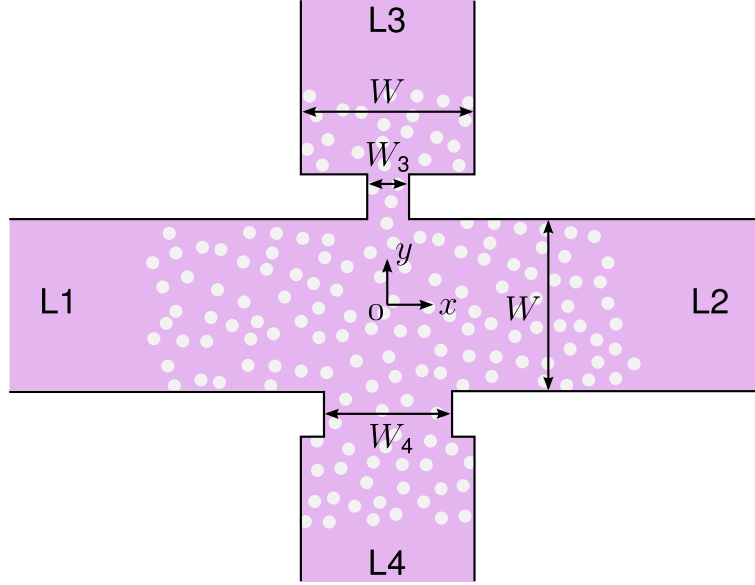


Figure 4.12: Four-terminal setup used for the detection of the CISA. The voltage probe leads L3 and L4 are connected to a Hall bar oriented in x -direction. The disorder, which is only present in the scattering region, is indicated by white circles.

from Eq. (4.18) for $i = 3, 4$:

$$V_3(T^{3,1} + T^{3,2} + T^{3,4}) = \frac{V_0}{2}(T^{3,1} - T^{3,2}) + V_4 T^{3,4}, \quad (4.19)$$

$$V_4(T^{4,1} + T^{4,2} + T^{4,3}) = \frac{V_0}{2}(T^{4,1} - T^{4,2}) + V_3 T^{4,3}. \quad (4.20)$$

The solution of these equations yields the voltage difference between the two side-coupled leads L3 and L4:

$$\Delta V_{34} = V_3 - V_4 = V_0 \frac{T^{3,1} T^{4,2} - T^{3,2} T^{4,1}}{\Omega}, \quad (4.21)$$

with

$$\Omega = T^{3,1}(T^{4,1} + T^{4,2} + T^{4,3}) + T^{3,2}(T^{4,1} + T^{4,2} + T^{4,3}) + T^{3,4}(T^{4,1} + T^{4,2}). \quad (4.22)$$

In the following we consider the transmission probabilities in Eq. (4.21) averaged over many disorder configurations, in order to get rid of the sample to sample fluctuations due to quantum interference.

If the lateral leads L3 and L4 are placed opposite each other and spins of either polarization can enter, there will be no significant voltage difference ΔV_{34} . However, upon making one of those lateral contacts spin sensitive (in our case the upper one), ΔV_{34}

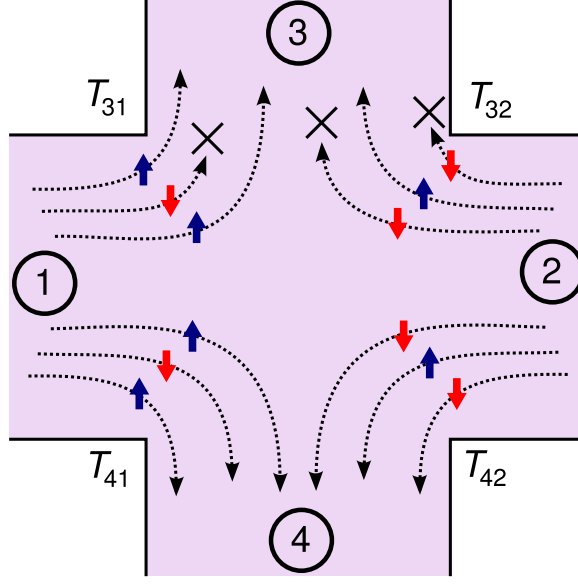


Figure 4.13: Sketch to facilitate the understanding of the emergence of a finite voltage difference ΔV_{34} , when the upper contact is spin selective. Electrons that originated from L1 on average possess a spin polarization $\sigma = \uparrow$ in the center of the wire due to the peculiar nature of SOI. On the contrary, electrons that originated from L2 on average possess a spin polarization $\sigma = \downarrow$ there. Since the lower contact accepts spins of either spin polarization, there is no significant difference in the transmission probabilities from L1 and L2 into L4: $T^{4,1} \approx T^{4,2}$. On the other hand the upper contact is spin selective, i.e. only spins with $\sigma = \uparrow$ polarization can diffuse into it. This results in a positive difference $T^{3,1} - T^{3,2} > 0$, yielding $\Delta V_{34} \neq 0$.

can have a finite, detectable value. The emergence of this voltage difference ΔV_{34} can be understood in the Landauer-Büttiker picture, by considering Eq. (4.21). To this end, we analyze the transmission probabilities in the four-terminal geometry, which we illustrate in Fig. 4.13. In the center of the disordered region, i.e. close to L3 and L4, the electrons originating from L1, which have moved in the positive x -direction, will on average have the opposite spin polarization (same magnitude, opposite direction) from electrons originating from L2, which on average have moved in the negative x -direction. This is due to the peculiar nature of the SOI, which upon finite bias gives rise to CISA. With respect to the spin sensitive upper contact, this results in a finite difference $T^{3,1} - T^{3,2} \neq 0$, as explained in Fig. 4.13. The sign and magnitude of this difference will depend on the preferred spin direction of the contact and the spin polarization of the electrons diffusing into it. Therefore, the difference in transmission probabilities $T^{3,1} - T^{3,2}$ is a measure for the polarization of the CISA with respect to the preferred spin polarization of the contact connected to L3. On the other hand the lower contact accepts electrons regardless of their spin polarization and therefore $T^{4,2} \approx T^{4,1}$, assuming that the influence of L3 on the transmission probabilities $T^{4,1}$ and $T^{4,2}$ can be neglected. This finally results in a finite voltage difference $\Delta V_{34} \approx V_0 T^{4,1} (T^{3,1} - T^{3,2}) / \Omega$

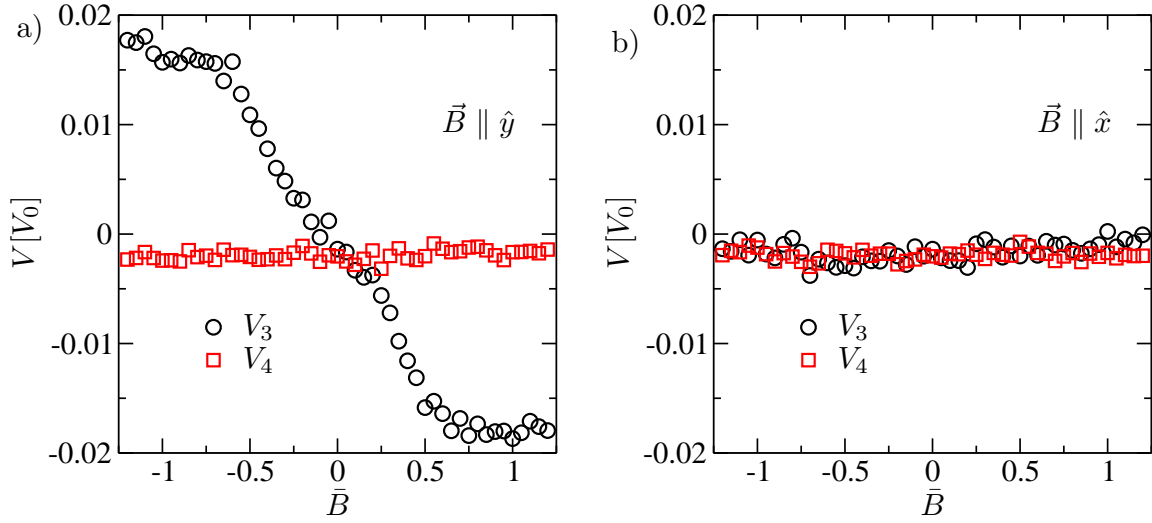


Figure 4.14: Voltages V_3 and V_4 with respect to the strength of the magnetic field \bar{B} in lead L3. a) $\vec{B} \parallel \hat{y}$; b) $\vec{B} \parallel \hat{x}$; Common parameters: $\bar{\alpha} = 0.15$, $\bar{E}_F = 0.4$, $N_d = 10000$.

whose magnitude is determined by the difference between the transmission probabilities $T^{3,1}$ and $T^{3,2}$. Therefore, ΔV_{34} can be directly related to the spin polarization of the current diffusing out of the Hall bar into the side contacts and in view of the previous section also to the magnitude of the CISA. In principle, also the spin Hall effect contributes to this voltage signal and can be detected in that way [171]. However, it can be differentiated from the CISA, since its polarization is out of plane, while the current-induced spins are polarized in the plane of the 2DEG.

4.4.2 Detection by a lead with strong Zeeman splitting

Having outlined the general detection principle we now turn our attention to a specific detection setup, namely the one depicted in Fig. 4.12 with $W = W_3 = W_4 = 40a$. In order to detect the CISA due to the uniform Rashba SOI in the system, see Eq. (2.11), we add a finite Zeeman splitting, see Eq. (2.9), in lead L3, making it selective for spins with polarization along the direction of the magnetic field \vec{B} . The Hamiltonian is then given by

$$H = \frac{p_x^2 + p_y^2}{2m^*} + \theta(y - W/2)H_Z + H_R + U_{\text{conf}}(x, y) + U_d(x, y), \quad (4.23)$$

where $U_{\text{conf}}(x, y)$ describes the confinement potential of the geometry and again $U_d(x, y)$ accounts for disorder, rendering the transport diffusive.

In order to confirm the feasibility of the detection mechanism we determine the voltages V_3 and V_4 from Eq. (4.18) by calculating the respective transmission probabilities of the geometry as outlined in section 2.3. In Fig. 4.14 we show the voltages V_3 and V_4

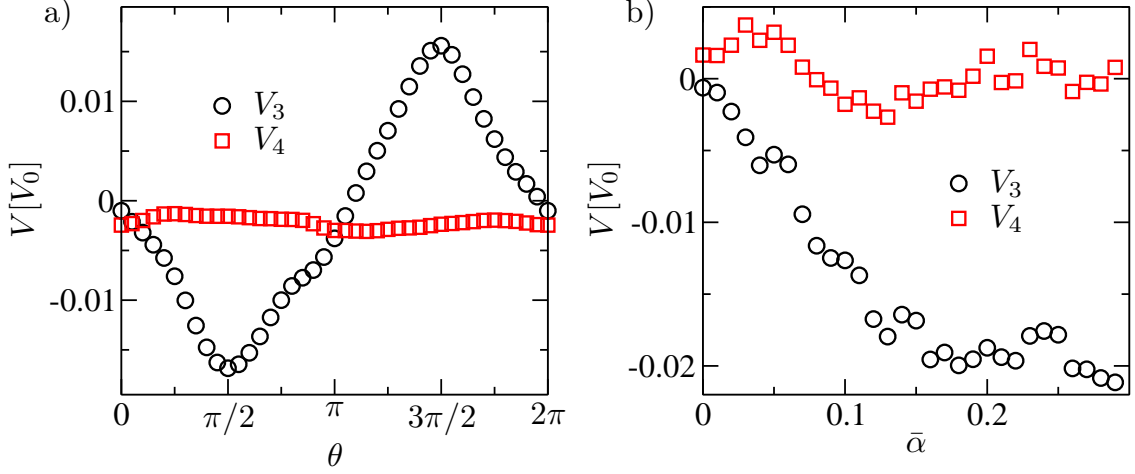


Figure 4.15: Dependence of V_3 and V_4 on a) the angle of the in-plane magnetic field, $\theta = \tan(B_y/B_x)$, for fixed $\bar{\alpha} = 0.15$ and b) on the strength of the Rashba SOI $\bar{\alpha}$ for fixed $\theta = \pi/2$. Common parameters: $\bar{B} = 0.7$, $\bar{E}_F = 0.4$, $N_d = 10000$.

for different orientations of the magnetic field with respect to its strength. When the magnetic field is absent, $\vec{B} = 0$, the voltages V_3 and V_4 have values close to zero due to their position in the center of the disordered region of the Hall bar. For finite Zeeman splitting along the polarization direction of the CISA ($\vec{B} \parallel \hat{y}$), shown in Fig. 4.14a, we observe a voltage difference $\Delta V_{34} = V_3 - V_4$, which – as expected – changes sign when inverting the direction of \vec{B} . For small magnetic field strengths it shows a linear dependence on \bar{B} , while it saturates at a higher value, when the lead L3 is fully spin polarized, i.e. when only states with one specific spin polarization are available at the Fermi energy. On the other hand when $\vec{B} \parallel \hat{x}$, i.e. perpendicular to the polarization of the current-induced spins, there is no change in ΔV_{34} with \bar{B} , see Fig. 4.14b. These findings are a clear indication that the observed voltage difference ΔV_{34} is related to the CISA, to be precise ΔV_{34} is a measure for the magnitude of the CISA along the direction of \vec{B} . This is furthermore confirmed by the results shown in Fig. 4.15a, where we observe a sinusoidal dependence of ΔV_{34} on the direction of \vec{B} .

In Fig. 4.15b we plot the dependence of V_3 and V_4 on the strength of the SOI at fixed, high magnetic field, which corresponds to a fully spin polarized lead L3. We see, that analog to the value for the CISA in the Hall bar, see Fig. 4.5a, ΔV_{34} increases linearly with $\bar{\alpha}$. However, it saturates at $\bar{\alpha} \approx 0.15$, which can be understood by taking into account the results from section 4.3. There it was shown that the amount of spin accumulation that can be extracted at a side-coupled contact is limited by the opening size of the contact. Namely, the spin accumulation diffusing into the contact saturates at $L_H \geq L_{SO}$. We numerically verify this expectation in Fig. 4.16, where we contrast the voltage difference ΔV_{34} and the spin accumulation that can be extracted from the Hall bar into the side contact connected to lead L3. To this end we consider the setup shown in Fig. 4.9b and calculate the spin accumulations $\langle s_y^P \rangle$ and $\langle s_y^B \rangle$ in the NSP or

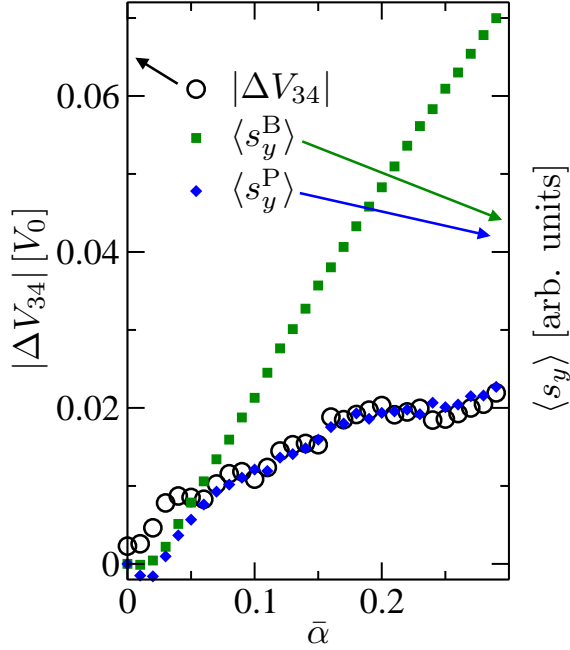


Figure 4.16: Dependence of $|\Delta V_{34}|$ on $\bar{\alpha}$ from Fig. 4.15 (open black circles), compared to the spin accumulations $\langle s_y^B \rangle$ (filled green squares) and $\langle s_y^P \rangle$ (filled blue diamonds) in the corresponding setup of Fig. 4.9b with the same size of the contact $L_H = W_3 = 40a$ and $N_d = 100000$.

RQW, respectively. In order to compare those results with the ones from Fig. 4.15b, we choose the opening size of the contact to be $L_H = 40a$, i.e. equal to the width of the spin selective contact, $W_3 = 40a$, in the detection setup. While the CISA increases linearly with $\bar{\alpha}$ in the RQW (green squares or see also Fig. 4.5a) it saturates inside the NSP for large $\bar{\alpha}$ (blue diamonds). The correspondence of ΔV_{34} and $\langle s_y^P \rangle$ is striking and therefore nicely explains that the saturation of ΔV_{34} is due to the limitation of extracting current-induced spins at side contacts with opening size $L_H \geq L_{SO}$.

Having shown the feasibility of this specific detection setup we now address its possible experimental implementation. The Zeeman splitting in lead L3 could be realized, e.g., by the deposition of a ferromagnetic thin film on top of the semiconductor heterostructure above lead L3. In such a setup magnetic fields up to 0.5T can be created [139]. In materials with large effective g -factor this results in a reasonable Zeeman splitting in lead L3, rendering the proposed detection method feasible.

However, there are also difficulties associated with the setup discussed here. Namely, it is not possible to achieve a completely uniform magnetic field in lead L3 by a ferromagnetic film on top of the 2DEG, but the direction and magnitude of \vec{B} will be dependent on the position. Close to the interface between lead 3 and the Hall bar, stray fields from the ferromagnet could induce spin-flips [175] or a local Hall effect [176] and could therefore disturb the detection.

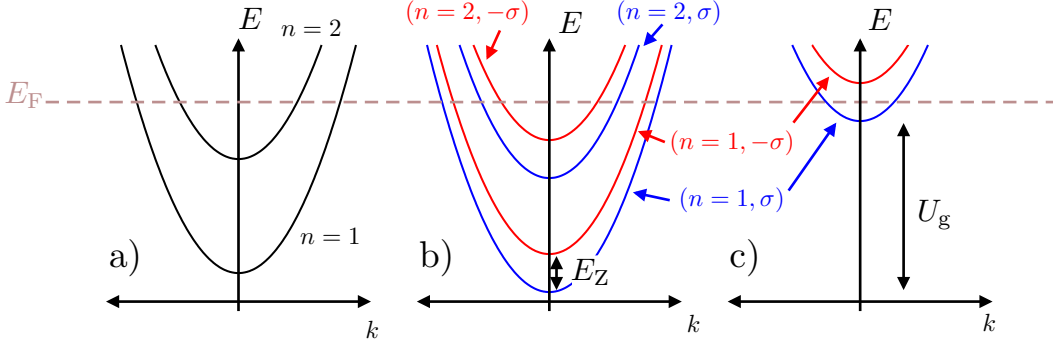


Figure 4.17: Sketch of the electronic energy dispersion of a point contact subject to Zeeman energy splitting of strength E_Z and an offset due to a gate voltage U_g . a) $E_Z = 0$, $U_g = 0$, b) $E_Z \neq 0$, $U_g = 0$, c) $E_Z \neq 0$, $U_g \neq 0$. For simplicity we neglect the effect of the SOI on the dispersion relation.

4.4.3 Detection by a spin selective point contact

Due to the experimental challenges posed by the setup investigated in the previous subsection, here we focus on a different configuration not involving the use of ferromagnets as sources for magnetic fields. It is based on the structure shown in Fig. 4.12, where the upper lead is connected to the central region by a narrow point contact whose width is of the order of the Fermi wavelength and thus supports only a few transversal subbands at the Fermi energy (see Fig. 4.17a). Furthermore a uniform in-plane magnetic field of reasonable strength is present in the entire 2DEG. The Zeeman coupling of the electron spin to this magnetic field causes the subbands of the point contact to split, as indicated in Fig. 4.17b. By the additional application of an appropriate gate voltage to this contact we can shift the subbands in a way, that only the lowest one, which is spin polarized, is populated at the Fermi energy, see Fig. 4.17c. Then it is possible to use such a point contact as an injector or detector of spins, as has been demonstrated experimentally [36, 131].

In our setup we use this spin selective point contact for the detection of the CISA. The Hamiltonian employed for the numerical calculations reads

$$H = \frac{p_x^2 + p_y^2}{2m^*} + H_R + H_Z + U_d(x, y) + U_{\text{conf}}(x, y) + U_g^3(x, y) \quad (4.24)$$

where U_{conf} accounts for the confinement potential of the geometry. We choose the width of the contact connecting lead 3 to the Hall bar ($W = 40a$) as narrow as $W_3 = 12a$, supporting 4 open channels at the Fermi energy $\bar{E}_F = 0.5$ in the disorder and magnetic field free limit. We furthermore include a finite electrostatic potential $U_g^3(x, y)$ inside the point contact, which models the influence of a gate voltage. The magnitude of the applied voltage is adjusted in a way that in the ballistic limit the conductance of this point contact is equivalent to or smaller than a single conductance quantum $G_0 = e^2/h$, i.e. at the Fermi energy only one subband in the point contact is

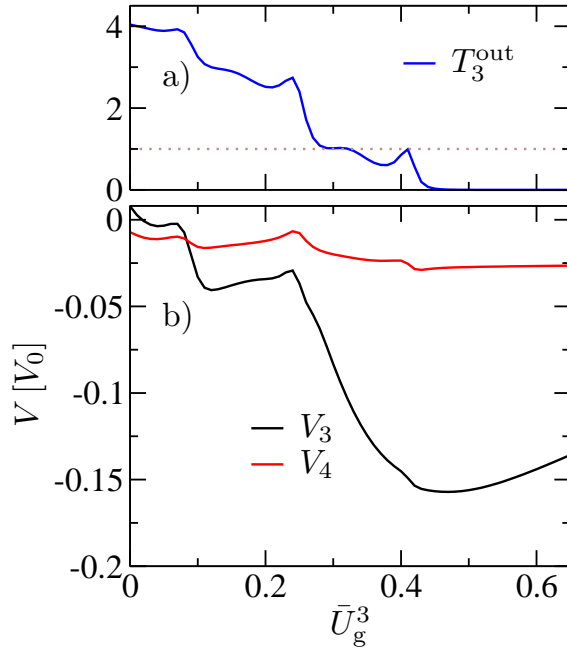


Figure 4.18: a) Transmission through the upper point contact T_3^{out} with respect to the gate potential \bar{U}_g^3 in the disorder free limit ($\bar{U}_{\text{dis}} = 0$) for $\vec{B} \parallel \hat{y}$ with strength $B = 0.08$ and $\bar{\alpha} = 0.15$. b) Corresponding voltages of the side contacts V_3 and V_4 with respect to the gate potential \bar{U}_g^3 .

populated. Due to the Zeeman splitting this subband is spin polarized and therefore the point contact only allows spins with a specific polarization (determined by the direction of the magnetic field) to enter. On the other hand the contact connecting lead L4 to the Hall bar supports several occupied subbands at the Fermi energy and therefore is not spin selective. In this setup we now expect to observe a voltage difference ΔV_{34} , which can be directly related to the CISA, as described in section 4.4.1.

Before we investigate the detection of the CISA in realistic, disordered systems it is insightful to take a closer look at the corresponding behavior in a clean system. Although we cannot define local quasichemical potentials or a local spin accumulation, still there exists a local spin polarization due to a ballistic electron current in such a structure [177]. In Fig. 4.18a we take a look at the gate voltage dependence of the outgoing transmission through the upper point contact $T_3^{\text{out}} = T^{3,1} + T^{3,2} + T^{3,4}$. We observe that for increasing gate potential \bar{U}_g^3 it decreases from $T_3^{\text{out}} \approx 4$ for $\bar{U}_g^3 = 0$ to $T_3^{\text{out}} \leq 1$ where only the lowest subband of the point contact is occupied. In Fig. 4.18b we show the corresponding dependence of the voltages V_3 and V_4 and observe that only in the range of gate voltages, where $T_3^{\text{out}} \leq 1$, a significant signal $\Delta V_{34} \neq 0$ is present due to the change of V_3 upon variation of U_g^3 , while due to its non spin selective nature $V_4 \approx \text{const}$.

Having seen that we can detect a local imbalance of spin-up and spin-down electrons in ballistic systems with a spin-polarized point contact, we now consider the experimentally more relevant situation where the electron mean free path is shorter than the width of the Hall bar using the same detection setup as in the calculations of Fig. 4.18. Since electron dynamics is diffusive now, we cannot observe conductance quantization in the point contact anymore. In Fig. 4.19 we plot the voltages V_3 and V_4 with respect to U_g^3 for finite $\vec{B} \parallel \hat{y}$ and α . As for the ballistic case also here a significant voltage difference ΔV_{34} establishes for $\bar{U}_g^3 \geq 0.3$.

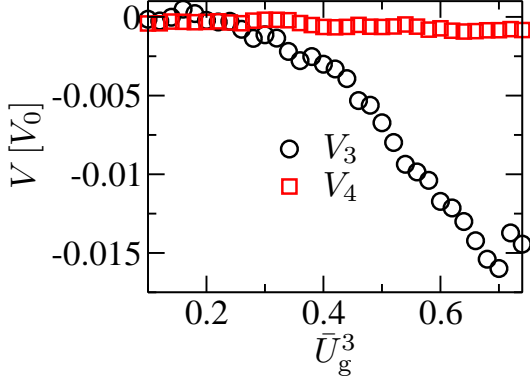


Figure 4.19: Voltages V_3 and V_4 of the side contacts with respect to the applied gate potential \bar{U}_g^3 for a system with diffusive dynamics ($\bar{U}_{\text{dis}} = 2$) for $\vec{B} \parallel \hat{y}$ with strength $\bar{B} = 0.08$, $\bar{\alpha} = 0.15$ and $N_d = 100000$.

In analogy to the previous subsection we also investigate the dependence of V_3 and V_4 on the direction of the magnetic field \vec{B} and on the strength of the Rashba SOI. The results shown in Fig. 4.20 exhibit a very similar behavior to the ones from the detection with a strong Zeeman splitting in lead L3, presented in Fig. 4.15. Especially the saturation of ΔV_{34} at finite $\bar{\alpha}$ is again due to the limited spin extraction capability of the side contact to lead L3 for $L_{\text{so}} < W_3$.

To summarize, in this section we put forward a feasible all-electrical detection setup for the CISA. It relies on the extraction of spins from a wide conductor, where those spins are electrically created via the CISA-mechanism, into a spin selective side contact. To determine the exact value of the CISA via this method requires the knowledge of the system parameters and especially of the spin extraction efficiency of the point contact used for the measurement setup. In any case it can serve as a quite precise tool for detecting the polarization direction of the CISA. Especially, when including also the Dresselhaus SOI, the proposed method represents a possible way to determine the relative strength of Rashba and Dresselhaus SOI, since the orientation of the CISA, \vec{s} , depends on the parameters α and β , see Eqs. (4.9a) and (4.9b).

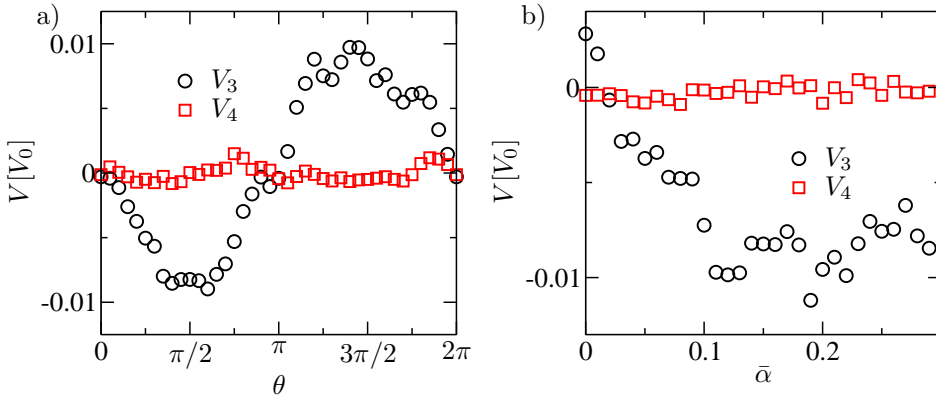


Figure 4.20: Dependence of V_3 and V_4 on a) the angle of the in-plane magnetic field, $\theta = \tan(B_y/B_x)$, for fixed $\bar{\alpha} = 0.15$ and b) on the strength of the Rashba SOI $\bar{\alpha}$ for fixed $\theta = \pi/2$. Common parameters: $\bar{B} = 0.08$, $\bar{E}_F = 0.5$, $\bar{U}_g^3 = 0.54$, $N_d = 50000$.

CHAPTER 5

Coherent spin transport in disordered wires and the detection of the ratio α/β

One key element for the operation of semiconductor spintronics devices is the efficient control of the electrons' spin degree of freedom. Even if electrons with a well defined spin state are created at a certain position, there are mechanisms that randomize the spins and thus diminish the efficiency of many promising device proposals, as e.g. the Datta-Das spin field effect transistor [18], that rely on coherent spin transport. In section 2.1.2 we outlined a variety of possible spin relaxation mechanisms in two-dimensional electron gases (2DEGs). In a disordered wire with spin-orbit interaction (SOI) as investigated here, the spin relaxation is provided by the interplay between the band-structure of a 2DEG with SOI and the scattering from static impurities.

However, there are certain situations when spin relaxation is strongly suppressed or even absent. Then the aforementioned device proposals, which require coherent spin transport, could be realized. Therefore, in this chapter we especially focus on identifying suitable systems and parameter regimes, not impeded by spin relaxation. We confirm this behavior by numerical transport calculations. Furthermore, we will use those results to put forward an efficient all-electrical detection method for the ratio α/β between the strengths of Rashba and Dresselhaus SOI.

5.1 System of choice

In this chapter we evaluate the transport properties of a disordered quantum wire with SOI linear in momentum and subject to an external magnetic field. The Hamiltonian of the wire, which is oriented in x -direction and embedded in a 2DEG located in the

(x, y) plane, reads

$$H = \frac{\pi_x^2 + \pi_y^2}{2m^*} + U_{\text{conf}}(y) + U_d(x, y) + \frac{\mu_B g^*}{2} (\vec{B}_{\parallel} + \vec{B}_{\text{so}}(\vec{\pi})) \cdot \vec{\sigma}, \quad (5.1)$$

with the external, in-plane magnetic field

$$\vec{B}_{\parallel} = B_{\parallel} [\cos(\theta - \phi)\hat{e}_x + \sin(\theta - \phi)\hat{e}_y], \quad (5.2)$$

and the effective magnetic field due to Rashba and Dresselhaus SOI as introduced in section 2.1.2

$$\begin{aligned} \vec{B}_{\text{so}}(\vec{\pi}) = \frac{2}{\mu_B g^* \hbar} & \left[\hat{e}_x (\alpha \pi_y + \beta (\pi_x \cos 2\phi - \pi_y \sin 2\phi)) \right. \\ & \left. + \hat{e}_y (-\alpha \pi_x - \beta (\pi_x \sin 2\phi + \pi_y \cos 2\phi)) \right]. \end{aligned} \quad (5.3)$$

The vector potential components A_i in $\pi_i = p_i + eA_i$ arise due to the perpendicular magnetic field B_z whose contribution to the Zeeman term we neglect, since it is chosen to be much smaller than the corresponding in-plane component \vec{B}_{\parallel} and the effective SOI field \vec{B}_{so} . Furthermore, ϕ/θ is the angle between the quantum wire/in-plane magnetic field and the [100] direction in a zinc-blende crystal for a quantum well grown in the [001] direction. The relative orientation of the wire, the magnetic field and the crystal is visualized in Fig. 5.1. In Eq. (5.1) $U_{\text{conf}}(y)$ denotes the hard-wall confining potential of the quantum wire and $U_d(x, y)$ the disorder potential. The disorder, which we choose to be of Anderson type as introduced in section 2.3.2, is only present in the central region of the quantum wire, where transport is assumed to be fully coherent. Phase-breaking occurs in the two electronic reservoirs to which the scattering region of length L is connected by ideal, disorder-free leads. For the evaluation of the relevant transport properties we calculate the total transmission probability $T(E)$ of the quantum wire as described in detail in section 2.3. Considering the linear response regime, the transmission probability at the Fermi energy $T(E_F)$ yields the conductance of a single disorder configuration in the Landauer approach:

$$G = G_0 T(E_F) \quad \text{with} \quad G_0 = e^2/h. \quad (5.4)$$

5.2 Quantum effects in the conductance of disordered wires

At low temperatures, phase breaking scattering, such as electron-phonon or electron-electron scattering, is strongly suppressed leading to an increase of the phase coherence

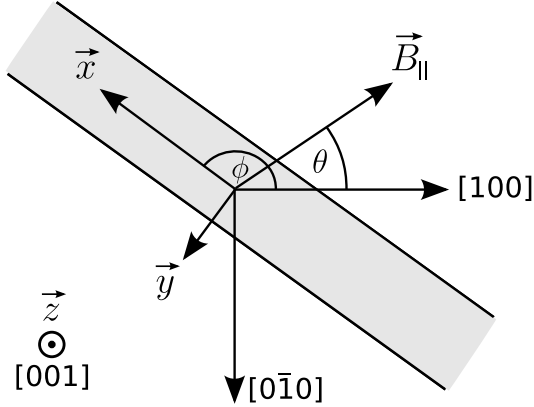


Figure 5.1: Relative orientation of the quantum wire (pointing in x -direction), the external magnetic field \vec{B}_{\parallel} and the underlying crystal lattice.

length. Therefore, electronic transport under those conditions is coherent and in turn quantum effects due to the interference of wavefunctions become observable. Two such effects are on the one hand the quantum correction to the classically expected conductance, which is called weak localization (WL) or weak antilocalization (WAL), depending on the sign of the correction, and on the other hand the universal conductance fluctuations (UCFs) around a mean value of G . Since we will encounter both effects in the course of this chapter, we now briefly review them.

Due to the focus on disordered quantum wires, in the following both effects will be explained considering systems, where the motion of the electrons is randomized by scattering at static impurities. However, WL/WAL and UCFs can also be observed in coherent transport through ballistic, chaotic cavities, where the randomization is due to the scattering at the walls of the cavity [178].

5.2.1 Weak localization and weak antilocalization

Classically the conductivity σ of a metal or a semiconductor is well described by the Drude formula [51]. It is given by $\sigma = ne^2\tau/m$, where n is the density and τ the momentum relaxation time of the charge carriers. Upon lowering the temperature, the conductivity of metals or extrinsic semiconductors typically increases, since scattering is reduced, which in turn leads to longer relaxation times τ , while n stays approximately constant.

However, in experiments on the temperature dependence of the conductivity (for the case of a 2DEG see e.g. Ref. [179]), a decrease of σ was found at low temperatures. This deviation from the Drude theory can be explained by a quantum interference correction, which leads to enhanced backscattering of the electrons. This effect, called weak localization (WL), was first studied in the context of diagrammatic perturbation theory [180, 181]. However, to gain better insight, we employ an alternative semiclassical description as described in Refs. [52, 182].

To this end we consider transport in a disordered wire where the motion of the electrons is randomized by scattering off impurities as illustrated in Fig. 5.2. It is based

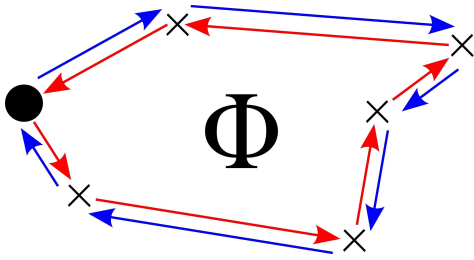


Figure 5.2: Sketch of two paths connected by time reversal symmetry. The clockwise/counter-clockwise propagating electrons (indicated by red/blue arrows) move along the same trajectory in opposite directions and return to their initial position after undergoing a number of scattering events. In the presence of a perpendicular magnetic field they pick up opposite phases $\exp\{\pm i\Phi\}$ upon completion of the trajectory.

on the motion along classical trajectories, but still taking into account the interference of electronic wavefunctions. For example, in the context of the scattering approach described in section 2.2.1, we can obtain the reflection probability of electrons coming in from mode n' in lead i and leaving the scattering region into mode $n \in i$ by summing up the amplitudes A_j of all possible Feynman paths between those modes and taking the square of this sum:

$$R_{n,n'}^{i,i} = |A_1 + A_2 + A_3 + \dots|^2 = \underbrace{\sum_j |A_j|^2}_{R_{\text{cl}}} + \underbrace{\sum_j \sum_{j' \neq j} A_j A_{j'}^*}_{R_{\text{in}}} \quad (5.5)$$

Here, the first term R_{cl} is given by the sum of the squares of the individual amplitudes representing the classical result, while interference terms of the different Feynman paths can be found the second term R_{in} . For different modes $n \neq n'$ this correction term can be neglected in general, since the amplitudes are uncorrelated and thus the sum of their products, R_{in} , averages to zero. This reasoning can also be used for the transmission probabilities $T_{n,n'}^{i,i'}$, where the corresponding quantum mechanical interference term also vanishes. On the contrary, for electrons being reflected back into the same mode from which they entered the scattering region, the interference term R_{in} contributes a finite value to the reflection probability, as we will argue now. For $n = n'$ in systems with time-reversal symmetry every Feynman path j possesses a time-reversed counterpart \tilde{j} with equal amplitude, i.e. $A_j = A_{\tilde{j}}$. For illustration purposes we show one such pair of trajectories connected by time-reversal in Fig. 5.2. The corresponding reflection probability reads

$$\begin{aligned} R_{n,n}^{i,i} &= |(A_1 + A_2 + A_3 + \dots) + (A_{\tilde{1}} + A_{\tilde{2}} + A_{\tilde{3}} + \dots)|^2 \quad (5.6) \\ &= \sum_j (|A_j|^2 + |A_{\tilde{j}}|^2) + \sum_j (A_j A_{\tilde{j}}^* + A_{\tilde{j}} A_j^*) + \dots \\ &\stackrel{A_j=A_{\tilde{j}}}{=} 4 \underbrace{\sum_j |A_j|^2}_{2R_{\text{cl}}} + \dots \quad , \end{aligned}$$

where in contrast to Eq. (5.5) we now sum over pairs of Feynman paths connected by time-reversal symmetry and not over all individual Feynman paths. Furthermore, we only kept the interference terms between paths j and \tilde{j} , while omitting the other interference terms that average out to zero. Due to this interference of paths connected by time-reversal the resulting reflection probability in the case of $n = n'$ is twice as large as the classically expected one. This naturally also causes an increased resistance (decreased conductance) that is observable in experiments at low temperatures [179]. At higher temperatures this interference correction is strongly reduced due to the shorter phase coherence lengths. Less Feynman paths contribute to R_{in} since the amplitudes of the electronic wavefunctions are randomized by phase-breaking scattering events. Another way of suppressing the effect of WL is the application of a magnetic field perpendicular to the 2DEG, which destroys time reversal symmetry. Upon completion of the trajectory the electrons pick up a phase $\exp\{\pm\Phi\}$ due to this field as indicated in Fig. 5.2. For paths connected by time-reversal this phase is opposite and thus their amplitudes are not equal anymore. For strong enough magnetic fields this correction term disappears upon averaging over all paths, yielding the classically expected result. In Fig. 5.3 we illustrate this behavior by showing the numerically determined magneto-conductance of a disordered quantum wire. In order to get rid of the UCFs (see section 5.2.2), which render the observability of the WL difficult for a single disorder configuration, here we show the quantity $\langle G \rangle$. It is given by the average of the conductance G over a large number of N_{d} disorder configurations:

$$\langle G \rangle = \sum_{i=1}^{N_{\text{d}}} G(i). \quad (5.7)$$

We observe that $\langle G \rangle$ (green squares) increases from its value at zero perpendicular magnetic field with increasing B_z until it saturates at $G_{\text{cl}} = G_0(M - R_{\text{cl}})$, where M is the number of occupied transversal modes in the disorder-free leads. Although, in experiments one cannot switch between different distributions of impurities, still there are other ways to achieve the averaging, among others, the measurement of an array of parallel wires at the same time [44, 183].

The reasoning above is valid for systems where spin-related effects can be neglected. However, in the presence of strong SOI the qualitative behavior is different. It was first shown in Ref. [184] that SOI causes an increase of the conductivity at low temperatures, contrary to the decrease observed in samples, where SOI did not play a role. For a disordered wire in the metallic regime with strong SOI a positive conductance correction $\Delta G = \frac{1}{3}e^2/h$ is predicted, which has half the magnitude of the negative correction in the case without SOI: $\Delta G = -\frac{2}{3}e^2/h$ [185]. This decrease in the resistance, or increase in the conductance, respectively, is called weak antilocalization (WAL) in correspondence to the WL, which describes a change in the resistance/conductance with opposite sign. It is a result of the precession of the electron spin in the presence of SOI. Since the precession axis is dependent on the momentum of the electron, the spin states of electrons travelling along different trajectories are rotated differently.

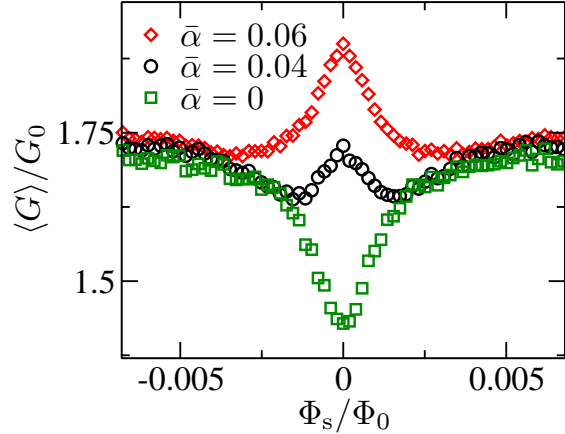


Figure 5.3: Magnetoconductance of a quantum wire with $W = 30a$, $\bar{E}_F = 0.5$ and disorder of strength $\bar{U}_{\text{dis}} = 1.4$ in a region of length $L = 150a$. Different strengths of the Rashba SOI $\bar{\alpha}$ are considered. The magnetic flux $\Phi_s = a^2 B_z$ is given in units of the magnetic flux quantum $\Phi_0 = h/(2e)$.

Opposed to the general case, where the relative spin orientation of two electrons travelling on different paths is random, for trajectories connected by time reversal, the relative spin orientation is correlated, yielding a destructive interference.

If the spin state is not sufficiently randomized, the interference of the electrons travelling on trajectories connected by time-reversal will be constructive and hence WL instead of WAL will be observed. This is an indication for the suppression of spin relaxation, a fact we will use in the course of this chapter. Namely, we consider two such cases, where in wires with SOI, spin relaxation is strongly suppressed (absent) and which show WL instead of WAL. To be specific, in section 5.3.1 we consider the case of very narrow wires, where the spin precession length exceeds the width of the wire, and in section 5.3.2 we treat the case of equal Rashba and Dresselhaus SOI strengths $\alpha = \beta$.

As for WL the effect of WAL can be destroyed by reducing the phase coherence length, e.g. by increasing the temperature, or by breaking the time-reversal symmetry via a perpendicular magnetic field. In view of the latter, in Fig. 5.3 we show the magnetoconductance of a disordered quantum wire with Rashba SOI. With increasing strength $\bar{\alpha}$ we witness a crossover from WL ($\langle G_s(\Phi = 0) \rangle < G_{\text{cl}}$) for $\bar{\alpha} = 0$ (green squares) to WAL ($\langle G_s(\Phi = 0) \rangle > G_{\text{cl}}$) for strong $\bar{\alpha} = 0.06$ (red diamonds). For all cases the conductance approaches G_{cl} with increasing B_z .

5.2.2 Universal conductance fluctuations

As we already argued in the preceding section on WL, for coherent electron transport the conductance is strongly influenced by quantum interference effects. Since the phases of the electronic wavefunctions very sensitively depend on the distribution of the

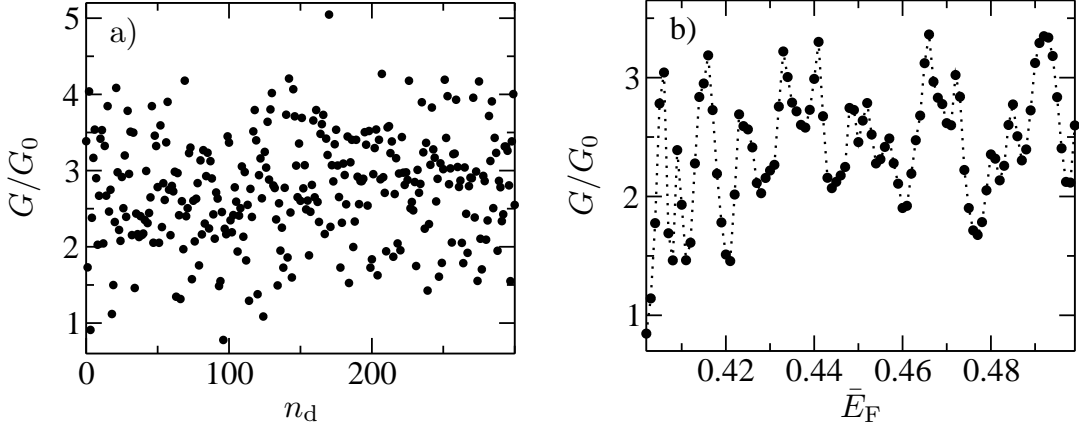


Figure 5.4: Conductance of a quantum wire shown a) for $n_d = 1, \dots, 300$ different disorder configurations at $\bar{E}_F = 0.5$ and b) as a function of the Fermi energy \bar{E}_F for a fixed disorder configuration. The dashed line only serves as a guide to the eye. Common parameters: $W = 50a$, $L = 150a$, $\bar{U}_{\text{dis}} = 1.4$.

impurities, we observe pronounced fluctuations in the conductance from configuration to configuration. Therefore, in Fig. 5.3 we presented the magneto-conductance averaged over a large number of different disorder configurations to remove these so-called universal conductance fluctuations (UCFs) around the mean value $\langle G \rangle$. The strength of the UCFs can be quantified by the variance of the conductance

$$\text{var } G = \langle G^2 \rangle - \langle G \rangle^2, \quad (5.8)$$

where $\langle \cdot \rangle$ again denotes the averaging over many different disorder configurations. As their name already suggests, the UCFs possess a universal value, which is of the order of one conductance quantum in diffusive systems: $\sqrt{\text{var } G} \simeq e^2/h$ [186, 187]. Their exact size is determined by the specific symmetry class the system belongs to [185] and therefore is dependent on the strength of SOIs and/or magnetic fields, as we will see in the course of this chapter. However, for diffusive transport it is independent of the system size and the magnitude of the disorder [54], hence the use of the term universal. Experimentally the UCFs become visible upon slight variation of system parameters, as e.g. the Fermi energy or a perpendicular magnetic field, which leads to changes in the interference pattern of the electronic wavefunctions and therefore has the same effect as altering the distribution of impurities [188]. We give numerical evidence for this correspondence in Fig. 5.4, where we computed the conductance of a disordered quantum wire for 300 randomly chosen disorder configuration, Fig. 5.4a, and for the variation of the Fermi energy, Fig. 5.4b.

Since the above reasoning is only correct for fully coherent transport, no UCFs are observed for either macroscopic samples or at high temperatures. Then the sample size exceeds the phase coherence length l_ϕ of the electrons and the quantum interference effects taking place on a length scale of l_ϕ are averaged out over the whole sample [52, 54].

5.3 Suppression of spin relaxation in quantum wires

Although semiconductors with strong SOI usually exhibit WAL, there are certain conditions under which we observe WL instead. In this section we will investigate two particular cases showing this behavior. To be specific, in section 5.3.1 we take a closer look at the conductance of narrow quantum wires and in section 5.3.2 we concern ourselves with the transport properties of systems where the strengths of Rashba and Dresselhaus SOI are equal, i.e. $\alpha = \pm\beta$.

5.3.1 Narrow quantum wires

In recent years it was shown, that confinement can lead to a suppression of spin relaxation in quantum dots [178, 189, 190] and quantum wires [78, 191]. Since spin relaxation is an essential ingredient for the appearance of WAL, a crossover from WAL to WL can be observed upon reducing the width of the wires. We numerically confirm this by computing the magneto-conductance for wires with finite Rashba SOI for different widths W . Figure 5.5a shows that WAL is suppressed when W is reduced, which is in line with several experimental [44, 183, 192], analytical [193] and numerical treatments [44]. In Ref. [44] it was argued that in the experiments where WL appeared, the spin relaxation length exceeded the phase coherence length. For the paths shorter than the phase coherence length¹, which are the only one contributing to the conductance correction, the spin state is not randomized efficiently. Hence, these paths interfere constructively and the conductance exhibits WL.

Symmetry analysis

We now determine the conditions, when WL instead of WAL appears in quantum wires even though SOI of reasonable strength is present. Here, we consider the absence of a perpendicular magnetic field $B_z = 0$, i.e. $\pi_i = p_i$, and introduce the angle

$$\xi = \arctan [\beta \cos 2\phi / (\beta \sin 2\phi - \alpha)] \quad (5.9)$$

and the parameter

$$\kappa = \sqrt{\alpha^2 + \beta^2 - 2\alpha\beta \sin 2\phi}. \quad (5.10)$$

Furthermore, we define two new Pauli matrices by

$$\sigma_1 = \cos \xi \sigma_x + \sin \xi \sigma_y, \quad \text{and} \quad \sigma_2 = -\sin \xi \sigma_x + \cos \xi \sigma_y, \quad (5.11)$$

¹In the numerical simulation the finite length L of the disordered region has a similar effect as the phase coherence length in the experiments, since it limits the possible length of paths contributing to the conductance correction.

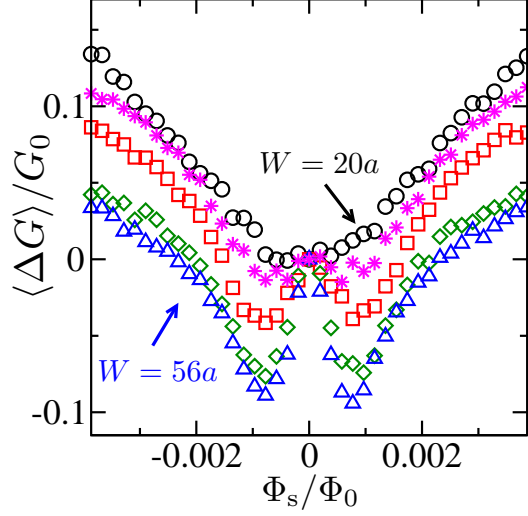


Figure 5.5: Magnetoconductance $\langle \Delta G \rangle = \langle G(\Phi_s) \rangle - \langle G(0) \rangle$ of a quantum wire plotted against the magnetic flux $\Phi_s = a^2 B_z$ in units of the magnetic flux quantum $\Phi_0 = h/(2e)$. Parameters: $\bar{\alpha} = 0.03$ (i.e. $L_{\text{so}}^\alpha \approx 105a$), $\bar{\beta} = 0.0$, $\bar{E}_F = 0.5$, $\bar{U}_{\text{dis}} = 1.4$, $N_d = 25000$ and widths $W = 20a, 30a, 36a, 46a, 56a$ from top to bottom.

which span a new spin coordinate system $(\sigma_1, \sigma_2, \sigma_z)$, corresponding to the original coordinate system $(\sigma_x, \sigma_y, \sigma_z)$ rotated around the z -axis by the angle ξ . The Pauli matrix σ_1 coincides with the direction of the effective magnetic field \vec{B}_{so} for momentum $\vec{p} \parallel \hat{y}$, i.e. perpendicular to the wire. Note that ξ is not defined for the cases $(\alpha = \beta, \phi = \pi/4)$ and $(\alpha = -\beta, \phi = 3\pi/4)$, since $\vec{B}_{\text{so}}(\vec{p} \parallel \hat{y}) = 0$. However, this does not constitute a problem, since for $\alpha = \pm\beta$ spin is a good quantum number regardless of the width of the quantum wire and the following treatment is unnecessary. This special condition will be investigated in more detail in section 5.3.2. In order to remove the dependence on p_y , similar to Ref. [189] we perform the unitary transformation $U = \exp[-i(\kappa/\hbar^2)m^*y\sigma_1]$ on the Hamiltonian from Eq. (5.1)

$$\begin{aligned} \tilde{H} &= U^\dagger H U = \frac{p_x^2 + p_y^2}{2m^*} + U_{\text{conf}}(y) + U_d(x, y) - \frac{\kappa^2 m^*}{2\hbar^2} \\ &+ \frac{\mu_B g^*}{2} \vec{B}_{\parallel} \cdot \vec{\sigma} + \frac{1}{\hbar} \left(-\alpha \sigma_y + \beta \cos 2\phi \sigma_x - \beta \sin 2\phi \sigma_y \right) p_x \\ &+ [\Delta_B + \Delta_{\text{so}}] \sigma_\delta, \end{aligned} \quad (5.12)$$

where we introduced the following parameters:

$$\Delta_B = \mu_B g^* (B_x \sin \xi - B_y \cos \xi), \quad (5.13)$$

$$\Delta_{\text{so}} = \frac{2}{\hbar} p_x \frac{\beta^2 - \alpha^2}{\kappa} \quad \text{and} \quad (5.14)$$

$$\sigma_\delta = \sin(\kappa m^* y / \hbar^2) \cos(\kappa m^* y / \hbar^2) \sigma_z + \sin^2(\kappa m^* y / \hbar^2) \sigma_2. \quad (5.15)$$

In the limit $W \ll \hbar^2/(\kappa m^*)$ and for a magnetic field strength B_{\parallel} not exceeding the maximum strength of \vec{B}_{so} , it is a reasonable approximation to neglect the terms of second or higher order in SOI strength, $\Delta_{\text{so}}\sigma_{\delta}$, or SOI strength times magnetic field strength, $\Delta_B\sigma_{\delta}$:

$$H_{\text{Q1D}} = \frac{p_x^2 + p_y^2}{2m^*} + U_{\text{conf}}(y) + U_{\text{d}}(x, y) + \frac{\mu_{\text{B}}g^*}{2} \left[\vec{B}_{\text{so}}(p_y = 0) + \vec{B}_{\parallel} \right] \cdot \vec{\sigma}. \quad (5.16)$$

The important difference between this quasi one-dimensional Hamiltonian, H_{Q1D} , and the general case of Eq. (5.1) is the different spin rotation symmetry exhibited by the spin-orbit part of the Hamiltonian. In Eq. (5.16) it possesses no dependence on the momentum perpendicular to the wire, p_y , and therefore the direction of \vec{B}_{so} is fixed. Hence, the spin orbit part of H_{Q1D} possesses U(1) spin rotation symmetry, in contrast to the general case exhibiting no spin rotation symmetry.

In order to fully understand the transport properties of narrow quantum wires, we investigate the symmetries of the quasi one-dimensional Hamiltonian H_{Q1D} . In the following we consider various situations, where the SOI and the in-plane magnetic field are either absent or sufficiently strong that the relevant spin rotation time is shorter than the escape time or the dephasing time and therefore are strong enough to change the symmetry class. Depending on the presence of \vec{B}_{so} and \vec{B}_{\parallel} and on their relative orientation, H_{Q1D} belongs to different symmetry classes as summarized in Table 5.1. Apart from the trivial case (a), where SOI and external magnetic fields are absent, spin is a good quantum number of H_{Q1D} also for the cases (b)-(d). Therefore, separate Hamiltonians for spin-up and spin-down can be written down, since they decouple:

$$H_{\text{Q1D}} = \begin{pmatrix} H_+ & 0 \\ 0 & H_- \end{pmatrix}, \quad \text{where} \quad (5.17)$$

$$H_{\pm} = \frac{p_x^2 + p_y^2}{2m^*} + U_{\text{conf}}(y) + U_{\text{d}}(x, y) \pm \frac{\mu_{\text{B}}g^*}{2} B_{\parallel} \pm \frac{1}{\hbar} \kappa' p_x,$$

with $\kappa' = \sqrt{\alpha^2 + \beta^2 + 2\alpha\beta \sin 2\phi}$. The parts H_{\pm} are both time-reversal symmetric, i.e. $[H_{\pm}, \hat{C}] = 0$ in cases (a) and (c), and $[\tilde{H}_{\pm}, \hat{C}] = 0$ in cases (b) and (d) after the

Table 5.1: Symmetry classes of H_{Q1D} , Eq. (5.16).

Case	Description	Symmetry class	Spin rotation symmetry
(a)	$\vec{B}_{\parallel} = 0, \vec{B}_{\text{so}} = 0$	orthogonal	SU(2)
(b)	$\vec{B}_{\parallel} = 0, \vec{B}_{\text{so}} \neq 0$	orthogonal	U(1)
(c)	$\vec{B}_{\parallel} \neq 0, \vec{B}_{\text{so}} = 0$	orthogonal	U(1)
(d)	$\vec{B}_{\parallel}, \vec{B}_{\text{so}} \neq 0, \vec{B}_{\parallel} \parallel \vec{B}_{\text{so}}$	orthogonal	U(1)
(e)	$\vec{B}_{\parallel}, \vec{B}_{\text{so}} \neq 0, \vec{B}_{\parallel} \perp \vec{B}_{\text{so}}$	orthogonal	–
(f)	$\vec{B}_{\parallel}, \vec{B}_{\text{so}} \neq 0, \vec{B}_{\parallel} \nparallel \vec{B}_{\text{so}}$ $\vec{B}_{\parallel} \nperp \vec{B}_{\text{so}}$	unitary	–

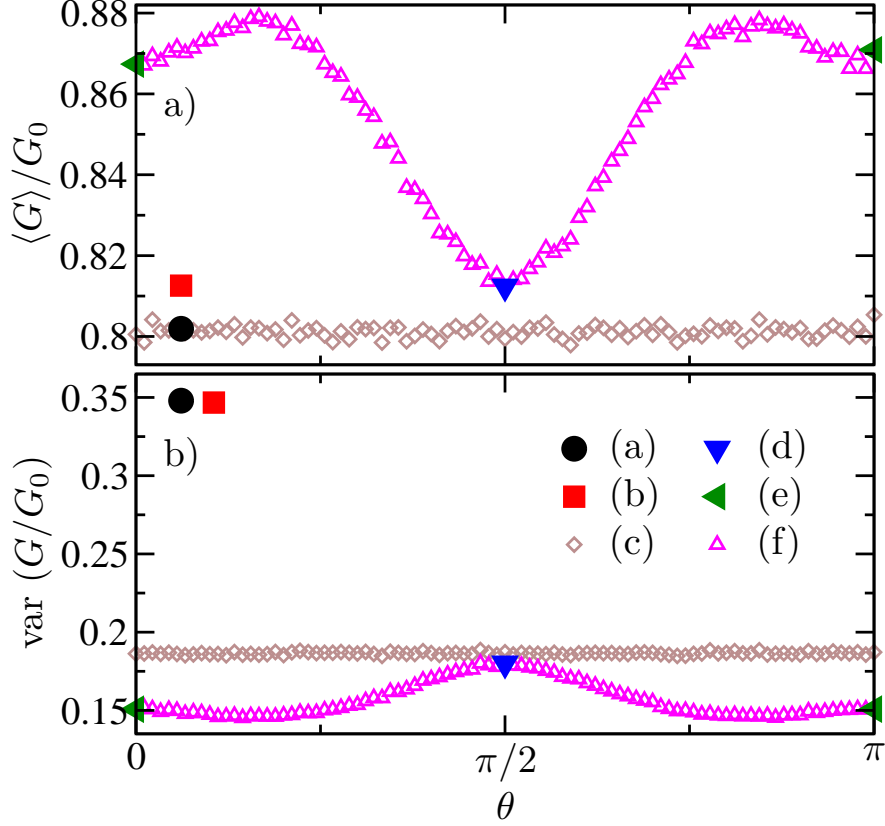


Figure 5.6: Averaged conductance $\langle G \rangle / G_0$ (panel a) and UCFs $\text{var}(G/G_0)$ (panel b) in a disordered quantum wire with $L = 150a$, $W = 20a$, $\bar{U}_{\text{dis}} = 1.4$, $\phi = 0$, $\bar{E}_F = 0.5$, $\beta = 0$ and $N_d = 100000$ as a function of the magnetic field direction θ . Different symmetry classes of H_{Q1D} , Eq. (5.16), were examined by changing \vec{B}_{\parallel} and \vec{B}_{so} . The cases (a)-(f) are summarized in table 5.1. Common parameters: $\bar{B}_{\parallel} = 0.008$ [cases (c)-(f)], $\bar{\alpha} = 0.02$ [cases (b),(d-f)].

additional gauge transformation $U_{\text{so},\pm} = \exp[\mp im^* \kappa' x / \hbar^2]$ with $\tilde{H}_{\pm} = U_{\text{so},\pm}^{-1} H_{\pm} U_{\text{so},\pm}$. $\hat{\mathcal{C}}$ is the operator of complex conjugation. Therefore, H_{\pm} belongs to the orthogonal symmetry class. Although, H_{Q1D} obviously mixes spins in case (e) when $\vec{B}_{\parallel} \perp \vec{B}_{\text{so}}$, i.e. it cannot be written in block-diagonal form as for case (d), it nevertheless belongs to the orthogonal symmetry class due to the antiunitary symmetry exhibited by H_{Q1D} at this angle.: $\hat{\mathcal{C}}^{-1} \tilde{H}_{\text{Q1D}} \hat{\mathcal{C}} = \tilde{H}_{\text{Q1D}}$. There, \tilde{H}_{Q1D} is the spin rotated version of H_{Q1D} where \vec{B}_{\parallel} is aligned along the x -direction. Finally, in case (f) the spin states mix and time-reversal symmetry is broken. Hence, H_{Q1D} possesses only unitary symmetry. Those symmetries given in table 5.1 have important consequences for the transport properties of the disordered quantum wire. In random matrix theory (RMT) developed for coherent quantum transport [185] it was shown that systems with unitary, orthogonal and symplectic symmetry exhibit different quantum corrections to the conductance and different magnitudes of the UCFs [194, 195]. Although RMT gives

quantitative predictions only for quantum wires with a large number of transversal modes, it can help us to understand the qualitative behavior of both the average conductance and the UCFs for the narrow quantum wires treated in this section.

In Fig. 5.6 we show the numerically calculated averaged conductance² and the UCFs of a quantum wire with only Rashba SOI. For the cases (a), (b), (d) and (e) they are presented as isolated symbols and for the cases (c) and (f) as a function of the angle θ of the magnetic field. The width of the wire was chosen smaller than the length scale introduced by SOI, $W < \hbar^2/(\kappa m^*)$, but still wide enough for the wire to support four transversal modes in the ballistic regime. In the cases (a)-(d) the values of $\langle G \rangle$ are similar and show weak localization, i.e. a negative correction to the classically expected conductance. This behavior stems from the suppression of the spin relaxation due to lateral confinement, making those cases interesting for spintronics applications where long spin coherence lengths are favorable. Since the physical systems of cases (a)-(d) are different, also the values of the classically expected conductance can be different. For this reason the values of $\langle G \rangle$ differ slightly for the cases (a)-(d), although we expect the quantum correction to be the same in each case. Unfortunately we cannot compute the quantum interference corrections to the conductance directly but only the total conductance.

On the other hand the averaged conductance in cases (e) and (f) is increased compared to cases (a)-(d). This reduction of the negative quantum correction to the conductance is both due to the mixing of the spins and due to the absence of orthogonal symmetry. For case (e) only the former is effective and the orthogonal symmetry yields a conductance value which is lower than the conductance of neighboring angles θ , which belong to the unitary case (f). Hence, a dip in $\langle G \rangle$ can be observed at the angle $\vec{B}_{||} \perp \vec{B}_{so}$.

Considering the numerically determined values for the UCFs presented in Fig. 5.6b we observe that, although cases (a)-(d) have orthogonal symmetry, for (a) and (b) $\text{var}(G/G_0)$ has approximately twice the value than for (c) and (d). This can be understood by considering correlations between H_+ and H_- from Eq. (5.17). In cases (a) and (b) H_+ and H_- are the time-reversed of each other ($H_+^* = H_-$), resulting in double the value for the UCFs [196] compared to cases (c) and (d), where due to the Zeeman splitting the two separate Hamiltonians are uncorrelated, i.e. $H_+^* \neq H_-$. On the other hand for cases (e) and (f) the variance $\text{var}(G/G_0)$ is lower than for (a)-(d), since the system then mixes spins. We observe a small additional peak at the angle $\vec{B}_{||} \perp \vec{B}_{so}$ due to the orthogonal symmetry of case (e) compared to the unitary symmetry of case (f).

The different values of the conductance and the UCFs for the different symmetry classes shown in Fig. 5.6 are qualitatively in line with the expectations from RMT [189, 196]. Furthermore, the symmetry classes given in Table 5.1 can be

²Since, owing to the Onsager relations, all the effects observed in the range $\theta \in [0; \pi]$ naturally repeat themselves at an angle $\theta + \pi$ in the range $\theta \in [\pi; 2\pi]$, we restrict the presentation of $\langle G \rangle/G_0$ and $\text{var}(G/G_0)$ to $\theta \in [0; \pi]$.

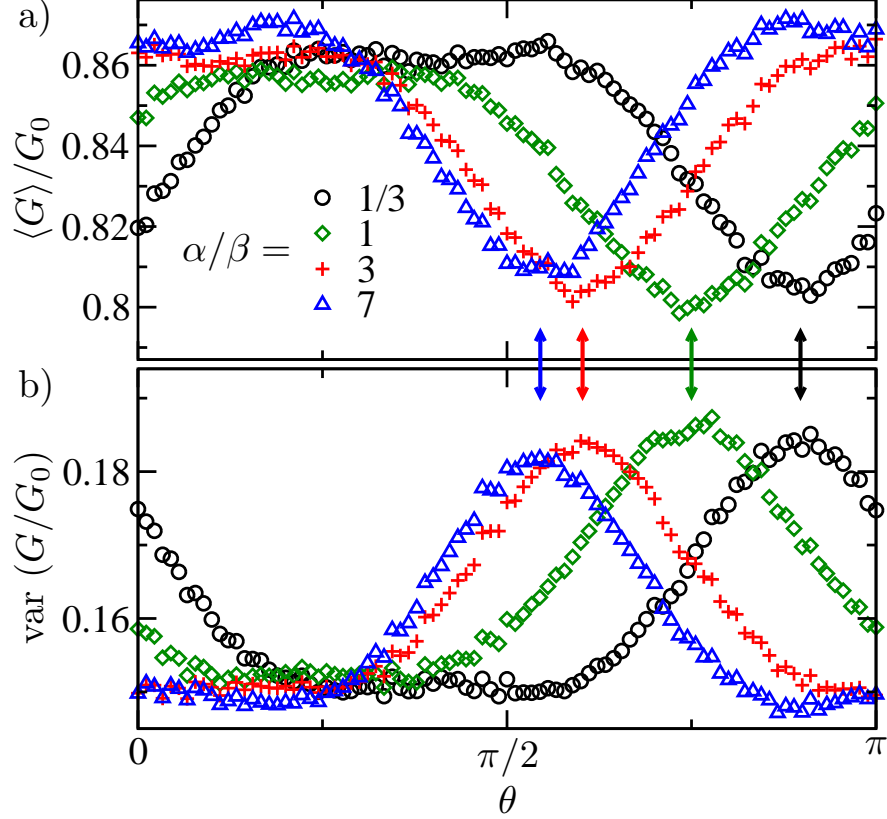


Figure 5.7: Conductance (panel a) and UCFs (panel b), as a function of the magnetic field direction θ for a quantum wire with $W = 20a$, $L = 150a$, $\bar{E}_F = 0.5$, $\bar{U}_{\text{dis}} = 1.4$ (i.e. $l \approx 17.3a$), $\phi = 0$, $N_d = 100000$, $\bar{B}_{\parallel} = 0.008$, $\bar{\alpha} + \bar{\beta} = 0.02$ with varying ratio $\alpha/\beta = 7$ (blue triangles), 3 (red plus-signs), 1 (green diamonds), $1/3$ (black circles). The arrows indicate the respective angles, where $\vec{B}_{\parallel} \parallel \vec{B}_{\text{so}}(p_y = 0)$, i.e. where we expect the extrema of $\langle G \rangle / G_0$ and $\text{var}(G/G_0)$.

identified as the origin for the angular dependence of different transport quantities found in several works on the interplay of Rashba SOI, Dresselhaus SOI, an in-plane magnetic field and quantum confinement [197–199].

In view of table 5.1 and Fig. 5.6 we can state in summary, that when both SOI and an in-plane magnetic field are present in the 2DEG, the conductance and the UCFs of a narrow quantum wire are strongly dependent on the direction of the magnetic field. We observe a pronounced absolute minimum/maximum in the conductance/UCFs when $\vec{B}_{\parallel} \parallel \vec{B}_{\text{so}}(p_y = 0)$, corresponding to case (d) in table 5.1. Since $\vec{B}_{\text{so}}(p_y = 0)$ depends on the orientation of the wire and the relative size of Rashba and Dresselhaus SOI, also the position of this minimum will depend on those parameters.

Therefore, in Fig. 5.7 we present the averaged conductance and the UCFs of a quantum wires with different ratios α/β as a function of the angle of the magnetic field θ . Indeed we observe that the position of the extremum changes in the expected way upon

variation of α/β , where we indicated the angle corresponding to $\vec{B}_{\parallel} \parallel \vec{B}_{\text{so}}(p_y = 0)$ by an arrow of the respective color. For the choice of parameters used in the calculations of Fig. 5.7 the orthogonal case (e) is not very pronounced showing (almost) the same values of $\langle G \rangle / G_0$ and $\text{var}(G/G_0)$ as the surrounding angles, which belong to case (f). The dip/peak in the averaged conductance/UCFs, as present in Fig. 5.7, is most pronounced, when B_{\parallel} and $|\vec{B}_{\text{so}}|$ are of comparable strength, because then spin mixing, i.e. spin relaxation, is strongest. For B_{\parallel} much smaller/larger than $|\vec{B}_{\text{so}}|$ the total magnetic field $\vec{B}_{\parallel} + \vec{B}_{\text{so}}$ is strongly aligned along \vec{B}_{so} or \vec{B}_{\parallel} , respectively, reducing the mixing of the spins. Then weak localization [200, 201] is recovered for all angles θ .

Semiclassical model

Apart from the explanation using RMT the results shown in Fig. 5.6 can also be understood intuitively from the path integral approach, which we already used in section 5.2 to explain the effects of WL and WAL. To account for the lateral confinement of the quantum wire, we employ a toy model (one-dimensional) Hamiltonian, which we receive from Eq. (5.1) by setting $p_y = 0$. Therefore, only motion along the x -axis, i.e. the wire direction, is allowed with two possible wave-vectors $k_x = \pm k_F$. We consider the spin evolution of an electron on a classical trajectory. After starting at the position x_0 , it undergoes $N - 1$ scattering events at x_i (with $i = 1, \dots, N - 1$) and finally returns to its initial position $x_N = x_0$. In-between those scattering events the motion of the electron is ballistic and its spin precesses around the fixed total magnetic field composed of the in-plane magnetic field and the effective magnetic field due to SOI. During the ballistic motion from x_{i-1} to x_i this precession axis $\vec{B}_{\text{tot}}(p_{x,i}) = \vec{B}_{\text{so}}(p_{x,i}) + \vec{B}_{\parallel}$ can have two different orientations depending on the direction of motion of the electron ($p_{x,i} = \pm \hbar k_F$):

$$\vec{B}_{\text{tot},i} \in \{\vec{B}_{\text{tot}}^+, \vec{B}_{\text{tot}}^-\} \quad \text{with} \quad \vec{B}_{\text{tot}}^{\pm} = \vec{B}_{\text{so}}(p_x = \pm \hbar k_F) + \vec{B}_{\parallel}. \quad (5.18)$$

At the final position x_N the spin state ξ_N of the electron is related to its initial spin state ξ_0 via [190]

$$\xi_N = \mathcal{K} \xi_0, \quad \text{with} \quad \mathcal{K} = \mathcal{K}_N \mathcal{K}_{N-1} \dots \mathcal{K}_2 \mathcal{K}_1, \quad (5.19)$$

where

$$\mathcal{K}_i = \exp \left\{ -i\eta |x_i - x_{i-1}| (\vec{\sigma} \cdot \vec{B}_{\text{tot},i}) \right\} \quad (5.20)$$

is the spin propagator between scattering events $i - 1$ and i , while $\eta = \mu_B g^* m^* / (2\hbar^2 k_F)$.

Now we can distinguish between two cases:

(I) $\vec{B}_{\text{tot}}^+ \parallel \vec{B}_{\text{tot}}^-$, which corresponds to the cases (a)-(d) given in table 5.1 and

(II) $\vec{B}_{\text{tot}}^+ \nparallel \vec{B}_{\text{tot}}^-$, for cases (e) and (f).

In case (I) all of the individual spin propagators

$$\mathcal{K}_i = \exp \left\{ -i\eta(\vec{\sigma} \cdot \hat{\nu}) \left[(x_i - x_{i-1})B_{\text{so}}^+ + |x_i - x_{i-1}|B_{\parallel} \right] \right\} \quad (5.21)$$

commute, $[\mathcal{K}_i, \mathcal{K}_j] = 0$, and the total spin propagator can be written as:

$$\begin{aligned} \mathcal{K} &= \exp \left\{ -i\eta(\vec{\sigma} \cdot \hat{\nu}) \left[B_{\text{so}}^+ \underbrace{\sum_{i=1}^N (x_i - x_{i-1})}_{=0} + B_{\parallel} \sum_{i=1}^N |x_i - x_{i-1}| \right] \right\} \\ &= \exp \left\{ -i\eta(\vec{\sigma} \cdot \hat{\nu}) B_{\parallel} L \right\}. \end{aligned} \quad (5.22)$$

Here we introduced the parameters $B_{\text{so}}^+ = |\vec{B}_{\text{so}}(p_x = +\hbar k_{\text{F}})|$, $L = \sum_{i=1}^N |x_i - x_{i-1}|$ and the unit vector $\hat{\nu} = \vec{B}_{\text{so}}(p_x = +\hbar k_{\text{F}})/B_{\text{so}}^+$.

We observe that the spin propagator \mathcal{K} does neither depend on the SOI nor on the exact path of the electron but only on the strength of the in-plane magnetic field B_{\parallel} and the total length L of the trajectory. Therefore, electrons travelling the same trajectory in opposite directions will undergo the same spin propagation upon completion of the trajectory, since L is equal in both cases. This results in constructive interference of backscattered paths connected by time-reversal, hence WL.

On the contrary, in case (II) the direction of $\vec{B}_{\text{tot},i}$ is different for electrons travelling in $+\hat{x}$ or $-\hat{x}$ -direction, yielding $[\mathcal{K}_i, \mathcal{K}_j] \neq 0$ when $k_{x,i} = -k_{x,j}$. Hence, the spin states of the electrons travelling on paths connected by time reversal do not have to be equal at their final position x_N . Therefore, their interference need not be constructive and when averaging over all Feynman paths this results in a suppression of WL, i.e. an increased conductance in comparison to cases (a)-(d). As a consequence we observe the minimum in $G(\theta)$ for $\vec{B}_{\parallel} \parallel \vec{B}_{\text{so}}(k_x)$.

5.3.2 Rashba and Dresselhaus spin-orbit interaction of equal strength

Having seen that confinement can cause a reduction of spin relaxation and hence WL instead of WAL, we now turn our attention to a regime, where spin relaxation is suppressed even for a bulk 2DEG. When the Rashba and linear Dresselhaus terms are of equal strength, i.e. $\alpha = \pm\beta$, the spin-orbit Hamiltonian [see Eqs. (2.11) and (2.14) with $\phi = \pi/4$ and $\alpha = \beta$]

$$H_{\text{so}} = -\frac{2\alpha}{\hbar} \sigma_y p_x \quad (5.23)$$

possesses $U(1)$ spin-rotation symmetry. Then spin is a good quantum number and for any momentum the effective magnetic field due to SOI is oriented along the $[\bar{1}10]$ -direction for $\alpha = \beta$, or the $[110]$ -direction for $\alpha = -\beta$, respectively. Hence, for this special case spin relaxation is absent and it constitutes a promising regime for the use in spintronics applications. For this reason, there has been increasing interest in this topic recently. On the theoretical side, new devices were proposed making use of this special condition [19, 202] and on the side of experiments several groups succeeded in the preparation of quantum wells showing $\alpha \approx \pm\beta$ [42, 43, 183].

Due to the absence of spin relaxation the magneto-conductance of 2DEGs with $\alpha = \pm\beta$ shows WL [203]. This fact can be understood easily by considering the evolution of the spin state of an electron on a specific trajectory. Namely, the final spin state is determined only by the initial state and the initial and final position of the electron but is independent of the specific trajectory travelled [168]. Specifically, for electrons returning to their initial position the final spin state is equal to the initial one. Since only the interference of such wavefunctions (which is constructive here) is important for the quantum correction to the conductance, we observe WL.

In Fig. 5.8a we confirm this behavior by showing the magneto-conductance for a wire with fixed α but variable β . For $\beta = 0$ the wire exhibits WAL due to the efficient randomization of the spins for a wire of this width. However, for increasing β we observe a crossover from WAL to WL for $\alpha = \beta$ as expected. This transition for $\beta \rightarrow \alpha$ can be understood when taking a closer look at the transformed Hamiltonian \tilde{H} , given in Eq. (5.12). Even though the condition $W \ll L_{\text{so}}^{\kappa}$ is not necessarily fulfilled, still the term $\Delta_{\text{so}}\sigma_{\delta}$ becomes small for $|\beta| \rightarrow |\alpha|$ causing a reduction of the spin relaxation and thus results in a crossover from WAL to WL.

As for the case of narrow quantum wires, here we also investigate the influence of an additional in-plane magnetic field on the conductance. As a measure of the relative strength of the in-plane magnetic field and the effective magnetic field due to SOI, we define the ratio $\lambda = B_{\parallel}/|\vec{B}_{\text{so}}(p_x = \hbar k_{\text{F}})|$, see Eqs. (5.2) and (5.3), where we used the strength of \vec{B}_{so} for momentum along the quantum wire. In view of table 5.1, we expect the magneto-conductance of the wire to be strongly dependent of the direction of the magnetic field. Indeed, for $\vec{B}_{\parallel} \parallel \vec{B}_{\text{so}}$, i.e. $\vec{B}_{\parallel} \parallel [\bar{1}10]$ for $\alpha = \beta$, or $\vec{B}_{\parallel} \parallel [110]$ for $\alpha = -\beta$, respectively, the wire exhibits WL as if \vec{B}_{\parallel} were not present. For all other directions $\vec{B}_{\parallel} \not\parallel \vec{B}_{\text{so}}$, in turn causing spin relaxation, which leads to a suppression of the WL. In Fig. 5.8b we show the numerically calculated magneto-conductance for the latter case of $\alpha = \beta$ and $\vec{B}_{\parallel} \not\parallel \vec{B}_{\text{so}}$ for several values of λ . For zero perpendicular magnetic field, $\Phi_s = 0$, the conductance increases with λ until the in-plane magnetic field and the magnetic field due to SOI are of comparable strength, i.e. $\lambda \approx 1$. Then no quantum correction to the conductance is present, i.e. $(\partial G/\partial \Phi_s) \approx 0$. For $\lambda \gg 1$, the magneto-conductance again shows a WL dip, because then the total magnetic field is aligned along \vec{B}_{\parallel} .

We can understand the form of the magneto-conductance curves in Fig. 5.8b by considering the expression for the conductance correction from diagrammatic perturbation

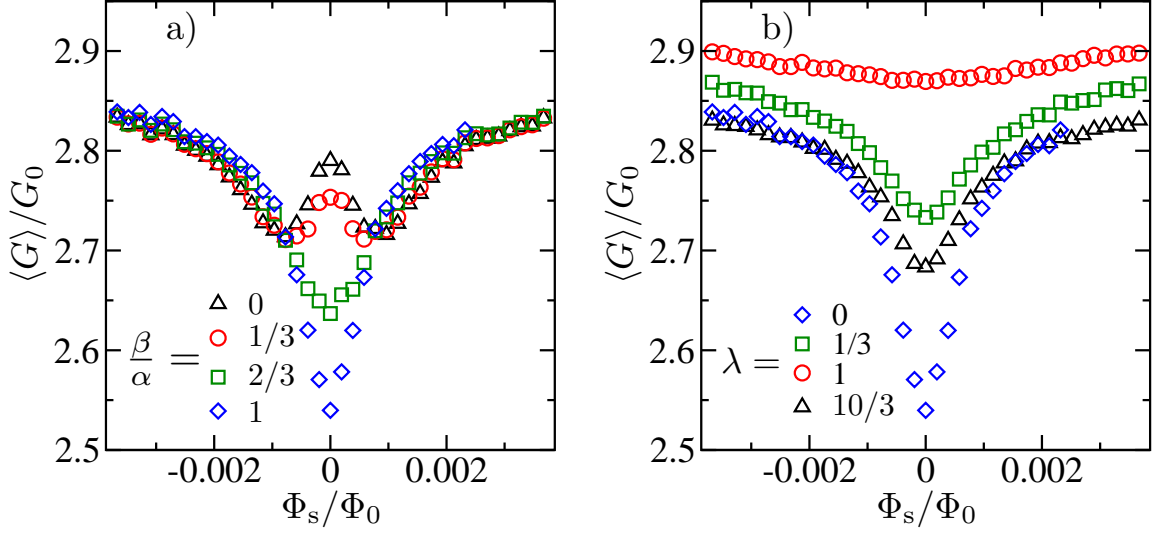


Figure 5.8: a) Magnetoconductance of a quantum wire for several values of $\bar{\beta}$ at fixed $\bar{\alpha} = 0.03$ and zero in-plane magnetic field $B_{||} = 0$. b) Magnetoconductance for a wire with $\bar{\alpha} = \bar{\beta} = 0.03$ and $\theta = \pi$ for several values of λ . Common parameters: $W = 46a$, $\phi = \pi/2$, $\bar{E}_F = 0.5$, $\bar{U}_{\text{dis}} = 1.4$, $N_d = 25000$. The magnetic flux $\Phi_s = a^2 B_z$ is given in units of $\Phi_0 = h/(2e)$.

theory [184]:

$$\Delta G \propto (C_{00} - \sum_{m=-1}^1 C_{1m}). \quad (5.24)$$

The singlet term C_{00} gives a positive contribution to the conductance, while the (second) triplet term contributes negatively. For strong spin relaxation the triplet term is suppressed [184] and the magnetoconductance shows WAL, $\Delta G > 0$, due to the finite C_{00} . The singlet term on the other hand is reduced in an in-plane magnetic field [204]. For the parameters used in Fig. 5.8b, it is absent for $\lambda \geq 0.15$. Hence, in Fig. 5.8b for the curves with finite λ only the triplet term is present in the conductance correction resulting in $\Delta G < 0$. While the spin relaxation is strong for comparable strengths of $\vec{B}_{||}$ and \vec{B}_{so} , yielding a reduction of the triplet term and hence $\Delta G \approx 0$ (red circles in Fig. 5.8b), for $\lambda \ll 1$ or $\lambda \gg 1$, on the other hand, the total magnetic field $\vec{B}_{\text{tot}} = \vec{B}_{\text{so}} + \vec{B}_{||}$ is aligned along \vec{B}_{so} or $\vec{B}_{||}$, respectively. Therefore, spin relaxation is suppressed, causing WL (see green squares or black triangles in Fig. 5.8b). In the complementary case, when WAL is present at $B_{||} = 0$, a transition from WAL to WL is observed with increasing $B_{||}$ [200, 201]. This is a consequence of the reduction of the singlet term caused by $\vec{B}_{||}$.

5.4 All-electrical detection of the ratio α/β

For the efficient manipulation of spins and the operability of many spintronics devices (see e.g. Ref. [19]) it is essential to be able to control the ratio α/β . While it is possible to determine α/β very precisely by using optical techniques [68, 74, 205], in certain situations an all-electrical detection scheme is highly desirable. For instance, when the Rashba SOI strength α is tuned electrically by a top gate [22], it is very difficult to utilize optical methods.

In principle also transport measurements of the magneto-conductance can be used to determine both α and β by fitting the data to analytical predictions [206, 207]. However, since the theory involves several fitting parameters the results can bear a certain ambiguity, and the error margins can be quite large.

Therefore, in this section we propose an alternative, all-electrical method to determine the relative strength of Rashba and Dresselhaus SOI, α/β , from measuring the conductance or the UCFs of narrow quantum wires subject to an in-plane magnetic field. This method, which constitutes the main result of this chapter, uses the results from the previous sections, namely that for $\vec{B}_{||} \parallel \vec{B}_{so}(p_y = 0)$ spin relaxation is suppressed, while for all other directions it is present. No fit parameters are required, and α/β is straightforwardly related to this specific field direction, where the conductance is minimal or the UCFs are maximal, respectively.

5.4.1 Outline of the detection mechanism

Since the direction of the effective magnetic field \vec{B}_{so} depends on both α and β , the extremum in the conductance traces, i.e. the minimum (maximum) of the conductance (UCFs), can be used to determine the relative strength of Rashba and Dresselhaus SOI. For momentum along the wire, the direction of \vec{B}_{so} is given by

$$\theta_{\text{ext}} = \arctan \left(-\frac{\alpha \cos \phi + \beta \sin \phi}{\beta \cos \phi + \alpha \sin \phi} \right). \quad (5.25)$$

We have seen in Fig. 5.7 that, if the two requirements $W \ll L_{so}^\kappa = \pi \hbar^2 / (m^* \kappa)$ and $|\vec{B}_{||}| < |\vec{B}_{so}|$ are fulfilled, the minimum/maximum of the conductance/UCFs appears precisely at this angle θ_{ext} . In Fig. 5.9, we plot Eq. (5.25) as solid lines for three different wire orientations ϕ as a function of the relative strength of Rashba and Dresselhaus SOI. Its validity is nicely confirmed by the values of θ_{ext} (shown as symbols), which were extracted from the numerically determined θ -dependence of $\langle G \rangle$ (see e.g. Fig. 5.7). In order to use this feature for the determination of the ratio α/β we suggest to measure $G(\theta)$ or $\text{var}G(\theta)$ for quantum wires oriented either along the [100]- or the [010]-direction. Then θ_{ext} directly provides the unambiguous value for the relative strength and signs

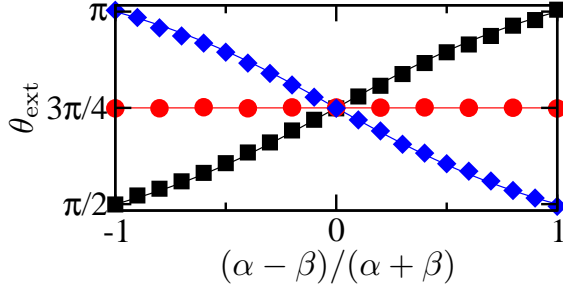


Figure 5.9: Minimum θ_{ext} of the numerically determined $\langle G \rangle$ for a system with $W = 20a$, $\bar{\alpha} + \bar{\beta} = 0.04$, $\bar{E}_F = 0.5$, $\bar{U}_{\text{dis}} = 1.2$, $\bar{B}_{\parallel} = 0.01$ and $N_d = 20000$. Black squares: $\phi = \pi/2$; red circles: $\phi = \pi/4$; blue diamonds: $\phi = 0$. The solid lines represent Eq. (5.25) for the respective angles ϕ .

of α and β , which is then given by

$$\frac{\alpha}{\beta} = \begin{cases} -\tan \theta_{\text{ext}} & \text{for } \phi = 0 \\ -\cot \theta_{\text{ext}} & \text{for } \phi = \pi/2 \end{cases}. \quad (5.26)$$

Considering quantum wires realized in an InAlAs/InGaAs heterostructure (typical values $m^* = 0.05 m_0$, $g^* = 3$) and fixing the width $W = 350$ nm, we see that the parameters used in Fig. 5.9 ($l \approx 412$ nm, $B_{\parallel} \approx 0.17$ T and $\alpha + \beta \approx 3.5 \cdot 10^{-12}$ eVm) are well in reach of present day experiments [200, 208].

5.4.2 Applicability of the detection mechanism

In order to assess possible limitations of this detection method, we perform calculations varying several parameters, while keeping the ratio $\alpha/\beta = 3$ and the direction of the wire $\theta = \pi/2$ constant. In Fig. 5.10 we confirm that Eq. (5.25), $\theta_{\text{ext}} = \arctan(-1/3) \approx 0.9\pi$, is fulfilled for a wide range of a) SOI strengths $\bar{\alpha} + \bar{\beta}$, b) mean free paths l and c) Fermi energies \bar{E}_F . Specifically, in Fig. 5.10b we give numerical proof that the detection method is independent of the ratio between mean free path and the width of the wire as long as l is significantly shorter than the length L of the disordered region to ensure diffusive transport.

In Figs. 5.9 and 5.10a,b we considered wires of a width $W = 20a$ and a Fermi energy $\bar{E}_F = 0.5$, which corresponds to 4 open transversal modes in the leads³. Since in a realistic experimental situation the number of transversal orbital channels is usually much higher, in Fig. 5.10c we extend our considerations to a higher number of channels. Keeping the width W of the wire constant, but choosing a smaller lattice spacing a and consequently rescaling $\bar{\alpha}$, $\bar{\beta}$ and \bar{B}_{\parallel} , we are able to go to higher Fermi energies E_F in the simulation, since $E_F \propto a^{-2}$. In Fig. 5.10c we were able to simulate quantum wires with up to 13 open channels in the leads, thereby confirming the robustness of the detection mechanism also for systems with a higher electron density, i.e. higher Fermi energy and a higher number of transversal orbital channels. When fixing the lattice

³Not including the factor 2 for the spin degree of freedom.

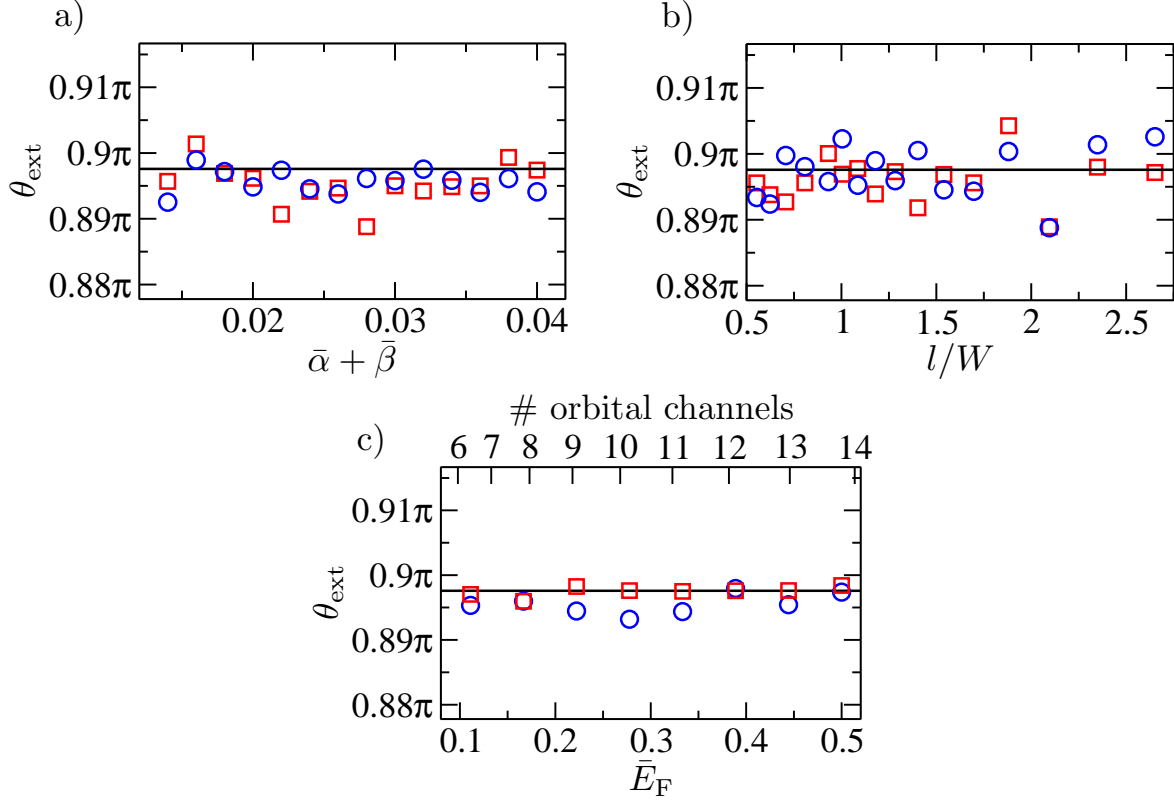


Figure 5.10: The values of θ_{ext} determined from the minimum (maximum) of the conductance (UCFs) for a quantum wire with $\phi = \pi/2$ and $\alpha/\beta = 3$ are presented as circles (squares). They are compared to the expected value $\theta_{\text{ext}} = \arctan(-\beta/\alpha) = \arctan(-1/3) \approx 0.898\pi$ from Eq. (5.25), shown as solid line. Panel a) Variation of the SOI strength $\bar{\alpha} + \bar{\beta}$ for fixed mean free path $l \approx 17.3a$ and Fermi energy $\bar{E}_F = 0.5$. Panel b) Variation of the mean free path l for fixed SOI strength $\bar{\alpha} + \bar{\beta} = 0.02$ and Fermi energy $\bar{E}_F = 0.5$. Common parameters for panels a) and b): $W = 20a$, $L = 150a$, $\bar{B}_{\parallel} = 0.01$ and $N_d = 8000$. Panel c) Variation of the Fermi energy \bar{E}_F , respectively the number of open channels, for fixed $\bar{\alpha} = 1/20$, $\bar{\beta} = 1/60$, $W = 60a$, $L = 450a$, $\bar{U}_{\text{dis}} = 0.785$, $\bar{B}_{\parallel} = 1/900$, and $N_d = 15000$.

spacing $a = 4\text{nm}$ and using the typical values of an InAlAs/InGaAs heterostructure ($m^* = 0.05m_0$, $g^* = 3$), the parameters used in Fig. 5.10c correspond to $W = 240\text{nm}$, $\alpha \approx 1.9 \cdot 10^{-12}\text{eVm}$, $\beta \approx 6.3 \cdot 10^{-13}\text{eVm}$, $B_{\parallel} \approx 0.61\text{T}$ and for the highest Fermi energy considered $E_F = 0.5\hbar^2/(2m^*a^2) \approx 24\text{meV}$.

Although we have seen that Eq. (5.25) is fulfilled for a wide range of parameters, there are nevertheless conditions that have to be met in the experimental setup for the proposed detection scheme to work efficiently. We refer to the magnitude of $\Delta_B\sigma_{\delta}$ and $\Delta_{\text{so}}\sigma_{\delta}$ which should be small compared to the energy scale set by the SOI, see Eq. (5.12). To be specific, it is important to keep the conditions $W \ll L_{\text{so}}^{\kappa} = \hbar^2/(\kappa m^*)$

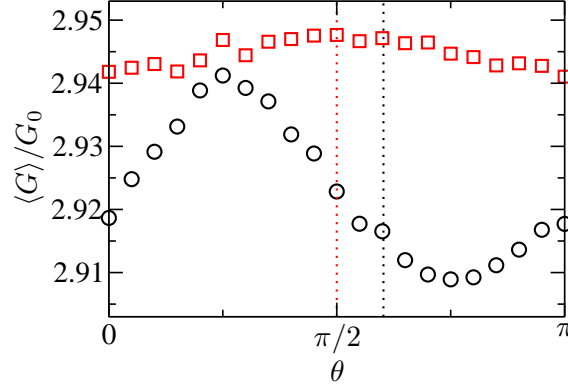


Figure 5.11: Conductance of a wire with $W = 60a$, $L = 200a$, $\phi = 0$, $\bar{\alpha} = 0.045$, $\bar{E}_F = 0.5$, $\bar{U}_{\text{dis}} = 1.4$, $\bar{B}_{\parallel} = 0.01$ and $N_d = 100000$ as a function of the in-plane magnetic field direction θ for $\bar{\beta} = 0$ (red squares) and $\bar{\beta} = 0.015$ (black circles). The red and black dotted lines indicate the respective minima expected in narrow quantum wires according to Eq. (5.25).

and $B_{\parallel} \leq |\vec{B}_{\text{so}}|$ because otherwise the experimentally detected minimum/maximum in the conductance/UCFs can be different from the expression given in Eq. (5.25).

For instance, when increasing the width of the wire beyond L_{so}^{κ} , the angular dependence of the conductance $G(\theta)$ evolves into the one typical of a 2DEG [204, 209]. There $G(\theta)$ is only anisotropic, if both $\alpha, \beta \neq 0$. Opposed to the narrow quantum wires considered here, where θ_{ext} is a function of ϕ , α and β [see Eq. (5.25)], in a 2DEG the minimum of the conductivity appears either at $\theta = \pi/4$ or $3\pi/4$, depending on the sign of the product $(\alpha \cdot \beta)$, but independent of the ratio α/β . Also in the wire structures investigated here, we can observe this behavior. In Fig. 5.11 we show the conductance of a wire whose width is of the order of the spin precession length of the dominating (Rashba) SOI component. For $\bar{\beta} = 0$, the conductance shows no strong dependence on the angle of the magnetic field, while for finite Dresselhaus SOI, as expected, a clear minimum at $\theta = 3\pi/2$ is present. This is in contrast to wires obeying the condition $W \ll L_{\text{so}}^{\kappa}$, where the minimum in this case appears at $\theta_{\text{ext}} = \arctan(-\alpha/\beta) \approx 0.6\pi$ (indicated by a dotted black line in Fig. 5.11).

Furthermore, for strong B_{\parallel} the term $\Delta_B \sigma_{\delta}$ in Eq. (5.12) is no longer negligible and spin relaxation is present for all angles θ , leading to an increase of $\langle G \rangle$ also at $\vec{B}_{\parallel} \parallel \vec{B}_{\text{so}}(p_y = 0)$. Consequently also the minimum in the conductance can change its position with increasing λ . This situation is shown in Fig. 5.12a.

However, both limitations just described do not apply to a 2DEG with $\alpha = \pm\beta$, since there spin relaxation is absent for $\vec{B}_{\parallel} \parallel \vec{B}_{\text{so}}$ regardless of the width of the wire or the strength of the in-plane magnetic field. Therefore, the position of the extremum in the conductance or UCFs remains at the angle $\theta = 3\pi/4$ or $\pi/4$, respectively. In Fig. 5.12b this fact is confirmed for the case of a strong in-plane magnetic field.

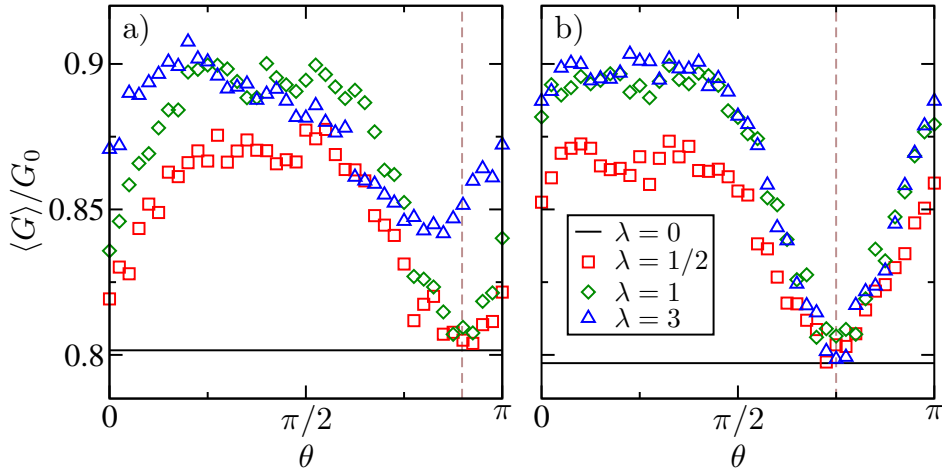


Figure 5.12: Conductance of a wire with $W = 20a$, $L = 150a$, $\phi = \pi/2$, $\bar{E}_F = 0.5$, $\bar{U}_{\text{dis}} = 1.4$ and $N_d = 10000$ as a function of the in-plane magnetic field direction θ for different values of λ . a) $\bar{\alpha} = 3\bar{\beta} = 0.03/\sqrt{5}$. b) $\bar{\alpha} = \bar{\beta} = 0.01$. The angle θ_{ext} from Eq. (5.25) is indicated by a dashed vertical line.

5.4.3 Influence of the cubic Dresselhaus term

So far we have neglected effects due to the cubic Dresselhaus SOI term, Eq. (2.15), although it is always present in the III-V semiconductor quantum wells grown in [001]-direction consider here. It becomes increasingly important for wide quantum wells or high electron densities and in general it induces additional randomization of the spin state. However, when considering the dependence of the cubic Dresselhaus SOI on the relative orientation of the electron momentum and the underlying crystal lattice, we see that it vanishes for k -vectors along the [100]- or [010]-directions. Indeed it has been verified experimentally, that for narrow quantum wires along the [100]- or [010]-direction spin relaxation due to the cubic Dresselhaus term is suppressed compared to wires along the [110]- or $[\bar{1}10]$ -direction [210]. In those experiments spin relaxation was induced only by the cubic Dresselhaus term, since the linear Rashba and Dresselhaus SOI contributions were suppressed due to the narrow width of the wires. Since we propose to use quantum wires oriented along the [100]- or [010]-direction for the detection method, we expect the effect of the cubic Dresselhaus SOI to be small.

To confirm this speculation, we numerically calculate the conductance of narrow quantum wires with both Rashba and linear Dresselhaus SOI, an in-plane magnetic field and now also including the cubic Dresselhaus contribution. In Fig. 5.13 we show the values of θ_{ext} extracted from the θ -dependence of the conductance and the UCFs for fixed $\alpha/\beta = 3$ as a function of $\bar{\gamma}$. We observe a shift of the extremum to higher angles with increasing cubic Dresselhaus SOI strength. In order to understand this shift, we now determine a new value $\bar{\beta}'$ from θ_{ext} via Eq. (5.25), while using the value of $\bar{\alpha}$ from

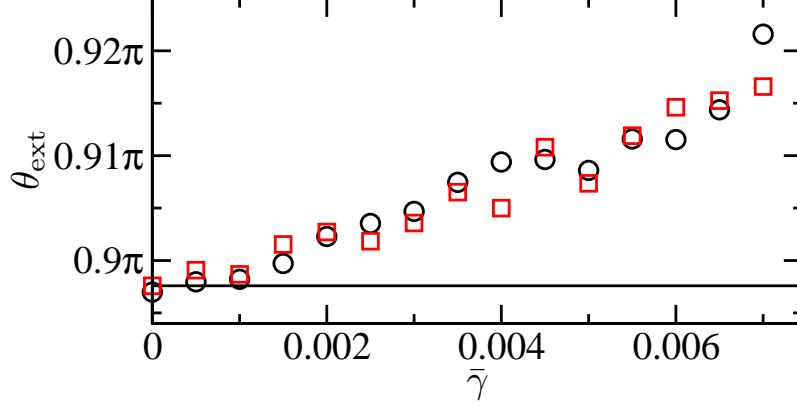


Figure 5.13: Minimum/maximum of the conductance (black circles) or the UCFs (red squares) as a function of the strength of the cubic Dresselhaus SOI $\bar{\gamma}$. Parameters: $\bar{E}_F = 0.5$, $W = 20a$, $L = 150a$, $\bar{U}_{\text{dis}} = 1.4$, $\bar{B}_{\parallel} = 0.01$, $\bar{\alpha} = 3\bar{\beta} = 0.015$, $\phi = \pi/2$, $N_d = 8000$.

the calculations:

$$\bar{\beta}' = -\bar{\alpha} \tan \theta_{\text{ext}}. \quad (5.27)$$

The resulting $\bar{\beta}'$, which is plotted in Fig. 5.14a, shows a nice linear dependence on the strength $\bar{\gamma}$ of the cubic Dresselhaus contribution. As we will argue now, this γ -dependent rescaling of β is a direct consequence of the lateral confinement.

The linear Dresselhaus term in a quantum well, Eq. (2.14), was obtained from the cubic bulk term, Eq. (2.13), by replacing the momentum in the direction of the confinement p_z^n by its value $\langle p_z^n \rangle$ averaged over the first subband of the quantum well. Since we consider the case of quantum wires with strong lateral confinement, we now follow the same approach for this confinement along the y -direction. We begin by writing down the total SOI Hamiltonian of the quantum well, Eq. (2.11), Eq. (2.14) and Eq. (2.15), fixing $\phi = 0$:

$$H_{\text{so}} = \frac{\alpha}{\hbar} (\sigma_x p_y - \sigma_y p_x) + \frac{\beta}{\hbar} (\sigma_x p_x - \sigma_y p_y) + \frac{\gamma}{\hbar^3} (-\sigma_x p_x p_y^2 + \sigma_y p_x^2 p_y). \quad (5.28)$$

We now replace all powers p_y^n with the averaged value $\langle p_y^n \rangle$, noting that odd powers vanish due to the symmetric hard-wall confinement potential of the quantum wire, yielding

$$H_{\text{so}} = -\frac{\alpha}{\hbar} \sigma_y p_x + \frac{1}{\hbar} \sigma_x p_x \left(\beta - \frac{\gamma}{\hbar^2} \langle p_y^2 \rangle \right). \quad (5.29)$$

As in Eq. (5.16) we end up with a Hamiltonian, where spin is a good quantum number. Hence, spin relaxation is absent and WL instead of WAL can be observed. The only difference to Eq. (5.16), where the cubic term was neglected, is the presence of the term $-\frac{\gamma}{\hbar^2} \langle p_y^2 \rangle$, which rescales the strength β of the linear Dresselhaus SOI. This rescaling

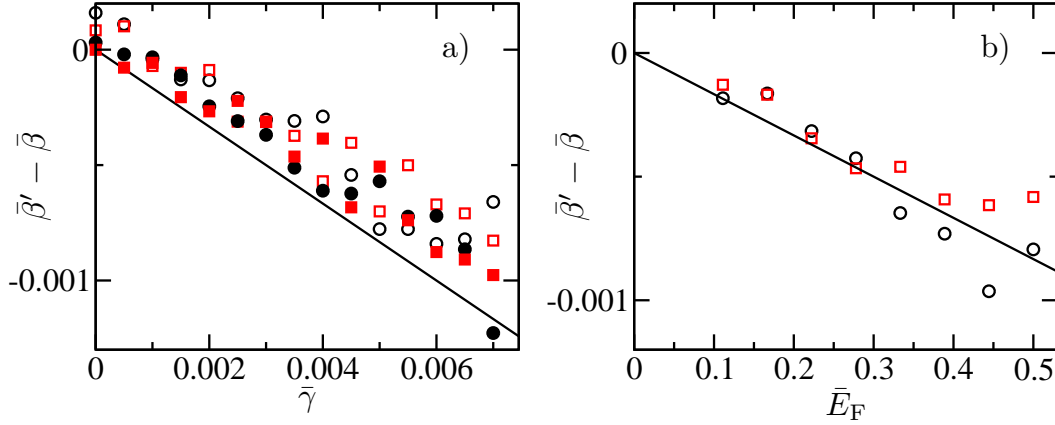


Figure 5.14: Rescaled linear Dresselhaus SOI strength $\bar{\beta}' - \bar{\beta}$ as a function of the strength of the cubic Dresselhaus SOI $\bar{\gamma}$ (panel a) and the Fermi energy \bar{E}_F (panel b) determined from the minimum/maximum of the conductance (black circles) or the UCFs (red squares), respectively. Parameters: a) $\bar{E}_F = 0.5$, $W = 20a$, $L = 150a$, $\bar{U}_{\text{dis}} = 1.4$, $\bar{B}_{\parallel} = 0.01$, $\bar{\alpha} = 3\bar{\beta} = 0.15$ (filled symbols), $\bar{\alpha} = 2\bar{\beta} = 0.2$ (open symbols), $\phi = \pi/2$ (filled symbols), $\phi = 0$ (open symbols), $N_d = 8000$; b) $\bar{\gamma} = 0.005$, $W = 60a$, $L = 450a$, $\bar{U}_{\text{dis}} \approx 0.785$, $\bar{B}_{\parallel} = 1/900$, $\bar{\alpha} = 3\bar{\beta} = 0.005$, $\phi = \pi/2$, $N_d = 6000$.

causes the shift of θ_{ext} in Fig. 5.13. The value of θ_{ext} is still given by Eq. (5.25), however with β replaced by

$$\beta' = \beta - \frac{\gamma}{\hbar^2} \langle p_y^2 \rangle. \quad (5.30)$$

Therefore, we have to estimate the value of $\langle p_y^2 \rangle$ in order to compare the prediction of Eq. (5.30) to the numerical results shown in Fig. 5.14. For simplicity we consider the transversal wave-functions of a hard-wall quantum wire without SOI, where the value of $\langle p_y^2 \rangle$ for mode n is given by

$$\langle p_y^2(n) \rangle = \frac{\hbar^2 \pi^2}{W^2} n^2. \quad (5.31)$$

Next, we naively take the average over all occupied transversal modes ($n = 1, \dots, M$)

$$\langle p_y^2 \rangle = \frac{1}{M} \sum_{n=1}^M \langle p_y^2(n) \rangle = \frac{\hbar^2 \pi^2}{W^2} \frac{1}{M} \sum_{n=1}^M n^2 \approx \frac{\hbar^2 \pi^2}{3W^2} M^2 \quad (5.32)$$

where we assumed $M \gg 1$, which allowed us to rewrite the sum as an integral. Now we use the fact that the n -th transversal mode of the quantum wire opens at energy $E_n = \hbar^2 \pi^2 n^2 / (2m^* W^2)$ yielding

$$M \approx W \sqrt{2m^* E_F} / (\hbar \pi). \quad (5.33)$$

This approximation lets us write $\langle p_y^2 \rangle$ as a function of solely the Fermi energy of the system

$$\langle p_y^2 \rangle \approx \frac{2m^*}{3} E_F. \quad (5.34)$$

We insert this expression into Eq. (5.30) and rewrite it in terms of dimensionless tight-binding parameters

$$\bar{\beta}' = \bar{\beta} - \frac{1}{3} \bar{\gamma} \bar{E}_F. \quad (5.35)$$

In Fig. 5.14 we check the validity of this relation (shown as black line), comparing it to the numerically determined values of $\bar{\beta}'$ from the conductance, $\langle G(\theta) \rangle$ (black circles), and the UCFs, $\text{var} G(\theta)$ (red squares). We show $\bar{\beta}'$ as a function of the SOI strength $\bar{\gamma}$, Fig. 5.14a, and the Fermi energy \bar{E}_F , Fig. 5.14b, respectively. We observe that the numerically extracted $\bar{\beta}'$ is linearly dependent on both $\bar{\gamma}$ and \bar{E}_F , as expected from Eq. (5.35). Also the qualitative agreement is good, especially in view of the approximations used to obtain the estimate value Eq. (5.35). The difference between Eq. (5.35) and the numerical calculations in Fig. 5.14a can be due to the overestimation of the channel number in Eq. (5.33), which is especially important for small M .

To summarize, we were able to show that the inclusion of the cubic Dresselhaus term does not limit the detection mechanism, but has to be accounted for only by rescaling the parameter β .

CHAPTER 6

Summary and perspectives

In this thesis we studied several spin-related phenomena in two-dimensional electron gases (2DEGs). The topics presented ranged from the investigation of fundamental physical phenomena to specific proposals for devices or measurement setups. The latter can be useful for the realization of semiconductor spintronics devices, which require the efficient creation, control and detection of spins for their operation [23]. In the following we will briefly review our main findings.

In chapter 3 we extended the particle ratchet mechanism to the realm of spin. Spin ratchets give rise to directed spin transport upon application of an unbiased ac-driving. We confirmed the operability of two particular realizations of spin ratchets based on quantum wire geometries. In one setup we made use of spin-dependent resonant tunneling of the electrons through a double quantum dot structure in the presence of an inhomogeneous magnetic field. In the other setup we exploited the interplay of electrostatic potential barriers and spin-orbit interaction (SOI) in a quantum wire. For both devices we showed that in the absence of net charge transport, spin ratchet currents of reasonable magnitude can be created. By self-consistently calculating the voltage drop in the ratchet setups, we furthermore extended previous theoretical treatments of coherent ratchets, which were based on heuristic voltage drop models, see e.g. [111, 157]. In addition, we confirmed the robustness of these pure spin currents against several possibly limiting influences, as e.g. disorder.

In a 2DEG with SOI a charge current causes an orientation of the electron spins. This phenomenon, known as current-induced spin accumulation (CISA), was the topic of chapter 4. We showed that quantum confinement and/or the interplay of Rashba and Dresselhaus SOI can lead to a suppression of the CISA from the value expected in a bulk 2DEG. We also confirmed the feasibility of extracting current-induced spins from a region with strong SOI into a region without SOI. This can be achieved very

efficiently by using narrow Hall contacts, where the spin precession length exceeds the opening size of the contacts. The extracted spins can be useful for spintronics applications due to the long spin lifetimes in regions with little or vanishing SOI. At the end of that chapter we presented proof-of-principle calculations for an all-electrical detection mechanism of the CISA. To this end, we employed a spin-selective voltage probe lead in a four terminal setup, allowing to directly relate the magnitude of the CISA to the voltage of this lead.

Finally in chapter 5 we considered quantum interference effects observable in the conductance of disordered wires. In the presence of Rashba SOI, Dresselhaus SOI and an in-plane magnetic field we were able to identify different transport regimes, yielding different values for the quantum mechanical conductance correction and the universal conductance fluctuations. For instance, when the spin precession length exceeds the width of the wire, or the strengths of Rashba and linear Dresselhaus SOI are equal, the conductance shows a negative correction to the classically expected one (weak localization) in contrast to the generic case of a 2DEG with strong SOI, which exhibits a positive conductance correction (weak antilocalization).

In narrow wires, both the conductance and the universal conductance fluctuations show a pronounced anisotropy with respect to the direction of an in-plane magnetic field. This anisotropy is directly related to the strength of the Rashba SOI, the Dresselhaus SOI and the orientation of the quantum wire with respect to the underlying crystal lattice. Using those results, we proposed an all-electrical method for the precise determination of the relative strength of Rashba and linear Dresselhaus SOI, whose knowledge is of great importance in several promising proposals for spintronics devices [19, 202].

The calculations presented in this thesis include a number of approximations. Therefore, the question arises, to what extent our results will be altered by the consideration of additional, possibly relevant physical potentials, interactions, etc.

A natural extension of the results obtained in this thesis is the inclusion of the cubic Dresselhaus term H_{D3} , see Eq. (2.15). It is generally present in III-V semiconductor quantum wells and becomes increasingly important compared to the linear Dresselhaus contribution for high electron densities and in wide quantum wells. In view of the results presented in this thesis, we expect observable modifications due to H_{D3} especially when the effects of Rashba SOI and linear Dresselhaus SOI cancel each other. For instance, the cubic Dresselhaus contribution gives rise to finite spin relaxation at the special condition $\alpha = \pm\beta$ of equal Rashba and linear Dresselhaus SOI strengths. The extension of our results to the case also including H_{D3} is straightforward. The numerical calculation scheme outlined in section 2.3.2 — based on the tight-binding Hamiltonian (2.92) — is ideally suited for this purpose.

In section 5.4.3 we already investigated the influence of the cubic Dresselhaus term on the proposed detection scheme for the ratio α/β . We were able to show that the cubic contribution in a narrow quantum wire can be accounted for by renormalizing

the strength of the linear Dresselhaus SOI. However, there are many other interesting implications of the cubic Dresselhaus term.

Following a recent experiment [183] the question arises whether spin relaxation due to the cubic Dresselhaus term can also be suppressed by lateral confinement. The authors of Ref. [183] observed weak localization in narrow quantum wires, where theory predicted weak antilocalization due to the spin relaxation induced by H_{D3} [193]. The experimental data and the theory of Ref. [193] showed nice agreement only when the cubic Dresselhaus contribution was neglected in the fitting procedure [183]. Motivated by this discrepancy we performed preliminary numerical calculations on the magnetoconductance of narrow wires with a finite cubic Dresselhaus term. There we observed a transition from weak antilocalization to weak localization upon reduction of the wire width [211]. Therefore, our results indicate that spin relaxation due to H_{D3} is suppressed in narrow wires, in analogy to the case of Rashba (see Fig. 5.5) and/or linear Dresselhaus SOI.

In other recent experiments Nitta's group observed a pronounced anisotropy of the confinement-induced crossover from WAL to WL with respect to the relative orientation of the quantum wire and the underlying crystal lattice [212]. Preliminary numerical calculations indicate that this anisotropy is related to the presence of H_{D3} [211].

The effect of the cubic Dresselhaus contribution on the CISA in extended 2DEGs was investigated in Ref. [170] by performing analytical calculations based on diffusion equations. It was found that the inclusion of a small cubic term has a strong influence close to $\alpha = \pm\beta$. As in the case of a finite-sized system (see e.g. Fig. 4.7), it causes a suppression of the CISA around $\alpha = \pm\beta$. Naturally, the question arises, how those results are altered for finite-sized geometries or for a cubic Dresselhaus contribution, which is of comparable strength to the linear one.

The examples we just outlined are only a small selection of interesting physical phenomena related to the presence of the cubic Dresselhaus SOI. Since it is desirable to better understand its influence on the transport in 2DEGs, further calculations have to be carried out in the future.

In this thesis we put forward proposals for a variety of measurement setups and devices for the creation of spin currents/accumulations, confirming their realizability by choosing parameters that are well in reach of present day experiments. For a few of them, we now briefly discuss the chances for their experimental realization in the near future.

First experiments related to the all-electrical detection scheme of the ratio α/β , which we proposed in section 5.4, indicate that the conductance shows a pronounced anisotropy with respect to the direction of an in-plane magnetic field [213]. Since the detection mechanism is based on this effect, we soon expect the first experimental, all-electrical detection of the relative strength of Rashba and Dresselhaus SOI. After experimental confirmation of its functionality it will be a valuable addition to the existing optical techniques [68, 74, 205, 214].

Only recently a local spin accumulation in a quantum dot was detected electrically via

spin-polarized point contacts [215]. Since, the detection scheme for the CISA, which we outlined in section 4.4, also makes use of such a spin-selective point contact, we are confident that also this setup will be realized in the near future.

Although the spin ratchet setups proposed in chapter 3 can be realized in principle, the confirmation of the spin ratchet mechanism is less straightforward. So far the detection of spin currents is only possible in an indirect way. On the one hand, spin currents can give rise to non-equilibrium spin accumulations at the boundaries of the system, which can be detected optically [164]. On the other hand, one can make use of effects, which create a charge current or a voltage drop in response to a spin current. Promising candidates include the detection via spin-polarized point contacts [36], mesoscopic Stern-Gerlach type spin filters [216] or the inverse spin Hall effect [134]. However, the functionality of all those detection methods is limited to specific situations and there is no mechanism that can generically be applied for the detection of spin currents. Therefore, following the proof-of-principle calculations on coherent spin ratchets presented in this thesis, as a next step a setup should be worked out, which allows for the unambiguous detection of the spin ratchet currents.

References

- [1] C. Cohen-Tannoudji, B. Diu, and F. Laloë, *Quantenmechanik Teil 2*. Walter de Gruyter, Berlin, 1999.
- [2] W. Pauli, *The Connection Between Spin and Statistics*, Phys. Rev. **58**, 716 (1940).
- [3] W. Pauli, *Über den Zusammenhang des Abschlusses der Elektronengruppen im Atom mit der Komplexstruktur der Spektren*, Z. Phys. **31**, 765 (1925).
- [4] A. J. Leggett, *Quantum Liquids*, Science **319**, 1203 (2008).
- [5] *Nature Milestones in Spin*, Nature Phys. **4**, S1–S20 (2008).
- [6] A. Trabesinger, *Physics is set spinning*, Nature Phys. **4**, S5 (2008).
- [7] C. Cohen-Tannoudji, B. Diu, and F. Laloë, *Quantenmechanik Teil 1*. Walter de Gruyter, Berlin, 1999.
- [8] W. Pauli, *Über den Einfluß der Geschwindigkeitsabhängigkeit der Elektronenmasse auf den Zeemaneffekt*, Z. Phys. **31**, 373 (1925).
- [9] P. A. M. Dirac, *The quantum theory of the electron*, Proc. R. Soc. Lond. A **117**, 610 (1928).
- [10] M. N. Baibich, J. M. Broto, A. Fert, F. N. Van Dau, F. Petroff, P. Eitenne, G. Creuzet, A. Friederich, and J. Chazelas, *Giant Magnetoresistance of (001)Fe/(001)Cr Magnetic Superlattices*, Phys. Rev. Lett. **61**, 2472 (1988).
- [11] G. Binasch, P. Grünberg, F. Saurenbach, and W. Zinn, *Enhanced magnetoresistance in layered magnetic structures with antiferromagnetic interlayer exchange*, Phys. Rev. B **39**, 4828 (1989).

-
- [12] S. A. Wolf, D. D. Awschalom, R. R. Buhrmann, J. M. Daughton, S. von Molnár, M. L. Roukes, A. Y. Chtchelkanova, and D. M. Treger, *Spintronics: A Spin-Based Electronics Vision for the Future*, Science **294**, 1488 (2001).
- [13] P. C. Lauterbur, *Image formation by induced local interactions - Examples employing nuclear magnetic-resonance*, Nature **242**, 190 (1973).
- [14] G. E. Moore, *Cramming more components onto integrated circuits*, Electronics **38**, 114 (1965).
- [15] J. D. Meindl, Q. Chen, and J. A. Davis, *Limits on Silicon Nanoelectronics for Terascale Integration*, Science **293**, 2044 (2001).
- [16] I. Žutić, J. Fabian, and S. Das Sarma, *Spintronics: Fundamentals and applications*, Rev. Mod. Phys. **76**, 323 (2004).
- [17] D. D. Awschalom and M. E. Flatté, *Challenges for semiconductor spintronics*, Nature Phys. **3**, 153 (2007).
- [18] S. Datta and B. Das, *Electronic analog of the electro-optic modulator*, Appl. Phys. Lett. **56**, 665 (1990).
- [19] J. Schliemann, J. C. Egues, and D. Loss, *Nonballistic Spin-Field-Effect Transistor*, Phys. Rev. Lett. **90**, 146801 (2003).
- [20] G. Cuniberti, G. Fagas, and K. Richter, eds., *Introducing Molecular Electronics*. Springer-Verlag, Berlin, 2005.
- [21] A. K. Geim and K. S. Novoselov, *The rise of graphene*, Nature Mater. **6**, 183 (2007).
- [22] J. Nitta, T. Akazaki, H. Takayanagi, and T. Enoki, *Gate Control of Spin-Orbit Interaction in an Inverted $In_{0.53}Ga_{0.47}As/In_{0.52}Al_{0.48}As$ Heterostructure*, Phys. Rev. Lett. **78**, 1335 (1997).
- [23] D. D. Awschalom, D. Loss, and N. Samarth, eds., *Semiconductor spintronics and quantum computation*. Springer-Verlag, Berlin, 2002.
- [24] J. Fabian, A. Matos-Abiague, C. Ertler, P. Stano, and I. Žutić, *Semiconductor spintronics*, Acta Phys. Slovaca **57**, 565 (2007).
- [25] H. C. Koo, J. H. Kwon, J. Eom, J. Chang, S. H. Han, and M. Johnson, *Control of Spin Precession in a Spin-Injected Field Effect Transistor*, Science **325**, 1515 (2009).
- [26] G. Schmidt, D. Ferrand, L. W. Molenkamp, A. T. Filip, and B. J. van Wees, *Fundamental obstacle for electrical spin injection from a ferromagnetic metal into a diffusive semiconductor*, Phys. Rev. B **62**, R4790 (2000).

-
- [27] A. T. Hanbicki, B. T. Jonker, G. Itskos, G. Kioseoglou, and A. Petrou, *Efficient electrical spin injection from a magnetic metal/tunnel barrier contact into a semiconductor*, Appl. Phys. Lett. **80**, 1240 (2002).
- [28] V. F. Motsnyi, J. D. Boeck, J. Das, W. V. Roy, G. Borghs, E. Goovaerts, and V. I. Safarov, *Electrical spin injection in a ferromagnet/tunnel barrier/semiconductor heterostructure*, Appl. Phys. Lett. **81**, 265 (2002).
- [29] R. Fiederling, M. Keim, G. Reuscher, W. Ossau, G. Schmidt, A. Waag, and L. W. Molenkamp, *Injection and detection of a spin-polarized current in a light-emitting diode*, Nature **402**, 787 (1999).
- [30] Y. Ohno, B. Young, B. Beschoten, F. Matsukura, H. Ohno, and D. D. Awschalom, *Electrical spin injection in a ferromagnetic semiconductor heterostructure*, Nature **402**, 790 (1999).
- [31] S. D. Ganichev, E. L. Ivchenko, S. N. Danilov, J. Eroms, W. Wegscheider, D. Weiss, and W. Prettl, *Conversion of Spin into Directed Electric Current in Quantum Wells*, Phys. Rev. Lett. **86**, 4358 (2001).
- [32] F. Vasko and N. Prima, *Spin splitting of the spectrum of two-dimensional electrons*, Sov. Phys. Solid State **21**, 994 (1979).
- [33] A. Aronov and Y. Lyanda-Geller, *Nuclear electric resonance and orientation of carrier spins by an electric field*, JETP Lett. **50**, 431 (1989).
- [34] M. I. D'yakonov and V. I. Perel', *Possibility of orienting electron spins with current*, JETP Lett. **13**, 467 (1971).
- [35] J. Sinova, D. Culcer, Q. Niu, N. A. Sinitsyn, T. Jungwirth, and A. H. MacDonald, *Universal Intrinsic Spin Hall Effect*, Phys. Rev. Lett. **92**, 126603 (2004).
- [36] R. M. Potok, J. A. Folk, C. M. Marcus, and V. Umansky, *Detecting Spin-Polarized Currents in Ballistic Nanostructures*, Phys. Rev. Lett. **89**, 266602 (2002).
- [37] X. Lou, C. Adelmann, S. A. Crooker, E. S. Garlid, J. Zhang, K. S. M. Reddy, S. D. Flexner, C. J. Palmstrom, and P. A. Crowell, *Electrical detection of spin transport in lateral ferromagnet-semiconductor devices*, Nature Phys. **3**, 197 (2007).
- [38] S. Crooker, M. Furis, X. Lou, C. Adelmann, D. Smith, C. Palmstrom, and P. Crowell, *Imaging spin transport in lateral ferromagnet/semiconductor structures*, Science **309**, 2191 (2005).

-
- [39] P. Kotissek, M. Bailleul, M. Sperl, A. Spitzer, D. Schuh, W. Wegscheider, C. H. Back, and G. Bayreuther, *Cross-sectional imaging of spin injection into a semiconductor*, Nature Phys. **3**, 872 (2007).
- [40] S. Bandyopadhyay and M. Cahay, *Introduction to Spintronics*. CRC Press, Boca Raton, 2008.
- [41] V. V. Bel'kov, P. Olbrich, S. A. Tarasenko, D. Schuh, W. Wegscheider, T. Korn, C. Schüller, D. Weiss, W. Prettl, and S. D. Ganichev, *Symmetry and Spin Dephasing in (110)-Grown Quantum Wells*, Phys. Rev. Lett. **100**, 176806 (2008).
- [42] J. D. Koralek, C. P. Weber, J. Orenstein, B. A. Bernevig, S.-C. Zhang, S. Mack, and D. D. Awschalom, *Emergence of the persistent spin helix in semiconductor quantum wells*, Nature **458**, 610 (2009).
- [43] V. Lechner, L. E. Golub, P. Olbrich, S. Stachel, D. Schuh, W. Wegscheider, V. V. Bel'kov, and S. D. Ganichev, *Tuning of structure inversion asymmetry by the delta-doping position in (001)-grown GaAs quantum wells*, Appl. Phys. Lett. **94**, 242109 (2009).
- [44] T. Schäpers, V. A. Guzenko, M. G. Pala, U. Zülicke, M. Governale, J. Knobbe, and H. Hardtdegen, *Suppression of weak antilocalization in $Ga_xIn_{1-x}As/InP$ narrow quantum wires*, Phys. Rev. B **74**, 081301 (2006).
- [45] D. Loss and D. P. DiVincenzo, *Quantum computation with quantum dots*, Phys. Rev. A **57**, 120 (1998).
- [46] B. A. Bernevig and S.-C. Zhang, *Quantum Spin Hall Effect*, Phys. Rev. Lett. **96**, 106802 (2006).
- [47] Y. Kato, R. Myers, A. Gossard, and D. Awschalom, *Observation of the spin hall effect in semiconductors*, Science **306**, 1910 (2004).
- [48] M. Koenig, S. Wiedmann, C. Bruene, A. Roth, H. Buhmann, L. W. Molenkamp, X.-L. Qi, and S.-C. Zhang, *Quantum spin hall insulator state in HgTe quantum wells*, Science **318**, 766 (2007).
- [49] P. Reimann, *Brownian motors: noisy transport far from equilibrium*, Phys. Rep. **361**, 57 (2002).
- [50] V. M. Edelstein, *Spin polarization of conduction electrons induced by electric current in two-dimensional asymmetric electron systems*, Solid State Commun. **73**, 233 (1990).
- [51] N. W. Ashcroft and N. D. Mermin, *Solid State Physics*. Saunders College Publishing, Fort Worth, 1976.

-
- [52] S. Datta, *Electronic Transport in Mesoscopic Systems*. Cambridge University Press, Cambridge, 1995.
- [53] E. O. Kane, *Band structure of indium antimonide*, J. Phys. Chem. Solids **1**, 249 (1957).
- [54] C. W. J. Beenakker and H. van Houten, *Quantum transport in semiconductor nanostructures*, Solid State Phys. **44**, 1 (1991).
- [55] D. J. BenDaniel and C. B. Duke, *Space-Charge Effects on Electron Tunneling*, Phys. Rev. **152**, 683 (1966).
- [56] D. K. Ferry and S. M. Goodnick, *Transport in Nanostructures*. Cambridge University Press, Cambridge, 1997.
- [57] R. Winkler, *Spin-orbit coupling effects in two-dimensional electron and hole systems*. Springer, Berlin, 2003.
- [58] L. M. Roth, B. Lax, and S. Zwerdling, *Theory of optical magneto-absorption effects in semiconductors*, Phys. Rev. **114**, 90 (1959).
- [59] R. Lassnig, $\vec{k} \cdot \vec{p}$ theory, effective-mass approach, and spin splitting for two-dimensional electrons in GaAs-GaAlAs heterostructures, Phys. Rev. B **31**, 8076 (1985).
- [60] E. A. de Andrada e Silva, G. C. La Rocca, and F. Bassani, *Spin-orbit splitting of electronic states in semiconductor asymmetric quantum wells*, Phys. Rev. B **55**, 16293 (1997).
- [61] E. I. Rashba, *Properties of semiconductors with an extremum loop i. cyclotron and combinational resonance in a magnetic field perpendicular to the plane of the loop*, Sov. Phys. Solid State **2**, 1109 (1960).
- [62] D. Stein, K. v. Klitzing, and G. Weimann, *Electron Spin Resonance on GaAs-Al_xGa_{1-x}As Heterostructures*, Phys. Rev. Lett. **51**, 130 (1983).
- [63] H. L. Stormer, Z. Schlesinger, A. Chang, D. C. Tsui, A. C. Gossard, and W. Wiegmann, *Energy Structure and Quantized Hall Effect of Two-Dimensional Holes*, Phys. Rev. Lett. **51**, 126 (1983).
- [64] Y. A. Bychkov and E. I. Rashba, *Oscillatory effects and the magnetic susceptibility of carriers in inversion layers*, J. Phys. C **17**, 6039 (1984).
- [65] G. Lommer, F. Malcher, and U. Rössler, *Spin splitting in semiconductor heterostructures for $B \rightarrow 0$* , Phys. Rev. Lett. **60**, 728 (1988).

- [66] E. A. de Andrada e Silva, G. C. La Rocca, and F. Bassani, *Spin-split subbands and magneto-oscillations in III-V asymmetric heterostructures*, Phys. Rev. B **50**, 8523 (1994).
- [67] B. Das, D. C. Miller, S. Datta, R. Reifenberger, W. P. Hong, P. K. Bhattacharya, J. Singh, and M. Jaffe, *Evidence for spin splitting in $In_xGa_{1-x}As/In_{0.52}Al_{0.48}As$ heterostructures as $B \rightarrow 0$* , Phys. Rev. B **39**, 1411 (1989).
- [68] S. Giglberger, L. E. Golub, V. V. Bel'kov, S. N. Danilov, D. Schuh, C. Gerl, F. Rohlfing, J. Stahl, W. Wegscheider, D. Weiss, W. Prettl, and S. D. Ganichev, *Rashba and Dresselhaus spin splittings in semiconductor quantum wells measured by spin photocurrents*, Phys. Rev. B **75**, 035327 (2007).
- [69] E. Bernardes, J. Schliemann, M. Lee, J. C. Egues, and D. Loss, *Spin-Orbit Interaction in Symmetric Wells with Two Subbands*, Phys. Rev. Lett. **99**, 076603 (2007).
- [70] G. Dresselhaus, *Spin-Orbit Coupling Effects in Zinc Blende Structures*, Phys. Rev. **100**, 580 (1955).
- [71] J. J. Krich and B. I. Halperin, *Cubic Dresselhaus Spin-Orbit Coupling in 2D Electron Quantum Dots*, Phys. Rev. Lett. **98**, 226802 (2007).
- [72] R. Eppenga and M. F. H. Schuurmans, *Effect of bulk inversion asymmetry on $[001]$, $[110]$, and $[111]$ GaAs/AlAs quantum wells*, Phys. Rev. B **37**, 10923 (1988).
- [73] A. Łusakowski, J. Wróbel, and T. Dietl, *Effect of bulk inversion asymmetry on the Datta-Das transistor*, Phys. Rev. B **68**, 081201 (2003).
- [74] L. Meier, G. Salis, I. Shorubalko, E. Gini, S. Schön, and K. Ensslin, *Measurement of Rashba and Dresselhaus spin-orbit magnetic fields*, Nature Phys. **3**, 650 (2007).
- [75] M. I. D'yakonov and V. I. Perel', *Spin relaxation of conduction electrons in noncentrosymmetric semiconductors*, Sov. Phys. Solid State **13**, 3023 (1972).
- [76] R. J. Elliott, *Theory of the Effect of Spin-Orbit Coupling on Magnetic Resonance in Some Semiconductors*, Phys. Rev. **96**, 266 (1954).
- [77] Y. Yafet, *g factors and spin-lattice relaxation of conduction electrons*, Solid State Phys. **14**, 2 (1963).
- [78] A. W. Holleitner, V. Sih, R. C. Myers, A. C. Gossard, and D. D. Awschalom, *Suppression of Spin Relaxation in Submicron InGaAs Wires*, Phys. Rev. Lett. **97**, 036805 (2006).

-
- [79] G. Bir, A. Aronov, and G. Pikus, *Spin relaxation of electrons scattered by holes*, Sov. Phys. JETP **69**, 1382 (1975).
- [80] R. Landauer, *Electrical Resistance of Disordered One-dimensional Lattices*, Phil. Mag. **21**, 863 (1970).
- [81] M. Büttiker, Y. Imry, R. Landauer, and S. Pinhas, *Generalized many-channel conductance formula with application to small rings*, Phys. Rev. B **31**, 6207 (1985).
- [82] H. Bruus and K. Flensberg, *Many-body Quantum Theory in Condensed Matter Physics: An Introduction*. Oxford University Press, Oxford, 2004.
- [83] M. Wimmer, *Quantum transport in nanostructures: From computational concepts to spintronics in graphene and magnetic tunnel junctions*. PhD thesis, Universität Regensburg, 2008.
- [84] E. I. Rashba, *Spin dynamics and spin transport*, J. Supercond. **18**, 137 (2005).
- [85] M. Scheid, *Directed quantum transport in non-uniform magnetic fields*, Master's thesis, Universität Regensburg, 2006.
- [86] M. Scheid, D. Bercioux, and K. Richter, *Zeeman ratchets: pure spin current generation in mesoscopic conductors with non-uniform magnetic fields*, New J. Phys. **9**, 401 (2007).
- [87] E. I. Rashba, *Spin currents in thermodynamic equilibrium: the challenge of discerning transport currents*, Phys. Rev. B **68**, 241315(R) (2003).
- [88] B. K. Nikolic, L. P. Zârbo, and S. Souma, *Imaging mesoscopic spin hall flow: spatial distribution of local spin currents and spin densities in and out of multiterminal spin-orbit coupled semiconductor nanostructures*, Phys. Rev. B **73**, 075303 (2006).
- [89] J. Schliemann, *Spin Hall effect*, Int. J. Mod. Phys. B **20**, 1015 (2006).
- [90] L. P. Kadanoff and G. Baym, *Quantum Statistical Mechanics*. W. A. Benjamin, New York, 1962.
- [91] L. Keldysh, *Diagram technique for nonequilibrium processes*, Sov. Phys. JETP **20**, 1018 (1965).
- [92] H. Haug and A.-P. Jauho, *Quantum kinetics in transport and optics of semiconductors*. Springer-Verlag, Berlin, 1997.
- [93] W. Nolting, *Grundkurs theoretische Physik 5/1, Quantenmechanik – Grundlagen*. Springer-Verlag, Berlin, 2002.

-
- [94] Y. Meir and N. S. Wingreen, *Landauer formula for the current through an interacting electron region*, Phys. Rev. Lett. **68**, 2512 (1992).
- [95] D. S. Fisher and P. A. Lee, *Relation between conductivity and transmission matrix*, Phys. Rev. B **23**, 6851 (1981).
- [96] A. D. Stone and A. Szafer, *What is measured when you measure a resistance? - The Landauer formula revisited*, IBM J. Res. Dev. **32**, 384 (1988).
- [97] H. U. Baranger and A. D. Stone, *Electrical linear-response theory in an arbitrary magnetic field: A new Fermi-surface formation*, Phys. Rev. B **40**, 8169 (1989).
- [98] G. E. Kimball and G. H. Shortley, *The Numerical Solution of Schrödinger's Equation*, Phys. Rev. **45**, 815 (1934).
- [99] D. Eberly, *Derivative Approximation by Finite Differences*, <http://www.geometrictools.com/Documentation/FiniteDifferences.pdf> (2008).
- [100] P. W. Anderson, *Absence of Diffusion in Certain Random Lattices*, Phys. Rev. **109**, 1492 (1958).
- [101] P. A. Lee and D. S. Fisher, *Anderson Localization in Two Dimensions*, Phys. Rev. Lett. **47**, 882 (1981).
- [102] A. D. Stone, *Magnetoresistance Fluctuations in Mesoscopic Wires and Rings*, Phys. Rev. Lett. **54**, 2692 (1985).
- [103] T. Ando, *Quantum point contacts in magnetic fields*, Phys. Rev. B **44**, 8017 (1991).
- [104] A. MacKinnon, *The calculation of transport-properties and density of states of disordered solids*, Z. Phys. B **59**, 385 (1985).
- [105] M. Wimmer, M. Scheid, and K. Richter, *Spin-polarized Quantum Transport in Mesoscopic Conductors: Computational Concepts and Physical Phenomena*, in *Encyclopedia of Complexity and System Science*, R. A. Meyers, ed., pp. 8597–8616. Springer, New York, 2009. arXiv:0803.3705v1.
- [106] M. Wimmer and K. Richter, *Optimal block-tridiagonalization of matrices for coherent charge transport*, J. Comp. Phys. (in press); arXiv:0806.2739v1 (2009).
- [107] B. L. Altshuler and L. I. Glazman, *Pumping Electrons*, Science **283**, 1864 (1999).

-
- [108] P. Hänggi and F. Marchesoni, *Artificial Brownian motors: Controlling transport on the nanoscale*, Rev. Mod. Phys. **81**, 387 (2009).
- [109] R. D. Astumian, *Thermodynamics and Kinetics of a Brownian Motor*, Science **276**, 917 (1997).
- [110] R. D. Astumian and P. Hänggi, *Brownian Motors*, Physics Today **no. 11**, 33 (2002).
- [111] H. Linke, T. E. Humphrey, A. Löfgren, A. O. Sushkov, R. Newbury, R. P. Taylor, and P. Omling, *Experimental Tunneling Ratchets*, Science **286**, 2314 (1999).
- [112] H. Linke, T. E. Humphrey, P. E. Lindelof, A. Löfgren, R. Newbury, P. Omling, A. O. Sushkov, R. P. Taylor, and H. Xu, *Quantum ratchets and quantum heat pumps*, Appl. Phys. A **75**, 237 (2002).
- [113] P. Reimann, M. Grifoni, and P. Hänggi, *Quantum Ratchets*, Phys. Rev. Lett. **79**, 10 (1997).
- [114] A. M. Song, A. Lorke, A. Kriele, J. P. Kotthaus, W. Wegscheider, and M. Bichler, *Nonlinear electron transport in an asymmetric microjunction: a ballistic rectifier*, Phys. Rev. Lett. **80**, 3831 (1998).
- [115] H. Linke, W. Sheng, A. Löfgren, H. Xu, P. Omling, and P. E. Lindelof, *A quantum dot ratchet: experiment and theory*, Europhys. Lett. **44**, 341 (1998).
- [116] M. Scheid, M. Wimmer, D. Bercioux, and K. Richter, *Zeeman ratchets for ballistic spin currents*, Phys. Status Solidi (c) **3**, 4235 (2006).
- [117] B. Braunecker, D. E. Feldman, and F. Li, *Spin current and rectification in one-dimensional electronic systems*, Phys. Rev. B **76**, 085119 (2007).
- [118] S. Smirnov, D. Bercioux, M. Grifoni, and K. Richter, *Quantum Dissipative Rashba Spin Ratchets*, Phys. Rev. Lett. **100**, 230601 (2008).
- [119] S. Smirnov, D. Bercioux, M. Grifoni, and K. Richter, *Interplay between quantum dissipation and an in-plane magnetic field in the spin ratchet effect*, Phys. Rev. B **78**, 245323 (2008).
- [120] S. Smirnov, D. Bercioux, M. Grifoni, and K. Richter, *Extrinsic and intrinsic ratchet response of a quantum dissipative spin-orbit medium*, arXiv:0903.2765v1 (unpublished) (2009).
- [121] A. Lassl, *Spin-dependent transport of interacting electrons in mesoscopic systems*. PhD thesis, Universität Regensburg, 2007.

-
- [122] S. E. Laux, D. J. Frank, and F. Stern, *Quasi-one-dimensional electron states in a split-gate GaAs/AlGaAs heterostructure*, Surf. Sci. **196**, 101 (1988).
- [123] Y. Xue, S. Datta, and M. A. Ratner, *First-principles based Matrix Green's function approach to molecular electronic devices: General formalism*, Chem. Phys. **281**, 151 (2002).
- [124] A. Nitzan, M. Galperin, G.-L. Ingold, and H. Grabert, *On the electrostatic potential profile in biased molecular wires*, J. Chem. Phys. **117**, 10837 (2002).
- [125] A. Trellakis, A. T. Galick, A. Pacelli, and U. Ravaioli, *Iteration scheme for the solution of the two-dimensional Schrödinger-Poisson equations in quantum structures*, J. Appl. Phys. **81**, 7880 (1997).
- [126] R. Lake, G. Klimeck, R. C. Bowen, and D. Jovanovic, *Single and multiband modeling of quantum electron transport through layered semiconductor devices*, J. Appl. Phys. **81**, 7845 (1997).
- [127] P. W. Brouwer, *Scattering approach to parametric pumping*, Phys. Rev. B **58**, R10135 (1998).
- [128] M. Governale, F. Taddei, and R. Fazio, *Pumping spin with electrical fields*, Phys. Rev. B **68**, 155324 (2003).
- [129] E. R. Mucciolo, C. Chamon, and C. M. Marcus, *Adiabatic Quantum Pump of Spin-Polarized Current*, Phys. Rev. Lett. **89**, 146802 (2002).
- [130] S. K. Watson, R. M. Potok, C. M. Marcus, and V. Umansky, *Experimental Realization of a Quantum Spin Pump*, Phys. Rev. Lett. **91**, 258301 (2003).
- [131] S. M. Frolov, A. Venkatesan, W. Yu, J. A. Folk, and W. Wegscheider, *Electrical Generation of Pure Spin Currents in a Two-Dimensional Electron Gas*, Phys. Rev. Lett. **102**, 116802 (2009).
- [132] J.-I. Inoue, G. E. W. Bauer, and L. W. Molenkamp, *Suppression of the persistent spin Hall current by defect scattering*, Phys. Rev. B **70**, 041303 (2004).
- [133] J. Sinova, S. Murakami, S.-Q. Shen, and M.-S. Choi, *Spin-hall effect: back to the beginning at a higher level*, Solid State Commun. **138**, 214 (2006).
- [134] E. M. Hankiewicz, L. W. Molenkamp, T. Jungwirth, and J. Sinova, *Manifestation of the spin hall effect through charge-transport in the mesoscopic regime*, Phys. Rev. B **70**, 241301(R) (2004).
- [135] E. Cota, R. Aguado, C. E. Creffield, and G. Platero, *Spin-polarised pumping in a double quantum dot*, Nanotechnology **14**, 152 (2003).

-
- [136] E. Cota, R. Aguado, and G. Platero, *ac-Driven Double Quantum Dots as Spin Pumps and Spin Filters*, Phys. Rev. Lett. **94**, 107202 (2005).
- [137] Q.-f. Sun, H. Guo, and J. Wang, *A Spin Cell for Spin Current*, Phys. Rev. Lett. **90**, 258301 (2003).
- [138] D. J. Kittel, *Introduction to solid state physics*. John Wiley & Sons, New York, 1996.
- [139] V. Kubrak, A. C. Neumann, B. L. Gallagher, P. C. Main, M. Henini, C. H. Marrows, and M. A. Howson, *Longitudinal and hall resistance induced by large-amplitude magnetic barriers*, Physica E **6**, 755 (2000).
- [140] J. Jackson, *Classical Electrodynamics*. John Wiley & Sons, New York, 1999.
- [141] D. J. Craik, *Magnetism: principles and applications*. John Wiley & Sons, Chichester, 1995.
- [142] D. Uzur, A. Nogaret, H. E. Beere, D. A. Ritchie, C. H. Marrows, and B. J. Hickey, *Probing the annular electronic shell structure of a magnetic corral*, Phys. Rev. B **69**, 241301 (2004).
- [143] A. Slobodskyy, C. Gould, T. Slobodskyy, C. R. Becker, G. Schmidt, and L. W. Molenkamp, *Voltage-Controlled Spin Selection in a Magnetic Resonant Tunneling Diode*, Phys. Rev. Lett. **90**, 246601 (2003).
- [144] C. Ertler and J. Fabian, *Resonant tunneling magnetoresistance in coupled quantum wells*, Appl. Phys. Lett. **89**, 242101 (2006).
- [145] S. J. Koester, B. Brar, C. R. Bolognesi, E. J. Caine, A. Patlach, E. L. Hu, H. Kroemer, and M. J. Rooks, *Length dependence of quantized conductance in ballistic constrictions fabricated on InAs/AlSb quantum wells*, Phys. Rev. B **53**, 13063 (1996).
- [146] E. M. Höhberger, A. Lorke, W. Wegscheider, and M. Bichler, *Adiabatic pumping of two-dimensional electrons in a ratchet-type lateral superlattice*, Appl. Phys. Lett. **78**, 2905 (2001).
- [147] A. Pfund, *A ratchet mechanism for directed spin transport in nanostructures*, Master's thesis, Universität Regensburg, 2005.
- [148] M. Eto, T. Hayashi, and Y. Kurotani, *Spin Polarization at Semiconductor Point Contacts in Absence of Magnetic Field*, J. Phys. Soc. Jpn. **74**, 1934 (2005).
- [149] B. J. van Wees, H. van Houten, C. W. J. Beenakker, J. G. Williamson, L. P. Kouwenhoven, D. van der Marel, and C. T. Foxon, *Quantized conductance of point contacts in a two-dimensional electron gas*, Phys. Rev. Lett. **60**, 848 (1988).

-
- [150] D. A. Wharam, T. J. Thornton, R. Newbury, M. Pepper, H. Ahmed, J. E. F. Frost, D. G. Hasko, D. C. Peacock, D. A. Ritchie, and G. A. C. Jones, *One-dimensional transport and the quantisation of the ballistic resistance*, J. Phys. C **21**, L209 (1988).
- [151] L. Landau, *On the theory of transfer of energy at collisions II*, Phys. Z. Sov. **2**, 46 (1932).
- [152] C. Zener, *Non-Adiabatic Crossing of Energy Levels*, Proc. R. Soc. London, Ser. A **137**, 696 (1932).
- [153] M. Strehl, *Coherent spin ratchets: Transport and noise properties*, Master's thesis, Universität Regensburg, 2007.
- [154] F. Zhai and H. Q. Xu, *Spin filtering and spin accumulation in an electron stub waveguide with spin-orbit interaction*, Phys. Rev. B **76**, 035306 (2007).
- [155] F. Zhai and H. Q. Xu, *Symmetry of Spin Transport in Two-Terminal Waveguides with a Spin-Orbital Interaction and Magnetic Field Modulations*, Phys. Rev. Lett. **94**, 246601 (2005).
- [156] M. J. McLennan, Y. Lee, and S. Datta, *Voltage drop in mesoscopic systems: A numerical study using a quantum kinetic equation*, Phys. Rev. B **43**, 13846 (1991).
- [157] M. Scheid, A. Pfund, D. Bercioux, and K. Richter, *Coherent spin ratchets: A spin-orbit based quantum ratchet mechanism for spin-polarized currents in ballistic conductors*, Phys. Rev. B **76**, 195303 (2007).
- [158] D. Grundler, *Large Rashba Splitting in InAs Quantum Wells due to Electron Wave Function Penetration into the Barrier Layers*, Phys. Rev. Lett. **84**, 6074 (2000).
- [159] M. Johnson and R. H. Silsbee, *Interfacial charge-spin coupling: Injection and detection of spin magnetization in metals*, Phys. Rev. Lett. **55**, 1790 (1985).
- [160] A. G. Aronov, Y. Lyanda-Geller, and G. Pikus, *The spin polarization of electrons due to the electric-current*, Sov. Phys. JETP **73**, 537 (1991).
- [161] A. Y. Silov, P. A. Blajnov, J. H. Wolter, R. Hey, K. H. Ploog, and N. S. Averkiev, *Current-induced spin polarization at a single heterojunction*, Appl. Phys. Lett. **85**, 5929 (2004).
- [162] S. Ganichev, S. Danilov, P. Schneider, V. Bel'kov, L. Golub, W. Wegscheider, D. Weiss, and W. Prettl, *Electric current-induced spin orientation in quantum well structures*, J. Magn. Magn. Mater. **300**, 127 (2006).

-
- [163] Y. K. Kato, R. C. Myers, A. C. Gossard, and D. D. Awschalom, *Current-Induced Spin Polarization in Strained Semiconductors*, Phys. Rev. Lett. **93**, 176601 (2004).
- [164] V. Sih, R. Myers, Y. Kato, W. Lau, A. Gossard, and D. Awschalom, *Spatial imaging of the spin Hall effect and current-induced polarization in two-dimensional electron gases*, Nature Phys. **1**, 31 (2005).
- [165] A. V. Chaplik, M. V. Entin, and L. I. Magarill, *Spin orientation of electrons by lateral electric field in 2D system without inversion symmetry*, Physica E **13**, 744 (2002).
- [166] J.-I. Inoue, G. E. W. Bauer, and L. W. Molenkamp, *Diffuse transport and spin accumulation in a Rashba two-dimensional electron gas*, Phys. Rev. B **67**, 033104 (2003).
- [167] M. Trushin and J. Schliemann, *Anisotropic current-induced spin accumulation in the two-dimensional electron gas with spin-orbit coupling*, Phys. Rev. B **75**, 155323 (2007).
- [168] B. A. Bernevig, J. Orenstein, and S.-C. Zhang, *Exact $SU(2)$ Symmetry and Persistent Spin Helix in a Spin-Orbit Coupled System*, Phys. Rev. Lett. **97**, 236601 (2006).
- [169] O. E. Raichev, *Frequency dependence of induced spin polarization and spin current in quantum wells*, Phys. Rev. B **75**, 205340 (2007).
- [170] M. Duckheim, D. Loss, M. Scheid, K. Richter, I. Adagideli, and P. Jacquod, *Spin accumulation in diffusive conductors with Rashba and Dresselhaus spin-orbit interaction*, arXiv:0909.4253v1 (unpublished) (2009).
- [171] I. Adagideli and G. E. W. Bauer, *Intrinsic Spin Hall Edges*, Phys. Rev. Lett. **95**, 256602 (2005).
- [172] Y. Tserkovnyak, B. I. Halperin, A. A. Kovalev, and A. Brataas, *Boundary spin Hall effect in a two-dimensional semiconductor system with Rashba spin-orbit coupling*, Phys. Rev. B **76**, 085319 (2007).
- [173] I. Adagideli, M. Scheid, M. Wimmer, G. E. W. Bauer, and K. Richter, *Extracting current-induced spins: spin boundary conditions at narrow Hall contacts*, New J. Phys. **9**, 382 (2007).
- [174] I. Adagideli, G. E. W. Bauer, and B. I. Halperin, *Detection of Current-Induced Spins by Ferromagnetic Contacts*, Phys. Rev. Lett. **97**, 256601 (2006).
- [175] F. Zhai and H. Q. Xu, *Spin filtering in single magnetic barrier structures revisited*, Appl. Phys. Lett. **88**, 032502 (2006).

-
- [176] F. G. Monzon, M. Johnson, and M. L. Roukes, *Strong Hall voltage modulation in hybrid ferromagnet/semiconductor microstructures*, Appl. Phys. Lett. **71**, 3087 (1997).
- [177] A. Reynoso, G. Usaj, and C. A. Balseiro, *Spin Hall effect in clean two-dimensional electron gases with Rashba spin-orbit coupling*, Phys. Rev. B **73**, 115342 (2006).
- [178] O. Zaitsev, D. Frustaglia, and K. Richter, *Role of Orbital Dynamics in Spin Relaxation and Weak Antilocalization in Quantum Dots*, Phys. Rev. Lett. **94**, 026809 (2005).
- [179] H. van Houten, B. J. van Wees, M. G. J. Heijman, and J. P. André, *Submicron conducting channels defined by shallow mesa etch in GaAs-AlGaAs heterojunctions*, Appl. Phys. Lett. **49**, 1781 (1986).
- [180] P. W. Anderson, E. Abrahams, and T. V. Ramakrishnan, *Possible Explanation of Nonlinear Conductivity in Thin-Film Metal Wires*, Phys. Rev. Lett. **43**, 718 (1979).
- [181] L. Gorkov, A. Larkin, and D. Khmel'nitskii, *Particle conductivity in a two-dimensional random potential*, JETP Lett. **30**, 228 (1979).
- [182] S. Chakravarty and A. Schmid, *Weak localization: the quasiclassical theory of electrons in a random potential*, Phys. Rep. **140**, 193 (1986).
- [183] Y. Kunihashi, M. Kohda, and J. Nitta, *Enhancement of Spin Lifetime in Gate-Fitted InGaAs Narrow Wires*, Phys. Rev. Lett. **102**, 226601 (2009).
- [184] S. Hikami, A. Larkin, and Y. Nagaoka, *Spin-orbit interaction and magnetoresistance in the 2 dimensional random system*, Prog. Theor. Phys. **63**, 707 (1980).
- [185] C. W. J. Beenakker, *Random-matrix theory of quantum transport*, Rev. Mod. Phys. **69**, 731 (1997).
- [186] B. Altshuler, *Fluctuations in the extrinsic conductivity of disordered conductors*, JETP Lett. **41**, 648 (1985).
- [187] P. A. Lee and A. D. Stone, *Universal Conductance Fluctuations in Metals*, Phys. Rev. Lett. **55**, 1622 (1985).
- [188] B. Altshuler, V. Kravtsov, and I. Lerner, *Statistical properties of mesoscopic fluctuations and similarity theory*, JETP Lett. **43**, 441 (1986).
- [189] I. L. Aleiner and V. I. Fal'ko, *Spin-Orbit Coupling Effects on Quantum Transport in Lateral Semiconductor Dots*, Phys. Rev. Lett. **87**, 256801 (2001).

-
- [190] O. Zaitsev, D. Frustaglia, and K. Richter, *Semiclassical theory of weak antilocalization and spin relaxation in ballistic quantum dots*, Phys. Rev. B **72**, 155325 (2005).
- [191] A. A. Kiselev and K. W. Kim, *Progressive suppression of spin relaxation in two-dimensional channels of finite width*, Phys. Rev. B **61**, 13115 (2000).
- [192] P. Lehnen, T. Schäpers, N. Kaluza, N. Thilloßen, and H. Hardtdegen, *Enhanced spin-orbit scattering length in narrow $Al_xGa_{1-x}N/GaN$ wires*, Phys. Rev. B **76**, 205307 (2007).
- [193] S. Kettemann, *Dimensional Control of Antilocalization and Spin Relaxation in Quantum Wires*, Phys. Rev. Lett. **98**, 176808 (2007).
- [194] P. A. Mello, *Macroscopic approach to universal conductance fluctuations in disordered metals*, Phys. Rev. Lett. **60**, 1089 (1988).
- [195] P. A. Mello and A. D. Stone, *Maximum-entropy model for quantum-mechanical interference effects in metallic conductors*, Phys. Rev. B **44**, 3559 (1991).
- [196] Y. B. Lyanda-Geller and A. D. Mirlin, *Novel symmetry of a random matrix ensemble: Partially broken spin rotation invariance*, Phys. Rev. Lett. **72**, 1894 (1994).
- [197] S. Bandyopadhyay and M. Cahay, *Proposal for a spintronic femto-Tesla magnetic field sensor*, Physica E **27**, 98 (2005).
- [198] F. Dolcini and L. Dell'Anna, *Multiple Andreev reflections in a quantum dot coupled to superconducting leads: Effect of spin-orbit coupling*, Phys. Rev. B **78**, 024518 (2008).
- [199] R. G. Nazmitdinov, K. N. Pichugin, and M. Valín-Rodríguez, *Spin control in semiconductor quantum wires: Rashba and Dresselhaus interaction*, Phys. Rev. B **79**, 193303 (2009).
- [200] F. E. Meijer, A. F. Morpurgo, T. M. Klapwijk, T. Koga, and J. Nitta, *Competition between spin-orbit interaction and Zeeman coupling in Rashba two-dimensional electron gases*, Phys. Rev. B **70**, 201307 (2004).
- [201] F. E. Meijer, A. F. Morpurgo, T. M. Klapwijk, and J. Nitta, *Universal Spin-Induced Time Reversal Symmetry Breaking in Two-Dimensional Electron Gases with Rashba Spin-Orbit Interaction*, Phys. Rev. Lett. **94**, 186805 (2005).
- [202] X. Cartoixà, D. Z.-Y. Ting, and Y.-C. Chang, *A resonant spin lifetime transistor*, Appl. Phys. Lett. **83**, 1462 (2003).

-
- [203] F. G. Pikus and G. E. Pikus, *Conduction-band spin splitting and negative magnetoresistance in A_3B_5 heterostructures*, Phys. Rev. B **51**, 16928 (1995).
- [204] A. G. Mal'shukov, K. A. Chao, and M. Willander, *Magnetoresistance of a weakly disordered III-V semiconductor quantum well in a magnetic field parallel to interfaces*, Phys. Rev. B **56**, 6436 (1997).
- [205] S. D. Ganichev, V. V. Bel'kov, L. E. Golub, E. L. Ivchenko, P. Schneider, S. Giglberger, J. Eroms, J. De Boeck, G. Borghs, W. Wegscheider, D. Weiss, and W. Prettl, *Experimental Separation of Rashba and Dresselhaus Spin Splittings in Semiconductor Quantum Wells*, Phys. Rev. Lett. **92**, 256601 (2004).
- [206] W. Knap, C. Skierbiszewski, A. Zduniak, E. Litwin-Staszewska, D. Bertho, F. Kobbi, J. L. Robert, G. E. Pikus, F. G. Pikus, S. V. Iordanskii, V. Mosser, K. Zekentes, and Y. B. Lyanda-Geller, *Weak antilocalization and spin precession in quantum wells*, Phys. Rev. B **53**, 3912 (1996).
- [207] J. B. Miller, D. M. Zumbühl, C. M. Marcus, Y. B. Lyanda-Geller, D. Goldhaber-Gordon, K. Campman, and A. C. Gossard, *Gate-Controlled Spin-Orbit Quantum Interference Effects in Lateral Transport*, Phys. Rev. Lett. **90**, 076807 (2003).
- [208] T. Bergsten, T. Kobayashi, Y. Sekine, and J. Nitta, *Experimental Demonstration of the Time Reversal Aharonov-Casher Effect*, Phys. Rev. Lett. **97**, 196803 (2006).
- [209] A. G. Mal'shukov, V. A. Frolov, and K. A. Chao, *Crystal anisotropy effects on the weak-localization magnetoresistance of a III-V semiconductor quantum well in a magnetic field parallel to interfaces*, Phys. Rev. B **59**, 5702 (1999).
- [210] A. W. Holleitner, V. Sih, R. C. Myers, A. C. Gossard, and D. D. Awschalom, *Dimensionally constrained D'yakonov-Perel' spin relaxation in n-InGaAs channels: transition from 2D to 1D*, New J. Phys. **9**, 342 (2007).
- [211] M. Scheid (unpublished) (2009).
- [212] Y. Kunihashi, M. Kohda, and J. Nitta, *Anisotropic spin splitting in InGaAs wire structures*, (unpublished) (2009).
- [213] J. Nitta. private communication.
- [214] N. S. Averkiev, L. E. Golub, A. S. Gurevich, V. P. Evtikhiev, V. P. Kochereshko, A. V. Platonov, A. S. Shkolnik, and Y. P. Efimov, *Spin-relaxation anisotropy in asymmetrical (001) $Al_xGa_{1-x}As$ quantum wells from Hanle-effect measurements: Relative strengths of Rashba and Dresselhaus spin-orbit coupling*, Phys. Rev. B **74**, 033305 (2006).

-
- [215] E. J. Koop, B. J. van Wees, D. Reuter, A. D. Wieck, and C. H. van der Wal, *Spin Accumulation and Spin Relaxation in a Large Open Quantum Dot*, Phys. Rev. Lett. **101**, 056602 (2008).
- [216] J.-I. Ohe, M. Yamamoto, T. Ohtsuki, and J. Nitta, *Mesoscopic Stern-Gerlach spin filter by nonuniform spin-orbit interaction*, Phys. Rev. B **72**, 041308 (2005).

List of publications

- N. G. Fytas, F. K. Diakonov, P. Schmelcher, **M. Scheid**, A. Lassel, K. Richter, and G. Fagas, *Magnetic-field dependence of transport in normal and Andreev billiards: a classical interpretation to the averaged quantum behavior*, Phys. Rev. B **72**, 085336 (2005).
- **M. Scheid**, M. Wimmer, D. Bercioux, and K. Richter, *Zeeman ratchets for ballistic spin currents*, Phys. Status Solidi (c) **3**, 4235 (2006).
- I. Adagideli, **M. Scheid**, M. Wimmer, G. E. W. Bauer, and K. Richter, *Extracting current-induced spins: spin boundary conditions at narrow Hall contacts*, New J. Phys. **9**, 382 (2007).
- **M. Scheid**, A. Pfund, D. Bercioux, and K. Richter, *Coherent spin ratchets: A spin-orbit based quantum ratchet mechanism for spin-polarized currents in ballistic conductors*, Phys. Rev. B **76**, 195303 (2007).
- **M. Scheid**, D. Bercioux, and K. Richter, *Zeeman ratchets: pure spin current generation in mesoscopic conductors with non-uniform magnetic fields*, New J. Phys. **9**, 401 (2007).
- **M. Scheid**, M. Kohda, Y. Kunihashi, K. Richter, and J. Nitta, *All-electrical detection of the relative strength of Rashba and Dresselhaus spin-orbit interaction in quantum wires*, Phys. Rev. Lett. **101**, 266401 (2008).
- **M. Scheid**, I. Adagideli, J. Nitta, and K. Richter, *Anisotropic universal conductance fluctuations in disordered quantum wires with Rashba and Dresselhaus spin-orbit interaction and applied in-plane magnetic field*, Semicond. Sci. Technol. **24**, 064005 (2009).
- **M. Scheid**, A. Lassel, and K. Richter, *Resonant tunneling-based spin ratchets*, EPL **87**, 17001 (2009).
- M. Wimmer, **M. Scheid**, and K. Richter, *Spin-polarized Quantum Transport in Mesoscopic Conductors: Computational Concepts and Physical Phenomena*, in *Encyclopedia of Complexity and System Science*, R. A. Meyers, ed., pp. 8597–8616. Springer, New York, 2009. arXiv:0803.3705v1.
- M. Duckheim, D. Loss, **M. Scheid**, K. Richter, I. Adagideli, and P. Jacquod, *Spin accumulation in diffusive conductors with Rashba and Dresselhaus spin-orbit interaction*, Phys. Rev. B **81**, 085303 (2010).

Danksagung

Abschließend möchte ich an dieser Stelle einer Vielzahl von Menschen danken, die zum Gelingen dieser Arbeit beigetragen haben.

An erster Stelle möchte ich mich ganz herzlich bei meinem Betreuer Prof. Dr. Klaus Richter bedanken, dass er es mir ermöglicht hat, die hier vorliegende Arbeit unter seiner Betreuung anzufertigen. Er hatte stets ein offenes Ohr für mich und hat mich immer in all meinen Bemühungen unterstützt.

Während der vergangenen drei Jahre hatte ich das große Glück, an einer Vielzahl von Fragestellungen mit verschiedenen Kollegen und Freunden zusammenarbeiten zu können. Besonders durch die Diskussionen mit und die Ratschläge von Dr. Dario Bercioux, Prof. Inanc Adagideli, Dr. Michael Wimmer, Prof. Junsaku Nitta und Dr. Andreas Lassl wurde die Arbeit in der jetzigen Form erst ermöglicht.

Ein spezieller Dank sei dabei an Michael Wimmer gerichtet, der mir nicht nur seinen Programmcode als Grundlage für meine Rechnungen zur Verfügung gestellt hat, sondern sich auch stets Zeit für mich genommen hat, wenn ich Unterstützung verschiedenster Art benötigte.

Allen übrigen Mitgliedern des Lehrstuhls, insbesondere Angela Reißer, gebührt ein großer Dank für die nette und herzliche Atmosphäre, die ich seit einigen Jahren hier genießen konnte. In diesem Zusammenhang seien auch noch einmal gesondert meine Bürokollegen Michael Wimmer, Michael Hartung (danke besonders für die zahllose Hilfe in technischen Dingen), Timo Hartmann und Arseni Goussev erwähnt.

Für ihre Gastfreundschaft während meiner beiden Aufenthalte an der Tohoku University in Sendai möchte ich mich herzlich bei Prof. Junsaku Nitta und allen Mitgliedern seiner Arbeitsgruppe bedanken. Ich habe die Zeit in Japan sehr genossen.

Des Weiteren gebührt folgenden Personen ein großer Dank für das Probelesen von Teilen meiner Arbeit: Inanc Adagideli, Dario Bercioux, Jan Bundesmann, Tobias Dollinger, Timo Hartmann, Viktor Krückl, Jack Kuipers, Juan-Diego Urbina, Michael Wimmer und Jürgen Wurm.

Ohne die finanzielle Unterstützung verschiedenster Organisationen wäre es mir nicht möglich gewesen, diese Arbeit durchzuführen. Dafür ein herzlicher Dank an die Studienstiftung des Deutschen Volkes, die DFG im Rahmen des SFB 689, die Japan Society for the Promotion of Science (JSPS) und an die Universität Regensburg.

Schließlich möchte ich mich noch bei meinen Eltern und meiner Schwester Sabine für deren stetige Unterstützung bedanken und zum Schluß danke ich Anita, dass sie während der letzten Jahre Teil meines Lebens war und es so ungemein bereichert hat.

Regensburg, Oktober 2009.